Interaction of Metal Complexes with Nucleic Acids

A Thermodynamic and Kinetic Study, with an Eye on Photoreactive Processes

A Thesis submitted for the degree of
Doctor of Advanced Chemistry

Matteo Lari

Universidad de Burgos
Departamento de Química
Área de Química Física
Burgos, January 2018

Universidad de Burgos

Departamento de Química

Área de Química Física

Prof. Begoña García Ruiz y Prof. José María Leal Villalba, Profesores del Área de Química Física de la Universidad de Burgos

Certifican

Que el licenciado Matteo Lari ha realizado bajo sus direcciones el trabajo titulado *"Interaction of Metal Complexes with Nucleic Acid. A Thermodynamic and Kinetic Study, with an Eye on Photoreactive Processes"*.
Considerando que dicho trabajo reúne los requisitos exigidos para ser presentado como Tesis Doctoral, expresan su conformidad con dicha presentación.
Y para que conste, firman el presente certificado en Burgos a veinte de Noviembre de dos mil diecisiete.

Burgos, a 20 de Noviembre de 2017

Prof. Begoña García Ruiz Prof. José Maria Leal Villalba

A Mio Papà

At the end of such an important journey, now it's the time to acknowledge all the people making part of it. As my PhD coincides with a new adventure in a foreign State, I really feel it part of my training period.
First of all, I would acknowledge my supervisors, Professor Begoña García and Professor José Maria Leal, which gave me the opportunity to enjoy their group and to introduce me in the research world. In addition, I acknowledge the Obra Social la Caixa for the received grant during these years of PhD from the OSCL-2012-007 Caixa Project.
Thanks to the group of QuiFis Lab, which share together these years of study with: Dr. Natalia Busto, for her support with the methods and techniques in the Phys Chem lab, and for making this Thesis more biologically attractive, and my colleagues, (Dr. !) Hector, Cristina, Ana Rosa, Javi, Jesus, Carolina and all the people who have joined the group along these years. Thank you for the time spent together and for all the help you provided me.
In addition, I would like to acknowledge the people of the laboratories which I collaborated with during my PhD period. First of all, I want to thank Prof. Tarita Biver, which was my supervisor in the Università di Pisa during my Master's Degree and, together with Professor Fernando Secco, an important collaborator for our group. Thank you for your help before, during and (I hope!) after my PhD.
Then, I really want to thank Professor Gustavo Espino, for let me work in his laboratory and teach me the synthesis processes, always helping me when I went to his office and for the mountain excursions around the Burgos province (I really need them!). And thanks to the guys of the lab for their support: Marta, Jairo, Igor and Monica.
Many thanks to the group of Parque Científico Tecnológico, Marta, Pilar, Jacinto, David, Raquel and the Instrument Service, for all the proofs I performed with their instruments and for all the help they provided me.
I'd like to thank my supervisor during my stay period at CNR research center of Bologna Italy, Dr. Ilse Manet, which kindly received and helped me. Many thanks also to Francesco for teaching me the techniques of the laboratory, I really appreciated it.
Thanks to my mum, which stands me for all the time I have forgotten to send her a message ("Do you remember you still have a mother?"). And, of course, thanks to my uncles and aunts Marco, Piero, Lucilla and Loretta, and my cousins, Elisa and Mirco.
Then, I have to thank my brother and Mabe, which have been so brave to visit me twice at Burgos (the first one was enough to me, too), always refusing to return a third time. Thanks also to my colleagues in the Università di Pisa, especially Sergio and Carlo Andrea.
Thanks to my favourite roommates, Iñigo and Daniel, for the good time spent together (I'm sure that you still owe me money). And thanks to Iñaki and Stella, for their friendship.
And finally, I'd like to thank the most important gift Burgos gave to me: thanks Chiara, for your support and for the wonderful period we spent in Burgos and we will spend, now, together.

I don't care if it's science or magical power. No, I guess if I had to choose, I'd rather put my money on the power of science. Humans who used to only roam around on the ground are able to fly now! And finally, we're about to go into outer space. Science is a "Power" created and developed by humans. And science just might be what saves this planet. I was able to earn my living thanks to science. So to me, there's nothing greater!

Final Fantasy VII
Cid Highwind

Contents

Aim of the Thesis **1**

1 Introduction **3**
1.1 Nucleic Acids . . . 3
1.1.1 DNA . . . 7
1.1.2 Non-Canonical DNA Structures . . . 9
1.1.3 RNA . . . 12
1.2 Nucleic Acids Reactivity . . . 14
1.2.1 Interaction with Metal Ions . . . 14
1.2.2 Interaction with Small Molecules . . . 18
1.3 Metal Complexes in Anticancer Strategy . . . 20
1.3.1 From Platinum Complexes... . . . 20
1.3.2 ...to Non-Platinum Complexes . . . 20
1.4 Enhancement of Compounds Selectivity . . . 21
1.4.1 Selectivity Towards Specific Targets: G-Quadruplex Binders 22
1.4.2 Photodynamic Therapy Strategy . . . 23
1.5 The Metal Complexes in the Thesis . . . 25
1.5.1 Arene Ruthenium(II) Complexes . . . 26
1.5.2 Biscyclometalated Iridium(III) and Rhodium(III) Complexes 27
1.5.3 Ancillary Ligands . . . 28

Bibliography **29**

2 Materials and Methods **47**
2.1 Materials . . . 47
2.1.1 Nucleic Acids . . . 47
2.1.2 Aluminium . . . 48
2.1.3 Ruthenium, Iridium and Rhodium Complexes . . . 48
2.2 Methods . . . 49
2.2.1 Synthesis Procedure . . . 49
2.2.2 UV-vis Spectrophotometry . . . 51
2.2.3 Spectrofluorimetry . . . 52
2.2.4 Circular Dichroism . . . 55
2.2.5 Thermal Denaturation . . . 57
2.2.6 Isothermal Titration Calorimetry . . . 59
2.2.7 Viscometry . . . 61
2.2.8 Nuclear Magnetic Resonance . . . 61
2.2.9 Mass Spectrometry . . . 64

2.2.10 Irradiation Instrumentation 65
2.2.11 Photocleavage Study 66
2.2.12 FRET Assay 67
2.2.13 Other Techniques 68
2.2.14 Determination of the Equilibrium Constant of the Interaction Between a Metal Centre M and a Ligand L [18] . . . 70
2.2.15 Scatchard Plot [19] and McGhee and von Hippel Equation [20] 71
2.2.16 Determination of the Dimerization Constant [21] 73
2.2.17 Determination of the Time Constant Equation 74

Bibliography **75**

I Aluminum and Its Interaction with RNA **77**

3 Stabilization of Al(III) Solutions by Complexation with Cacodylic Acid: Speciation and Binding Features **81**
3.1 Materials and Methods 82
3.1.1 Materials 82
3.1.2 Methods 82
3.2 Results and Discussion 83
3.2.1 Evaluation of the $pK_{A,1}$ and $pK_{A,2}$ Acidity Constants of Cacodylic Acid 83
3.2.2 Speciation of Aluminium Forms 84
3.2.3 The Aluminium/Cacodylate System 86
3.2.4 Determination of K_{app} of Aluminium/Cacodylate Complexes 91
3.2.5 DFT Calculation 93
3.3 Conclusion 96

Bibliography **96**

Supporting Information **101**
3.A Determination of the Equilbrium Constant by NMR 108
3.B Determination of Equation (3.8) 109

4 Binding of Al(III) to Synthetic RNA. Metal-Mediated Strand Aggregation **111**
4.1 Materials and Methods 112
4.1.1 Materials 112
4.1.2 Methods 112
4.2 Results 113
4.2.1 Properties of Aluminium/Cacodylate System at pH 5.0 and 7.0 113
4.2.2 Binding of Al/Cac to Riboadenosine Monophosphate (AMP) 114
4.2.3 Binding of Al/Cac to Poly(rA) and Poly(rU) 114
4.3 Discussion 123
4.4 Conclusion 125

Bibliography **127**

Supporting Information **129**
4.A Determination of the Initial Rate Equation for the Al/Cac-Poly(rU) System at pH=5.0 . . . 137
4.B Determination of the Initial Rate Equation for the Al/Cac-Poly(rA) and the Al/Cac-Poly(rU) Systems at pH=7.0 . . . 138
4.C Determination of the Initial Rate Equation for the Al/Cac-$[Poly(rA)]_2$ System at pH=5.0 . . . 139

II Metal Complexes: Interaction with DNA and Photoreactivity **141**

5 Ruthenium Arene Complex with Arylazole Ligand: Two-Step Binding to DNA and Photoreactivity **145**
5.1 Materials and Methods . . . 146
5.1.1 Materials . . . 146
5.1.2 Methods . . . 147
5.2 Results and Discussion . . . 147
5.2.1 Physico-Chemical Properties . . . 147
5.2.2 Interaction of **aquo-[Ru-1]** with *d*GMP . . . 152
5.2.3 Interaction of **HL-1** and **aquo-[Ru-1]** with CT-DNA . . . 154
5.2.4 Photoreactivity and Plasmid Photocleavage . . . 157
5.2.5 Cytotoxic activity . . . 160
5.3 Conclusions . . . 160

Bibliography **163**

Supporting Information **167**
5.A Determination of Equation (5.6) . . . 170

6 Biscyclometalated Iridium and Rhodium Complexes. DNA Binding and Photoreactivity **171**
6.1 Materials and Methods . . . 172
6.1.1 Materials . . . 172
6.1.2 Methods . . . 173
6.2 Results and Discussion . . . 173
6.2.1 Metal Complex Properties . . . 173
6.2.2 Interaction with CT-DNA . . . 175
6.2.3 Photoreactivity . . . 181
6.2.4 Cytotoxic Activity in the Dark and under Irradiation . . . 185
6.3 Conclusion . . . 186

Bibliography **189**

Supporting Information **193**

7 Biscyclometalated Iridium and Rhodium Complexes. Photoreactivity and Selective Binding to G-Quadruplex **197**
7.1 Materials and Methods . . . 198
7.1.1 Materials . . . 198
7.1.2 Methods . . . 198

7.2 Results and Discussion . . . 200
7.2.1 Synthesis Procedure . . . 200
7.2.2 Characterization . . . 203
7.2.3 UV-vis Absorption Spectra . . . 206
7.2.4 Luminescence . . . 207
7.2.5 Singlet Oxygen Production . . . 210
7.2.6 Dimerization . . . 211
7.2.7 Photoreactivity . . . 212
7.2.8 Binding study to G-Quadruplexes . . . 216
7.3 Conclusions . . . 222
7.4 Synthesis and Characterization Data . . . 223
7.4.1 2-(2'-pyridyl)benzothiazole (pybtz) . . . 223
7.4.2 2-(2'-quinolinyl)benzothiazole (qibtz) . . . 224
7.4.3 2-phenylisoquinoline (piqi) . . . 224
7.4.4 $Ir_2(ppy)_4Cl_2$ . . . 225
7.4.5 $Rh_2(ppy)_4Cl_2$ . . . 225
7.4.6 $Ir_2(piqi)_4Cl_2$ . . . 226
7.4.7 $Rh_2(piqi)_4Cl_2$ . . . 227
7.4.8 **[Ir-2]**Cl ($[Ir(ppy)_2(pybtz)]Cl$) . . . 228
7.4.9 **[Ir-3]**Cl ($[Ir(ppy)_2(qibtz)]Cl$) . . . 229
7.4.10 **[Ir-4]**Cl ($[Ir(piqi)_2(pybtz)]Cl$) . . . 230
7.4.11 **[Ir-5]**Cl ($[Ir(piqi)_2(qibtz)]Cl$) . . . 231
7.4.12 **[Rh-2]**Cl ($[Rh(ppy)_2(pybtz)]Cl$) . . . 232
7.4.13 **[Rh-4]**Cl ($[Rh(piqi)_2(pybtz)]Cl$) . . . 233
7.4.14 **[Rh-5]**Cl ($[Rh(piqi)_2(qibtz)]Cl$) . . . 234

Bibliography **237**

Supporting Information **243**

Overall Conclusions **259**

Articles and Congresses **261**

Aim of the Thesis

Cancer is one of the leading causes of death in our modern society. The development of new anticancer drugs has been central in scientific research. Although a huge number of metal complexes have been continuously synthesized, only a slight number of them have entered in clinical trials, and only few of them have been accepted as anticancer drugs.
Aim of the Thesis is the study of the interaction between metal complexes and nucleic acids, namely RNA and DNA, from thermodynamic and kinetic standpoints. Different metal centers and classes of complexes have been taken into account.
But...*why RNA? why DNA?* Although the study of new molecular targets (e.g. proteins) has increased over the last years, nucleic acids are considered the most important biological targets inside the cell. Actually, DNA and RNA drive the essential steps of the central dogma of molecular biology, being involved in the replication, transcription and translation processes. The possibility to alter the functions of polynucleotides by interaction of small molecules is a fascinating tool for the anticancer strategy: the interaction of a huge number of organic, inorganic and organometallic molecules with DNA and RNA has been tested in order to obtain information about the effects of such drugs.
Concerning the nature of the drug, metal complexes are generally less employed respect to organic molecules in many biological applications. Nevertheless, metal compounds exhibit more suitable properties in so many aspects respect to organic-based drugs, offering wide structural diversity (e.g. ligand type and geometry), different redox states, optimal photophysical properties and the possibility to sum the intrinsic properties of the metal center and of its organic ligands.
The structure of the Thesis is composed by:

- **Introduction**, where we introduce the reader to the different species involved in the Thesis, namely nucleic acids, metal cations and metal complexes, and their interactions. In particular, a section was dedicated to two newly proposed strategies in anticancer therapy, which will be treated in our study: selectivity towards G-Quadruplex and Photodynamic Therapy;

- **Materials and Methods**, where we briefly listed the chemical reagents we used and the theoretical bases of the techniques we have employed;

- **Results and Discussion**: even though the Thesis has a unique focus, namely the interaction of metal complexes with nucleic acids, we divided the results into two Parts. First of all, the effect of aluminium ions were

tested in the presence of synthethic RNA in Part I. Aluminium is a toxic element which is believed to be potentially reliable to various disorders, such as Parkinson's and Alzheimer's diseases and, recently, breast cancer. The characterization of the complex formed between aluminium and cacodylate anion is exposed in Chapter 3. Cacodylate stabilizes aluminium and avoids its precipitation, even at neutral pH. This finding enables the study of the effect of aluminium/cacodylate complex under physiological condition, and the interaction towards synthetic RNAs is examined in Chapter 4. This topic was developed in collaboration with Prof. Tarita Biver of Dipartimento di Chimica e Chimica Industriale, Università di Pisa, Italia.
In Part II, our study was focused on metal complexes of ruthenium, iridium and rhodium. The classes of complexes taken into account have been extensively studied as anticancer drugs. Our work is the study of novel compounds obtained by changing the nature of the ligands bound to the metal center.
Firstly, the study of the new [($p-$cym)Ru(L-1)SCN] ruthenium η^6-arene complex (HL-1 = 2-(2'-hydroxyphenyl)benzothiazole), was carried out in Chapter 5. Interaction of the metal complex and its ancillary ligand was examined with CT-DNA. In addition, a study of the photoreactivity was performed.
After the arene complexes, we focused on a new class of metal compounds, namely the biscyclometalated complexes. Iridium and rhodium biscyclometalated complexes have been considered in this study. Firstly, a comparison of two complexes, $[Ir(ppy)_2(pyboz)]Cl$ and $[Rh(ppy)_2(pyboz)]Cl$ (pyboz = 2-(2'-pyridyl)benzoxazole), differing by the nature of the metal center, was carried ou in Chapter 6. Interaction of the metal complexes with CT-DNA was conducted in the dark by means of different analytical methods, whereas cleavage study of plasmid DNA was used to test the photoreactivity of the compounds.
Since remarkable photoreactive effects have been found for the biscyclometalated complexes, the last part of the Thesis was centered on the synthesis of new iridium and rhodium complexes, varying the ligands. The synthesis and the characterization of the new compounds were developed in collaboration with Prof. Gustavo Espino of the Inorganic Chemistry Lab. of Universidad de Burgos. Then, the photoreactivity and the selectivity towards the non-canonical forms of DNA, namely the G-Quadruplexes, were tested. The results are summarized in Chapter 7. Part of this project was carried out in collaboration with the laboratory of Istituto per la Sintesi Organica e la Fotoreattività, Centro Nazionale delle Ricerche, Bologna, Italy, under the supervision of Dr. Ilse Manet.

- **Conclusions**: an overall conclusion was provided at the end of the Thesis.

Chapter 1

Introduction

1.1 Nucleic Acids

Nucleic acids are natural polymers formed by repetitive monomeric units, the nucleotides (Figure 1.1).

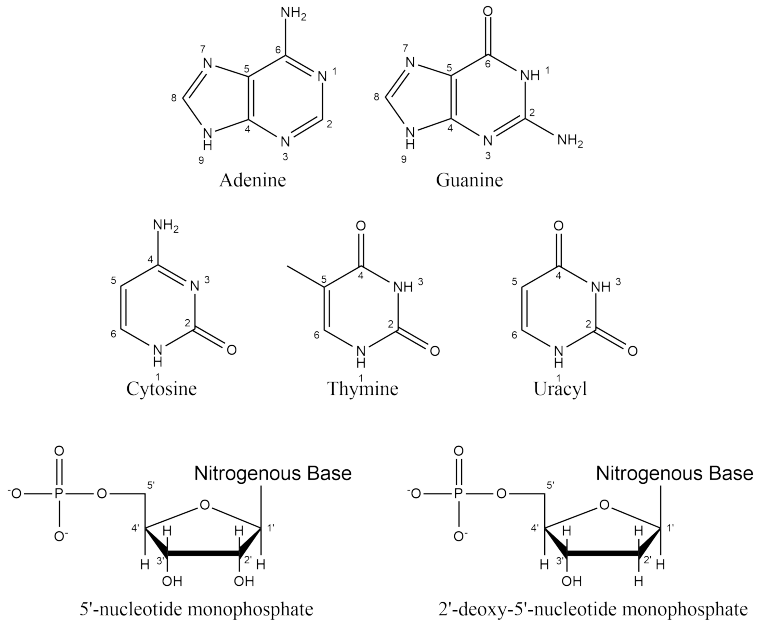

Figure 1.1: Molecular structure of the nitrogenous bases and the nucleotidic units.

The nucleotides are composed by:

- a nitrogenous base, namely, adenine, guanine, cytosine, thymine (the last one is exclusive to DNA) and uracyl (exclusive to RNA);
- a sugar molecule, which is 2'-deoxyribose for DNA and ribose for RNA. Purinic nitrogenous bases (Adenine and Guanine) are covalently bound to

$C_{1'}$ of the sugar moiety through N_9, whereas pyrimidinic bases (Cytosine, Thymine and Uracyl) bind through N_1. This bond is called *N-glycosidic*. In addition, all the nucleotides are β-anomers, as to say, the bases are placed upon the plane of the cyclic sugar, on the same side of $C_{5'}$.

- a phosphate group, bound to $C_{5'}$ of the sugar ring.

Such a structure permits two possible orientations for the nitrogenous bases: the *syn* conformation, where the base is oriented towards the sugar molecule, and the *anti* conformation, where the base is on the opposite side of the ribose (Figure 1.2). The torsion angle χ, defined as the angle of the base orientation, is $90°/180°$ in *anti* and $-90°/90°$ in *syn* conformation.

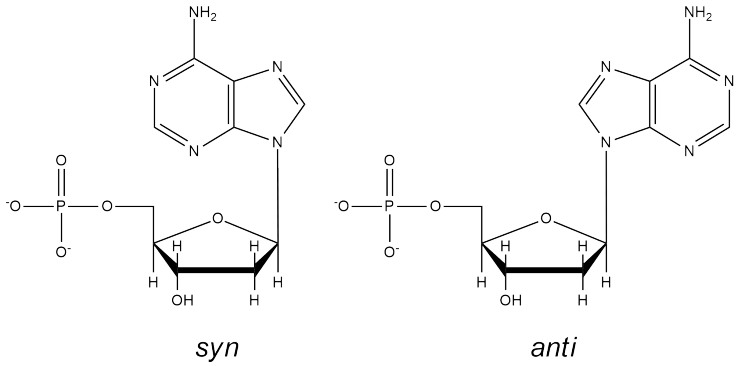

Figure 1.2: *Syn* and *anti* conformations of nucleotides.

In addition, the $C_{2'}$ and $C_{3'}$ carbons can be placed upon the plane of the sugar cycle, on the same side of $C_{5'}$, in *endo* position, or down the plane, in *exo* position (Figure 1.3). The generally available nucleotide conformation in DNA has $C_{2'}$ in *endo* geometry and nucleotides have *anti* conformation because of steric hindrance.

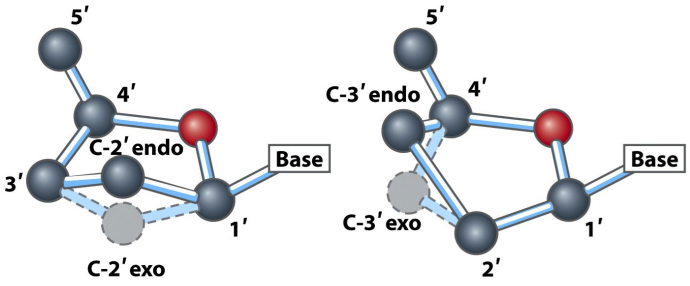

Figure 1.3: *Endo* and *exo* positions of $C_{2'}$ and $C_{3'}$ in the sugar moiety.

Nucleotides are linked together by a phosphodiester bond between the phos-

phate group and the hydroxyl group in C_3, position. The repetition of this bond between the monomeric units leads to the polynucleotidic chain.
Concerning nucleotides properties, the nitrogenous bases exhibit acid base behaviour and their pK_A values are listed in Table 1.1 [1]. On the other hand, the phosphate group has two different pK_A values, around 1.0 and 6.2.

Table 1.1: *pK_A values of the functional groups of the nitrogenous bases* [1].

Base	**Atom**	pK_A **Base**	pK_A **Nucleotide**
Adenine	N_1	4.1	3.8
Cytosine	N_3	4.5	4.4
Guanine	N_7	2.9	2.4
	N_1	9.4	9.5
Thymine	N_3	9.8	9.9
Uracil	N_3	9.5	9.6

Moreover, the nitrogenous bases display absorption in the UV region and the maximum of absorption is different for each nucleotide (Table 1.2 [2]). It follows that the nucleic acids have also certain photophysical properties. Actually, when the nucleotides are bound together to form DNA, a resulting absorption peak at $\lambda = 260\,\text{nm}$ arises as the sum of the absorption spectra of the mononucleotides.

Table 1.2: *Absorption maxima and extinction molar coefficients of nucleosides* [2].

Nucleoside	λ^{max}, nm	ϵ_{260}, $M^{-1}cm^{-1}$
A	259	15020
dA	259	15060
C	271	7070
dC	271	7100
G	252	12080
dG	252	12180
U	262	9660
T	267	8560

Except to nucleic acids, nucleotides compose other biologically relevant compounds involved in various biochemical processes (Figure 1.4). For instance:

- **ATP**: ATP or adenosine 5'-triphosphate is the most important molecule involved in energetic processes. Actually, energy can be stored by formation of ATP from ADP and phoshporic acid inside the cell. Then, the energy is released by hydrolysis of ATP, together with the formation of ADP (release of a phosphate group) or AMP (release of a pyrophosphate). The hydrolysis process is exothermic, having $\Delta G = -7.3\,\text{kcal mol}^{-1}$ and $\Delta G = -10.9\,\text{kcal mol}^{-1}$ for ADP and AMP production, respectively;
- **cNMP**: cyclic nucleotides are 5'-monophosphate nucleotides where the phosphate group forms a further interaction with the oxygen in position 3'

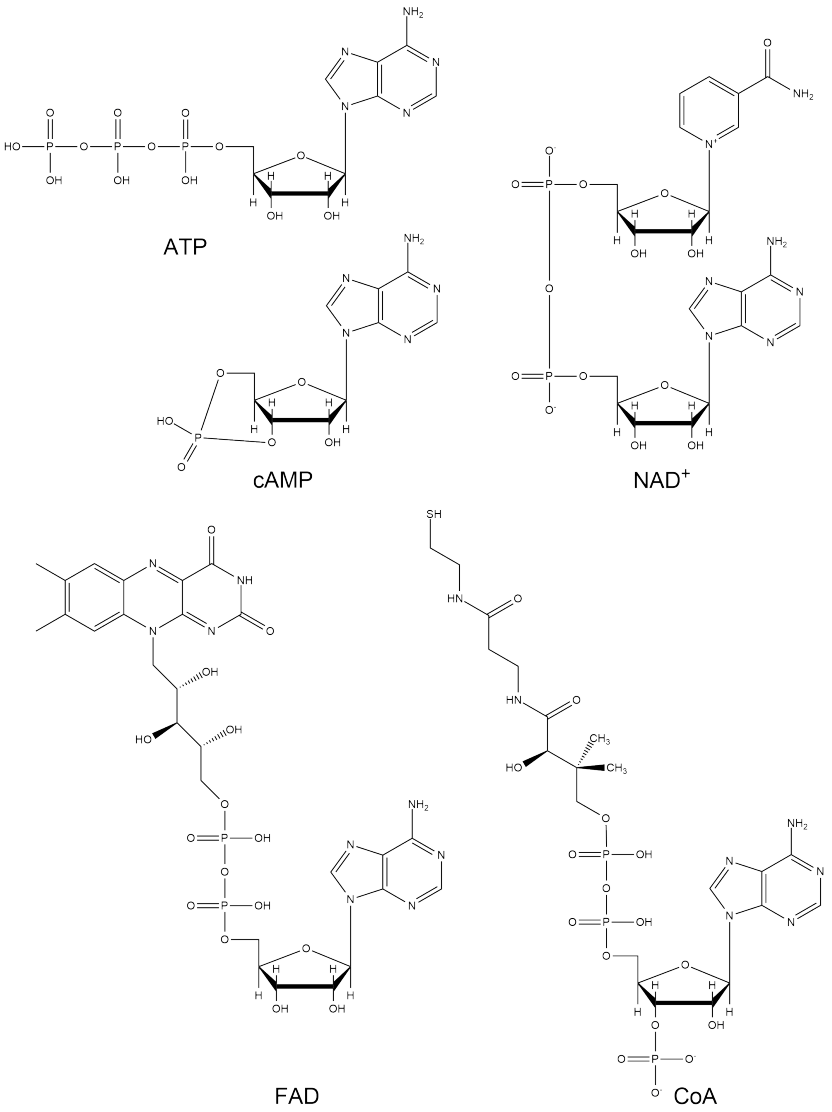

Figure 1.4: Examples of biologically relevant molecules composed by mononucleotidic units.

of ribose. cAMP, cGMP and cCMP are the most present cyclic nucleotides inside the cell and they are seen to interact with many proteins in specific sites, altering the protein structure and, consequently, its activity;

- **NAD^+**: the Nicotinamide Adenine Dinucleotide is a coenzyme whose function is based on its redox property. NAD^+ is the oxidizing species and NADH the reducing agent. The redox reaction is (Reaction (1.1)):

$$NAD^+ + H^+ + 2\,e^- \longrightarrow NADH \tag{1.1}$$

which involves the nitrogen in the aromatic ring of the nicotinamidic moiety. NAD is used in different processes;

- **FAD**: FAD is composed by an adenosine group bound to a riboflavine molecule by a pyrophosphate group. As the NAD^+ molecule, FAD is involved in many redox biological reaction (Equation (1.2)). The reaction mechanism leads to the reduction of both nitrogens of the riboflavine;

$$FAD + 2\,H^+ + 2\,e^- \longrightarrow FADH_2 \tag{1.2}$$

- **CoA**: coenzyme A is a transporter of acyl groups (under Acetyl−CoA form), and its function is remarkable in metabolism processes.

1.1.1 DNA

1.1.1.1 Double-Stranded DNA

DNA has a topic function in molecular biology: it contains the genetic heritage, and it is involved in the replication ($DNA \longrightarrow DNA$) and transcription ($DNA \longrightarrow RNA$) processes, being these the foundation of the central dogma of molecular biology, together with the translation process, leading to protein synthesis (Figure 1.5).

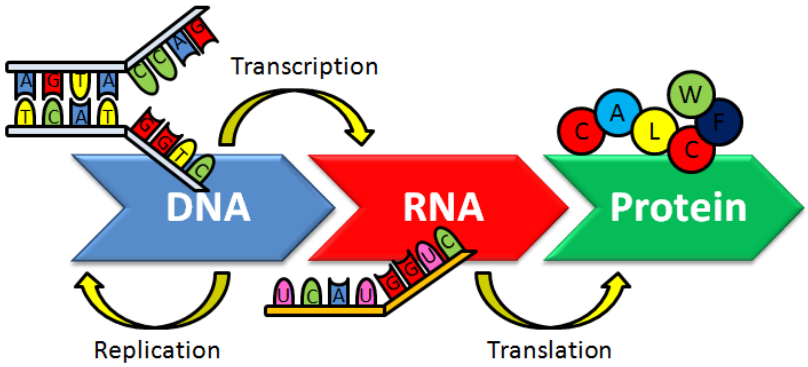

Figure 1.5: The dogma of molecular biology.

In DNA replication, the double-helix structure of DNA is opened and, by means of the DNA polymerase enzyme, complementary DNA strands are synthesized using triphosphate mononucleotides. It leads to the formation of two double-helices, each one containing an old and a new synthesized strand (semiconservative process).
DNA transcription is the process capable of transferring genetic information from DNA to RNA. In transcription process, the DNA opens in a transcription bubble and the RNA polymerase enzyme catalyzes the synthesis of the RNA strand from the complementary DNA strand.
The synthesized RNA is called messenger RNA (mRNA) and brings the gene information from the nucleus to the cytosol for the protein synthesis. Outside

the nucleus, the mRNA interacts with ribosome, a macromolecular system composed by proteins and nucleic acids. Every three nucleotides of mRNA, named *codon*, encode for a specific peptide, the monomeric unit of proteins. Peptide bond is formed by the interaction of a new kind of RNA, called transfer RNA or tRNA, with mRNA. Transfer RNA is composed by a stem, where the amino acid is linked, and three arms, the D-loop, the T-loop and the *anticodon* loop. The anticodon loop is placed on the opposite direction of the stem, and it is the reaction site for mRNA. The type of peptide depends on the combination of three nucleotides at the end of the anticodon loop. When a codon codifies a defined peptide, the tRNA having such peptide interacts with mRNA by means of its complementary anticodon sequence. When two tRNAs are close, the adjacent peptides form a bond between themselves by means of the peptidyl-transferase enzyme. The peptide chain remains in a RNA moiety and another tRNA is inserted inside the ribosome, which enables further peptide bond to the protein chain. The process continues until the entire protein is synthesized.
The DNA secondary structure was discovered by Watson and Crick in 1965 [3]. From the X-ray results the following characteristics can be derived:

- DNA consists of a right-handed helix formed by two strands running around the same axis. The strands are antiparallel, as to say they run in opposite directions, one having $5' \longrightarrow 3'$ direction and the other one $3' \longrightarrow 5'$. Each turn of the helix measures 34 Å, involving 10.5 basepairs;
- the sugar and the phosphate groups make the external hydrophylic backbone up, whereas nitrogenous bases are placed quasi-perpendicular to the helix axis inside the structure. Such a geometry generates a minor and a major groove in DNA;
- the double-helix structure is maintained by hydrogen bonds between the nitrogenous bases. In particular, a complementary interaction between the bases exists, being Adenine-Thymine (AT) and Guanosine-Cytosine (GC) base pairing, as shown in Figure 1.6 (the so-called *Watson-Crick basepairs*);

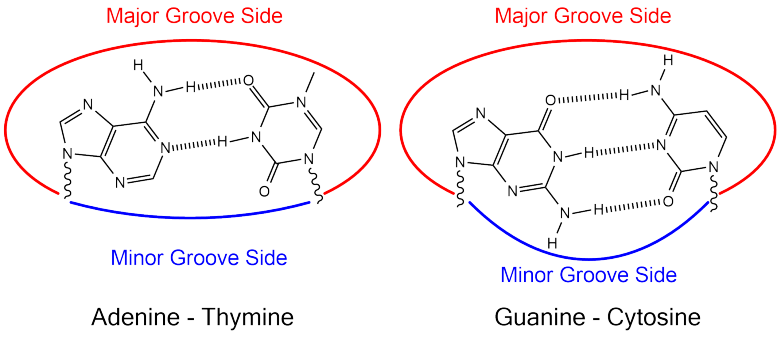

Figure 1.6: Hydrogen bonds between DNA nitrogenous bases.

- further stabilization of the structure is achieved externally by electrostatic interactions with metal ions (it generally involves Na^+ and K^+ in biological systems), and by stacking interactions between the bases inside the

structure, which predominantly are vertical interaction, such as London dispersion forces.

1.1.1.2 Further Double-Stranded Structures

Watson-Crick model is the so-called DNA *B Form*, and it is the normally available secondary structure of DNA in physiological conditions. However, other forms have been discovered. Regarding to double-helix conformations, the right-handed *A Form* and the left-handed *Z Form* are the most known. A Form derives from B Form because of environmental changes, such as low ionic strength and low water percentage. The A conformation is a crystalline structure, where the nitrogenous bases are 20° tilted respect to the helix axis and the difference between the major and minor grooves is more pronounced. On the other hand, DNA Z Form was discovered for the first time for a $d(GC)_3$ fragment, whose X-ray structure showed a left-handed double helix. In the Z Form, the purinic bases assume *syn* and $C_{3'}$ *endo* conformation, while the pyrimidinic groups remain in the *anti* and $C_{2'}$ *endo* conformation, and the secondary structure exhibits grooves of equal width [4]. Z Form is found to be a high-energy structure promoted in the transcription process by polymerase enzyme. The structural data of the different forms are listed in Table 1.3 [5].

Table 1.3: *Geometry values of the A, B and Z Forms of DNA [5].*

Properties	**A Form**	**B Form**	**Z Form**
Helix sense	right-handed	right-handed	left-handed
Rotation per bp	32.7°	34.3°	30.0°
bp per turn	11	10.5	12
Inclination bp-axis	19°	−1.2°	−9°
Height bp	2.6 Å	3.4 Å	3.7 Å
Height turn	28.6 Å	35.7 Å	45.7 Å
Phosphate distance	5.9 Å	7.0 Å	C 5.7 Å, G 6.1 Å
Glycosidic angle	anti	anti	C,T: anti, A,G: syn
Sugar pucker	$C_{3'}$-endo	$C_{2'}$-endo	C $C_{2'}$-endo G $C_{3'}$-endo
Diameter	23 Å	20 Å	18 Å

1.1.2 Non-Canonical DNA Structures

Besides the above-mentioned structures, other non-canonical forms exist. In particular, triplex and quadruplex moieties have been discovered in solution and it has been verified that they can be formed in specific genome regions under suitable conditions.

Concerning triplex structures, they are promoted from the pairing of nitrogenous bases by means of hydrogen bonds named *Hoogsteen basepairs*, different from the conventional Watson-Crick basepairs (Figure 1.7) [6]. DNA triplexes can be formed by insertion of a strand on the major groove of a double-helix DNA, where the pyrimidinic groups of the single helix interact with the purinic moieties

of the duplex, forming hydrogen bonds between N_3 and O_4 of thymine and N_7 and O_6 of guanine, respectively, and between protoned N_3 and amino group of cytosine with N_7 and O_6 of guanine, respectively. Single-stranded chains able to form triplex structures with the double helix of DNA are called TFO (triplex-forming oligonucleotide) [7] and these systems are of interest for their role in biological processes and for delivering drug strategies. From these, the *antisense* strategy involves the use of an oligonucleotide able to bind to specific bad functioning genes, inhibiting their expression [8].

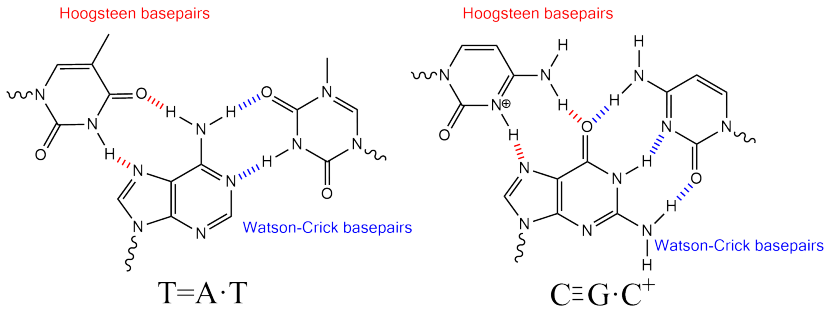

Figure 1.7: Hoogsteen basepairs in triple-stranded structures.

On the other side, quadruplex structures were hypothesized in 1962 [9]. Their stabilization is achieved by hydrogen bonds between the guanine moieties placed on the same plane (called G-tetrad). In particular, hydrogen bonds are formed between the amino group and N_7 and between the carbonyl group and the hydrogen of N_1 (Figure 1.8).

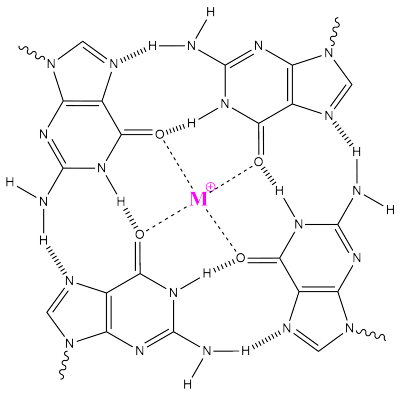

Figure 1.8: Hydrogen bonds of a G-Quadruplex moiety.

The insertion of monovalent cations, such as Na^+ and K^+, stabilizes the structure by interaction with the four carbonyl groups of the G-tetrad, being the preferential order affinity K^+>Na^+ [10]. G-Quadruplex (or G4) can be composed by one (unimolecular), two (bimolecular) or four (tetramolecular) strands. However, unimolecular forms are generally studied in laboratory. Their formula is

$$G_mX_nG_mX_oG_mX_pG_m \tag{1.3}$$

being m the number of guanosines and n, o and p the number of the remaining X nucleotides, named *connectors*, which can also include guanosine [11]. Since G_m and X_i can be of different lengths, the number of possible G-Quadruplex primary structures is almost infinite. Furthermore, variations in the primary motif imply different secondary structures. Actually, differences in the G-Quadruplex geometry are due to:

- **orientation of the guanosines**: if the guanosinic chains have the same orientation ($3' \rightarrow 5'$ or $5' \rightarrow 3'$), a *parallel* structure is obtained; otherwise, it is named *antiparallel*. The mixture of both orientations is defined as *hybrid* structure;
- **disposition of the connectors**: there are different possible types of connection of the G-tracts (Figure 1.9). Connectors can form *lateral*, *diagonal* and *propeller* loops, which determine parallel and antiparallel orientations. Lateral (or edge-wise) loops connect adjacent G-tracts while diagonal loops link opposite G-tracts, both forming antiparallel structures. Propeller (or chain-reversal) loops connect adjacent parallel strands.

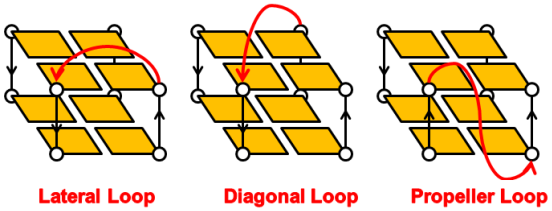

Figure 1.9: Connectors of G-Quadruplex.

The glycosidic angle in G-Quadruplex displays always *anti* geometry for the parallel conformation, while the antiparallel structure has an equal number of *anti* and *syn*. Many G-Quadruplex structures are named in specific ways because of their form, such as *basket*, *chair* or *propeller* forms (Figure 1.10).

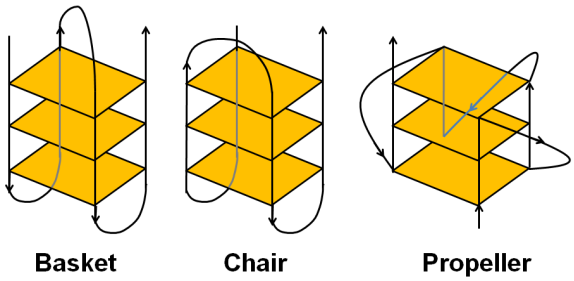

Figure 1.10: Different G-Quadruplex structures.

The resulting G-Quadruplexes have 4 grooves and exhibit different polarity, groove size, depending on the primary and secondary structure. It follows that the reactivity of G-Quadruplexes changes depending on the type. In addition, the structure can change depending on the metal ion inserted in the plane. For example, different conformations are found for the telomeric G-quadruplex: the presence of Na^+ leads to an anti-parallel structure, with a diagonal and two propeller loops [12]; X-Ray diffraction studies of a crystalline telomeric G-Quadruplex in the presence of K^+ show a parallel conformation having three propeller loops [13]; finally NMR analysis in K^+ solution reveals a hybrid structure [14]. Moreover it is found that sodium inserts into the G-tetrads, whereas potassium size is too large to fit in it, and it is positioned upon the plane.
A valuable tool in the knowledge of G-Quadruplex structures is the Protein Data Bank Database (PDB) [15]. This web site contains all the discovered G-Quadruplexes structures, characterized by NMR or X-Ray diffraction, and the files can be visualized by the JMOL free program [16].
Various guanosine-rich tracts are present in the genome, overall in telomere and in some proto-oncogene genes. Despite this, G-Quadruplex conformation has been demonstrated *in vivo* in prokaryotic and eucaryotic cells only in the last years [17]. Regarding the telomere, they are nucleoproteins found at the end of the chromosomes, and such DNA tracts are generally single-stranded. The telomere function is to prevent disruption of DNA sequences during DNA replication, which could cause loss of important genetic information. On the other hand, proto-oncogene genes are generally present in double-stranded tracts. Consequently, modifications have to occur in order to break Watson-Crick base pairs and form G-quadruplex motifs, and these are reached during the DNA replication and the transcription processes. For instance, *c-myc* is an example of proto-oncogene gene [18] and the nuclease hypersensitivity element (NHE) III_1 of this gene is accountable to 90 % of its transcriptional activity. It has a duplex conformation but, under certain circumstances, it can fold into a quadruplex structure.

1.1.2.1 Quaternary Structure

Inside the nucleus of eukaryotic cells, DNA organizes itself to form packed structures. Actually, DNA is coiled around histone proteins to form nucleosomes, which are structured as chromatin fibers, composing the chromosomes. The chromosomes are highly compacted and organized structures; however, they need to unwind in the transcription and replication processes.

1.1.3 RNA

1.1.3.1 Natural RNA

When RNA is synthesized inside the cell it displays a single-stranded conformation. However, a specific secondary structure does not exist for RNA, and local structures, such as internal double strands, inner loops, stem-loops or hairpin motifs, are possible (Figure 1.11). These conformations enhance the stabilization of RNA. Actually, hydrogen bonds can be formed between the nitrogenous bases, as well, being Guanine-Cytosine and Adenine-Uracil pairing (and, sometimes,

Guanine-Uracil, as well). RNA plays different roles inside the cell: it takes part in the transcription and translation processes and it is present in many nucleoproteins, such as the ribosomes.

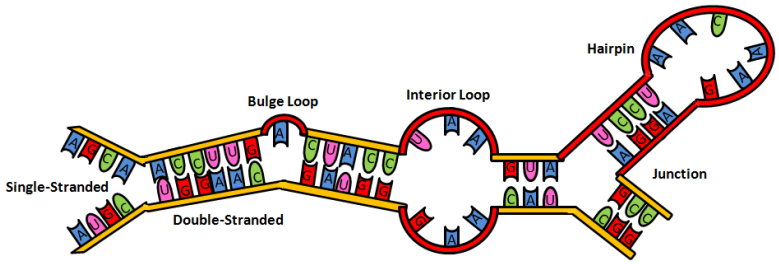

Figure 1.11: Examples of RNA secondary structures.

1.1.3.2 Synthetic RNA

Different types of synthesized RNA have been prepared over the years. In the present Thesis, we have focused on the poly-riboadenylic (poly(rA)) and poly-ribourydilic (poly(rU)) acids.
Poly(rA) is formed by the repetition of Adenosine 5'-Monophosphate monomeric units. Its secondary structure has been studied by means of various techniques, such as UV-vis spectrophotometry, X-Ray diffraction, circular dichroism and thermal stability measurements, in solid state [19–21] and in aqueous solution [22, 23], as well.
Poly(rA) exists as single-stranded form [22, 24] at room temperature and neutral pH, with partially ordered conformation due to stacking interactions between the nitrogenous bases. However, the poly(rA) secondary structure changes with pH: poly(rA) converts itself into the $[\text{poly(rA)}]_2$ bimolecular form at acidic pH (Figure 1.12 [20]).

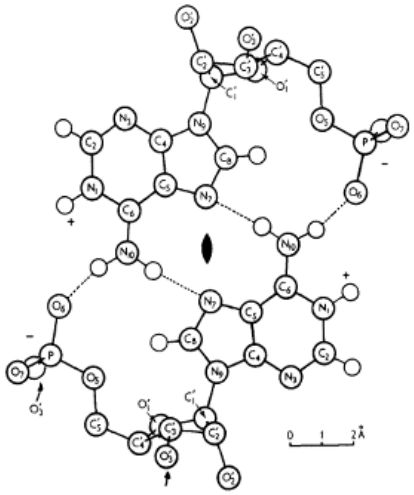

Figure 1.12: Hydrogen bonds in the $[\text{poly(rA)}]_2$ structure [20].

The formation of $[\text{poly(rA)}]_2$ is due to protonation of the N_1 site of the single helix ($pK_A = 3.8$, Table 1.1), obtaining poly(rA$-H^+$). This form evolves to a double helix by hydrogen bonding between the protons of N_{10} of a single strand with an oxygen of the phosphate group and the N_1 of the adenine of the second strand. The transition to $[\text{poly(rA)}]_2$ can be followed *via* spectrophotometry by the shift of the maximum, from λ=257 nm of the single helix to 252 nm of the double-stranded system, together with the appearance of a shoulder at 270 nm [25].
The reported equilibrium between the single and the double-stranded conformations is influenced by ionic strength and presence of small amount of divalent cations as well, promoting the formation of the single helix (Reaction (1.4)) [26].

$$\text{poly(rA}-\text{H}^+) + \text{poly(rA}-\text{H}^+) \rightleftharpoons [\text{poly(rA}-\text{H}^+)]_2 \tag{1.4}$$

At high temperature, the partially ordered structure of poly(rA) is disrupted to form a random coil system because of breakage of the stacking interactions between the adenine bases [23].
Extensive information is present on the interaction of poly(rA) with mono- and divalent cations as K^+, Mg^{2+} [27], Ni^{2+} [28]. Moreover, strand-aggregation of poly(rA) is observed in the case of high concentration of Mg^{2+} [27], Ca^{2+} [29] and Mn^{2+} [30].
Poly(rU) is composed by repetitive units of Uridin 5'-Monophosphate. It has a single-stranded random coil structure at room temperature and neutral pH [31]. However, at low temperature variation of the dichroic signal and hypochromic effect of the absorption maximum at 260 nm suggest the transition to an ordered or a partial-ordered structure [32, 33]. This behaviour is seen in the presence of certain ions like Mg^{2+} [34]. Such an ordered conformation is not due to the formation of double or multiple helices, but rather to intramolecular arrangements, with the formation of hairpin loops [31, 35].

1.2 Nucleic Acids Reactivity

1.2.1 Interaction with Metal Ions

In the biological environment DNA and RNA are surrounded by metal cations and the phosphate groups interact with sodium or potassium monocations. However, the presence of different metal ions (M^{n+}) can displace the monocation from the mononucleotide (NMP), as reported in the following Reaction (1.5).

$$M^{n+} + \text{Na}^+(\text{K}^+)\text{NMP}^- \rightleftharpoons \text{Na}^+(\text{K}^+) + M^{n+}\text{NMP}^- \tag{1.5}$$

Concerning the nature of the interaction, a mere electrostatic interaction with the phosphate is typical of the Group I metal series and the majority of Group II, like Mg^{2+} [36, 37] and Ca^{2+} [38], even if a certain interaction with the nitrogenous base is sometimes found [39]. On the other side, the increase of the ionic charge and the covalent properties of the species render prevailing the interaction with the nitrogenous bases, as seen for the transition metal cations. For instance, interaction with the nitrogenous base is observed for Ni^{2+} [36], Cu^{2+} [40], Mn^{2+} [37, 41], Zn^{2+} [38] and Cd^{2+} [38]. The coordination sites are

various because of the nucleophilic and the basic properties of the nitrogenous bases [42]:

- **Adenine**: the main interactions involve N_1 and N_7 coordination sites at neutral pH, while at basic pH the interaction can occur with the deprotoned amino group ($pK_A > 12$);
- **Cytosine**: the interaction is possible at N_3 position at physiological pH and with amino group at basic pH. In addition, the carbonylic group of cytosine exhibits good electron donor properties, which can promote interaction with metal ions;
- **Guanine**: interaction by means of N_3 and N_7 at neutral pH;
- **Uracil**: the carbonyl groups are the typical coordination sites for the uracyl base.

Less common interactions are found for Hg^{2+} with C_5 of cytidine or uridine [43] and C_5 of thymine by Os(VI) and Mn(VII), provoking oxidation [44].
Some attempts to rationalize the behaviour of monovalent and divalent ions have been carried out in order to obtain some general trend for the metal ion-nucleic acid reactivity. In particular, interest has been addressed on how the presence of a metal ion can modify polynucleotides secondary structures.
Shin et al. [45] report the interaction of various metal ions in the presence of single-stranded poly(rA), using absorption and circular dichroism. Concerning the interaction with the phosphate group, a slight decrease of poly(rA) absorption and circular dichroism is seen. The small variation of the signals points up that little modification on the secondary structure of the single strand system occurs. Differently, the interaction with the nitrogenous bases provokes a hyperchromism of absorption maximum together with a notable decrease of the dichroic signal. The decrease of the dichroic signal is due to modifications of the partially ordered poly(rA) structure because of unwinding of the nitrogenous bases, obtaining the following Reaction (1.6).

$$\text{poly(rA)}_{\text{SINGLEHELIX}} \rightleftharpoons \text{poly(rA)}_{\text{RANDOMCOIL}} \tag{1.6}$$

This transition is promoted by temperature, but the presence of metal ions interacting with adenine favours the reaction, even at room temperature.
Denaturation studies of DNA in the presence of metal ions show three different trends [46]:

- increase of the melting temperature (T_m) for increasing metal ion concentrations. Stabilization of double-helix DNA is observed for the metal ions exclusively interacting with the phosphate group. It is ascribable to the decrease of the linear charge, even if other kinds of stabilization are argued, like the stabilization of the ion-solvent-nucleic acid system [47];
- an initial increase of T_m followed by decrease at high concentration. The metal ions interact with phosphate and have some nitrogenous base affinity. Examples of metal ions interacting in such a way are Co^{2+}, Ni^{2+}, Mn^{2+} and Zn^{2+};

- a decrease of the T_m, for the metal exhibiting high affinity with nitrogenous bases. Such a behaviour is seen for Cd^{2+} and Cu^{2+}. Actually, the interaction with nitrogenous bases destabilizes the double-helices.

Regarding the double-stranded $[poly(rA)]_2$, the presence of a metal cation always provokes a decrease in melting temperature. It is due to the fact that the poly(rA) double-stranded conformation involves both phosphate and adenine groups. Consequently, the interaction of a metal ion destabilizes the hydrogen bonds, displacing the equilibrium towards the single-stranded RNA.
Sigel and his group [48] schematize the interaction of nucleotides with divalent ions, obtaining the global affinity for each nitrogenous base (Figure 1.13).

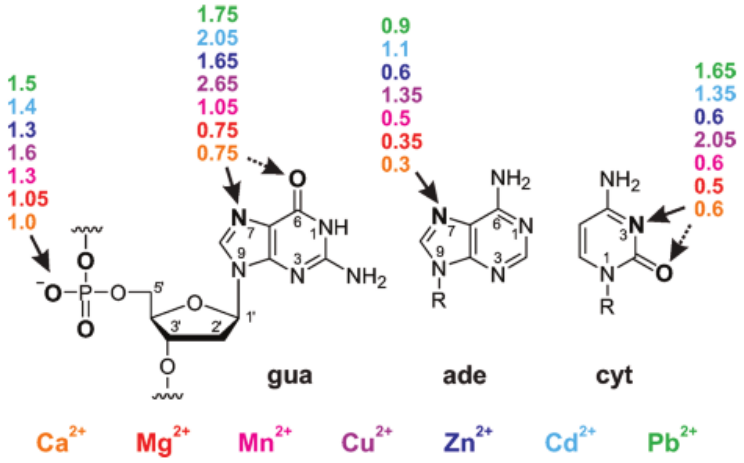

Figure 1.13: Affinity of divalent metal ions towards the nitrogenous bases and coordination sites [48]. Listed numbers are logarithmic values.

The whole interaction of a metal cation with a nucleotide is the sum of three interactions, as proposed in Equation (1.7).

$$Logk_{Na-cavity} = Logk_{PO_2} + Log\Delta + SFLog\Delta \tag{1.7}$$

where

- $k_{Na-cavity}$ is the total affinity constant of the metal ion-nucleic acid system;
- k_{PO_2} is the affinity towards the phosphate group (electrostatic interaction);
- Δ is the affinity for the nitrogenous base;
- $SFLog\Delta$ is a correction parameter due to the saturated coordination sphere;

In some cases a metal cation can interact with two phosphate moieties or a phosphate and a nitrogenous group at the same time. The resulting adducts are called *chelate* and *macrochelate* complexes, respectively.
Once the metal ion interacted with the nucleic acid, further interactions can

occur. One of these is the association of single or double-helix to form double, triplex and quadruplex systems [49]. Aggregation of poly(rA) and poly(rU) strands to form double poly(rA) · poly(rU) and triplex poly(rA) · 2 poly(rU) is known. Triplex structures are stabilized by ionic strength and the presence of small amount of divalent ions such as Mg^{2+} and Ni^{2+} [50–52]. Finally, as we have previously reported, G-Quadruplexes are stabilized by the presence of monovalent cations interacting inside the guanine tetrads [53–55].

1.2.1.1 Trivalent Metal Ions: Aluminium

In the above reported context, thermodynamic and kinetic studies of trivalent metal ions with nucleic acids are rather scarce, possibly due to their complex behaviour in aqueous solution (e.g. hydrolysis processes) [56]. The most investigated trivalent species are the lanthanides cations because of their use in medical fields and owing to their luminescent properties. Actually, enhancement of fluorescence is observed in the presence of mononucleotides and nucleic acids, together with an energy transfer process towards the nitrogenous base [57, 58]. On the other hand, only few articles on the reactivity of aluminium with polynucleotides have been published [59, 60]. In these studies the effect of aluminium ions was tested only for low metal concentrations, i.e. low metal/DNA ratio; noteworthy, possible interactions of aluminium with anionic ligands present in the reaction medium were disregarded [61].
Aluminium ion is prone to forming a variety of hydrolytic species [56] including the $Al_{13}O_4(OH)_{24}{}^{7+}$ polymeric form; it exhibits certain tendency to precipitate as $Al(OH)_3$ even at relatively acidic pH, and reacts with oxygen-containing ligands [62, 63]. The presence of different hydrolytic forms entails involvement of a number of equilibria and, consequently, many other possible complexes. These features render aluminium a very complex system.
Concerning biological effects, it should be noted that the hexahydrated and hydroxylic aluminium forms are toxic [64–66] and can affect human organs such as liver, heart and kidney [67–69]. In addition, aluminium is believed to be responsible for health disorders such as Alzheimer and Parkinson [70, 71], even though general agreement could not be found so far [72]. Lastly, increasing interest has been addressed in the last years towards aluminium for its possible relation with breast cancer because of its use as antiperspirant agent in underarm cosmetics [73–75]. Inside the cell, its bioavailability is significantly reduced not only because of precipitation, but also due to complexation with oxygenated functional groups present in biological molecules [76–78]. Despite all this, free aluminium can interact with the cell membrane and enter the cell [79].
In Chapter 3 and Chapter 4 (Part I of the Thesis) we focus our study on the interaction of aluminium and synthetic RNAs, and a preliminary complexation study was carried out with the dimethylarsinate anion, in order to obtain a stable aluminium compound in solution, in a suitable range of pH. Dimethylarsinic (cacodylic) acid, $(CH_3)_2AsOOH$, is largely used to study the interaction of biological molecules with organic dyes or metal ions [80]. Cacodylic acid (HCac, $pK_A = 6.2 \pm 0.1$), with a buffer window ranging pH 5.2-7.2 [81, 82], is quite a valuable tool to study nucleic acids and proteins under physiological conditions. On the other side, the cacodylate anion is unreactive towards many divalent metal ions [36]; for this reason it is thought to ensure buffer inactivity for many biomolecule/metal ion (or metal complex) systems. On the other

hand, there is evidence that the cacodylate anion can bind metal ions such as Sb(III), Bi(III) [83], Pd(II) [84] and some rare earth metals [85]. Formation of Al(III)/Cac complex [86] and, more recently, the synthesis of complexes of the dimethylarsinate anion and metal ions of the XIII group (Al, Ga, In, Tl) has been reported [87]. However, to the best of our knowledge, systematic thermodynamic studies of the aluminium/cacodylic acid system in solution under different experimental conditions are still lacking.

1.2.2 Interaction with Small Molecules

The interaction of a small molecule with nucleic acids can be sorted into covalent and non-covalent binding.

1.2.2.1 Covalent Binding

An electrophilic molecule can form a covalent bond with the nitrogenous base. The most accessible coordination site in DNA is the N_7 atom of the guanine and molecules having more than one coordination site can interact with both DNA chains, forming an intra-strand crosslinking. Such an interaction impedes the separation of the strands and inhibits biological processes, being this the mechanism of action of many anticancer drugs, such as cisplatin (see Section 1.3).

1.2.2.2 Noncovalent Binding

Organic and organometallic compounds can bind reversibly to DNA in different ways (Figure 1.14):

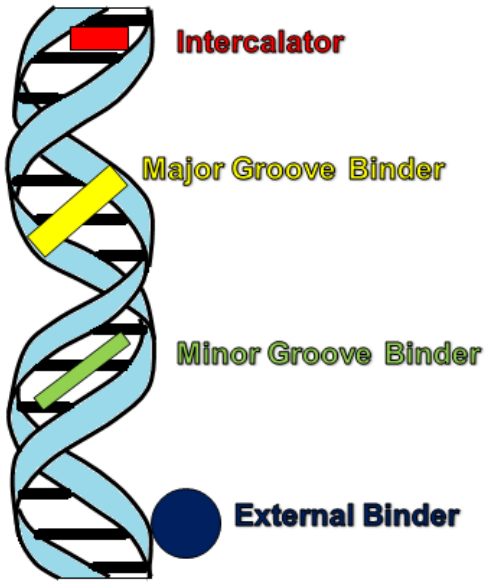

Figure 1.14: Noncovalent interactions with DNA.

- **External binding**: it is an electrostatic binding between the molecule and the phosphate backbone. It generally involves a positive charged molecule, displacing a sodium ion to interact with the DNA skeleton. The electrostatic interaction only seldom produces modifications on the DNA structure;

- **Groove binding**: the molecules insert into the DNA grooves. Since a major and a minor groove are present in B DNA form, two different binding sites are available. In general, molecules able to insert inside the minor groove are long molecules, with various coordination sites to pair inside the cavity. In particular, minor groove binders exhibit selectivity towards adenine-thymine basepairs [88]. This is explained because of the more rigid conformation of the GC pairing due to the presence of three hydrogen bonds; in addition, the amino group present in the minor groove of the GC tracts impedes a suitable positioning of the molecule. On the other side, the AT groove is more flexible and smooth than GC tracts, favouring a deep contact between the molecule and the bases of the groove. Major groove binders are less studied; nevertheless, as the major groove is a common recognition site for proteins, the research of systems binding to the major groove is of interest in the view of inhibition of the DNA-protein interactions. Various natural molecules and organometallic species are seen to interact in the major groove [89];

- **Intercalation**: intercalation is the insertion of the molecule between the DNA basepairs. Small aromatic molecules and organometallic complexes having extended and plane heteroaromatic ligands are viewed exhibiting good intercalative properties because of the extended π-stacking interaction with the bases [90]. In addition, the presence of a positive charge on the molecular structure enhances the interaction, promoting the approach of the molecule towards the DNA backbone. The intercalation can be total if the whole molecule is inserted between the basepairs, or partial, if the compound enters only partly. Intercalation generally provokes the biggest modification on the nucleic acid secondary structure and, because of this, it is the most interesting and inquired mode of binding. A non-common way of intercalation is the binding to the DNA base mismatches. It occurs because of failure in the replication process or for external agents (UV-radiation, genotoxic chemical regents). Systems with sterically bulky ligands preferentially bind to it, and they can be used as recognition site molecules of these regions [91]. Even more, some molecules are viewed to flip a base out by its insertion inside the DNA, provoking the positioning of the nitrogenous base outside the DNA helical stack [92].

For noncovalent binding it is possible to obtain an equilibrium constant (K), quantifying the affinity of the drug to DNA, and a site size (n). The site size is expressed as the number of adjacent basepairs being inhibited to a further interaction. For example, it is observed that bromide ethidium, an intercalating organic molecule, has a site size value of $\approx$2, which means that the interaction of each ethidium bromide involves a mean of 2 basepairs, which cannot further interact with other ethidium bromide molecules [93].

1.3 Metal Complexes in Anticancer Strategy

1.3.1 From Platinum Complexes...

The anticancer activity of cisplatin has been known since 1965 [94]. The mechanism of action involves a pre-reaction of the squared complex, which consists of substitution of the chloride anions by water molecules (Figure 1.15) [95]. The aquo-complex reacts with DNA of the cell through intra-strand cross linking, coordinating to two guanine groups in N_7 position. Such interaction inhibits the replication and the transcription of DNA [96], leading to the cell death.

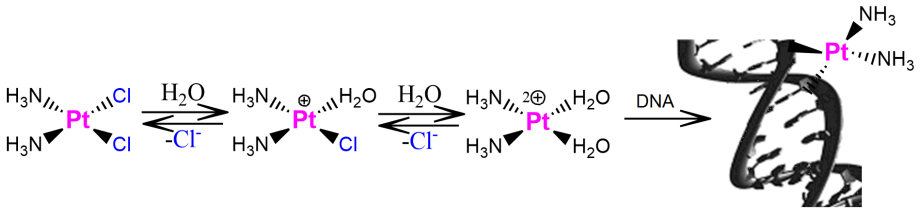

Figure 1.15: Mechanism of activation of cisplatin: formation of aqua-complex interacting with DNA *via* intra-strand binding.

From this serendipitous discovery, various Pt(II) complexes have been developed: cisplatin, carboplatin, oxaliplatin and nedaplatin are the currently marketed ones [96] (Figure 1.16).

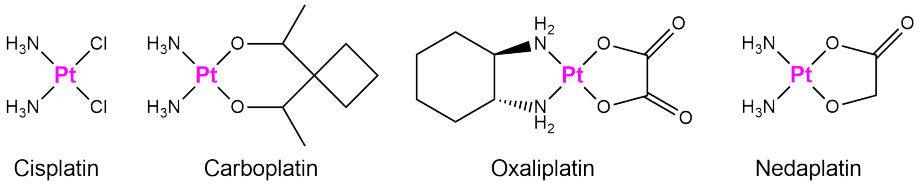

Figure 1.16: Marketed Pt(II) drugs.

However, Pt(II) complexes exhibit many inconveniences. Despite of the relentlessly research to bypass them, Pt(II) based drugs can display cellular resistance, side-reactions effects (e.g. proteins), low solubility and low lipophilicity [97]. Scientific studies have been continuously developing in order to overtake or minimize such negative features, and various Pt(II) complexes have been synthesized.

1.3.2 ...to Non-Platinum Complexes

1.3.2.1 Ruthenium Metal Complexes

Besides platinum complexes, new metal centers have been proposed in drugs delivery research in order to bypass the above mentioned side effects [98]. Except platinum(II), ruthenium(II) compounds are the most investigated metal drugs in anticancer strategy [99]. Actually, Ru(II) exhibits quite the same ligand exchange kinetics as Pt(II) and, in the meantime, ruthenium compounds are generally

less toxic than Pt(II) [100]. In addition, a valuable ruthenium property is the mimicking of iron [101], allowing ruthenium to interact with the iron-transport protein transferrin. Consequently, the interaction promotes the diffusion of the drug through the biological system. Even more, the discovered higher demand of iron and the higher concentration of transferrin receptor inside the cancer cell provide to the ruthenium based drugs certain selectivity towards cancer cells [99]. For these reasons ruthenium(II) complexes represent an ideal alternative to the platinum(II) compounds. Despite this, only two Ruthenium compounds have entered clinical trials, the [ImH][trans$-RuCl_4$(DMSO)Im] (NAMI-A) and [InH][trans$-RuCl_4In_2$], where Ru has oxidation number III.
The firstly synthesized Ru(II) complexes with anticancer property are Ru-amine [102] and RuCl-DMSO-complexes [103]. Interestingly, trans-[$Ru(Cl)_2DMSO_4$] is more cytotoxic than its cis-isomer. As the cisplatin results more toxic than transplatin, so it suggests a different pathway of reaction of Ru(II). In fact, on the one hand cisplatin reacts with DNA trough an intrastrand cross link; on the other hand, Ru(II) complexes generally react through a cross link between DNA strands.

1.3.2.2 Further Metal Centers

In the last years, other metal centers have been taken into account in anticancer strategy. Metal complexes having Osmium [104], Rhodium [105], Iridium [105], Copper [106], Cobalt [107] Gold [108] as metal center are present in literature. The metal center proportion to the metal complex different properties, such as the charge, the geometry, the photophysical properties (favouring MC or MLCT transitions) and the kinetics of ligand exchange. It follows that the choice of the metal center is essential when we plan to synthesize a new drug. Surely, the ligands bound to the metal center are also relevant, since they can favour interaction with the target (for example, the ligand can supply π-stacking interaction with the nucleic acids) and can influence other properties (solubility, kinetic rate of reaction and photoproperties, as well).

1.4 Enhancement of Compounds Selectivity

The strength of the interaction of a metal drug towards biological targets is not the only single paramater which must be taken into account in the development of an anticancer strategy. Actually, a selective interaction towards the cancer cells and a slight reactivity with the health cells should also be desirable. Selectivity can be enhanced by means of different methods:

- increase of the selectivity towards a specific target and slight interaction with other biomolecules [109, 110], in particular in the case of the target is overexpressed in some way inside the cancer cells;
- use of *prodrugs*. The exploitation of prodrugs is a valuable strategy, based on molecules which have no (or little) activity, but their reactivity is switched on under suitable conditions. The activation can be promoted by an internal stimulus, such as the pH or the presence of reductants inside the cell [111], or an external stimulus, such as the light [112]. Aim of the prodrugs strategy is the activation of the drugs in a specific region, in order to make the drug available only for the cancer cells.

Part of the Thesis is focused on two different ways of selective strategy: (i) selectivity towards G-Quadruplex structures and (ii) enhancement of the reactivity by means of photoirradiation. Both strategies will be explained in the following paragraphs.

1.4.1 Selectivity Towards Specific Targets: G-Quadruplex Binders

G-Quadruplex is a recently considered target for new drugs. G-rich tracts are present in the telomere of the genome and it is found that the majority of cancer cells overexpress telomerase, contributing to the immortalization of the cells [113]. In addition, it is verified that specific DNA regions, called proto-oncogenes, being these malfunctioning genes which can promote cancer cell formation, have G-rich tracts. Examples of proto-oncogenes are the *c-myc* [114] and the *c-kit* [115] regions. Mutations or overexpressions of such genes alter cell growth and proliferation.
In the last years, it has been demonstrated that G-Quadruplex formation can affect the gene functions. For instance, G-Quadruplex structure of the telomere inhibits the function of the telomerase enzyme [116]. Consequently, systems able to stabilize the G-quadruplex telomere conformation and inhibit genome lengthening could be exploited to obtain a selective cancer cell death. In addition, the expression of the c-myc promoter, which has a native duplex structure, can be silenced by stabilization of its quadruplex conformation [117, 118].
Different organic [119, 120] and organometallic complexes [121, 122] have been proposed as G-Quadruplex binders. Concerning metal complexes, various classes have been tested:

- **Metallo-porphirins**. Porphirins have been broadly tested with Quadruplexes. A well known porphirinic compound is TMPyP4 (5,10,15,20-tetra-(N-methyl-4-pyridyl)porphyrin), which is verified to inhibit the telomerase [123]. Metallo-porphirins analogues of TMPyP4 are able to interact externally of the G-tetrads by means of π-stacking interactions. In addition, the presence of a metal ion in the porphirinic structure enhances the interaction strength, proportioning electrostatic interaction [124];

- **Planar metal complexes**. Such classes of complexes are metal ions coordinated with ligands which are not planar when they are unbound. Differently to porphirins, the free ligands slightly interact with the G-Quadruplex, since they cannot form extended stacked interaction. However, the complexation renders the ligand geometry planar, increasing the affinity towards G-Quadruplex, coupled to the electrostatic interaction of the metal ion. Examples of planar metal complexes are salphen, salen [125, 126], phenantroline [127] and terpyridine [128] ligands coordinated to various metal centers (Ni^{2+}, Cu^{2+}, Zn^{2+}, V^{4+}, Pt^{2+} and Ru^{3+}). The degree of planarity induced by the metal center influences the affinity with the G-Quadruplex;

- **Supramolecular systems**. Nonplanar systems can exhibit a certain selectivity for G-Quadruplex moiety. Some examples are the supramolecular squares of multinuclear Pt(II) [129], cylinders formed by the interaction of

ditopic ligands with two metal ions, with general formula M_2L_3 [130], and supramolecular cubes, obtained by association of two Zn-porphyrins [131];

- **Octahedral systems**. Mono- and bimetallic Ruthenium polypyridyl complexes show good interaction with G-Quadruplex. In addition to these, biscyclometalated complexes display remarkable affinity [132, 133]. In particular, the modification of the ancillary NN and the CN ligands reflects in the selectivity towards G-Quadruplex [134].

1.4.2 Photodynamic Therapy Strategy

In this Thesis, part of the efforts has been devoted to the study of photoactivation of the metal complexes, which is the topic of Photodynamic Therapy, or PDT. In PDT strategy a photosensitizer S is excited to S*. The excited S* can react through different pathways with DNA (Figure 1.17) [135, 136]:

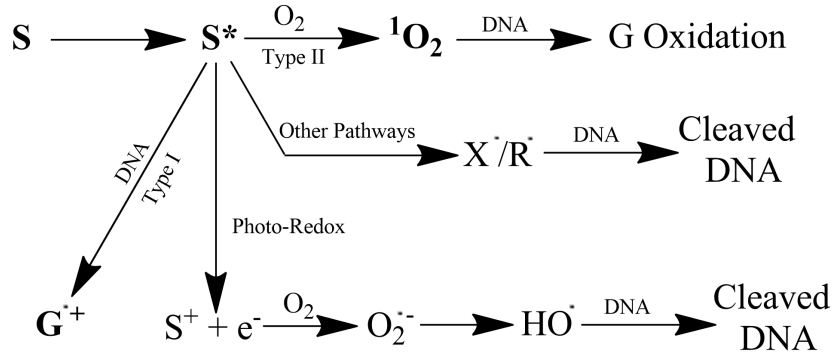

Figure 1.17: Possible mechanisms of action of a photosensitizer (S).

- **Type II mechanism**: it is a dioxygen-dependent pathway, occurring in classical photodynamic therapy. The excited photosensitizer transfers its energy to the oxygen in its triplet ground state. Consequently, the triplet oxygen converts into singlet oxygen, a reactive species damaging DNA [136, 137]. Singlet oxygen target generally is the guanine nucleobase, producing 8-oxo-guanine;

- **Type I mechanism**: it is a dioxygen-independent pathway, which occurs in the nonclassical photodynamic therapy. In this case, the compounds can photorelease radicals, or they are photooxidant or photoreductant molecules. So, they cause DNA photocleavage without the presence of dioxygen. Note that an oxygen-independent mechanism of action is of remarkable interest for the reason that the majority of the cancer cells are generally hypoxic, reducing the effect of an oxygen-based mechanism;

- **Photoredox pathway**: the molecule evolves due to a photoredox reaction, releasing an electron. The electron can directly reduce a nucleobases or reduce the molecular oxygen to superoxide or hydroxyl radicals, which react with the nucleic acid;

- **Other pathways**: other pathways can involve the release of specific molecules. For instance, photo-NO-releasing molecules [138] and the photo-CO-releasing molecules [139] can release nitric oxide (NO) or carbon monoxide (CO) after irradiation, respectively. Concerning the NO molecule, even if it promotes the cell growth, at higher concentration (high µM to mM) can cause the cell death. The effect of the NO molecule involves an irreversible reaction with DNA, promoting his fragmentation.

Various parameters are involved in the photoreactivity of a molecule and the sum of them makes the compound suitable for PDT. The optimal properties of a photosensitizer are [140]:

- no or low activity in the dark;
- photostability;
- activation at $\lambda_{irr} > 300\,\text{nm}$ because high energy irradiation can provoke damage to the skin. In particular, the optimal region is the red visible region ($600\,\text{nm} < \lambda_{irr} < 900\,\text{nm}$) because below 600 nm the radiation is partially absorbed by the tissue, especially by haemoglobin and myoglobin [141];
- high absorption at the wavelength of irradiation;
- high quantum yield of the transition to the photoactive excited state;
- for the oxygen-dependent photosensitizer, high singlet oxygen quantum yield.

Although the photoactivation strategy was developed for organic molecules (e.g. porphyrins), in the last years various classes of metal complexes have been taken into account.
Platinum complexes were the first class of metal complexes to be tested for the Photodynamic Therapy, using Pt(IV) [95, 140, 142]. Pt(IV) octahedral complexes are mainly inert, but they can be activated by the photorelease of the axial ligands, to obtain the squared Pt(II) active species. The first generation of photoactivatable Pt(IV) complexes were the diiodo complex [142], such as *cis,trans*-$[PtCl_2(en)I_2]$ [143] and *cis,trans*-$[Pt(OAc)_2(en)I_2]$ [144], which react with DNA after irradiation with a source of light ($\lambda > 375\,\text{nm}$), provoking the loss of both iodides. The second generation of photoactivated Pt(IV) complexes were the Pt(IV) diazido complexes ($\lambda > 300\,\text{nm}$) [145]. These complexes exhibit higher stability in the dark and in the presence the biological reductants than diiodo Pt(IV) species. Moreover, the N_3 radicals from the photolysis of the metal complex generally evolve to N_2 [140]. Further studies involve combination of different functional groups inside the ligands in order to increase the antitumoral effect of the drug and in order to decrease the irradiation wavelength by means of the *multiphoton excitation* [140].
Furthermore, the anticancer activity can be enhanced by the presence of targeting or bioactive axial ligands having anticancer or pharmacokinetic properties, as well [146–148]. In general, the use of an inactive metal centre, which is able to release small molecules with biological and anticancer activity (called *caged* metal compounds), is the topic of a large study in contemporary literature [149, 150]. The use of such a kind of ligands is powerful with Platinum

(IV), for the reason that the release of bioactive organic molecules follows the reduction of the ineffective Pt(IV) form to the active Pt(II) form (Figure 1.18), obtaining a dual mode of action [150].

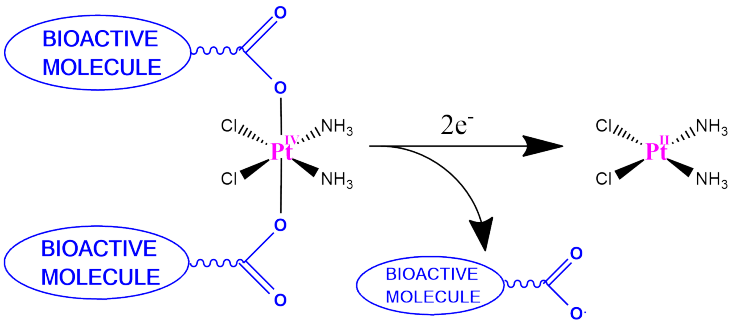

Figure 1.18: Scheme of the release of a bioactive ligand.

Examples of bioactive ligands used in the synthesis of metal complexes are intercalators (which are able to insert between the DNA basepairs and induce important modifications of the secondary structure of the polynucleotide) [151], neuroactive molecules, which are amines such as γ-aminobutyric acid, typtamine, serotonin, tyramine and butylamine, α-aminoacids and peptides [152], peptide receptor [153], estradiol [154], nanotubes [148].
Various classes of ruthenium complexes exhibit photocleavaging properties and, among these, the most investigated ones are the polypyridyl complexes, which have high singlet oxygen quantum yields. In addition, their photoluminescent properties and their ability to intercalate between the base pairs of DNA make them suitable as DNA photocleavaging agents ($\lambda > 440\,\text{nm}$) [155–157].
In the same way as polypyridyl complexes, many biscylometalated complexes produce singlet oxygen and, recently, iridium complexes have been proposed as photosensitizer in PDT [158, 159].
Rhodium polypyridyl complexes exhibit good photocleavaging properties, as well. In particular, it is found that they can intercalate between the nitrogenous basepairs or into the groove and cleave DNA. Interestingly, the ancillary intercalating ligand plays a fundamental role in the recognition site [90]. Actually, variation in the shape and functional groups of the ligands provide certain preference of binding to the DNA secondary structure because of steric exclusion and noncovalent interactions. It follows that the development of octahedral systems able to intercalate into the DNA and cleave the DNA in the region where the interaction is placed is of remarkable interest [160]. In addition, dirhodium complexes can form covalent adducts with nitrogenous bases under irradiation [161, 162], a behaviour observed for ruthenium complexes, as well [163]. The reaction involves the photorelease of a ligand, allowing the interaction with N_7 of guanine.

1.5 The Metal Complexes in the Thesis

In Part II of the Thesis we treat different classes of metal complexes, with various metal centers and ligands. Regarding the metal complexes, we used η^6-arene

and biscyclometalated complexes.

1.5.1 Arene Ruthenium(II) Complexes

Arene Ruthenium(II) complexes are an extensively studied class of compounds for their high stability and their known cytotoxic activity (Figure 1.19).

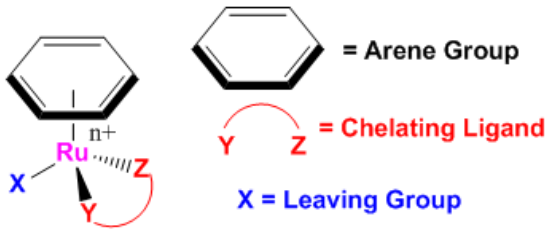

Figure 1.19: The pseudo-octahedral structure of an arene Ru(II) complex. YZ is the chelating group, X is the leaving group and n is the charge.

The reactivity of these compounds depends on various factors [99, 164]:

- **Nature of the arene (intercalative or nonintercalative group)**. Arene is used to stabilize the ruthenium II oxidation state. In addition, it provides an important contribution on the reactivity of the drug; actually, the increase of the aromatic size of the arene group favours the intercalation inside the DNA, which greatly enhances the activity of the metal complex [165]. Moreover, the arene ligand is the hydrophobic part of the metal complex, and it favours the passage through the cell membrane. On the other hand, the presence of polar functional groups on the arene rings (such as amides, esthers and alcohols) lowers the drug efficiency [166];
- **Leaving group (X)**: it generally is a halide group; it is substituted by the more reactive water group in aqueous solution. The rate of hydrolysis depends on the ligands nature (arene, chelating-group, leaving group) and the release of the leaving group can allow the ruthenium to form covalent binding with the DNA by displacement of the water molecule, in particular with the N_7 atom of the guanine [167, 168];
- **Chelating ligand (YZ)**: investigated groups are, for instance, NN, NO and OO-chelating ligands. It is assessed that the chelating ligand influences the binding to the nucleobase and its selectivity, as well (and it remarkably rises the anticancer activity of the drug [100, 164, 168]). For example, the ancillary ligand can form hydrogen bonds with the functional groups of the guanine, promoting the covalent binding of the arene complex after the release of the leaving group, In addition, the ancillary ligand can interact *via* noncovalent binding to DNA due to its intrinsic properties [169];
- **Charge (n)**: it influences the solubility of the drug and the partition coefficient;
- **Counterion**: it changes the solubility of the drug and, in few cases, the reactivity, as well.

The large variety of arene, leaving, and chelating groups implies almost infinite possibilities of Ru-arene compounds, achieving various thermodynamic and kinetic properties, which is a useful tool in the tuning of the pharmacokinetics of the drug.

1.5.2 Biscyclometalated Iridium(III) and Rhodium(III) Complexes

Good anticancer activity has been recently reported for Iridium and Rhodium species [105], and a recent developed class containing such metal centers are the biscyclometalated complexes. Biscyclometalated complexes are composed by two CN cyclometalating ligands and an ancillary ligand (Figure 1.20; in the present Thesis, we worked with NN ancillary ligands).

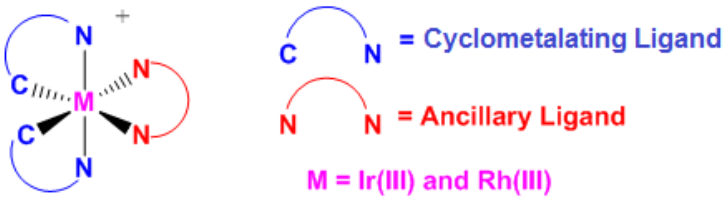

Figure 1.20: Biscyclometalated complex structure. CN is the cyclometalating ligand and NN is the ancillary ligand.

This class of complexes has been applied in different fields for their promising photophysical properties [170]. Actually, Iridium(III) biscylometalated complexes exhibit long lifetimes, large stokes shifts and high quantum yields. Cyclometalating ligands are strong fields ligands which split the d orbitals of the metal centers into high energy; it follows that the MC transition is not the lowest electronic transition, but other excitation states are favoured. In particular, for Iridium biscyclometalated complexes, the metal-to-ligand charge transfer (MLCT) transition is the lowest one, even though ligand centered (LC) transition can exhibit a similar energy. It provokes a mixing of both states. On the other hand, Rhodium complexes generally exhibit a LC lowest state.
The possibility to easily change the nature of the ligands, allows one to tune the fluorescence of the complexes, obtaining almost infinite possible luminescent species [171–173]. Concerning biological applications, biscyclometalated iridium complexes have been proposed as labelling reagents of biological molecules [174–177] and, in the last years, the cyclometalated complexes were suggested as candidates for photodynamic therapy (PDT) [179–181].
On the other hand, Rhodium biscylometalated complexes are less studied because of their poor photophysical properties. Nevertheless, it is verified that rhodium metal center generally exhibits higher cytotoxic activity than iridium does, which makes it a good candidate for anticancer strategy [182, 183].

1.5.3 Ancillary Ligands

The chosen ancillary ligands bound to the metal complexes are the arylazole chelating ligands, which have been seen to exhibit interesting biological properties and metal complexes coordinated to them have shown good properties. Actually, the possibility to link the reactivity of a positive charged metal ion and the mode of binding to nucleic acids of heteroaromatic planar ligand (e. g. groove binding, intercalation) can increase the reactivity of the drug.
Benzoimidazole, benzoxazole, benzothiazole and species derived from them like 2-arylbenzazoles have been used as agents against Alzheimer disease [184] and in other biomedical applications [185, 186]. Even more interestingly, derivatives of benzothiazole [187,188] or benzoimidazole [189] have proven to exhibit antitumor activity. In addition different arene [190–192] and non-arene [193] ruthenium compounds with ligands containing a core of benzoimidazole or benzothiazole bonded to a 2-pyridine unit or other organic moieties have been reported to exhibit antitumoral activity and other biological properties [194–197].

Bibliography

[1] R. B. Martin (1985). *Nucleoside Sites for Transition Metal Ion Binding*, Accounts of Chemical Research, 18 (2), 32-38.

[2] M. J. Cavaluzzi and P. N. Borer (2004). *Revised UV Extinction Coefficients for Nucleoside-5'-Monophosphates and Unpaired DNA and RNA*, Nucleic Acids Research, 32 (1), e13-e13.

[3] J. D. Watson and F. H. Crick (1953). *Molecular Structure of Nucleic Acids*, Nature, 171 (4356), 737-738.

[4] A. Rich and S. Zhang (2003). *Z-DNA: the Long Road to Biological Function*, Nature Reviews Genetics, 4 (7), 566-572.

[5] D. L. Nelson, A. L. Lehninger and M. M. Cox (2008). *Lehninger Principles of Biochemistry*, 5 th Edition, Mcmillan.

[6] M. D. Frank-Kamenetskii and S. M. Mirkin (1995). *Triplex DNA Structures*, Annual Review of Biochemistry, 64 (1), 65-95.

[7] F. Geinguenaud, E. Guenin, Y. Lalatonne and L. Motte (2016). *Vectorization of Nucleic Acids for Therapeutic Approach: Tutorial Review.*, ACS Chemical Biology, 11 (5), 1180-1191.

[8] J. Jiao, Q. Zou, M. H. Zou, R. M. Guo, S. Zhu and Y. Zhang (2016). *Aptamer-Modified PLGA Nanoparticle Delivery of Triplex Forming Oligonucleotide for Targeted Prostate Cancer Therapy*, Neoplasma, 63 (4), 569-575.

[9] M. Gellert, M. N. Lipsett and D. R. Davies (1962). *Helix formation by guanylic acid*, Proceedings of the National Academy of Sciences, 48 (12), 2013-2018.

[10] F. Zaccaria, G. Paragi and C. F. Guerra (2016). *The Role of Alkali Metal Cations in the Stabilization of Guanine Quadruplexes: Why K^+ is the Best*, Physical Chemistry Chemical Physics, 18 (31), 20895-20904.

[11] N. H. Campbell and S. Neidle (2012). *G-quadruplexes and Metal Ions*, in Interplay between Metal Ions and Nucleic Acids, Vol. 10, pp. 119-134, Springer, Netherlands.

[12] G. N. Parkinson, M. P. Lee and S. Neidle (2002). *Crystal Structure of Parallel Quadruplexes from Human Telomeric DNA*, Nature, 417 (6891), 876-880.

[13] Y. Wang and D. J. Patel (1993). *Solution structure of the human telomeric repeat d[$AG_3(T_2AG_3)_3$] G-tetraplex*, Structure, 1 (4), 263-282.

[14] J. Dai, C. Punchihewa, A. Ambrus, D. Chen, R. A. Jones and D. Yang (2007). *Structure of the Intramolecular Human Telomeric G-Quadruplex in Potassium Solution: a Novel Adenine Triple Formation*, Nucleic Acids Research, 35 (7), 2440-2450.

[15] H. M. Berman, T. Battistuz, T. N. Bhat, W. F. Bluhm, P. E. Bourne, K. Burkhardt, Z. Feng, G. L. Gilliland, L. Iype, S. Jain, P. Fagan, J. Marvin, D. Padilla, V. Ravichandran, B. Schneider, N. Thanki, H. Weissig, J. D. Westbrook and C. Zardecky (2002). *The Protein Data Bank*, Acta Crystallographica Section D: Biological Crystallography, 58 (6), 899-907.

[16] A. Herraez (2006). *Biomolecules in the Computer: Jmol to the Rescue*, Biochemistry and Molecular Biology Education, 34 (4), 255-261.

[17] H. J. Lipps and D. Rhodes (2009). *G-quadruplex Structures: in Vivo Evidence and Function*, Trends in Cell Biology, 19 (8), 414-422.

[18] A. T. Phan, Y. S. Modi and D. J. Patel (2004). *Propeller-Type Parallel-Stranded G-Quadruplexes in the Human c-myc Promoter*, Journal of the American Chemical Society, 126 (28), 8710–8716.

[19] M. L. Gleghorn, J. Zhao, D. H. Turner and L. E. Maquat (2016). *Crystal Structure of a Poly(rA) Staggered Zipper at Acidic pH: Evidence that Adenine N1 Protonation Mediates Parallel Double-Helix Formation*, Nucleic Acids Research, 44 (17), 8417-8424.

[20] A. Rich, D. R. Davis, F. H. C. Crick and J. D. Watson (1961). *The Molecular Structure of Polyadenylic Acid*, Journal of Molecular Biology, 3 (1), 71-86.

[21] M. Szabat and R. Kierzek (2017). *Parallel-Stranded DNA and RNA Duplexes: Structural Features and Potential Applications*, The FEBS Journal, 93 (4), 529-534.

[22] J. R. Fresco and P. Doty (1957). *Polynucleotides I. Molecular Properties and Configurations of Polyriboadenilic Acid in Solution*, Journal of the American Chemical Society, 79 (14), 3928-3929.

[23] J. Brahms, A. M. Michelson and K. E. Van Holde (1966). *Adenylate Oligomers in Single- and Double-strand Conformation*, Journal of Molecular Biology, 15 (2), 467-488.

[24] T. N. Holcomb and I. Jr. Tinoco (1965). *Conformation of Polyriboadenylic Acid: pH and Temperature Dependence*, Biopolymers, 3 (2), 121-133.

[25] J. Brahms (1963). *Optical Activity and the Conformation of Polynucleotides*, Journal of the American Chemical Society, 85 (20), 3298-3300.

[26] R. Maggini, F. Secco and M. Venturini (1994). *Kinetic Study of Double-Helix Formation and Double-Helix Dissociation of Polyadenylic Acid*, Journal of the Chemical Society, Faraday Transactions, 90 (16), 2359-2363.

[27] B. I. Kankia (2003). *Binding of Mg^{2+} to Single-Stranded Polynucleotides: Hydration and Optical Studies*, Biophysical Chemistry, 104 (3), 643-654.

[28] V. A. Sorokin, V. A. Valeev, G. O. Gladchenko, M. V. Degtiar and Y. P. Blagoi (2001). *Ni^{2+} Ion Effect of Conformation on Single-,Double- and Three Stranded Homopolynucleotides Containing Adenine and Uracil*, Macromolecular Bioscience, 1 (5), 191-203.

[29] V. A. Sorokin, Y. P. Blagoi and V. A. Valeev (1983). *Spectroscopic Study of Complexation of Polyriboadenylic Acid with Calcium Ions*, Doklady Akademii Nauk BSSR, 27 (10), 942-945.

[30] V. A. Sorokin, Y. P. Blagoi, L. K. Silina, E. B. Dalyan, Y. S. Babayan and V. M. Aslanyan (1982). *Spectroscopic Study of the Effect of Divalent Manganese Ion Binding on the Conformation of Polyriboadenylic Acid*, Molekulyarnaya Biologiya (Moscow), 16 (6), 1223-1233.

[31] J. C. Thrierr, M. Dourlent and M. Leng (1971). *A Study of Polyuridylic Acid*, Journal of Molecular Biology, 58 (3), 815-830.

[32] M. N. Lipsett (1960). *Evidence fo Helical Structure in Polyuridilc Acid*, Proceedings of the National Academy of Sciences of the United States of America, 46 (4), 445-446.

[33] D. L. Inners and G. Fensenfeld (1970). *Conformation of Polyribouridylic Acid in Solution*, Journal of Molecular Biology, 50 (2), 373-389.

[34] D. Bode, M. Heinecke and U. Schernau (1973). *An IR-Investigation of the Helix-Coil Conversion of PolyU*, Biochemical and Biophysical Research Communications, 52 (4), 1234-1240.

[35] S. Z. Jakabhazy and S. W. Fleming (1966). *Electro-Optical Studies of Conformation and Interaction of Polynucleotides*, Biochemistry, 4 (7), 793-813.

[36] H. Diebler, F. Secco and M. Venturini (1987). *The Binding of Mg(II) and Ni(II) to Syntetic Polynucleotides*, Biophysical Chemistry, 26 (2-3), 193-205.

[37] G. Luck and C. Zimmer (1972). *Conformational Aspects and Reactivity of DNA. Effect of Manganese and Magnesium Ions on Interaction with DNA*, European Journal of Biochemistry, 29 (3), 528-536.

[38] M. Langlais, H. A. Tajmir-Riahi and R. Savoie (1990). *Raman Spectroscopy Study of the Effects of Ca^{2+}, Mg^{2+}, Zn^{2+}, and Cd^{2+} Ions on Calf Thymus DNA: Binding Sites and Conformational Changes*, Biopolymers, 30 (7-8), 743-752.

[39] R. V. Gessner, G. J. Quigley, A. H. J. Wang, G. A. van der Marel, J. H. van Boom and R. Alexander (1985). *Structural Basis for Stabilization of Z-DNA by Cobalt Hexaammine and Magnesium Cations*, Biochemistry, 24 (2), 237-240.

[40] G. L. Eichhorn and P. Clark (1965). *Interactions of Metal Ions with Polynucleotides and Related Compounds. V. The Unwinding and Rewinding of DNA Strands under the Influence of Cu(II) Ions*, Proceedings of the National Academy of Sciences of the United States of America, 53 (3), 586-593.

[41] B. I. Kankia (2004). *Inner-Sphere Complexes of Divalent Cations with Single-Stranded Poly(rA) and Poly(rU)*, Biopolymers, 74 (3), 232-239.

[42] S. A. Kazakov and S. M. Hecht (2006). *Nucleic Acid-Metal Ion Interactions*, Encyclopedia of Inorganic Chemistry, 1, 1-34.

[43] E. Sletten and W. Nerdal (1997). *Interaction of Mercury with Nucleic Acids and Their Components*, Metal Ions in Biological Systems, 34, 479-501.

[44] T. R. Jack (1979). *Heavy Metals Labeling of Nucleotides and Polynucleotides for Electron Microscopy Studies*, Metal Ions in Biological Systems, 8, 159-182.

[45] Y. A. Shin, J. M. Heim and G. L. Eichhorn (1972). *Interactions of Metal Ions with Polynucleotides and Related Compounds. XX. Control of the Conformation Polyriboadenylic Acid by Divalent Metal Ions*, Bioinorganic Chemistry, 1 (2), 149-163.

[46] G. L. Eichhorn and Y. A. Shin (1968). *Interactions of Metal Ions with Polynucleotides and Related Compounds. XII. The Relative Effect of Various Metal Ions on DNA Helicity*, Journal of the American Chemical Society, 90 (26), 7323-7328.

[47] D. E. Dix and D. B. Straus (1972). *DNA Helix Stability. Differential Stabilization by Counter Cations*, Archives of Biochemistry and Biophysics, 152 (1), 299-310.

[48] R. K. O. Sigel and H. Sigel (2010). *A Stability Concept for Metal Ion Coordination to Single-Stranded Nucleic Acids and Affinities of Individual Sites*, Accounts of Chemical Research, 40 (7), 974-984.

[49] T. Biver (2013). *Stabilisation of Non-Canonical Structures of Nucleic Acids and Small Molecules*, Coordination Chemistry Reviews, 257 (19), 2765-2783.

[50] T. Biver, N. Busto, B. García, J. M. Leal, L. Menichetti, F. Secco and M. Venturini (2015). *Mg(II) and Ni(II) Induce Aggregation of Poly(rA)Poly(rU) to either Tetra-Aggregate or Triplex Depending on the Metal Ion Concentration*, Journal of inorganic biochemistry, 151, 115-122.

[51] C. L. Stevens and G. Felsenfeld G (1964). *The Conversion of Two-Stranded Poly(A+U) to Three-Strand Poly(A+2U) and PolyA by Heat*, Biopolymers, 2 (4), 293-314.

[52] B. I. Kankia (2003). *Mg^{2+}-Induced Triplex Formation of an Equimolar Mixture of Poly(rA) and Poly(rU)*, Nucleic Acids Research, 31 (17), 5101-5107.

[53] B. G. Kim, H. M. Evans, D. N. Dubins and T. V. Chalikian (2015). *Effects of Salt on the Stability of a G-Quadruplex from the Human c-MYC Promoter*, Biochemistry, 54 (22), 3420-3430.

[54] D. Bhattacharyya, G. M. Arachchilage and S. Basu (2016). *Metal Cations in G-Quadruplex Folding and Stability*, Frontiers in Chemistry, 4, 1-14.

[55] D. G. Wei, G. N. Parkinson, A. P. Reszka and S. Neidle (2012). *Crystal Structure of a c-kit Promoter Quadruplex Reveals The Structural Role of Metal Ions and Water Molecules in Maintaining Loop Conformation*, Nucleic Acids Research, 40 (10), 4691-4700.

[56] C. F. Baes and R. E. Mesmer (1976). *Hydrolysis of Cations*, Ch. 6, pp. 112-123, John Wiley and Sons, New York.

[57] J. Georges (1993). *Lanthanide-Sensitized Luminescence and Applications to the Determination of Organic Analytes. A review*, Analyst, 118 (12), 1481-1486.

[58] P. K. L. Fu and C. Turro (1999). *Energy Transfer from Nucleic Acids to Tb(III): Selective Emission Enhancement by Single DNA Mismatches*, Journal of the American Chemical Society, 121 (1), 1-7.

[59] S. J. Karlik, G. L. Eichhorn, P. N. Lewis and D. R. Crapper (1980). *Interaction of Aluminum Species with Deoxyribonucleic Acid*, Biochemistry, 19 (26), 5991-5998.

[60] S. J. Karlik and G. L. Eichhorn (1989). *Polynucleotide Cross-Linking by Aluminum*, Journal of Inorganic Biochemistry, 37 (4), 259-269.

[61] A. T. Sarpola, V. K. Hietapelto, J. E. Jalonen, J. Jokela and J. H. Ramo (2006). *Comparison of Hydrolysis Products of $AlCl_3 \cdot 6\,H_2O$ in Different Concentrations by Electrospray Ionization Time of Flight Mass Spectrometer (ESI TOF MS)*, International Journal of Environmental and Analytical Chemistry, 86 (13), 1007-1018.

[62] M. Lamberti, I. D'Auria, M. Mazzeo, S. Milione, V. Bertolasi and D. Pappalardo (2012). *Phenoxy-Thioether Aluminum Complexes as ϵ-Caprolactone and Lactide Polymerization Catalysts*, Organometallics 31 (15), 5551-5560.

[63] J. I. Mujika, J. M. Ugalde and X. Lopez (2012). *Aluminum Speciation in Biological Environments. The Deprotonation of Free and Aluminum Bound Citrate in Aqueous Solution*, Physical Chemistry Chemical Physics, 14 (36), 12465-12475.

[64] S. P. Fricker (2007). *Metal Based Drugs: from Serendipity to Design*, Dalton Transactions, (43), 4903-4917.

[65] P. Nayak (2002). *Aluminum: Impacts and Disease*, Environmental Research, 89 (2), 101-115.

[66] M. A. Rogers and D. G. Simon (1999). *A Preliminary Study of Dietary Aluminium Intake and Risk of Alzheimer's Disease*, Age and Ageing, 28 (2), 205-209.

[67] R. J. Mailloux, J. Lemire and V. D. Appanna (2011). *Hepatic Response to Aluminum Toxicity: Dyslipidemia and Liver Diseases*, Experimental Cell Research, 317 (16), 2231-2238.

[68] A. H. Panhwar, T. G. Kazi, H. I. Afridi, S. A. Arain, M. S. Arain, K. D. Brahaman and S. S. Arain (2016). *Correlation of Cadmium and Aluminum in Blood Samples of Kidney Disorder Patients with Drinking Water and Tobacco Smoking: Related Health Risk*, Environmental Geochemistry and Health, 38 (1), 265-274.

[69] E. H. Jeffery, K. Abreo, E. Burgess, J. Cannata, and J. L. Greger (1996). *Systemic Aluminum Toxicity: Effects on Bone, Hematopoietic Tissue, and Kidney*, Journal of Toxicology and Environmental Health Part A, 48 (6), 649-666.

[70] V. Rondeau, D. Commenges, H. Jacqmin-Gadda and J. F. Dartigues (2000). *Relation Between Aluminum Concentrations in Drinking Water and Alzheimer's Disease: an 8-Year Follow-up Study*, American Journal of Epidemiology, 152 (1), 59-66.

[71] T. Stahl, S. Falk, A. Rohrbeck, S. Georgii, C. Herzog, A. Wiegand, S. Hotz, B. Boschek, H. Zorn and H. Brunn (2017). *Migration of Aluminum from Food Contact Materials to Food - a Health Risk for Consumers? Part I of III: Exposure to Aluminum, Release of Aluminum, Tolerable Weekly Intake (TWI), Toxicological Effects of Aluminum, Study Design, and Methods*, Environmental Sciences Europe, 29 (1), 19-26.

[72] M. W. Bourassa and L. M. Miller (2012). *Metal Imaging in Neurodegenerative Diseases*, Metallomics, 4 (8), 721-738.

[73] K. G. McGrath (2003). *An Earlier Age of Breast Cancer Diagnosis Related to More Frequent Use of Antiperspirants/Deodorants and Underarm Shaving*, European Journal of Cancer Prevention, 12 (6), 479-485.

[74] P. D. Darbre, F. Mannello and C. Exley (2013). *Aluminium and Breast Cancer: Sources of Exposure, Tissue Measurements and Mechanisms of Toxicological Actions on Breast Biology*, Journal of Inorganic Biochemistry, 128, 257-261.

[75] S. J. Mandriota (2017). *A Case-control Study Adds a New Piece to the Aluminium/Breast Cancer Puzzle*, EBioMedicine, 22, 22-23.

[76] E. Furia, T. Marino and N. Russo (2014). *Insights into the Coordination Mode of Quercetin with the Al(III) Ion from a Combined Experimental and Theoretical study*, Dalton Transactions, 43 (19), 7269-7274.

[77] S. J. Karlik, E. Tarien, G. A. Elgavish, and G. L. Eichhorn (1983). *Aluminum-27 Nuclear Magnetic Resonance Study of Aluminum (III) Interactions with Carboxylate Ligands*, Inorganic Chemistry, 22 (3), 525-529.

[78] W. R. Harris, G. Berthon, J. P. Day, C. Exley, T. P. Flaten, W. F. Forbes, T. Kiss, C. Orvig and P. F. Zatta (1996). *Speciation of Aluminum in Biological Systems*, Journal of Toxicology and Environmental Health Part A, 48 (6), 543-568.

[79] C. Exley and J. D. Birchall (1992). *The Cellular Toxicity of Aluminium*, Journal of Theoretical Biology, 159 (1), 83-98.

[80] S. A. Latt and H. A. Sober (1967). *Protein-Nucleic Acid Interactions. III. Cation Effect on Binding Strength and Specificity*, Biochemistry, 6 (10), 3307-3314.

[81] K. B. Jacobson, B. D. Sarma and J. B. Murphy (1972). *Reaction of Cacodylic Acid with Organic Thiols*, FEBS letters, 22 (1), 80-82.

[82] T. W. Shin, K. Kim and I. J. Lee (1997). *Spectrophotometric Determination of the Acid Dissociation Constants for Cacodylic Acid and p-nitrophenol at Elevated Temperatures*, Journal of Solution Chemistry, 26 (4), 379-390.

[83] P. V. Ioannou (2012). *Dimethylphosphinato and Dimethylarsinato Complexes of Sb(III) and Bi(III) and their Chemistry*, Monatshefte für Chemie-Chemical Monthly, 143 (10), 1349-1356.

[84] P. V. Ioannou (2010). *Dimethylphosphinato and Dimethylarsinato Complexes of Palladium(II), $[Pd(Me_2PO_2)_2]_3$ and $Pd(Me_2AsO_2)_2$, and their Adducts*, Zeitschrift für Anorganische und Allgemeine Chemie, 636 (7), 1347-1353.

[85] C. F. Whittemore and C. James (1913). *Sebacates and Cacodylates of the Rare Earths*, Journal of the American Chemical Society, 35 (2), 127-132.

[86] R. Pietsch (1958). *Metallfällungen mit Mono-und Dimethylarsinsäure*, Microchimica Acta, 46 (2), 220-224.

[87] P. V. Ioannou (2013). *Dimethylphosphinato and Dimethylarsinato Complexes of Group 13 Metals and their Chemistry*, Monatshefte für Chemie-Chemical Monthly, 144 (6), 793-802.

[88] S. Neidle (2001). *DNA Minor-Groove Recognition by Small Molecules*, Natural Product Reports, 18 (3), 291-309.

[89] P. L. Hamilton and D. P. Arya (2012). *Natural Product DNA Major Groove Binders*, Natural Product Reports, 29 (2), 134-143.

[90] K. E. Erkkila, D. T. Odom, and J. K. Barton (1999). *Recognition and Reaction of Metallointercalators with DNA*, Chemical Reviews, 99 (9), 2777-2796.

[91] E. Rüba, J. R. Hart and J. K. Barton (2004). *[Ru(bpy)$_2$(L)]Cl$_2$: Luminescent Metal Complexes that Bind DNA Base Mismatches*, Inorganic Chemistry, 43 (15), 4570-4578.

[92] L. A. Lipscomb, F. X. Zhou, S. R. Presnell, R. J. Woo, M. E. Peek, R. R. Plaskon and L. D. Williams (1996). *Structure of a DNA-Porphyrin Complex*, Biochemistry, 35 (9), 2818-2823.

[93] Y. Wang, A. Sischka, V. Walhorn, K. Tönsing and D. Anselmetti (2016). *Nanomechanics of Fluorescent DNA Dyes on DNA Investigated by Magnetic Tweezers*, Biophysical Journal, 111 (8), 1604-1611.

[94] B. Rosenberg, L. Vancamp and T. Krigas (1965). *Inhibition of Cell Division in Escherichia coli by Electrolysis Products from a Platinum Electrode*, Nature, 205 (4972), 698.

[95] T. C. Johnstone, K. Suntharalingam and S. J. Lippard (2016). *The Next Generation of Platinum Drugs: Targeted Pt(II) Agents, Nanoparticle Delivery, and Pt(IV) Prodrugs*, Chemical Reviews, 116 (5), 3436-3486.

[96] Y. Jung and S. J. Lippard (2007). *Direct Cellular Responses to Platinum-Induced DNA Damage*, Chemical Reviews, 107 (5), 1387-1407.

[97] A. Bergamo and G. Sava (2015). *Linking the Future of Anticancer Metal-Complexes to the Therapy of Tumour Metastases*, Chemical Society Reviews, 44 (24), 8818-8835.

[98] A. Levina, A. Mitra and P. A. Lay (2009). *Recent Developments in Ruthenium Anticancer Drugs*, Metallomics, 1 (6), 458-470.

[99] P. C. A. Bruijnincx and P. J. Sadler (2011). *Controlling Platinum, Ruthenium and Osmium Reactivity for Anticancer Drug Design*, Advances in Inorganic Chemistry, 61, 1-59.

[100] V. Brabec and O. Nováková (2006). *DNA Binding Mode of Ruthenium Complexes and Relationship to Tumor Cell Toxicity*, Drug Resistance Updates, 9 (3), 111-122.

[101] C. S. Allardyce and P. J. Dyson (2001). *Ruthenium in Medicine: Current Clinical Uses and Future Prospects*, Platinum Metal Reviews, 45 (2), 62-69.

[102] J. R. Durig, J. Danneman, W. D. Behnke and E. E. Mercer (1976). *The Induction of Filamentous Growth in Escherichia Coli by Ruthenium and Palladium Complexes*, Chemico-Biological Interactions, 13 (3-4), 287-294.

[103] E. Alessio, G. Mestroni, G. Nardin, W. M. Attia, M. Calligaris, G. Sava and S. Zorzet (1988). *Cis-and Trans- Dihalotetrakis (Dimethyl Sulfoxide) Ruthenium (II) Complexes (RuX$_2$(DMSO)$_4$; X= Cl, Br): Synthesis, Structure, and Antitumor Activity*, Inorganic Chemistry, 27 (23), 4099-4106.

[104] S. Medici, M. Peana, V. M. Nurchi, J. I. Lachowicz, G. Crisponi and M. A. Zoroddu (2015). *Noble metals in medicine: Latest advances*, Coordination Chemistry Reviews, 284, 329-350.

[105] C. H. Leung, H. J. Zhong, D. S. H. Chan and D. L. Ma (2013). *Bioactive Iridium and Rhodium Complexes as Therapeutic Agents*, Coordination Chemistry Reviews, 257 (11), 1764-1776.

[106] S. S. Hindo, M. Frezza, D. Tomco, M. J. Heeg, L. Hryhorczuk, B. R. McGarvey, Q. P. Dou and C. N. Verani (2009). *Metals in Anticancer Therapy: Copper(II) Complexes as Inhibitors of the 20S Proteasome*, European journal of medicinal chemistry, 44 (11), 4353-4361.

[107] L. N. Ji, X. H. Zou and J. G. Liu (2001). *Shape and Enantioselective Interaction of Ru(II)/Co(III) Polypyridyl Complexes with DNA*, Coordination Chemistry Reviews, 216, 513-536.

[108] A. Casini, C. Hartinger, C. Gabbiani, E. Mini, P. J. Dyson, B. K. Keppler and L. Messori (2008). *Gold(III) Compounds as Anticancer Agents: Relevance of Gold–Protein Interactions for their Mechanism of Action*, Journal of inorganic biochemistry, 102 (3), 564-575.

[109] N. P. Barry and P. J. Sadler (2013). *Exploration of the Medical Periodic Table: towards New Targets*, Chemical Communications, 49 (45), 5106-5131.

[110] K. Nepali, S. Sharma, M. Sharma, P. M. S. Bedi and K. L. Dhar (2014). *Rational Approaches, Design Strategies, Structure Activity Relationship and Mechanistic Insights for Anticancer Hybrids*, European Journal of Medicinal Chemistry, 77, 422-487.

[111] W. A. Denny (2001). *Prodrug Strategies in Cancer Therapy*, European Journal of Medicinal Chemistry, 36 (7), 577-595.

[112] H. Ali and J. E. Van Lier (1999). *Metal Complexes as Photo-and Radiosensitizers*, Chemical Reviews, 99 (9), 2379-2450.

[113] R. Hänsel-Hertsch, M. Di Antonio and S. Balasubramanian (2017). *DNA G-quadruplexes in the Human Genome: Detection, Functions and Therapeutic Potential*, Nature Reviews Molecular Cell Biology, 18 (5), 279-284.

[114] T. Simonsson, M. Kubista and P. Pecinka (1998). *DNA Tetraplex Formation in the Control Region of c-myc*, Nucleic Acids Research, 26 (5), 1167-1172.

[115] A. T. Phan, V. Kuryavyi, S. Burge, S. Neidle and D. J. Patel (2007). *Structure of an Unprecedented G-Quadruplex Scaffold in the Human c-kit Promoter*, Journal of the American Chemical Society, 129 (14), 4386-4392.

[116] D. Sun, B. Thompson, B. E. Cathers, M. Salazar, S. M. Kerwin, J. O. Trent, T. C. Jenkins, S. Neidle and L. H. Hurley (1997). *Inhibition of Human Telomerase by a G-Quadruplex-Interactive Compound*, Journal of Medicinal Chemistry, 40 (14), 2113-2116.

[117] J. Seenisamy, S. Bashyam, V. Gokhale, H. Vankayalapati, D. Sun, A. Siddiqui-Jain, N. Streiner, K. Shin-ya, E. White, W. D. Wilson and L. H. Hurley (2005). *Design and Synthesis of an Expanded Porphyrin*

that Has Selectivity for the c-MYC G-Quadruplex Structure, Journal of the American Chemical Society, 127 (9), 2944-2959.

[118] A. Ambrus, D. Chen, J. Dai, R. A. Jones and D. Yang (2005). *Solution Structure of the Biologically Relevant G-Quadruplex Element in the Human c-MYC Promoter. Implications for G-Quadruplex Stabilization*, Biochemistry, 44 (6), 2048-2058.

[119] D. Y. Zeng, G. T. Kuang, S. K. Wang, W. Peng, S. L. Lin, Q. Zhang, X. X. Su, M. H. Hu, H. Wang, J. H. Tan, Z. S. Huang, L. Q. Gu and T. M. Ou (2017). *Discovery of Novel 11-Triazole Substituted Benzofuro[3, 2-b]quinolone Derivatives as c-myc G-Quadruplex Specific Stabilizers via Click Chemistry*, Journal of Medicinal Chemistry, 60 (13), 5407-5423.

[120] S. K. Noureini, H. Esmaeili, F. Abachi, S. Khiali, B. Islam, M. Kuta, A. A. Saboury, M. Hoffmann, J. Sponer, G. Parkinson and S. Haider (2017). *Selectivity of Major Isoquinoline Alkaloids from Chelidonium Majus towards Telomeric G-Quadruplex: A Study Using a Transition-FRET (t-FRET) Assay*, Biochimica et Biophysica Acta (BBA)-General Subjects, 1861 (8), 2020-2030.

[121] S. N. Georgiades, N. H. Abd Karim, K. Suntharalingam and R. Vilar (2010). *Interaction of Metal Complexes with G-Quadruplex DNA*, Angewandte Chemie International Edition, 49 (24), 4020-4034.

[122] Q. Cao, Y. Li, E. Freisinger, P. Z. Qin, R. K. Sigel and Z. W. Mao (2017). *G-Quadruplex DNA Targeted Metal Complexes Acting as Potential Anticancer Drugs*, Inorganic Chemistry Frontiers, 4 (1), 10-32.

[123] P. Zhao, M. C. Liu, M. Zheng, S. F. Jin, D. T. Tang, J. Chen, Y. N. Ma, J. Q. Lin, X. H. Wang and H. J. Liu (2016). *G-Quadruplex DNA Interactions, Docking and Cell Photocytotoxicity Research of Porphyrin Dyes*, Dyes and Pigments, 128, 41-48.

[124] D. F. Shi, R. T. Wheelhouse, D. Sun and L. H. Hurley (2001). *Quadruplex-Interactive Agents as Telomerase Inhibitors: Synthesis of Porphyrins and Structure-Activity Relationship for the Inhibition of Telomerase*, Journal of Medicinal Chemistry, 44 (26), 4509-4523.

[125] L. Lecarme, E. Prado, A. De Rache, M. L. Nicolau-Travers, R. Bonnet, A. V. D. Heyden, C. Philouze, D. Gomez, J. L. Mergny, H. Jamet E. Defrancq, O. Jarjayes and F. Thomas (2014). *Interaction of Polycationic Ni(II)-Salophen Complexes with G-Quadruplex DNA*, Inorganic Chemistry, 53 (23), 12519-12531.

[126] A. Terenzi, D. Lötsch, S. van Schoonhoven, A. Roller, C. R. Kowol, W. Berger, B. K. Keppler and G. Barone (2016). *Another Step toward DNA Selective Targeting: Ni^{II} and Cu^{II} Complexes of a Schiff Base Ligand Able to Bind Gene Promoter G-Quadruplexes*, Dalton Transactions, 45 (18), 7758-7767.

[127] K. J. Castor, J. Mancini, J. Fakhoury, N. Weill, R. Kieltyka, P. Englebienne, N. Avakyan, A. Mittermaier, C. Autexier, N. Moitessier and

H. F. Sleiman (2012). *Platinum(II) Phenanthroimidazoles for Targeting Telomeric G-Quadruplexes*, ChemMedChem, 7 (1), 85-94.

[128] S. Gama, I. Rodrigues, F. Mendes, I. C. Santos, E. Gabano, B. Klejevskaja, J. Gonzalez-García, M. Ravera, R. Vilar and A. Paulo (2016). *Anthracene-Terpyridine Metal Complexes as New G-Quadruplex DNA Binders*, Journal of Inorganic Biochemistry, 160, 275-286.

[129] R. Kieltyka, P. Englebienne, J. Fakhoury, C. Autexier, N. Moitessier and H. F. Sleiman (2008). *TA Platinum Supramolecular Square as an Effective G-Quadruplex Binder and Telomerase Inhibitor*, Journal of the American Chemical Society, 130 (31), 10040-10041.

[130] H. Yu, X. Wang, M. Fu, J. Ren and X. Qu (2008). *Chiral Metallo-Supramolecular Complexes Selectively Recognize Human Telomeric G-Quadruplex DNA*, Nucleic Acids Research, 36 (17), 5695-5703.

[131] N. P. Barry, N. H. A. Karim, R. Vilar and B. Therrien (2009). *Interactions of Ruthenium Coordination Cubes with DNA*, Dalton Transactions, (48), 10717-10719.

[132] K. J. Castor, K. L. Metera, U. M. Tefashe, C. J. Serpell, J. Mauzeroll and H. F. Sleiman (2015). *Cyclometalated Iridium(III) Imidazole Phenanthroline Complexes as Luminescent and Electrochemiluminescent G-Quadruplex DNA Binders*, Inorganic Chemistry, 54 (14), 6958-6967.

[133] H. Yang, V. P-Y Ma, D. S-H Chan, H. Z. He, C. H. Leung and D. L. Ma (2013). *A Cyclometallated Iridium(III) Complex as a c-myc G-Quadruplex Stabilizer and Down-Regulator of c-myc Oncogene Expression*, Current Medicinal Chemistry, 20 (4), 576-582.

[134] D. L. Ma, D. S. H. Chan and C. H. Leung (2014). *Group 9 Organometallic Compounds for Therapeutic and Bioanalytical Applications*, Accounts of Chemical Research, 47 (12), 3614-3631.

[135] A. R. Chakravarty and M. Roy (2011). *Photoactivated DNA Cleavage and Anticancer Activity of 3d Metal Complexes*, Progress in Inorganic Chemistry, 57, 119.

[136] Z. Zhou, J. Song, L. Nie and X. Chen (2016). *Reactive Oxygen Species Generating Systems Meeting Challenges of Photodynamic Cancer Therapy*, Chemical Society Reviews, 45 (23), 6597-6626.

[137] J. Cadet, T. Douki, J. L. Ravanat and P. Di Mascio (2016). *Reactions of Singlet Oxygen with Nucleic Acids*, in Singlet Oxygen: Applications in Biosciences and Nanosciences, Vol., 1 Ch. 20, pp. 393-407, Royal Society of Chemistry.

[138] A. E. Pierri, D. A. Muizzi, A. D. Ostrowski and P. C. Ford (2014). *Photo-Controlled Release of NO and CO with Inorganic and Organometallic Complexes*, in Photoactive Transition Metal Complexes as Biomolecular Probes and Cellular Reagents. Structure and Bonding, Vol. 165, pp. 1-45, Springer Berlin Heidelberg.

[139] Z. Li, A. E. Pierri, P. J. Huang, G. Wu, A. V. Iretskii and P. C. Ford (2017). *Dinuclear PhotoCORMs: Dioxygen-Assisted Carbon Monoxide Uncaging from Long-Wavelength-Absorbing Metal–Metal-Bonded Carbonyl Complexes*, Inorganic Chemistry, 56 (11), 6094-6104.

[140] N. J. Farrer and P. J. Sadler (2008). *Photochemotherapy: Targeted Activation of Metal Anticancer Complexes*, Australian Journal of Chemistry, 61 (9), 669-674.

[141] N. J. Farrer, L. Salassa and P. J. Sadler (2009). *Photoactivated Chemotherapy (PACT): the Potential of Excited State d-block Metals in Medicine*, Dalton Transactions, (48), 10690-10701.

[142] N. A. Kratochwil, J. A. Parkinson, P. J. Bednarski and P. J. Sadler (1999). *Nucleotide Platination Induced by Visible Light*, Angewandte Chemie International Edition, 38 (10), 1460-1463.

[143] N. A. Kratochwil, P. J. Bednarski, H. Mrozek, A. Vogler and J. K. Nagle (1996). *Photolysis of an Iodoplatinum(IV) Diamine Complex to Cytotoxic Species by Visible Light*, Anti-Cancer Drug Design, 11 (2), 155-171.

[144] N. A. Kratochwil, M. Zabel, K. J. Range and P. J. Bednarski (1996). *Synthesis and X-ray Crystal Structure of trans, cis-[Pt(OAc)$_2$I$_2$(en)]: a Novel Type of Cisplatin Analog that can be Photolyzed by Visible Light to DNA-Binding and Cytotoxic Species in Vitro*, Journal of Medicinal Chemistry, 39 (13), 2499-2507.

[145] L. Ronconi and P. J. Sadler (2011). *Photoreaction Pathways for the Anticancer Complex trans,trans,trans-[Pt^{IV}(N$_3$)(OH)$_2$(NH$_3$)$_2$]*, Dalton Transactions, 40 (1), 262-268.

[146] M. D. Hall and T. W. Hambley (2002). *Platinum(IV) Antitumor Compounds: Their Bioinorganic Chemistry*, Coordination Chemistry Reviews, 232 (1), 49-67.

[147] M. D. Hall, H. R. Mellor, R. Callaghan and T. W. Hambley (2007). *Basis for Design and Development of Platinum(IV) Anticancer Complexes*, Journal of Medicinal Chemistry, 50 (15), 3403-3411.

[148] P. C. A. Bruijnincx and P. J. Sadler (2008). *New Trends for Metal Complexes with Anticancer Activity*, Current Opinion in Chemical Biology, 12 (2), 197-206.

[149] N. Graf and S. J. Lippard (2012). *Redox Activation of Metal Based Prodrugs as a Strategy of Drug Delivery*, Advanced Drug Delivery Reviews, 64 (11), 993-1004.

[150] M. Fanelli, M. Formica, V. Fusi, L. Giorgi, M. Micheloni and P. Paoli (2016). *New Trends in Platinum and Palladium Complexes as Antineoplastic Agents*, Coordination Chemistry Reviews, 310, 41-79.

[151] U. Schatzschneider (2010). *Photoactivated Biological Activity of Transition-Metal Complexes*, European Journal of Inorganic Chemistry, 2010 (10), 1451-1567.

[152] S. Mukhopadhyay, C. M. Barnes, A. Haskel, S. M. Short, K. R. Barnes and S. J. Lippard (2008). *Conjugated Platinum(IV) Peptide Complexes for Targeting Angiogenic Tumor Vasculature*, Bioconjugate Chemistry, 19 (1), 39-49

[153] D. Y. Q. Wong, C. H. F. Yeo, W. H. Ang (2014). *Immuno-Chemotherapeutic Platinum(IV) Prodrugs of Cisplatin as Multimodal Anticancer Agents*, Angewandte Chemie International Edition, 53 (26), 6752-6756.

[154] K. R. Barnes, A. Kutikov and S. J. Lippard (2004). *Synthesis, Characterization, and Cytotoxicity of a Series of Estrogen-Tethered Platinum(IV) Complexes*, Chemistry & Biology, 11 (4), 557-564.

[155] S. Swavey, M. Wang, N. Lundy and J. Allen (2017). *Photoreactions of DNA with a Bimetallic Ruthenium(II) Polypyridyl Complex Bridged by an Organic Chromophore*, Inorganica Chimica Acta, 454, 234-239.

[156] Y. J. Liu, C. H. Zeng, H. L. Huang, L. X. He and F. H. Wu (2010). *Synthesis, DNA-Binding, Photocleavage, Cytotoxicity and Antioxidant Activity of Ruthenium(II) Polypyridyl Complexes*, European Journal of Medicinal Chemistry, 45 (2), 564-571.

[157] E. Wachter, D. K. Heidary, B. S. Howerton, S. Parkin and E. C. Glazer (2012). *Light-Activated Ruthenium Complexes Photobind DNA and are Cytotoxic in the Photodynamic Therapy Window*, Chemical Communications, 48 (77), 9649-9651.

[158] D. Ashen-Garry and M. Selke (2014). *Singlet Oxygen Generation by Cyclometalated Complexes and Applications*, Photochemistry and Photobiology, 90 (2), 257-274.

[159] O. J. Stacey and S. J. Pope (2013). *New Avenues in the Design and Potential Application of Metal Complexes for Photodynamic Therapy*, RSC Advances, 3 (48), 25550-25564.

[160] A. Sitlani, E. C. Long, A. M. Pyle, and J. K. Barton (1992). *DNA Photocleavage by Phenanthrenequinone Diimine Complexes of Rhodium(III): Shape-Selective Recognition and Reaction*, Journal of the American Chemical Society, 114 (7), 2303-2312.

[161] P. K. L. Fu, P. M. Bradley and C. Turro (2001). *DNA Cleavage by Photogenerated* $Rh_2(O_2CCH_3)_4(H_2O)^{2+}$, Inorganic Chemistry, 40 (11), 2476-2477.

[162] D. A. Lutterman, P. K. L. Fu and C. Turro (2006). *cis-*$[Rh_2(\mu{-}O_2CCH_3)_2(CH_3CN)_6]^{2+}$ *as a Photoactivated Cisplatin Analog*, Journal of the American Chemical Society, 128 (3), 738-739.

[163] L. Jacquet, R. J. H. Davies, A. Kirsch-De Mesmaeker and J. M. Kelly (1997). *Photoaddition of* $Ru(tap)_2(bpy)^{2+}$ *to DNA: a New Mode of Covalent Attachment of Metal Complexes to Duplex DNA*, Journal of the American Chemical Society, 119 (49), 11763-11768.

[164] A. F. A. Peacock and P. J. Sadler (2008). *Medicinal Organometallics Chemistry: Designing Metal Arene Complexes as Anticancer Agents*, Chemistry - An Asian Journal, 3 (11), 1890-1899.

[165] O. Novakova, J. Kasparkova, V. Bursova, C. Hofr, M. Vojtiskova, H. Chen and V. Brabec (2005). *Conformation of DNA Modified by Monofunctional Ru(II) Arene Complexes: Recognition by DNA Binding Proteins and Repair. Relationship to cytotoxicity*, Chemistry & Biology, 12 (1), 121-129.

[166] A. Habtemariam, M. Melchart, R. Fernández, S. Parsons, I. D. Oswald, A. Parkin and P. J. Sadler (2006). *Structure Activity Relationships for Cytotoxic Ruthenium(II) Arene Complexes Containing N,N-, N,O-, and O,O-Chelating Ligands*, Journal of Medicinal Chemistry, 49 (23), 6858-6868.

[167] C. M. Clavel, E. Paunescu, P. Nowak-Sliwinska, A. W. Griffioen, R. Scopelliti and P. J. Dyson (2015). *Modulating the Anticancer Activity of Ruthenium(II)-Arene Complexes*, Journal of Medicinal Chemistry, 58 (8), 3356-3365.

[168] H. Chen, J. A. Parkinson, S. Parsons, R. A. Coxall, R. O. Gould and P. J. Sadler (2002). *Organometallic Ruthenium(II) Diamine Anticancer Complexes: Arene-Nucleobase Stacking and Stereospecific Hydrogen-Bonding in Guanine Adducts*, Journal of the American Chemical Society, 124 (12), 3064-3082.

[169] N. Busto, J. Valladolid, M. Martínez-Alonso, H. J. Lozano, F. A. Jaloón, B. R. Manzano, A. M. Rodriguez, M. C. Carrión, T. Biver, J. M. Leal, G. Espino and B. García (2013). *Anticancer Activity and DNA Binding of a Bifunctional Ru(II) Arene Aqua-Complex with the 2,4-diamino-6-(2-pyridyl)-1,3,5-triazine Ligand*, Inorganic Chemistry, 52 (17), 9962-9974.

[170] S. Lamansky, P. Djurovich, D. Murphy, F. Abdel-Razzaq, H. E. Lee, C. Adachi, P. E. Burrows, S. R. Forrest and M. E. Thompson (2001). *Highly Phosphorescent Bis-Cyclometalated Iridium Complexes: Synthesis, Photophysical characterization, and Use in Organic Light Emitting Diodes*, Journal of the American Chemical Society, 123 (18), 4304-4312.

[171] M. S. Lowry and S. Bernhard (2006). *Synthetically Tailored Excited States: Phosphorescent, Cyclometalated Iridium(III) Complexes and their Applications*, Chemistry – A European Journal, 12 (31), 7970-7977.

[172] Y. You and S. Y. Park (2005). *Inter-Ligand Energy Transfer and Related Emission Change in the Cyclometalated Heteroleptic Iridium Complex: Facile and Efficient Color Tuning over the Whole Visible Range by the Ancillary Ligand Structure*, Journal of the American Chemical Society, 127 (36), 12438-12439.

[173] K. Hasan, A. K. Bansal, I. D. Samuel, C. Roldán-Carmona, H. J. Bolink and E. Zysman-Colman (2015). *Tuning the Emission of Cationic Iridium(III) Complexes towards the Red through Methoxy Substitution of the Cyclometalating Ligand*, Inorganic Chemistry, 44 (6), 1713-1727.

[174] Y. You (2013). *Phosphorescence Bioimaging Using Cyclometalated Ir(III) Complexes*, Current Opinion in Chemical Biology, 17 (4), 699-707.

[175] H. W. Liu, W. H. Law, L. C. Lee, J. C. Lau and K. K. Lo (2017). *Cyclometalated Iridium(III) Bipyridine-Phenylboronic Acid Complexes as Luminescent Probes for Sialic Acids and Bioimaging Reagents*, Chemistry - an Asian Journal, 12 (13), 1545-1556.

[176] C. Jin, J. Liu, Y. Chen, R. Guan, C. Ouyang, Y. Zhu, L. Ji and H. Chao (2016). *Cyclometalated Iridium(III) Complexes as AIE Phosphorescent Probes for Real-Time Monitoring of Mitophagy in Living Cells*, Scientific Reports, 6, 22039-22051.

[177] D. L. Ma, S. Lin, W. Wang, C. Yang, and C. H. Leung (2017). *Luminescent Chemosensors by Using Cyclometalated Iridium(III) Complexes and Their Applications*, Chemical Science, 8 (2), 878-889.

[178] S. Lamansky, P. Djurovich, D. Murphy, F. Abdel-Razzaq, H. E. Lee, C. Adachi, P. E. Burrows, S. R. Forrest and M. E. Thompson (2001). *Highly Phosphorescent Bis-Cyclometalated Iridium Complexes: Synthesis, Photophysical Characterization, and Use in Organic Light Emitting Diodes*, Journal of the American Chemical Society, 123 (18), 4304-4312.

[179] S. P. Y. Li, C. T. S. Lau, M. W. Louie, Y. W. Lam, S. H. Cheng and K. K. W. Lo (2013). *Mitochondria-Targeting Cyclometalated Iridium(III)–PEG Complexes with Tunable Photodynamic Activity*, Biomaterials, 34 (30), 7519-7532.

[180] R. R. Ye, C. P. Tan, L. He, M. H. Chen, L. N. Ji and Z. W. Mao (2014). *Cyclometalated Ir(III) Complexes as Targeted Theranostic Anticancer Therapeutics: Combining HDAC Inhibition with Photodynamic Therapy*, Chemical Communications, 50 (75), 10945-10948.

[181] E. Palao, R. Sola-Llano, A. Tabero, H. Manzano, A. R. Agarrabeitia, A. Villanueva, I. Lopéz-Arbeloa, V. Martinez-Martinez and M. J. Ortiz (2017). *AcetylacetonateBODIPY-Biscyclometalated Iridium(III) Complexes: Effective Strategy towards Smarter Fluorescent-Photosensitizer Agents*, Chemistry - A European Journal, 23 (42), 10139-10147.

[182] M. Harlos, I. Ott, R. Gust, H. Alborzinia, S. Wölfl, A. Kromm and W. S. Sheldrick (2008). *Synthesis, Biological Activity, and Structure-Activity Relationships for Potent Cytotoxic Rhodium(III) Polypyridyl Complexes*, Journal of Medicinal Chemistry, 51 (13), 3924-3933.

[183] M. Dobroschke, Y. Geldmacher, I. Ott, M. Harlos, L. Kater, L. Wagner, R. Gust, W. S. Sheldrick and A. Prokop (2009). *Cytotoxic Rhodium(III) and Iridium(III) Polypyridyl Complexes: Structure–Activity Relationships, Antileukemic Activity, and Apoptosis Induction*, ChemMedChem, 4 (2), 177-187.

[184] S. Noël, S. Cadet, E. Gras and C. Hureau (2013). *The Benzazole Scaffold: a SWAT to Combat Alzheimer's Disease*, Chemical Society Reviews, 42 (19), 7747-7762.

[185] C. S. Lentz, V. S. Halls, J. S. Hannam, S. Strassel, S. H. Lawrence, E. K. Jaffe, M. Famulok, A. Hoerauf and K. M. Pfarr (2014). *wALADin Benzimidazoles Differentially Modulate the Function of Porphobilinogen Synthase Orthologs*, Journal of Medicinal Chemistry, 57 (6), 2498-2510.

[186] R. Schiffmann, A. Neugebauer and C. D. Klein (2006). *Metal-Mediated Inhibition of Escherichia Coli Methionine Aminopeptidase: Structure-Activity Relationships and Development of a Novel Scoring Function for Metal-Ligand Interactions*, Journal of Medicinal Chemistry, 49 (2), 511-522.

[187] T. Akhtar, S. Hameed, N. Al-Masoudi, R. Loddo and P. Colla (2008). *In Vitro Antitumor and Antiviral Activities of New Benzothiazole and 1,3,4-Oxadiazole-2-Thione Derivatives*, Acta Pharmaceutica, 58 (2), 135–149.

[188] P. Chaudhary, K. Sharma, A. Sharma and J. Varshney (2010). *Recent Advances in Pharmacological Activity of Benzothiazole Derivatives*, International Journal of Current Pharmaceutical Research, 2 (4), 5–11.

[189] G. Zimmermann, B. Papke, S. Ismail, N. Vartak, A. Chandra, M. Hoffmann, S. A. Hahn, G. Triola, A. Wittinghofer, P. I. H. Bastiaens and H. Waldmann (2013). *Small Molecule Inhibition of the KRAS-PDEδ Interaction Impairs Oncogenic KRAS Signalling*, Nature, 497 (7451), 638–642.

[190] W. Ginzinger, G. Mühlgassner, V. B. Arion, M. A. Jakupec, A. Roller, M. Galanski, M. Reithofer, W. Berger and B. K. Keppler (2012). *A SAR Study of Novel Antiproliferative Ruthenium and Osmium Complexes with Quinoxalinone Ligands in Human Cancer Cell Lines*, Journal of Medicinal Chemistry, 55 (7), 3398–3413.

[191] G. S. Yellol, A. Donaire, J. G. Yellol, V. Vasylyeva, C. Janiak and J. Ruiz (2013). *On the Antitumor Properties of Novel Cyclometalated Benzimidazole Ru(II), Ir(III) and Rh(III) Complexes*, Chemical Communications, 49 (98), 11533.

[192] S. Kottukulam Subran, S. Banerjee, A. Mondal and P. Paira (2016). *Amberlite IR-120 (H)-Mediated "on Water" Synthesis of Novel Anticancer Ruthenium(II)–p-cymene 2-Pyridinylbenzothiazole (BTZ), 2-Pyridinylbenzoxazole (BOZ) & 2-Pyridinylbenzimidazole (BIZ) scaffolds*, New Journal of Chemistry, 40 (12), 10333–10343.

[193] C. B. Spillane, N. C. Fletcher, S. M. Rountree, H. van den Berg, S. Chanduloy, J. L. Morgan and F. R. Keene (2007). *Benzothiazole Bipyridine Complexes of Ruthenium(II) with Cytotoxic Activity*, Journal of Biological Inorganic Chemistry, 12 (6), 797–807.

[194] J. X. Ong, C. W. Yap and W. H. Ang (2012). *Rational Design of Selective Organoruthenium Inhibitors of Protein Tyrosine Phosphatase 1B*, Inorganic Chemistry, 51 (22), 12483–12492.

[195] G. S. Yellol, J. G. Yellol, V. B. Kenche, X. M. Liu, K. J. Barnham, A. Donaire, C. Janiak and J. Ruiz (2015). *Synthesis of 2-Pyridyl-Benzimidazole Iridium(III), Ruthenium(II), and Platinum(II) Complexes.*

Study of the Activity as Inhibitors of Amyloid-β Aggregation and Neurotoxicity Evaluation, Inorganic Chemistry, 54 (2), 470–475.

[196] C. B. Spillane, J. L. Morgan, N. C. Fletcher, J. G. Collins and F. R. Keene (2006). *Inert Benzothiazole Functionalised Ruthenium(II) Complexes; Potential DNA Hairpin Binding Agents*, Dalton Transactions, (25), 3122-3133.

[197] C. B. Spillane, M. N. V. Dabo, N. C. Fletcher, J. L. Morgan, F. R. Keene, I. Haq, N. J. Buurma (2006). *The Dichotomy in the DNA-Binding Behaviour of Ruthenium(II) Complexes Bearing Benzoxazole and Benzothiazole Groups*, Journal of Inorganic Biochemistry, 102 (4), 673–683.

Chapter 2

Materials and Methods

2.1 Materials

All the experiments of characterization and reactivity in water have been performed using bidistilled water by a Puranity TU+ equipment (VWR) and autoclaving the water by means of a Typ Vapour Line 80-M (VWR). The experiments were carried out always fixing the ionic strength and the pH, depending on the type of involved system. Ionic strength was kept constant by means of different salt: $NaClO_4$ (Fluka, as monohydrate salt), NaCl (Panreac, Montplet & Esteban) or KCl (Fluka). pH was fixed by means of sodium dimethylarsinate (NaCac, also called cacodylate, Carlo Erba), having $pK_A = 6.2$, or potassium phosphate buffer (obtained by mixing of KH_2PO_4 and K_2HPO_4, $pK_A = 7.2$).

2.1.1 Nucleic Acids

Different kinds of nucleic acids have been tested in the present Thesis:

- **Synthethic RNA:** poly-riboadenylic (poly(rA)) and poly-ribouridylic (poly(rU)) acids were employed in the interaction with Al(III)/cacodylate complex (Chapter 4). Poly(rA) and poly(rU) were purchased from Sigma as lyophilized potassium salts. Standardization of the RNA stock solutions was attained spectrophotometrically to $\epsilon_{257} = 10\,100\,M^{-1}cm^{-1}$ for poly(rA) and $\epsilon_{260} = 8900\,M^{-1}cm^{-1}$ for poly(rU), at I=0.1 M (NaCl), pH=7.0 and T=25.0 °C. It is worth to remind you that the polyriboadenylic acid secondary structure changes with pH, as we discussed in Chapter 1: poly(rA) converts itself into the $[poly(rA)]_2$ double helix form at acidic pH, while it remains as a single helix at neutral pH [1], with partially ordered conformation. On the other hand, polyribourydilic acid has a random coil conformation in both experimental conditions [2];
- **Calf Thymus DNA:** Liophylized Calf Thymus (CT) DNA sodium salt was purchased from Sigma Aldrich. It was dissolved in bidistilled water and sonicated in order to obtain a mean length of 1000 bp, confirmed by electrophoretic assay in the presence of a molecular weight marker. Standardization of stock solutions was performed spectrophotometrically (ϵ_{260}=13 200 $M^{-1}cm^{-1}$ in basepairs at I=0.1 M (NaCl), pH=7.0 (NaCac) and T=25.0 °C);

- **Plasmid pUC18:** pUC18 is a plasmid cloning vector present in *E.Coli*, composed by 2686 bp. Plasmid was extracted by bacteria using a kit protocol (HP Plasmid Midi Kit, OMEGA Bio-Tek). The purity of the extracted plasmid was checked by the $\frac{Abs_{260}}{Abs_{280}}$ ratio, which assures the absence of proteins. The secondary structure of the extracted plasmid was checked by electrophoresis, confirming the predominance of the native Form I (Supercoiled). C_P is referred to the molar concentration of the nitrogenous bases. pUC18 was used in the photocleavage study with Ruthenium, Iridium and Rhodium complexes;

- **Oligonucleotides:** oligonucleotides are short sequences of defined length and primary structure. In the Thesis we used different oligonucleotides: the 5'-CAATCGGATCGAATTCGATCCGATTG-3' 26-mer (7974 u m a), self associating to give a double strand structure (named 52B), the 5'-$[GAGGGTGGG]_2$GAAG-3' Pu22 (7070 u m a), forming an unimolecolar G-Quadruplex moiety, mimicking the c-myc quadruplex conformation, and 5'-$[AGGGTT]_3$AGGG-3' Tel22 (6970 u m a), which has an unimolecolar G-Quadruplex structure as well, but displaying the conformation of the telomere. All the nucleotides were purchased from Sigma-Aldrich. The oligonucleotides stock solutions were prepared in KCl=0.09 M and potassium phosphate buffer, obtaining I=0.1 M and pH=7.0. The stock solutions were heated 10 °C above the melting temperature of the Quadruplex, being T_m=74.7, 76.3, 64.0 °C for 52B, Pu22 and Tel22, respectively. Then, the solution was left to slowly return to 25.0 °C, in order to assure that all the sequences adopt the most stable quadruplex conformation. Standardization of the stock solutions came spectrophotometrically, using ϵ_{260}=414 000 $M^{-1}cm^{-1}$, 232 000 $M^{-1}cm^{-1}$, 228 500 $M^{-1}cm^{-1}$ for 52B, Pu22 and Tel22, respectively. In this case, the concentration C_P is referred to the molar concentration of the oligonucleotide. Titrations of the oligonucleotides with iridium and rhodium complexes are reported in Chapter 7.

2.1.2 Aluminium

Aluminium will be treated in Chapter 3 and 4. Aluminium ion source was the octahydrate perchlorate salt form ($Al(ClO_4)_3 \cdot 8\,H_2O$) and was purchased from Fluka. Aluminium stock solutions were prepared in doubly distilled water, adding $HClO_4$ to obtain pH=2.0, in order to avoid precipitation. Standardization of aluminium was attained by EDTA titrations, using Eriochrome Black-T as visual indicator. Briefly, the titration was carried out adding an EDTA excess to an aluminium aliquot. The solution was boiled and acetate buffer was added to achieve pH=6.0. After that, the solution was titrated with a standardized Zn^{2+} solution.

2.1.3 Ruthenium, Iridium and Rhodium Complexes

All the studied complexes were synthesized in the Inorganic Chemistry Laboratory of the Facultad de Ciencias, Universidad de Burgos. [(*p*-cym)Ru(L-1)(NCS)] (named [**Ru-1**], where *p*-cym is *p*-cymene and **HL-1** = 2-(2'-hydroxyphenyl)ben-

zothiazole) arene complex was studied in Chapter 5. Then, we tested the $[Ir(ppy)_2(pyboz)]Cl$ (**[Ir-1]**Cl) and $[Rh(ppy)_2(pyboz)]Cl$ (**[Rh-1]**Cl) biscyclometalated complexes (Hppy = 2-phenylpyridine and pyboz = 2-(2'-pyridyl)benzoxazole ligands) in Chapter 6. Finally, eight new synthesized complexes of general formula $[M(CN)_2(NN)]Cl$, being M = Ir, Rh, (CN) = ppy, piqi (2-phenylisoquinoline) and (NN) = pybtz (2-(2'-pyridyl)benzothiazole), qibtz (2-(2'-quinolinyl)benzothiazole), were discussed in Chapter 7 (**[Ir-2]**Cl-**[Ir-5]**Cl and **[Rh-2]**Cl-**[Rh-5]**-Cl). As the syntheses, the purification and characterization of the complexes in Chapter 7 are part of the present Thesis, they will be extensively discussed.

2.2 Methods

2.2.1 Synthesis Procedure

The synthesis of the organic ligands and the metal complexes was carried out under a nitrogenous atmosphere (if oxygen is not required as reactant), using a *Schlenk line* (also called *vacuum gas manifold*) apparatus, which consists of two manifolds (Figure 2.1):

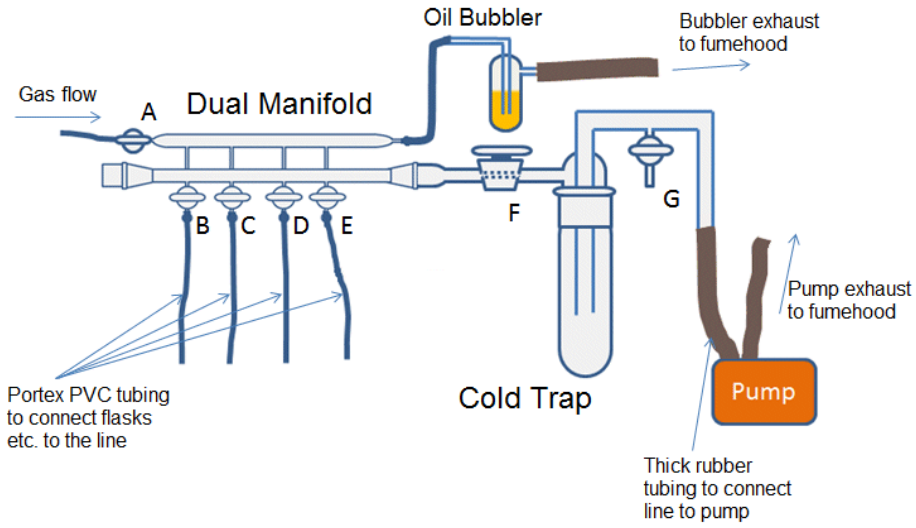

Figure 2.1: Scheme of a Schlenk line.

- the first manifold is connected to a vacuum pump, which is linked to a trap to avoid the contamination of the pump with chemical solvents;
- the second manifold is a nitrogenous line, passing through an oil bubbler to prove the gas flowing through the line;
- four ports are available to connect flasks or other chemical glassware. In each line a tap is present, allowing to select vacuum or nitrogen. To obtain an inert atmosphere in a Schlenk three cycles of vacuum-N_2 are performed and the reagents are inserted in the presence of a nitrogen flux.

In addition, other procedures can be carried out using the Schlenk line:

- **solvent evaporation**: the solvent can be evaporated under vacuum condition. The solvent passes through a cold trap inserted in a dewer and it is freezed by means of liquid nitrogen. It avoids the liquid reaching the pump.
- **solvent filtering**: the solvent can be filtered under pressure obtained by a nitrogen flow. It is achieved blocking the gas flow and forcing it to pass only to the Schlenk. A *cannula transfer* with a filter is put in the Schlenk and the solvent passes from the cannula to a second flask because of the nitrogen pressure.

Operations of separation and purification of the ligands were achieved using a chromatographic column (Figure 2.2).

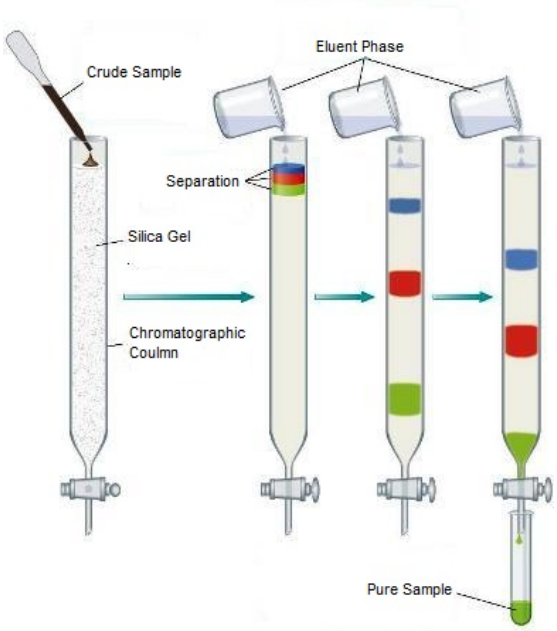

Figure 2.2: Scheme of the chromatographic procedure with a silica column gel.

Preliminary proofs of the elution of the crude product was carried out by means of Thin Layer Chromatography (TLC) on silica gel. The retention time of a molecule on the silica column depends on its polarity. The higher the polarity, the higher the retention time. On the contrary, the lower the polarity, the higher the affinity for the eluent phase, which means low retention times. The choice of the eluent phase is crucial to obtain separation of all the subproducts present in the crude sample. The different signals of the product and subproducts are visualized on the TLC by their fluorescence with a UV lamp. When a suitable elution phase is found, the dissolved product is passed through the column and aliquots of 5 mL are collected and checked by TLC. Then the aliquots containing only the product are put together and dried.

2.2.2 UV-vis Spectrophotometry

Spectrophotometry is an analytical technique based on the Lambert Beer's law (Equation 2.1),

$$Abs = Log\frac{I_0}{I} = \epsilon bC \tag{2.1}$$

where Abs is the absorption, I and I_0 are the resulting light intensities passing through the sample and the solvent, respectively, ϵ the molar extinction coefficient, b the path of the light through the sample and C is the molar concentration of the molecule absorbing the radiation. The law is valid for diluted solution and monochromatic light. If k molecules absorb radiation at a defined wavelength, the total absorption will be the sum of the k contributions (Equation 2.2).

$$Abs = \epsilon_a bC_a + \epsilon_b bC_b + \epsilon_c bC_c + ... + \epsilon_k bC_k = \sum_{i=1}^{k} \epsilon_i bC_i \tag{2.2}$$

Thus, the absorption can be used to follow the progress of a reaction because of its relationship with the concentration. Thermodynamic (spectrophotometric titrations) and kinetic studies (variation of the absorbance with time) can be performed with a spectrophotometer.
Regarding the spectrophotometric titrations, they can be carried out (i) adding increasing aliquots of the titrant to a solution of the titrate at fixed pH, ionic strength and temperature, or (ii) preparing i solutions at different titrant-titrate ratios (*batchwise* titration).
On the other hand, kinetic curves were obtained by acquiring the absorption value at a specific wavelength *versus* time.
The employed spectrophotometers in this Thesis are the double beam spectrophotometer and the diode array spectrophotometer. The schemes of both instruments are reported below.

2.2.2.1 Double Beam Spectrophotometer

The scheme of a double beam spectrophotometer is reported in Figure 2.3.

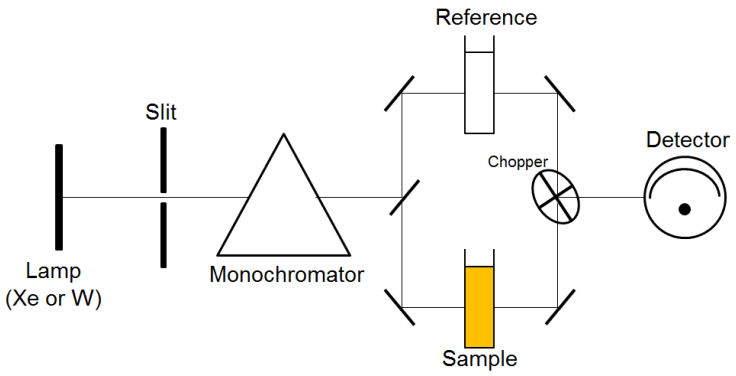

Figure 2.3: Scheme of a double beam spectrophotometer.

The instrument consists of a tungsten lamp (W) for the emission in the visible region, and a xenon lamp (Xe) for the UV region. The light is divided into the different wavelengths by means of a monochromator and the entire spectrum is obtained by scanning the selected wavelength range. The radiation is splitted by means of reflectant mirrors, sending part of the radiation to the reference, which generally is the solvent of the reaction, and the other part to the sample. Both beams are collided again to the same path and pass through a chopper, sending them to the detector at different times. By comparing the intensity of the signals, the detector expresses the difference by the absorption value. A scan of the wavelengths is required to record the entire spectrum. The cells containing the reference and the sample are made of quartz and have a 1 cm path length. The system is maintained at 25.0 °C by means of a water thermostat.

2.2.2.2 Diode Array Spectrophotometer

Unlike the double beam system, the diode array spectrophotometer does not measure the ratio of the intensity of the radiation, but rather it detects the absolute intensity of the radiation. To achieve the same conditions of the double beam spectrophotometer, an initial measurement of the blank is required, which is subtracted from the sample. The scheme of the instrument is summarized in Figure 2.4. The light strikes the cell containing the sample and then the wavelengths are splitted by means of a monochromator, which sends the wavelengths to the diode array detector. The diode array detector collects all the wavelengths at the same time. The advantage of such a kind of instrument is the rate of acquisition of the spectra. However, the use of a single beam does not allow a constant comparison of the signal of the sample and the reference, with a lower stabilization of the baseline respect to the double beam system.

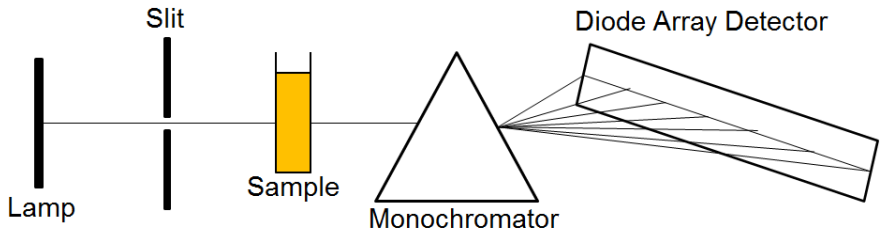

Figure 2.4: Scheme of a diode array spectrophotometer.

2.2.3 Spectrofluorimetry

The excitation of a molecule and the subsequent radiative process can be expressed by means of the Jablonsky Diagram, drawn in Figure 2.5 [3]. Actually, when a photon having an energetic accessible wavelength strikes a molecule, the photon will be absorbed and the molecule is promoted from the singlet ground state S_0 to the singlet excited state S_1 (or S_2). Vibrational relaxations dissipate part of the acquired energy and the molecule switches from the excited vibrational states to the fundamental vibrational state of S_1. At this level, the system

can evolve to:

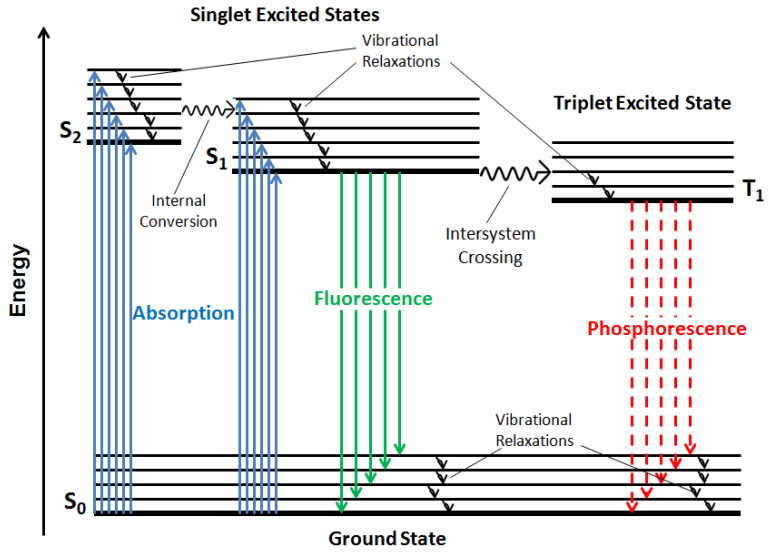

Figure 2.5: Jablonski diagram.

- a non-radiative process: the energy is transferred to solvent molecules by collisions;
- a radiative process: the system spontaneously emits a photon to return to its singlet grounds state, always being $\nu_{em} < \nu_{ex}$. The transition is called **fluorescence** and it is a spin allowed transition. On the other hand, an *intersystem crossing* of the excited states can occur, which provokes a transition from the singlet excited state S_1 to a triplet excited state T_1. In such a case an emission occurs as well, but the transition to S_0 is theoretically spin forbidden, impeding a fast decay. It follows that T_1 is a long lived excited state. Such a decay is defined as **phosphorescence**.

Fluorescence is used for different kinds of experiments, which can be sorted into steady-state and lifetime measurements.

2.2.3.1 Fluorescence Steady-State

In steady-state measurements the intensity and the shape of the fluorescence spectra are recorded. Expressing the fluorescence quantum yield (Φ) as the ratio between the emitted and absorbed photons, a relationship between fluorescence and concentration of the emitting molecule can be obtained (Equation (2.3)).

$$\Phi = \frac{F}{I - I_0} \tag{2.3}$$

Since I and I_0 are related to the absorption, it is possible to express fluorescence as a function of Abs. In the case of diluted solution ($Abs < 0.1$) the formula is

approximated by the Taylor series (Equation 2.4).

$$\frac{I}{I_0} = e^{-2.3\epsilon bC} \Rightarrow I = I_0(1 - 2.3\epsilon bC) \tag{2.4}$$

Inserting Eq. (2.4) into Eq. (2.3) we obtain the relation between the fluorescence intensity and the concentration (Equation 2.5).

$$F = \phi C \tag{2.5}$$

$2.3\Phi I_0 \epsilon b$ is named ϕ and it has the same function of ϵ for absorption. However, note that the absorption is an universal value because ϵ is fixed at specific conditions (solvent, pH and temperature). Differently, ϕ is not universal because it depends on the amount of light reaching the sample; hence it greatly depends on the instrumentation geometry. It means that fluorescence absolute value obtained in different laboratories under the same experimental conditions can be different.
Concerning the equipment, in a fluorimeter the radiation crosses a slit and a monochromator and strikes the sample. As the light is emitted in all the directions by the fluorescent molecule, the detector is generally placed perpendicular to the excitation light (*right angle geometry*), avoiding the interference of the excitation source. The emission light goes through a second monochromator and it is acquired by the detector. A block scheme of a fluorimeter is reported in Figure 2.6.

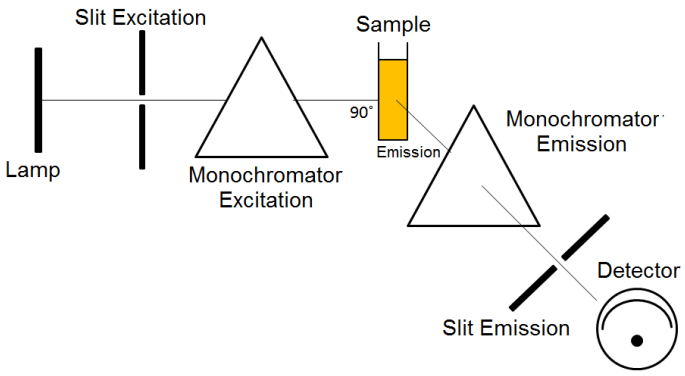

Figure 2.6: Block scheme of a fluorimeter.

2.2.3.2 Fluorescence Lifetime

In lifetime measurements the exponential decay of the fluorescent signal is acquired. For a monoexponential decay the fitting equation is given by Equation (2.6),

$$F(t) = F_0 e^{-\frac{t}{\tau}} \tag{2.6}$$

where F_0 is the fluorescence at $t = 0$ and τ the fluorescence lifetime. In the case of multiple lifetimes the total decay is the sum of the i single decays.

$$F(t) = \sum_{i=1}^{k} F_i e^{-\frac{t}{\tau_i}} \tag{2.7}$$

Regarding lifetime measurements, a pulsed nanoLED or a laser excite the sample at a specific wavelength. Detection method used is the time-correlated single photon counting (TCSPC). This method involves 4096 channels of detection, and each one acquires photons at a defined Δt after the pulse. The resulting graphic is the counts (or its logarithmic value) of the photons reaching the detector versus the channel number (which is converted into a time value, knowing the relation between channel and Δt). The mono-, bi- or multiexponential decays are fitted and the goodness of the fitting is expressed by the χ^2 value (1 is the ideal value). Subtraction of the instrument response (PROMPT) is required to correct the experimental curve, in particular for very short lifetimes.
Fluorescence decays were recorded in order to obtain the lifetimes of the metal complexes. In addition, titrations of metal complex-nucleic acids systems can be performed by means of this technique, as well.

2.2.3.3 Further Applications

Fluorimeter has been used also for:

- **Fluorescence quantum yield**: the fluorescence quantum yield Φ_S is calculated by comparing the area of the emission spectra of a complex with a reference. A $Ru(bpy)_3^{2+}$ solution was used as reference (Φ_R=0.028 in air-equilibrated water at 25.0 °C) and the quantum yield is obtained by the following Equation (2.8) [4]:

$$\Phi_S = \Phi_R \frac{Abs_S}{Abs_R} \frac{F_R}{F_S} (\frac{n_S}{n_R})^2 \tag{2.8}$$

  where n_i is the refractive index of the solvent. If the same solvent is used and the prepared sample and the reference have the same absorption at the excitation wavelength, the equation will be greatly simplified.

- **Singlet oxygen quantum yield** $\Phi_{^1\Delta_g}$: the phosphorescence of the singlet oxygen can be detected at 1270 nm. The ratio of the spectrum area of the studied complex and the phenalenone reference molecule is the singlet oxygen quantum yield, being the quantum yield of the reference 1.0 [5]. Solutions having the same absorption at the excitation wavelength were analysed. The singlet oxygen formation is observed in D_2O, as the singlet oxygen exhibits longer lifetime in the deuterated solvent.

2.2.4 Circular Dichroism

For a circularly polarized light the eletric field vector $\overrightarrow{E}$ has a circular trajectory along the direction of the wave, $\overrightarrow{E} = Re\overrightarrow{E_0}e^{i\Psi}$, where Ψ is the angle phase (Figure 2.7) [6].

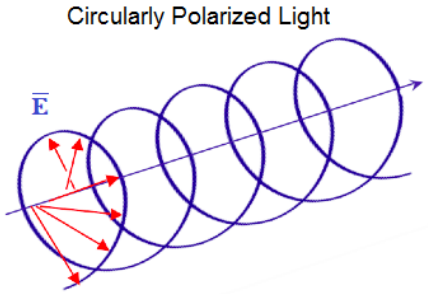

Figure 2.7: Electric field vector of the circularly polarized light.

For the circular radiation, two components are present, the left handed E_L and the right handed E_R. When an optical active molecule absorbs the excitation light, it will absorb only one of the components. It follows that the circularly polarized light is converted into an elliptical polarized light because of the intensity decrease of one vector (Figure 2.8).

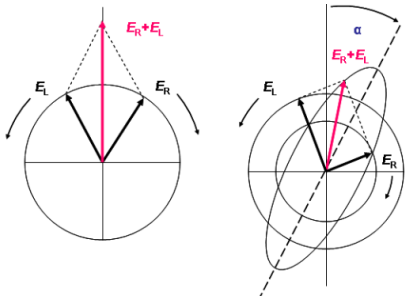

Figure 2.8: Formation of the elliptic polarized radiation from the cicularly polarized radiation due to the different absorption of E_R and E_L; α is the rotation angle of the light.

The elliciptity Θ can be calculated by the Equation (2.9).

$$tan\Theta = \frac{E_R - E_L}{E_R + E_L} \tag{2.9}$$

In diluted solution $tan\Theta$ can be approximated to Θ by Taylor series. Furthermore, the electric field can be expressed by the light intensity, and, consequently, it is possible to relate the ellipticity to aborption.

$$\Theta = \frac{I_R^{\frac{1}{2}} - I_L^{\frac{1}{2}}}{I_R^{\frac{1}{2}} + I_L^{\frac{1}{2}}} = \frac{I_0 e^{-\frac{Abs_R}{2}\ln 10} - I_0 e^{-\frac{Abs_L}{2}\ln 10}}{I_0 e^{-\frac{Abs_R}{2}\ln 10} - I_0 e^{-\frac{Abs_L}{2}\ln 10}} = \frac{e^{\frac{\Delta_{Abs}\ln 10}{2}} - 1}{e^{\frac{\Delta_{Abs}\ln 10}{2}} + 1} \tag{2.10}$$

If $\Delta Abs \ll 1$ another approximation is possible

$$\Theta = \frac{\Delta Abs \ln 10}{4} \tag{2.11}$$

The value is converted into radiant using the $\frac{180}{\pi}$ factor and the ellipticity is passed to *molar* ellipticity using $[\Theta] = \frac{100\Theta}{bC}$. The resulting Equation (2.12) is

$$[\Theta] = 100\Delta\epsilon(\frac{\ln 10}{4})(\frac{180}{\pi}) \cong 3300\Delta\epsilon = k'(\epsilon_R - \epsilon_L) \tag{2.12}$$

Hence, a direct relationship between molar ellipticity and the variation of the extinction coefficients of the right handed (ϵ_R) and left handed (ϵ_L) circularly polarized light is found. The resulting spectra has the same properties of a UV-vis absorption spectra with minima and maxima values. However, negative values are possible for a circular dichroic spectra.
Circular dichroism can provide useful information in the study of biological systems and it is routinely applied for the study of proteins and polynucleotides. The variation of the dichroic spectrum can be recorded in order to study the interaction between small molecules with the nucleic acids. In fact, organic dyes and metal complexes can provoke structural modification on DNA and RNA, and it produces a modification of the stacking interactions. In particular, electrostatic interactions provoke a small variation of the dichroic spectra, while the interaction to nitrogenous bases or intercalation causes an important variation of the dichroic signal. In addition, an achiral dye interacting with a macromolecule can acquire an *induced* circular dichroism and a dichroic signal in the visible region could be observed, as well.
The scheme of the instrument is summarized in Figure 2.9.

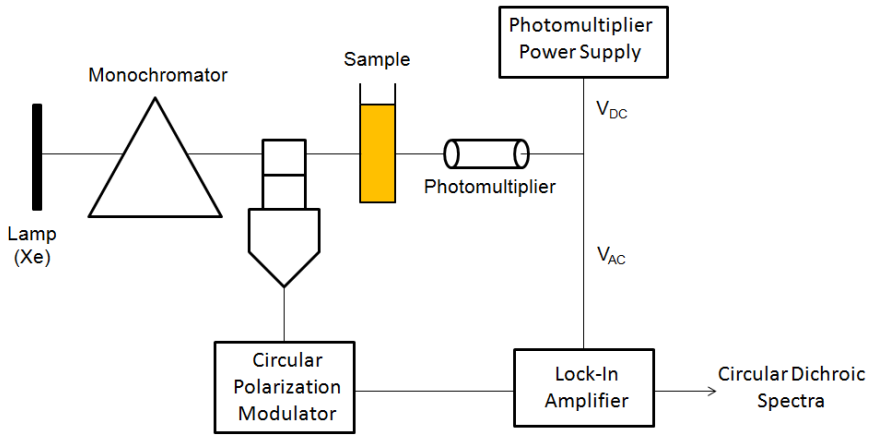

Figure 2.9: Scheme of the equipment for the circular dichroism acquisition.

2.2.5 Thermal Denaturation

Thermal denaturation involves structural modifications of a macromolecule because of the temperature. Concerning nucleic acids, they suffer notable variation of their secondary structure by increasing the temperature. The most important modification is the separation of two polynucleotidic chains to form two single helices in DNA (also called melting process).
Two techniques have been employed for melting studies: UV absorption and Differential Scanning Calorimetry (DSC).

2.2.5.1 Thermal denaturation in Absorption

Double-helix denaturation produces a hyperchromic effect in absorption because of the transition from the double- to single-stranded form. As the melting of polynucleotide is a cooperative process, a sigmoidal track at a specific wavelength versus the temperature can be observed (Figure 2.10).

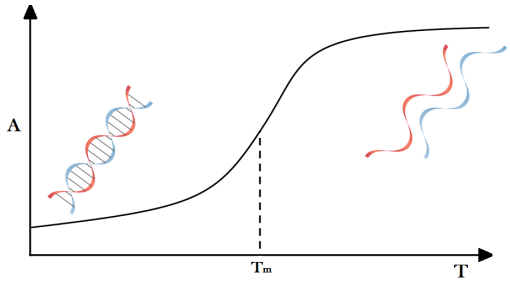

Figure 2.10: Thermal denaturation of a double helix structure. The T_m is the temperature corresponding to 50 % denaturation of the polynucleotide.

The curve is analysed by means of a sigmoid equation [7]. Alternatively, the differential of the function can be used, where the peak corresponds to the melting temperature T_m.

2.2.5.2 Differential Scanning Calorimetry

Differently from the melting study in absorption, Differential Scanning Calorimetry (DSC) records the heat of a sample versus the temperature [8]. The apparatus works providing a defined amount of heat to both sample and reference, which is necessary to reach a defined temperature. Differences in the heat capacity (also named *Excess Heat Capacity* $\Delta C_P^{sample-solvent}$) of two samples of equal volume, namely the solution containing the macromolecule (C_P^{sample}) and the solvent ($C_P^{solvent}$), is calculated [9].
The value of the C_P as a function of temperature is calculated by Equation (2.13), being m_M the mass of the solute M, $\bar{\nu}_M$ the partial specific volume of M and $\bar{\nu}_S$ the partial specific volume of the solvent:

$$C_P(T) = C_P^{solvent}\frac{\bar{\nu}_M}{\bar{\nu}_S} + \frac{\Delta C_P^{sample-solvent}}{m_M} \tag{2.13}$$

When a transition occurs, such as the melting of the double-helix DNA to form two single helices, a variation of the signal is recorded because the provided energy to the sample is spent also to break the hydrogen bonds of the double-helix. It follows that the sample needs more energy to reach the same temperature as the reference, because part of it is lost in the transition process. It results in the $\Delta C_P^{sample-solvent}$ value, and the resulting spectra is a peak corresponding to the melting process of the double-stranded polynucleotide. Thus, DSC instrumentation allows the study of the conformational transitions of biological

macromolecules. From the obtained graph it is possible to obtain different parameters, such as the melting temperature T_m, the enthalpy (ΔH, Equation (2.14)) and the entropy (ΔS, Equation (2.15)) of the transition,

$$\Delta H = \int_{T_1}^{T_2} C_P dT \tag{2.14}$$

$$\Delta S = \int_{T_1}^{T_2} \frac{C_P}{T} dT \tag{2.15}$$

where T_1 and T_2 are the initial and the final temperatures of the transition (Figure 2.11).

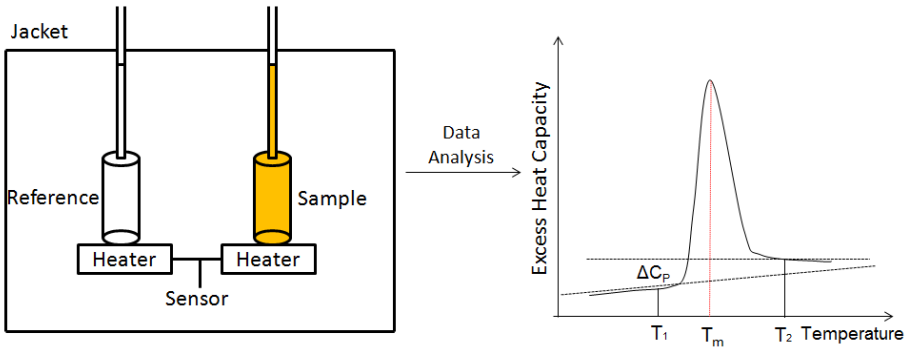

Figure 2.11: Differential scanning calorimetry scheme and data results.

DSC technique is generally employed in bioinorganic chemistry for the study of transition of macromolecules conformations, such as unfolding of the proteins, lipid membrane transitions and nucleic acid melting. Organic dyes, metal complexes and ionic metals interacting with a nucleic acid influence its thermal stabilization. For instance, an external binding such as electrostatic interaction and groove binding generally does not provoke significant variation of the T_m. On the other hand, intercalation causes an important increase in the melting temperature, for the reason that intercalators increase the stacking interaction inside the DNA, and it stabilizes the double-helix.

2.2.6 Isothermal Titration Calorimetry

Isothermal Titration Calorimetry (or ITC) is a method based on the measurement of released or acquired heat in a chemical reaction [10]. A reference, which generally is water, and a solution containing the nucleic acid are thermostated at 25.0 °C. When a reaction occurs in the sample cell, heat can be generated or spent, varying the temperature of the cell. The system provides the necessary energy to maintain the sample at 25.0 °C.
From the heat results at each titration point the equilibrium constant of the reaction can be evaluated [9]. We can consider the titration of a molecule M (the titrand), with a ligand L (the titrant). For each peak i of the titration it is

possible to calculate the apparent heat change $\Delta q_{i,app}$, which is the integration of the peak between $i-1$ and i addition:

$$\Delta q_{i,app} = q_{i-1} - q_i \tag{2.16}$$

The amount of heat depends on the amount of bound ligand ($[L]_{bound}$), the cell volume (V_{cell}) and the apparent enthalphy of reaction (ΔH_{app}, Equation (2.17)).

$$\Delta q_{i,app} = \Delta[L_i]_{bound} V_{cell} \Delta H_{app} \tag{2.17}$$

Note that V_{cell} is always known and ΔH_{app} is fixed at a specific pressure and temperature. However, $\Delta q_{i,app}$ has various contributions, which are due to the reaction itself (Δq_i), the dilution effect (Δq_{dil}) and other nonspecific effects (Δq_{ns}). To obtain Δq_i a blank proof is required, performing the addition of L in the solvent and recording the heat. Then the blank can be subtracted obtaining $\Delta q_i = \Delta q_{i,app} - \Delta q_{dil} - \Delta q_{ns}$.
The heat will be maximum for the first titration points and it will decrease with the diminishing of the bound ligand in the solution because of the saturation of M. Equation (2.17) can be converted into Equation (2.18),

$$\Delta q_i = n C_M V_{cell} \Delta H_{app} R \tag{2.18}$$

where n is the number of binding sites of M, C_M is the analytical concentration of M and R is a function defined by Equation (2.19),

$$Y_i^2 - Y_i(1 + \frac{1}{nK_A C_M} + \frac{C_{L,i}}{nC_M}) + nC_L C_M = 0 \tag{2.19}$$

where Y_i is the saturation degree at point i, being $Y_i = \frac{\Delta[L_i]_{bound}}{C_M}$, $C_{L,i}$ is the analytical concentration of L at the *ith* point. The resolution of the equation from the entire titration dataset by the NanoAnalyze program allows one to calculation n, K_A and ΔH.
A scheme of the equipment and an example of data treatment are provided in Figure 2.12.

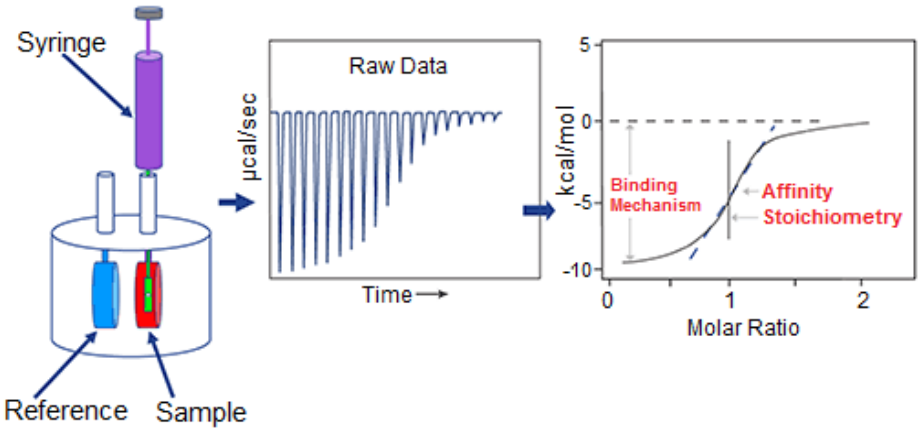

Figure 2.12: ITC equipment scheme and example of obtained data.

2.2.7 Viscometry

Viscometry is a technique that allows to evaluate the viscosity of a fluid by the measure of the elapsed time of a 1 mL sample volume to pass through a capillary tube. This technique is useful in order to understand the nature of the interaction between a small molecule and a polynucleotide. Actually, the variation of the viscosity of a solution containing DNA is associated to conformational variations of the system. For example, intercalation causes an elongation of the polynucleotides, which provokes an increase of the viscosity [11]. The viscometric equipment was an Ubbelhode's microviscometer, whose structure is shown in Figure 2.13. It was coupled with a thermostat at 25.0 °C (precision 0.1 °C). The microviscometer needs a small amount of solution (3 mL). The time is measured by means of a manual chronometer, with precision of 0.01 s.

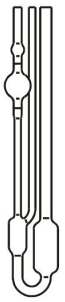

Figure 2.13: Ubbelhode's microviscometer.

The viscosity value is expressed as the cubic root of the viscosity ratio between the bound (η) and the free polynucleotide (η_0). This value is proportional to $\frac{L}{L_0}$, which is the ratio between the length of the bound DNA (L) and the free DNA (L_0). The viscosity of the sample is obtained by equation (2.20), where t, t_0 and t_S are the elapsed time of the bound polynucleotide, the free polynucleotide and the solvent, respectively.

$$(\frac{\eta}{\eta_0})^{\frac{1}{3}} = (\frac{t - t_S}{t_0 - t_S})^{\frac{1}{3}} \tag{2.20}$$

2.2.8 Nuclear Magnetic Resonance

2.2.8.1 ^{1}H–NMR

Nuclear magnetic resonance is a spectroscopic technique based on the excitation of the nuclear states of an atom in the presence of a magnetic field. The NMR instrument measures the relaxation process of the nucleus to return to the equilibrium condition after a radio frequency wavelength pulse.
Concerning the proton, in the absence of a magnetic field the $m_\alpha = +\frac{1}{2}$ and $m_\beta = -\frac{1}{2}$ nuclear spin states are degenerate (the level population of both states is equal); it follows that the magnetization vector $\overrightarrow{M}$ is null. However, when we apply a static magnetic field $\overrightarrow{B}$, the energy due to the interaction with the magnetic moment μ_z will be given by Equation (2.21),

$$E_{m_I} = g_I \mu_N B_0 m_I \tag{2.21}$$

with B_0 the magnetic field along z-axis, μ_N the nuclear magneton, g_I the nuclear factor and m_I the magnetic moment spin. Proton has $I = \frac{1}{2}$, which means two possible m_I values, $m_{+\frac{1}{2}}$ and $m_{-\frac{1}{2}}$. The energy difference is from Equation (2.22).

$$\Delta E = E_{-\frac{1}{2}} - E_{+\frac{1}{2}} = g_I \mu_N B_0 \tag{2.22}$$

Such an energy difference is very small, but it is enough to cause a difference in the level population, given by the following equation,

$$\frac{N_{+\frac{1}{2}}}{N_{-\frac{1}{2}}} = e^{-\frac{h\nu_L}{kT}} \tag{2.23}$$

where $N_{+\frac{1}{2}}$ is the level population of the $m_I = +\frac{1}{2}$ state, $N_{-\frac{1}{2}}$ the level population of the $m_I = -\frac{1}{2}$ state, ν_L the Larmor frequence of the transition and T the temperature.
The energy difference makes the magnetization vector $\overrightarrow{M}$ different from zero with the same direction as the $\overrightarrow{B_0}$ magnetic field. If a radiation having oscillating magnetic field $\overrightarrow{B_1}$ and frequency ν_L is sent perpendicularly to the magnetization vector, a precession of $\overrightarrow{M}$ is obtained and, if the radiation is pulsed, the vector passes to the xy plane. After the pulse, a relaxation process of the spin to return to the equilibrium condition can be followed along the *y-axis* and it is reported in Equation (2.24), being M_0 the maximum value of magnetization and T_2 the transversal relaxation time.

$$M_y(t) = M_0 cos(2\pi\nu_L t) e^{-\frac{t}{T_2}} \tag{2.24}$$

This signal is converted from time to frequency domain by means of the Fourier transform (Equation (2.25)).

$$I(\nu) = 2Re \int_0^{+\infty} S(t) e^{2\pi i \nu t} dt \tag{2.25}$$

This result could wrongly suggest that every proton suffers the same magnetic field and, consequently, that every proton present in a molecule gives rise to the same signal. However, each atom is influenced by a different chemical environment, which generates a $\overrightarrow{B} \neq \overrightarrow{B_0}$, differing from $\delta B = -\sigma B_0$, where σ is the shielding constant. In effect, the magnetic field produces an electronic orbital angular moment, generating a small δB opposing to $\overrightarrow{B}_0$. Hence, each proton suffers a different local magnetic field $B_{loc} = B_0(1-\sigma)$ and, consequently, the atoms are excited by different Larmor frequencies (Equation (2.26)).

$$\nu_{loc} = (1 - \sigma)\frac{\gamma B_0}{2\pi} \tag{2.26}$$

A NMR signal consists of three different parameters:

- the *chemical shift*, δ, as to say the position of the signal in the chemical shift scale (ppm unity), defined as

$$\sigma = \frac{\nu - \nu_0}{\nu_0} 10^6 \tag{2.27}$$

where ν_0 is the Larmor frequence of a reference, generally being tetramethylsilane;

- the *multiplicity* M, which is the number of peaks of a proton signal, being

$$M = 2nI + 1 \tag{2.28}$$

where n is the number of the scalar coupled atoms with the proton, and I is its magnetic moment. The multiplicity of the signal is due to the interaction of neighbouring nuclei (fine structure). The strength of the interaction between the different nuclei is expressed by the scalar coupling constant J (in Hertz);

- the *area*. It can be used for the quantification of the signal.

2.2.8.2 ^{13}C NMR

The NMR spectrum can be recorded for the carbon atom, as well. However, unlike proton, the active nucleus of the carbon is ^{13}C, which is 1 % of the total carbon nuclei (for proton, ^{1}H is 99.8 %). It means that the signal is very low and accumulation of the signal is needed. In addition, decoupling of the signal (expressed as ^{13}C$\{^1$H$\}$) is usually set up in order that each carbon has only one peak, which allows an increase of the peak signal.

2.2.8.3 Bidimensional Techniques

Bidimensional NMRs show correlations between the nuclei of a molecule (or between nuclei of different molecules, as well). Involved bidimensional techniques in this Thesis are:

- **COSY**: COSY technique allows to obtain a 2D map which correlates scalar coupled protons. Generally scalar three bond coupling is possible to detect, whereas four bond coupling is sometimes observed for aromatic systems. COSY is the first bidimensional technique which should be performed in the characterization of a metal complex for the identification and the assignements of the protons to a specific moiety of the metal complex (for example, a specific ligand) ;

- **NOESY**: NOESY bidimensional spectrum correlates the spatially coupled protons. Hence, in such a case the signal depends on the distance between the nuclei. The information provided by NOESY is useful to understand the tridimensional structure of the ligands and the distance between the ligands of a metal complex.

- **HSQC**: HSQC is a heteronuclear bidimensional technique correlating the protons and the carbons directly linked between themselves;

- **HMBC**: HMBC heteronuclear spectrum is a 2D map showing a signal between protons and carbons two or three bond coupled.

The contribution of all the cited bidimensional techniques makes possible the assignments of all the protons and the carbons of a molecule.

2.2.9 Mass Spectrometry

Mass spectrometry is a technique which separates molecules differing from their $\frac{m}{z}$ ratio value, where m is the mass and z the charge (Figure 2.14).

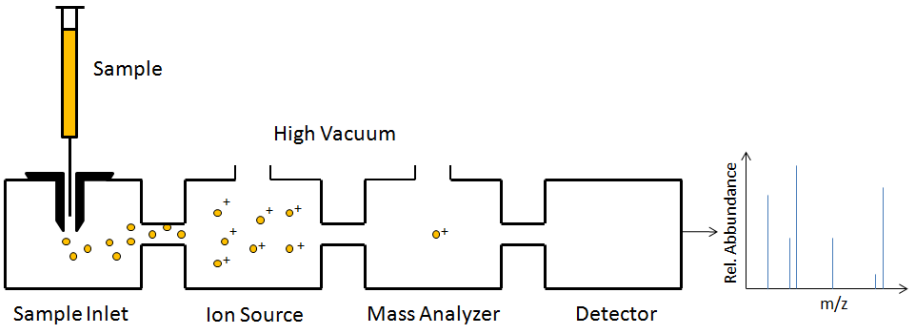

Figure 2.14: Mass spectrometer scheme.

The separation method depends on the analyzer of the mass spectrometer. Briefly, a mass spectrometer is composed by:

- an ion source, which induces ionization of the sample;
- an analyzer, which separates the ions by $\frac{m}{z}$;
- a detector, which generally is an electromultiplier.

Various ion sources are available, depending on the physical state and the properties of the sample. There are also different analyzers, which can be classified depending on the method used to separate the $\frac{m}{z}$ fractions. The choice of the analyzer affects the resolution, the sensitivity and the $\frac{m}{z}$ range.
In this Thesis two different mass spectrometers are employed. Both spectrometers have an electrospray ionisation source (ESI), where a solution containing the sample is passed through a capillary tube and a voltage is applied. When the solution comes out from the capillary it converts into an aerosol. A nitrogen flow is sent to the spray to reduce the droplet volume. When the volume is sufficiently decreased, the repulsion of the charge inside the droplet causes its explosion, further diminishing its size. The obtained small charged droplets are sent to the analyzer. Used analyzers are:

- the *Quadrupole*, which is formed by a fixed magnetic field and an oscillating field. The combination of the magnetic fields forces the ions to a specific trajectory. In particular, at a specific magnetic field condition only the ion having suitable $\frac{m}{z}$ value has a trajectory which permits to reach the detector. The value of the oscillating magnetic field is switched in order to scan all the $\frac{m}{z}$ range;

- the *Time of Flight* (or TOF) analyzer separates the ions depending on the arrival time to the detector. Actually, the ions acquire an energy E due to the magnetic field, as shown in Equation (2.29).

$$E = \frac{1}{2}mv^2 \tag{2.29}$$

It follows that the rate of an ion inside the analyzer depends on its mass (Equation (2.30))

$$v = \sqrt{\frac{2m}{E}} \tag{2.30}$$

Since the ions pass through a d distance, molecules having different mass arrive at different time, being $t = \frac{2md}{E}$.

Finally, the electromultiplier detector converts the ion into electrons by the impact on its surface, amplifying the signal. Signal amplification is attained for the reason that each collision generates 2 electrons. It means that n collisions form 2^n electrons.

2.2.10 Irradiation Instrumentation

Irradiation study was carried out by means of an illuminator system coupled with a double-beam spectrophotometer (Figure 2.15).

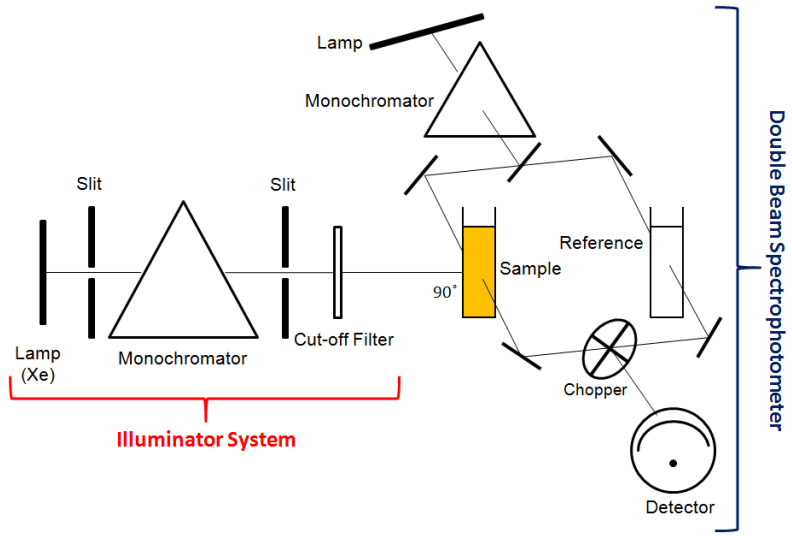

Figure 2.15: Scheme of the illuminator system.

It consists of an Ushio Xenon Short Arc Lamp and a monochromator. The selected wavelength goes through an optic fiber and a cutoff filter and reaches the sample. UV-vis spectra at different irradiation time can be recorded at a specific irradiation wavelength.

2.2.11 Photocleavage Study

Study of the cleavaging properties of the metal complexes was carried out by interaction with pUC18 plasmid DNA [12]. Natural plasmid has a supercoiled form (Form I). If the metal complex action cuts one of the strands, the open circular form (Form II) is created. Moreover, if another cut occurs to the other strand, the open circular form turns into the linear form (Form III, Figure 2.16).

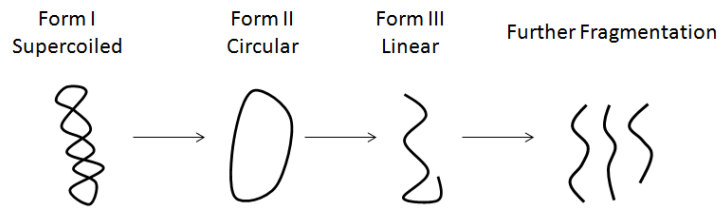

Figure 2.16: Different structures of plasmid DNA.

Detection of the different forms is obtained by electrophoretic assay. Electrophoresis is based on the application of an electric field. The samples are inserted in an agarose gel immersed in TBE solvent and the application of a potential causes the migration of positive charged species from the anode to the cathode, the migration rate depending on the molecular charge and shape. As the linear charge of the polynucleotides is the same, the migration depends only on their secondary structure. In the presence of TBE buffer, the migration order is (fastest) Form I > Form III > Form II (slowest). A scheme of the electrophoretic system is provided in Figure 2.17.

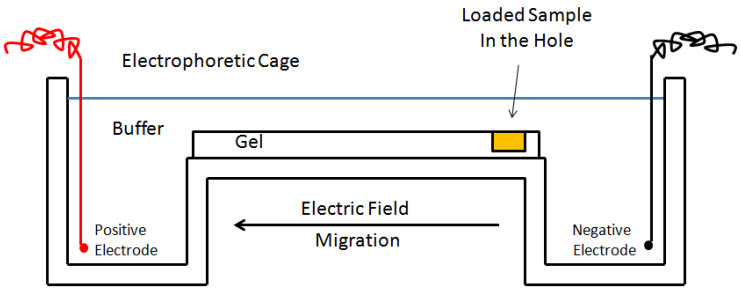

Figure 2.17: Scheme of the electrophoretic system.

The detection of the separated species is achieved by addition of ethidium bromide in the gel. This compound intercalates between the DNA basepairs and its fluorescence switches on. Irradiation of the gel with a UV lamp (Fisher BioBlock Scientific) allows to visualize the different plasmid forms and a photo is acquired. Quantification is evaluated by the densimetric data of the lanes corresponding to the different plasmid forms by means of the ImageJ program [13]. ImageJ program converts the lanes into peaks and their area can be quantified. The cleavage values derives from Equation (2.31) [14], being D_I, D_{II} and D_{III} the areas of the supercoiled, circular and linear forms, respectively. For D_I a cor-

rection factor of 1.4 is applied for the decreased ability of the dye to intercalate inside the supercoiled form [15].

$$Cleavage = \frac{D_{II} + 2D_{III}}{D_I + D_{II} + 2D_{III}} \tag{2.31}$$

For the cleavage assay, the solvent was the TBE buffer 1 % and the gel TBE 1 % containing 1 % of agarose. After irradiation, the samples were incubated overnight at 37.0 °C in a KS 4000 I control incubator (IKA) and, then, 10 µL of the solution (Plasmid concentration: 20 µM in bp) were mixed with 2 µL of loading buffer (Bio-Rad, Glycerol 25 %) and loaded in the hole. The run was performed at 80 V for 90 min.
An example of a lane and the data treatment is reported in Figure 2.18.

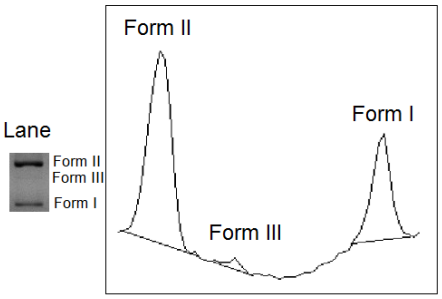

Figure 2.18: Example of the densimetric data of a lane by means of ImageJ program.

2.2.12 FRET Assay

Fluorescence Resonance Energy Transfer is a spectroscopic technique used to obtain information about the structural conformation of a molecule. The FRET effect involves energy transfer from a donor (D, or fluorophore) to an acceptor (A, or quencher) by a non-radiative process, quenching the fluorescence of the donor [16]. Energy transfer E depends on the distance of the molecules by the following equation (Equation (2.32)).

$$E = 1 + \frac{R^6}{R_0^6} \tag{2.32}$$

being R the donor-acceptor distance and R_0 the *Forster radius*, obtained by the formula reported in Equation (2.33),

$$R_0^6 = 8.8 \cdot 10^{-28} \Phi_D \kappa^2 n^{-4} J(\nu) \tag{2.33}$$

with Φ_D the fluorescence quantum yield of the donor, κ a parameter related to the D-A orientation, n is the solvent refractive index and $J(\nu)$ is the equation of the overlap between the emission of the donor and the absorption of the acceptor. The technique has been successfully applied in the study of G-Quadruplex stabilizers [17]. Actually, the synthesis of G-Quadruplex moieties with a donor (D) and an acceptor (A) covalently linked to both terminals of the oligonucleotide allows one to obtain information about the quadruplex folding. When the

oligonucleotide exhibits quadruplex structure no fluorescence is present due to the FRET mechanism. However, when denaturation of the four-stranded structure occurs, an increase of the fluorescence is visualized. The resulting graph is a sigmoidal track in fluorescence due to the cooperative process of unfolding (Figure 2.19).

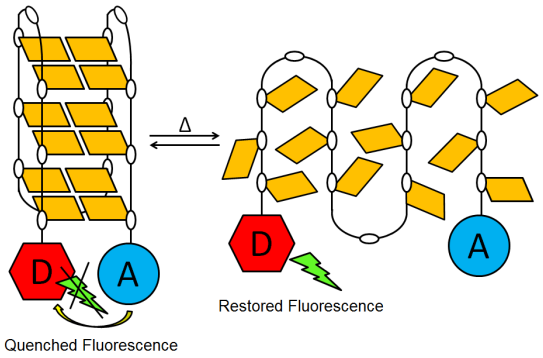

Figure 2.19: G-Quadruplex FRET scheme.

FRET assays were performed employing a PCR equipment. Polymerase Chain Reaction (PCR) instrumentation is typically used for the amplification of a DNA sequence. The DNA chain is incubated together with the dNTP monomers, a DNA polymerase enzyme and the primer, the latter being the complementary sequence of the extreme of the chain which is going to be amplified. The method is based on heating/cooling cycles. The heating causes the separation of the DNA strands and the synthesis of the complementary strands by the enzyme; the cooling returns the system to the native double-helix form. n cycles make 2^n chains up (for examples 20 cycles $\rightarrow 2^{20} \cong 1000000$ chains).

2.2.13 Other Techniques

2.2.13.1 Conductimetry

A Crison 522 conductimeter connected to a Crison 52 92 conductivity cell with platinum electrodes was used. The conductimeter measures the electrolytic conductimetry, as to say the capability of a solution to conduct electricity. Solutions of the synthesized complexes at 1.0×10^{-3} M in acetonitrile were prepared for the measurements.

2.2.13.2 Microanalysis CHNS

Elemental analysis is performed by combustion of the sample in the presence of oxygen. The products are CO_2, H_2O, N_2 and SO_2, which are trapped and quantified. The measures were performed with a LECO CHNS-932 microanalyzer. Results are the mean value of three samples of 1 mg weight.

2.2.13.3 Infrared Spectroscopy

Infrared spectroscopy involves the excitation of the vibrational states of the molecules. The resulting spectra is a sum of the peaks due to the different vibrational modes of the molecular groups: stretching, bending, scissoring, rocking, wagging and twisting. Functional groups have characteristic signal which can be identified in the infrared spectrum (4000-400 cm^{-1}). So, we can divide the spectrum into different regions:

- 4000-2800 cm^{-1}: X-H (X=heteroatom) and C-H stretching;
- 2300-2100 cm^{-1}: triple bond stretching;
- 1800-1500 cm^{-1}: double bond stretching and aromatic fingerprint;
- 1500-400 cm^{-1}: fingerprint of the molecule: single bond stretching and bending.

The instrument was a Jasco FT/IR-4200 system, equipped with an ATR accessory, which is based on the reflectance of the solid.

2.2.13.4 X-Ray Diffraction

X-ray diffraction is a technique used for the resolution of a molecular structure organized in a crystal. A beam is sent against the crystal and the atoms diffract the ray into different but specific directions. The study of the diffraction of the beam (intensity and angle of diffraction) allows to identify the structure of the molecules forming the crystal, obtaining the bond lengths and the angles values. Crystals of two synthesized complexes were obtained and characterized by means of X-Ray diffraction technique. Crystalization was achieved solving the complex powder in dichloromethane and adding a solution of MeOH and water saturated with NH_4PF_6, in order to form two different phases. PF_6^- anion forms crystals with iridium and rhodium complexes more efficiently respect to chloride anion, because of its size. Crystals were analysed with a Bruker Smart Apex CCD to obtain the geometric data of the unit cell and the length and angles of the bonds inside the complex. The resolution of the crystals was performed by Dr. Rodríguez Fernández-Pacheco from Universidad de Castilla La Mancha. Detailed information are obtained analysing the results with MERCURY 3.0 program.

2.2.13.5 MTT Assay

MTT assay quantifies the amount of live cells inside a sample. It is based on the use of the MTT dye (3-(4,5-dimethylthiazol-2-yl)-2,5-diphenyltetrazolium bromide), a molecule displaying yellow colour, which is reduced to formazan inside the cell, a purple compound, by oxyreductase enzyme. Such a behaviour can be exploited in the study of the cytotoxic activity of a metal complex [22]. The cells are seeded for 24 h in 96-well microplates in the presence of a growth medium. Then, the medium is removed and a new medium containing the drug is added, and the cells are incubated for a defined time. After that, the medium is removed and sodium dodecylsulfate is added to solubilize the formazan crystals. The formazan concentration is measured by absorption at $\lambda = 590$ nm, being

this related to the amount of live cells. Triplicate cultures are performed for each sample. Proofs at different concentrations allow to evaluate the IC_{50} value, which is the metal complex concentration corresponding to 50 % of cell survival. In addition, proofs were performed irradiating the sample for 20 min in the presence of a UV lamp (maximum at 365 nm). From the irradiation proof the *photoindex* value (PI) is calculated, which is the ratio between the IC_{50} value in the dark ($IC_{50}DARK$) and under irradiation ($IC_{50}IRR$, Equation (2.34)). The resulting number corresponds to the enhancement of the cytotoxic effect due to the light.

$$PI = \frac{IC_{50}DARK}{IC_{50}IRR} \tag{2.34}$$

All the MTT proofs in the present Thesis were performed by Dr. Busto of our Physical Chemistry laboratory, except to part of the MTT assays in Chapter 5, performed by the group of Prof. Fernando Dominguez from Universidad de Santiago de Compostela.

2.2.14 Determination of the Equilibrium Constant of the Interaction Between a Metal Centre M and a Ligand L [18]

Considering a reaction between a metal centre M and a ligand L

$$\mathrm{M} + \mathrm{L} \overset{K_{ML}}{\longleftrightarrow} \mathrm{ML} \tag{2.35}$$

the equilibrium constant K_{ML} results from Equation (2.36),

$$K_{ML} = \frac{[ML]}{[M][L]} \tag{2.36}$$

where $[M]$, $[L]$ and $[ML]$ are the equilibrium concentration of the unbound metal M, the unbound ligand L and the metal complex ML, respectively.
The analytical concentration of the metal (C_M) and the ligand (C_L) are

$$C_M = [M] + [ML] \tag{2.37}$$

$$C_L = [L] + [ML] \tag{2.38}$$

Inserting the (2.37) and (2.38) in the (2.36), (2.39) is obtained

$$K_{ML} = \frac{[ML]}{C_M C_L - (C_M + C_L)[ML] + [ML]^2} \tag{2.39}$$

If the ligand (L) and the complex (ML) both absorb, the absorption at a specific wavelength will be

$$Abs = \epsilon_L[L] + \epsilon_{ML}[ML] \tag{2.40}$$

Inserting the (2.38) in the (2.40), the (2.41) is given

$$Abs - \epsilon_L C_L = (\epsilon_{ML} - \epsilon_L)[ML] \tag{2.41}$$

ΔAbs and $\Delta\epsilon$ are defined by (2.42) and (2.43), respectively,

$$\Delta Abs = Abs - \epsilon_L C_L \tag{2.42}$$

$$\Delta\epsilon = \epsilon_{ML} - \epsilon_L \tag{2.43}$$

obtaining

$$[ML] = \frac{\Delta Abs}{\Delta\epsilon} \tag{2.44}$$

We put Equation (2.44) in the equation of the equilibrium constant (2.39),

$$\frac{1}{K_{ML}} = \frac{\Delta Abs}{\Delta\epsilon} - (C_M + C_L) + \frac{C_M C_L}{\frac{\Delta Abs}{\Delta\epsilon}} \tag{2.45}$$

and dividing by $\Delta\epsilon$ we obtain the complexometric equation (Equation 2.46).

$$\frac{C_M C_L}{\Delta Abs} + \frac{\Delta Abs}{\Delta\epsilon^2} = \frac{(C_M + C_L)}{\Delta\epsilon} + \frac{1}{K_{ML}\Delta\epsilon} \tag{2.46}$$

Expressing $x = (C_M + C_L)$ and $y = (\frac{C_M C_L}{\Delta Abs} + \frac{\Delta Abs}{\Delta\epsilon^2})$ a straight line is obtained, having slope $\frac{1}{\Delta\epsilon}$ and intercept $\frac{1}{K_{ML}\Delta\epsilon}$. Their ratio allows to determine the equilibrium constant.
Note that $\Delta\epsilon$ is present in the y formula, and it is initially unknown. To solve it, an iteration of the value is required, using the $\frac{\Delta Abs}{C_L}$ at the end of the titration as initial value.
From the same system it is possible to obtain a further equation for the determination of the equilibrium constant.
Using Equation (2.39) and expressing $[ML]$ by means of Equation (2.44) we obtain

$$K_{ML} = \frac{\frac{\Delta Abs}{\Delta\epsilon}}{[M](C_L - \frac{\Delta Abs}{\Delta\epsilon})} \tag{2.47}$$

and from (2.47), Eq. (2.48) is given

$$\frac{\Delta Abs}{C_L} = \frac{K_{ML}\Delta\epsilon[M]}{1 + K_{ML}[M])} \tag{2.48}$$

Expressing $y = \frac{\Delta Abs}{C_L}$ e $x = [M]$ a curve is obtained. K_{ML} comes from the iteration of $[M]$ to convergence, using C_M as initial value.

2.2.15 Scatchard Plot [19] and McGhee and von Hippel Equation [20]

The reaction between a dye D and a polymer site S is considered

$$\mathrm{D} + \mathrm{S} \overset{K_{SC}}{\longleftrightarrow} \mathrm{DS} \tag{2.49}$$

The equilibrium constant K_{SC} is obtained from equation (2.50),

$$K_{SC} = \frac{[DS]}{[D][S]} \tag{2.50}$$

where $[D]$, $[S]$ and $[DS]$ are the equilibrium concentrations of the free ligand, the free site and the complex, respectively. Defining C_P the analytical concentration of the monomeric unit and B the inverse of the site size, the total concentration of the free site is

$$[S]_0 = BC_P \tag{2.51}$$

The Scatchard hypothesis assumes an ordered disposition of the ligand on the polymer. So we can define the total concentration of the site $[S]_0$ as

$$[S]_0 = [S] + [DS] \tag{2.52}$$

We define the saturation degree r in Equation (2.53):

$$r = \frac{[DS]}{C_P} \tag{2.53}$$

inserting the equation (2.53) in the (2.51) the equation (2.54) is obtained.

$$[S] = C_P(B - r) \tag{2.54}$$

Putting the Equations (2.53) and (2.54) in the (2.50) the Scatchard equation results

$$\frac{r}{[D]} = K_{SC}B - K_{SC}r \tag{2.55}$$

Considering $y = \frac{r}{[D]}$ and $x = r$ a straight line is drawn with slope the equilibrium constant $-K_{SC}$ and intercept $K_{SC}B$. So, the Scatchard equation allows to obtain the equilibrium constant and the site size of the reaction.
However, the Scatchard model does not consider deviations in the case of high saturation degree, which provokes deviations from the linearity. The McGhee and von Hippel equation corrects the Scatchard model inserting a correction factor $f(r)$ for $[S]$:

$$f(r) = \frac{(1 - nr)^n}{[1 - (n - 1)r]^{n-1}} = \frac{[S]}{C_P} \tag{2.56}$$

obtaining the final Equation (2.57)

$$\frac{r}{[D]} = K\frac{(1 - nr)^n}{[1 - (n - 1)r]^{n-1}} \tag{2.57}$$

putting $y = \frac{r}{[D]}$ and $x = r$ we obtain a curve; the intercept on the $y - axis$ is K and the intercept on the $x - axis$ is $\frac{1}{n}$. The relationship between the site size $\frac{1}{B}$ from the Scatchard plot and n from McGhee and von Hippel equation is

$$n = \frac{1 + \frac{1}{B}}{2} \tag{2.58}$$

2.2.16 Determination of the Dimerization Constant [21]

Considering the reaction of a dye, D, to form the D_2 dimer

$$2\,D \underset{\longleftarrow}{\overset{K_{agg}}{\longrightarrow}} D_2 \tag{2.59}$$

the equilibrium constant K_{agg} results from Equation (2.60),

$$K_{agg} = \frac{[D_2]}{[D]^2} \tag{2.60}$$

being $[D_2]$ and $[D]$ the concentration at the equilibrium of the D_2 dimer and the D monomer, respectively.
The analytical concentration of the dye, C_D is given by Equation (2.61)

$$C_D = [D] + 2[D_2] \tag{2.61}$$

Considering that both dimer and monomer absorb at the working wavelength the absorption is expressed as

$$Abs = \epsilon_D[D] + \epsilon_{D_2}[D_2] \tag{2.62}$$

where ϵ_D and ϵ_{D_2} are the molar extinction coefficient of the monomer and the dimer, respectively.
Inserting the (2.61) in the (2.62) and, rearranging, we obtain the (2.63), being $\Delta\epsilon = \epsilon_{D_2} - 2\epsilon_D$

$$Abs - \epsilon_D C_D = \Delta\epsilon[D_2] \tag{2.63}$$

Dividing by C_D and rearranging we obtain

$$\frac{C_D}{[D_2]} = \frac{C_D \Delta\epsilon}{Abs - \epsilon_D C_D} \tag{2.64}$$

Considering the equilibrium constant and solving for Equation (2.64), it leads to:

$$[D]K_{agg} = \frac{[D_2]}{[D]} = \frac{[D_2]}{C_D - 2[D_2]} = \frac{\frac{[D_2]}{C_D}}{1 - \frac{2[D_2]}{C_D}} \tag{2.65}$$

resulting

$$\frac{C_D}{[D_2]} = 2 + \frac{1}{K_{agg}[D]} \tag{2.66}$$

Inserting the (2.66) in the (2.64) and dividing by $\Delta\epsilon$ the final Equation (2.67) is

$$\frac{C_D}{Abs - \epsilon_D C_D} = \frac{2}{\Delta\epsilon} + \frac{1}{K_{agg}\Delta\epsilon}\frac{1}{[D]} \tag{2.67}$$

Setting $y = \frac{C_D}{Abs - \epsilon_D C_D}$ and $x = \frac{1}{[D]}$ a straight line results, with allows one to determine K_{agg}. Note that the $[D]$ is obtained by iteration of the latter equation, using C_D as starting value.

2.2.17 Determination of the Time Constant Equation

Considering a simple reaction between a dye D and a monomeric unit P of a polynucleotide

$$\mathrm{D} + \mathrm{P} \underset{k_{-1}}{\overset{k_1}{\rightleftharpoons}} \mathrm{PD} \tag{2.68}$$

the variation of $[PD]$ with time is given by Equation (2.69)

$$\frac{d[PD]}{dt} = k_1[P][D] - k_{-1}[PD] \tag{2.69}$$

where k_1 and k_{-1} are the kinetic constants of the direct and the reverse reaction, respectively, and $[P]$, $[D]$ and $[PD]$ the concentration of the free P, the free D and the PD complex, respectively.
In a very short δt time the formula is converted into

$$\frac{d\delta PD}{dt} = k_1[D]\delta P + k_1[P]\delta D - k_{-1}\delta PD \tag{2.70}$$

Considering the anaytical concentration C_D and C_P of the dye and the monomeric unit, respectively

$$C_D = [D] + [PD] \tag{2.71}$$

$$C_P = [P] + [PD] \tag{2.72}$$

In a δt time we obtain

$$0 = \delta D + \delta PD \Rightarrow \delta D = -\delta PD \tag{2.73}$$

$$0 = \delta P + \delta PD \Rightarrow \delta P = -\delta PD \tag{2.74}$$

Inserting the (2.73) and (2.74) into the Equation (2.69) we obtain the (2.75)

$$\frac{d\delta PD}{dt} = -k_1[D]\delta PD - k_1[P]\delta PD - k_{-1}\delta PD \tag{2.75}$$

Expressing $-\frac{d\delta PD}{\delta PD dt} = \frac{1}{\tau}$

$$\frac{1}{\tau} = k_1([P] + [D]) + k_{-1} \tag{2.76}$$

If we work in an excess of P, $[P] + [D] \cong [P]$ and $[P] \cong C_P$

$$\frac{1}{\tau} = k_1 C_P + k_{-1} \tag{2.77}$$

If the reaction is an irreversible reaction, $k_{-1} = 0$ and the final Equation (2.78) will be

$$\frac{1}{\tau} = k_1 C_P \tag{2.78}$$

Bibliography

[1] M. L. Gleghorn, J. Zhao, D. H. Turner and L. E. Maquat (2016). *Crystal Structure of a Poly(rA) Staggered Zipper at Acidic pH: Evidence that Adenine N1 Protonation Mediates Parallel Double-Helix Formation*, Nucleic Acids Research, 44 (17), 8417-8424.

[2] J. C. Thrierr, M. Dourlent and M. Leng (1971). *A Study of Polyuridylic Acid*, Journal of Biological Chemistry, 58 (3), 815-830.

[3] J. R. Lakowicz (1999). *Principles of Fluorescence Spectroscopy*, 2 nd Edition, Kluwer Academic/Plenum Publisher, New York.

[4] G. A. Crosby and J. N. Demas (1971). *Measurement of Photoluminescence Quantum Yields. Review*, The Journal of Physical Chemistry, 75 (8), 991-1024.

[5] R. Schmidt, C. Tanielian, R. Dunsbach and C. Wolff (1994). *Phenalenone, a Universal Reference Compound for the Determination of Quantum Yields of Singlet Oxygen O_2 ($\Phi_{^1\Delta_g}$) Sensitization*, Journal of Photochemistry and Photobiology A: Chemistry, 79 (1), 11-17.

[6] H. Eyring, H. C. Liun and D. Caldwell (1968). *Optical Rotatory Dispersion and Circular Dichroism*, Chemical Reviews, 68 (5), 525-540.

[7] A. Böttcher, D. Kowerko and R. K. O. Sigel (2015). *Explicit Analytic Equations for Multimolecular Thermal Melting Curves*, Biophysical Chemistry, 202, 32-39.

[8] A. Cooper and C. M. Johnson (1994). *Differential Scanning Calorimetry* in Methods in Molecular Biology, Vol. 22: Microscopy, optical spectroscopy, and macroscopic techniques, Ch. 10, pp. 125-136, Humana Press Inc., Totowa, New York.

[9] I. Jelesarov and H. R. Bosshard (1999). *Isothermal Titration Calorimetry and Differential Scanning Calorimetry as Complementary Tools to Investigate the Energetics of Biomolecular Recognition*, Journal of Molecular Recognition, 12 (1), 3-18.

[10] N. E. Grossoehme, A. M. Spuches and D. E. Wilcox (2010). *Application of Isothermal Titration Calorimetry in Bioinorganic Chemistry*, Journal of Biological Inorganic Chemistry, 15 (8), 1183-1191.

[11] G. Cohen and H. Eisenberg (1969). *Viscosity and Sedimentation Study of Sonicated DNA-Proflavine Complexes*, Biopolymers, 8 (1), 45-55.

[12] A. J. Prussin, D. F. Zigler, A. Jain, J. R. Brown, B. S. Winkel and K. J. Brewer (2008). *Photochemical Methods to Assay DNA Photocleavage Using Supercoiled pUC18 DNA and LED or Xenon Arc Lamp Excitation*, Journal of Inorganic Biochemistry, 102 (4), 731-739.

[13] W. S. Rasband (1997). *ImageJ Software*, National Institutes of Health: Bethesda, MD, USA, 2012.

[14] Y. J. Liu, C. H. Zeng, H. L. Huang, L. X. He and F. H. Wu (2010). *Synthesis, DNA-Binding, Photocleavage, Cytotoxicity and Antioxidant Activity of Ruthenium(II) Polypyridyl Complexes*, European Journal of Medicinal Chemistry, 45 (2), 564-571.

[15] A. Neves, H. Terenzi, R. Horner, A. Horn Jr., B. Szpoganicz and J. Sugai (2001). *Hydrolytic DNA Cleavage Promoted by a Dinuclear Iron(III) Complex*, Inorganic Chemistry Communications, 4 (8), 388-391.

[16] P. G. Wu and L. Brand (1994). *Resonance Energy Transfer: Methods and Applications*, Analytical Biochemistry, 218 (1), 1-13.

[17] A. De Rache and J. L. Mergny (2015). *Assessment of Selectivity of G-Quadruplex Ligands via an Optimised FRET Melting Assay*, Biochimie, 115, 194-202.

[18] H. A. Benesi and J. H. Hildebrand (1949). *A Spectrophotometric Investigation of the Interaction of Iodine with Aromatic Hydrocarbons*, Journal of the American Chemical Society, 71 (8), 2703-2707.

[19] G. Scatchard (1949). *The Attractions of Proteins for Small molecules and Ions*, Annals of the New York Academy of Sciences, 51 (4), 660-672.

[20] J. D. McGhee and P. H. von Hippel (1974). *Theoretical Aspects of DNA-Protein Interactions: Co-operative and Non-Co-operative Binding of Large Ligands to a One-Dimensional Homogeneous Lattice*, Journal of Molecular Biology, 86 (2), 469-489.

[21] T. Biver, B. García, J. M. Leal, F. Secco, and E. Turriani (2010). *Left-Handed DNA: Intercalation of the Cyanine Thiazole Orange and Structural Changes. A Kinetic and Thermodynamic Approach*, Physical Chemistry Chemical Physics, 12 (40), 13309-13317.

[22] L. Tabrizi and H. Chiniforohsan (2017). *Designing New Iridium(II) Arene Complexes of Naphthoquinone Derivatives as Anticancer Agents, a Structure-Activity Relationship Study*, Dalton Transaction, (46) 7, 2339-2349.

Part I

Aluminum and Its Interaction with RNA

In Part I of the Thesis, we focused our study on aluminium and its reactivity with RNA.

In Chapter 3 we centered the study on the Al(III)/Cac system at different pH values to infer the nature and strength of the interaction between Al(III) and the ligand and to assess the possible use of cacodylate to provide Al(III) buffered solutions for biochemical studies at neutral pH. First of all, we performed a study on the speciation of the free metal and the free ligand by means of calculations and NMR analysis in order to observe the different free species involved in the reaction. Then, the complex between aluminium and cacodylate was characterized by means of mass spectrometry and NMR, which enables us to suggest a structure for the formed complex. This study was integrated by DFT calculations of the proposed structures, performed by Dr. Lozano from Universidad de Burgos. Moreover, UV-vis absorption titration allowed to calculate the apparent constants at the different pHs and, by the derivation of a mathematical model, the real equilibrium constants of the interaction.

Following the characterization of the aluminium/cacodylate complex, in Chapter 4 we present a study of the interaction of Al/Cac with two synthetic RNAs, namely, the poly-riboadenylic (poly(rA)) and the poly-ribouridylic (poly(rU)) acids, at pH 5.0 and 7.0. Neutral pH was chosen for mimicking biological conditions, while pH=5.0 was selected to observe the effect of aluminIum on $[poly(rA)]_2$, the double-stranded form of poly(rA). Preliminary proofs of the interaction of Al/Cac with AMP nucleotide were carried out by NMR. Then, the study of the interaction with poly(rA) and poly(rU) was carried out with different techniques, namely UV-vis absorption, circular dichroism, denaturation study and viscometry. In addition, a deeper kinetic study of the binding and of the strands aggregation process was performed using UV-vis absorption.

Chapter 3 and Chapter 4 are taken from published articles, *Phys. Chem. Chem. Phys.*, 2015, **17**, 29803-29813, and *Dalton Trans.*, 2017, **46**, 16671-16681, respectively.

Chapter 3

Stabilization of Al(III) Solutions by Complexation with Cacodylic Acid: Speciation and Binding Features

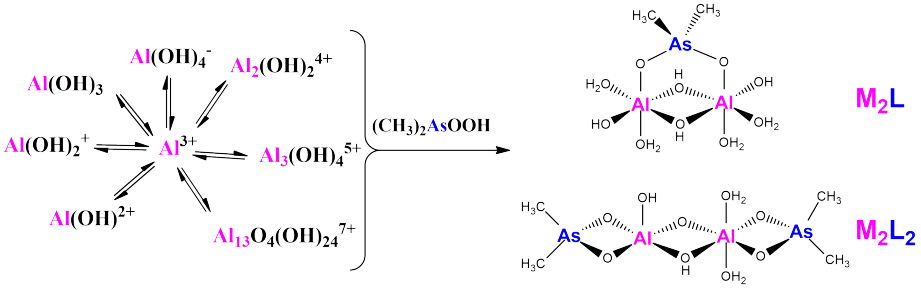

Aluminium ions are believed to play a role in a number of neurological and skeletal disorders in the human body. The wide variety of complex species that result from hydrolysis of Al^{3+} ions render a difficult task the study of the biological processes and molecular mechanisms that underlie these pathological disorders. In addition, this ion displays a pronounced tendency to precipitate as a hydroxide, so certain complexing agents should be envisaged to stabilize Al(III) solutions in near physiological conditions. In this work, we show that the common buffer cacodylic acid (dimethylarsinic acid, HCac) interacts with Al(III) to give stable complexes, even at pH 7. After preliminary analyses of the speciation of the metal ion and also of the ligand, a systematic study of the formation of different Al/Cac complexes at different pH values has been conducted. UV-vis absorption titrations, mass spectrometry, NMR measurements and DFT calculations were performed to enlighten the details of the speciation and stoichiometry of Al/Cac

complexes. The results altogether show that Al/Cac dimer complexes prevail, but monomer and trimer forms are also present. Interestingly, it was found that cacodylate promotes the formation of such relatively simple complexes, even under conditions where the polymeric form, $Al_{13}O_4(OH)_{24}{}^{7+}$, should predominate. The results obtained can help to shed some light into the reactivity of aluminium ions in biological environments.

3.1 Materials and Methods

3.1.1 Materials

The aluminium source was the $Al(ClO_4)_3 \cdot 8\,H_2O$ solid salt supplied by Fluka. Aluminium stock solutions were prepared by dissolving appropriate amounts of the solid in $HClO_4$ solutions, brought at pH=2.0 to avoid hydroxide precipitation. The standardization of aluminium stock solutions was reported in Chapter 2 (Section 2.1.2). Stock solutions of sodium dimethylarsinate ($(CH_3)_2AsOONa$, NaCac - Carlo Erba, purity 96 %) were prepared by dissolving weighed amounts of the solid in water and titrated with NaOH. The ionic strength (I) of the working solutions was kept constant at 0.1 M with sodium perchlorate (Merck) in order to reproduce the ionic strength at physiological condition, while the desired pH was attained by small additions of NaOH and $HClO_4$. $NaClO_4$ was chosen as the ionic buffer for the reason that perchlorate is an inert anion [1], while other species, such as chloride and phosphate, can form complexes with Al(III) [2]. All of the reactants were analytical grade and were used without further purification. Ultra-pure water from a Millipore MILLI-Q water purification system was used to prepare the solutions and as a reaction medium.

3.1.2 Methods

pH measurements were performed with a Metrohm 713 (Herisau, Switzerland) pH-meter equipped with a combined glass electrode. The uncertainty in the calibration of the instrument was 0.05, and it was considered as the uncertainty of the pH measurements. Spectrophotometric titrations were carried out with a Shimadzu 2450-Spectrophotometer, equipped with jacketed cell holders (thermostat precision 0.1 °C). All experiments were conducted at 25 °C. Titrations of Al(III)/Cac system were performed in the batchwise mode at the desired pH values and ionic strength 0.1 M ($NaClO_4$). Different samples were prepared for different metal-to-ligand ratios and left for 24 h to reach equilibration. For each sample, the absorbance spectrum was recorded in the 190-300 nm range (pathlength cell 1 cm) and the binding parameters were evaluated averaging out the results obtained at different selected wavelengths in the 205-193 nm range. Mass spectra in double distilled water recorded for samples at $\frac{C_L}{C_M} = 1$ ($C_M = 0.2$ mM), C_L and C_M being, respectively, the cacodylate and aluminium ion concentrations, were obtained by means of a TOF Mass Spectrometer Bruker Maxis Impact, with electrospray ionization (ESI). NMR samples were prepared by dissolving in 0.5 mL of the respective oxygen-free deuterated solvent the proper amount of Al^{3+} to 5 mM working solutions with the corresponding amount of sodium cacodylate for each $\frac{C_L}{C_M}$ ratio studied. Unless otherwise stated, the spectra were recorded at 25 °C on a Varian Unity Inova-400 (399.94 MHz for ^{1}H; 104.21 MHz

for ^{27}Al). Typically, 1D ^{1}H-NMR spectra were acquired with 32 scans into 32 k data points over 16 ppm spectral width; the spectra of ^{27}Al-NMR were acquired with 16 scans. ^{1}H chemical shifts were referenced internally to TMS via 1,4-dioxane in D_2O ($\delta = 3.75$ ppm). Chemical shift values are reported in ppm. All of the NMR data processing were carried out using MestReNova version 6.1.1. DFT calculations were carried out using B3LYP functional to optimize some proposed structures for the aluminium-sodium cacodylate complex; this procedure was used satisfactorily for DFT calculations of metals [3], and for aluminium specifically [4–6], applying 6-31G(d) basis set to C, H and O atoms. A double zeta function (LANL2DZ) was used for Al and As, including effective core potential calculation (ECP) for core electrons, diminishing the computational calculation costs. Water was used as solvent. All calculations and data analyses were performed with Gaussian 09 [7].

3.2 Results and Discussion

3.2.1 Evaluation of the $pK_{A,1}$ and $pK_{A,2}$ Acidity Constants of Cacodylic Acid

Cacodylic acid is a diprotic acid; its diprotonated form is here denoted as H_2Cac^+. This species undergoes acid dissociation according to Equations (3.1) and (3.2), which are characterized by the acid dissociation constants $K_{A,1}$ and $K_{A,2}$ respectively.

$$H_2Cac^+ + H_2O \overset{K_{A,1}}{\rightleftharpoons} HCac + H_3O^+ \tag{3.1}$$

$$HCac + H_2O \overset{K_{A,2}}{\rightleftharpoons} Cac^- + H_3O^+ \tag{3.2}$$

The ^{1}H-NMR spectra of cacodylate shows a singlet signal ascribable to the methyl groups of NaCac. The location of these peaks very much depends on the medium acidity for the higher acidity, the higher the chemical shift of the peaks (Fig. 3.1A).
The $pK_{A,1}$ and $pK_{A,2}$ values have been determined by the chemical shift analysis of the ^{1}H-NMR singlets of sodium cacodylate at different values of the pH and the acidity function H_0 (Fig. 3.1B); the latter function was employed at the highest acidity levels used, outside the boundary of the pH scale [8]. The two dissociation constants of cacodylic acid were evaluated according to Equation (3.3):

$$\delta = \frac{\delta_B - \delta_{BH^+}}{1 + 10^{-pH+pK_{A,i}}} + \delta_{BH^+} \tag{3.3}$$

where δ_B and δ_{BH^+} represent the chemical shift of the basic and acidic forms, respectively, and δ that at an intermediate acid concentration, according to species shown in Equations (3.1) and (3.2). To determine $pK_{A,1}$, Equation (3.3) was applied directly by adopting for δ_B the chemical shift at pH=4.0, whereas that for δ_{BH^+} was taken as the highest value in Fig. 3.1 B. The continuous line denotes the outcome of the two fittings. The $pK_{A,1}$ and $pK_{A,2}$ values obtained, 1.3 ± 0.2 and 6.2 ± 0.1 respectively, were in reasonable good agreement with the literature values, $pK_{A,1} = 1.1$ [9, 10] and 2.6 [10], and $pK_{A,2} = 6.2$ [9, 11–13].

Fig. 3.1C shows the speciation curves of cacodylic acid.

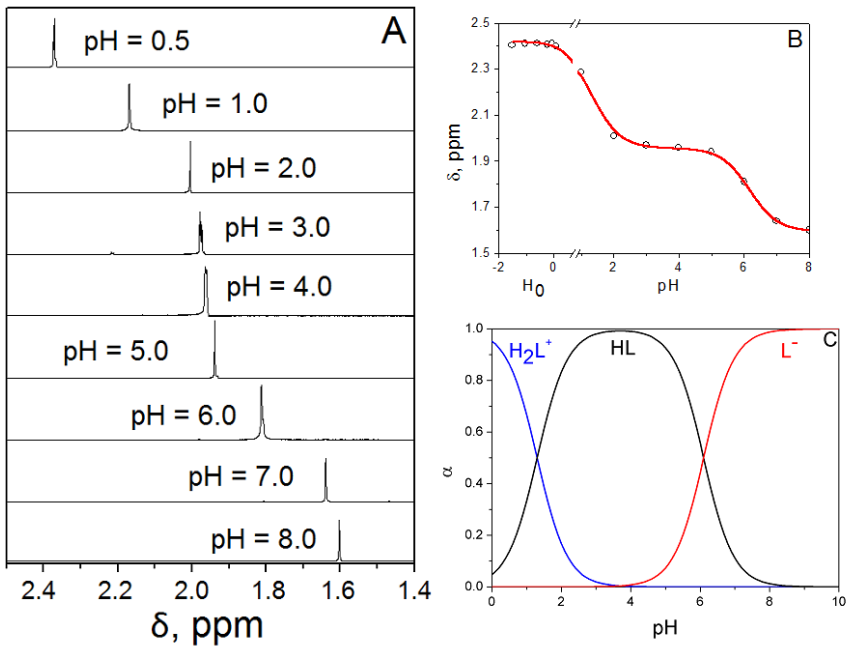

Figure 3.1: (A) ^{1}H-NMR spectra at pH=0.5, 1.0, 2.0, 3.0, 4.0, 5.0, 6.0, 7.0 and 8.0. (B) δ *versus* pH (or H_0) plot corresponding to $pK_{A,1}$ and $pK_{A,2}$. C_L=5.00 $\times$ 10^{-3} M. (C) Speciation of cacodylic acid ($pK_{A,1}$ = 1.3, $pK_{A,2}$ = 6.2). I=0.1 M ($NaClO_4$), T=25.0 °C.

As for the absorbance measurements, Fig. 3.S1 shows the spectra of cacodylic acid at different pH values (I=0.1 M, $NaClO_4$). The change in absorbance upon titration within the 2-10 pH range (Fig. 3.S1, inset) has enabled us to evaluate the second acid dissociation constant of cacodylic acid, the resulting value being: $pK_{A,2} = 6.0 \pm 0.2$. It is noteworthy to specify that the absorption spectra of cacodylate lies in the limit of the instrumental range, and the measure suffers from low signal to noise ratio. So, in order to ensure a reliable result, different measures were performed and the $K_{A,2}$ was calculated from each wavelength in the 195-205 nm range, and the mean values obtained were within the experimental error. Below pH 3, the shift of the 193 nm band to lower wavelengths can be ascribed to formation of the H_2Cac^+ species.

3.2.2 Speciation of Aluminium Forms

Fig. 3.2 shows the ^{27}Al-NMR spectra in the 1.0–6.0 pH range (above pH 6.0 the measurements could not be executed because aluminium precipitates). NMR measurements show that the hexaaquoaluminium(III) ion, $Al(OH)_6^{3+}$, prevails between pH 1.0 and 4.0. The wide band in ^{27}Al-NMR spectra observed be-

tween pH 5.0 and 6.0 can be ascribed to the polycation species $Al_{13}O_4(OH)_{24}{}^{7+}$ (also denoted as $Al_{13}-$mer) [14]. Between pH 6.0 and 7.0, partial or full neutralization of the polymer charge promotes aggregation of $Al_{13}-$mer, which tends to precipitate, and formation of more complex polymeric forms, such as $Al_2O_8Al_{28}(OH)_{56}(H_2O)_{26}{}^{18+}$ (also known as $Al_{30}-$mers) is likely to occur [15, 16].

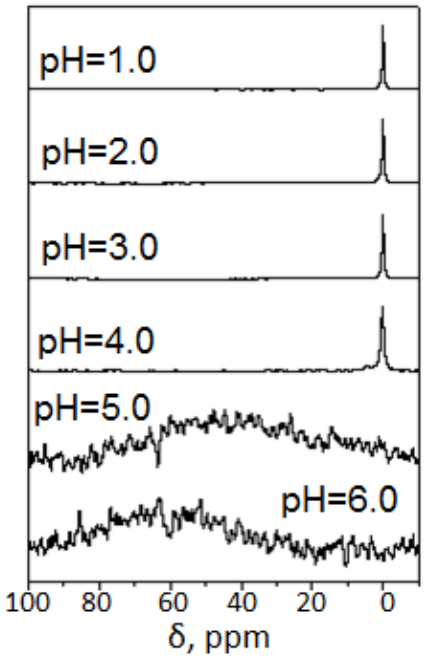

Figure 3.2: ^{27}Al-NMR spectra of Al(III) at different pH values. C_M=5.00 × 10^{-3} M, I=0.1 M (NaClO4) and T=25.0 °C. The pH-independent narrow peak at δ (roughly) 0 ppm, is ascribed to the monomeric species Al^{3+}, whereas the broad band observed at pH 5 and 6 is the $Al_{13}O_4(OH)_{24}{}^{7+}$ polymer.

The NMR findings are corroborated by literature data. The molar fraction (β) of the Al^{3+} hexahydrate ion and its hydrolytic forms can be calculated according to Equation (3.4) [17]:

$$LogQ_{x,y} = LogK_{x,y} + a\frac{\sqrt{I}}{1+\sqrt{I}} + bm_x \tag{3.4}$$

where I is the ionic strength of the medium, $Q_{x,y}$ is the equilibrium ratio related to formation of the hydrolyzed $Al_x(OH)_y{}^{(3x-y)+}$ species ($xAl+yH_2O \longrightarrow Al_x(OH)_y{}^{(3x-y)+} + yH^+$) and $K_{x,y}$ is the relevant thermodynamic equilibrium constant, a and b being fitting parameters and m_x is the overall aluminium molality [17]. This calculation was performed at different pH values and metal concentrations using the OCTAVE program [18], yielding the distribution plots shown in Fig. 3.3. This figure shows that the amount of dimer and trimer

species is negligible and that the predominant species in the 4.5 to 8.0 pH range is $Al_{13}O_4(OH)_{24}{}^{7+}$ whereas $Al(OH)^{4-}$ is the prevailing species above pH 8.0.

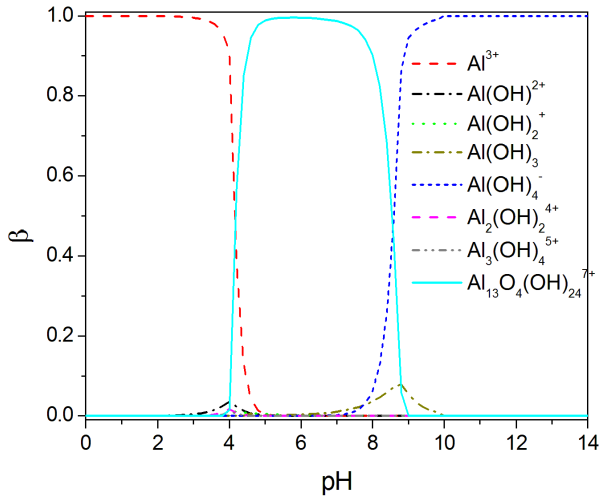

Figure 3.3: Speciation of Al(III). C_M=1.00 × 10^{-3} M, I=0.1 M and T=25.0 °C.

The results from Fig. 3.3 are compared in Fig. 3.S2 (A and B, Supporting Information) with other results obtained for Al^{3+} concentrations of 1.0 × 10^{-4} and 1.0 × 10^{-5} M, showing that polymeric species are absent in dilute solutions. Additionally, an increase in the aluminium concentration (C_M) causes a small diminution of β_{Al} and a sharp increase of the polymeric form $Al_{13}O_4(OH)_{24}{}^{7+}$.

3.2.3 The Aluminium/Cacodylate System

3.2.3.1 Mass Spectrometry

The different number of peaks recorded at different pH reveals the complexity of the distribution of the aluminum species (Fig. 3.S3 and 3.S4, Supporting Information). We focused the attention on the most representative peaks in the spectrum and determined four types of species: (i) free cacodylate, which is predominant and in particular the $[HCac+H]^+$ ($\frac{m}{z}$=139) and $[NaCac+H]^+$ ($\frac{m}{z}$=161) adducts and other peaks reported in literature [19,20], such as $\frac{m}{z}$=277, 259, 299, 281, 437, 419 (corresponding to $[H_2Cac_2 + H]^+$, $[H_2Cac_2 + H{-}H_2O]^+$, $[H_2Cac_2 + Na]^+$, $[H_2Cac_2 + Na{-}H_2O]^+$, $[H_3Cac_3 + Na]^+$, $[H_3Cac_3 + Na{-}H_2O]^+$), respectively; (ii) perchlorate and cacodylate salt clusters: $[Na(NaClO_4)_x]^+$ ($\frac{m}{z}$=145, 267, 389) and $[Na(NaCac)_x]^+$ ($\frac{m}{z}$=183, 343, 503, 663); (iii) Al uncomplexed forms: $Al(OH)_2(H_2O)_v{}^+$ ($\frac{m}{z}$=79, 115, 133); $Al_2O(OH_2)^{3+}$ ($\frac{m}{z}$=121) and (iv) Al/Cac complexes. By analogy with the formulation of aluminium(III) of aquo-chloro-complexes, we adopt the general formula $Al_xO_y(OH)_zCac_u(H_2O)_v{}^{n+}$ for the aluminium/cacodylate complexes [21]. The distribution of the different forms is shown in Fig. 3.4, whereas the respective formulas are summarized in the

Supporting Information (Table 3.S1).

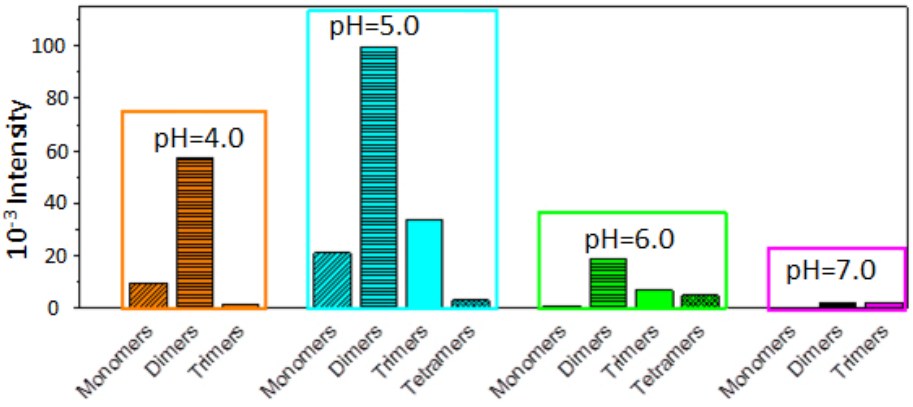

Figure 3.4: Distribution of the different forms of Al/Cac complexes at different pHs. C_L=C_M=2.00 × 10^{-4} M and T=25.0 °C.

However, it should be pointed out here that assignment of the proper formula is prone to certain ambiguity [22]. To a first place, the $(OH)_2{}^{2-}$ and $O(OH_2)^{2-}$ patterns, having the same value of the $\frac{m}{z}$ ratio, cannot be differentiated. Therefore, $Al_2O(OH)Cac_2(H_2O)^+$ could be replaced by $Al_2(OH)_3Cac^{2+}$. Moreover, some peaks can be assigned to either a free or a bound aluminium species. For instance, the peak at $\frac{m}{z} = 121$ can be ascribed to the free species $Al_2O(OH)^{3+}$ and to the $Al_2O(OH)Cac(H_2O)_v{}^{2+}$ complex, and the peaks at 301 and 319 to the 1:2 complex $AlCac_2(H_2O)_v{}^+$ or to the 3:1 $Al_3O(OH)Cac(H_2O)_v{}^+$ complex. The theoretical (see below) and literature data will allow us to suggest the most stable form [21–25].

At pH 4.0, 5.0 and 6.0 the most intense peaks are those associable to the dimeric forms. On the other hand, monomeric species are mainly present not only at pH 5, but also at pH 4. Trimeric forms display lower intensity signals and are detected at pH 5.0, 6.0 and 7.0. In particular, the signal at pH 7.0 is lower than those detected at pH 5.0 and 6.0, concurrent with the weakening of the interaction of cacodylate at neutral pH, observed in the NMR experiments as described below.

The high abundance of dimeric complexes contrasts with the β values, indicating rather modest presence of dimers when cacodylate is absent (Fig. 3.3). To support this view, previous studies [21–25] on aluminium complexes with organic ligands have shown that $Al_2O(OH)_3{}^+$ yields a small peak, suggesting that the dimeric aluminium free species are only poorly present in solution. Hence, it can be surmised that, in addition to the 1:1 complex, the presence of cacodylate induces the formation of ligand bound dimeric and (to a lesser extent) also trimeric and tetrameric species. Furthermore, the fact that the peaks of these species are present also at pH 5.0 and 6.0, where, in the absence of ligand, the polymeric form $Al_{13}-$mer is prevailing by far, suggests that the ligand induces the disintegration of $Al_{13}-$mer to give smaller entities.

3.2.3.2 ^{27}Al-NMR and ^{1}H-NMR Studies

Fig. 3.5A shows the ^{27}Al-NMR spectra for Al/Cac in the pH 1–7 range. Between pH 1.0 and 2.0, only the signal corresponding to free Al^{3+} was observed at 0 ppm. In addition to the signal at 0 ppm, at pH 3.0 and 4.0, two further signals, at 2 and 4 ppm, were observed, the former remaining very modest at the two pH values. The second displays a remarkable increase in intensity on going from pH 3.0 to pH 4.0. At pH 5.0 and 6.0, a wide band is observed at 8 and 12 ppm, respectively. At pH 7.0, the centre of the band is shifted to 60 ppm.

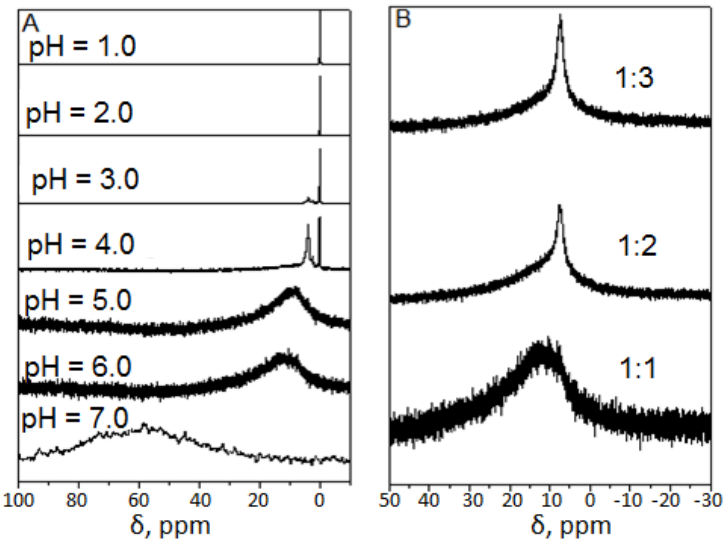

Figure 3.5: ^{27}Al-NMR spectra for (A) Al/NaCac system at pH = 1.0, 2.0, 3.0, 4.0, 5.0, 6.0 and 7.0, $\frac{C_M}{C_L}$=1 (B) Al/NaCac system at C_M:C_L=1:1,1:2,1:3, C_M=5.00 × 10^{-3} M, pH=6.0, I=0.1 M ($NaClO_4$) and T=25.0 °C.

Fig. 3.6 shows the ^{1}H-NMR spectra of the Al/NaCac system recorded at different pH values and different times. The peak of the free ligand (circled), and other peaks are displayed in the 4<pH<7 range, which are associated to the bound cacodylate. The whole of the ^{27}Al-NMR and ^{1}H-NMR experiments have contributed to interpret the behaviour of the aluminium/cacodylate system at different pH values.

No Al/Cac complex is formed at pH 1.0 and 2.0. However little amounts of complex are detected at pH 3.0 and the extent of binding becomes more and more important as the pH is raised, in agreement with the general behaviour displayed by complex formation reactions of metal ions with ligands protonated at the reaction site.

Concerning the data at pH 4.0, comparison of the ^{27}Al-NMR spectra of free (Fig. 3.2) and bound (Fig. 3.5A) aluminium shows a remarkable increase of the peak at 4 ppm, which can be associated to the dimeric aluminium/cacodilate form [26, 27]. In the ^{1}H-NMR spectrum (Fig. 3.6A), the singlet at 1.86 ppm could be related to the $AlCac^{2+}$ complex. Actually, the beta value of Al^{3+} at pH 4.0 is 0.9, and a singlet peak agrees with the symmetrical form of Al^{3+} with

the chelating ligand. In addition, it is supported by the fact that this peak is not seen at pH 5.0 (Fig. 3.6C), where $\beta_{Al} = 0.004$. The two peaks at 1.95 and 1.79, having the same intensity, most likely correspond to a dimeric form, in which the two methyl groups have different environment. Also other small peaks are present, in particular in the 1.88-1.85 ppm range and at 1.82 ppm, which could be related to other monomeric species, such as $Al(OH)Cac^{+}$.

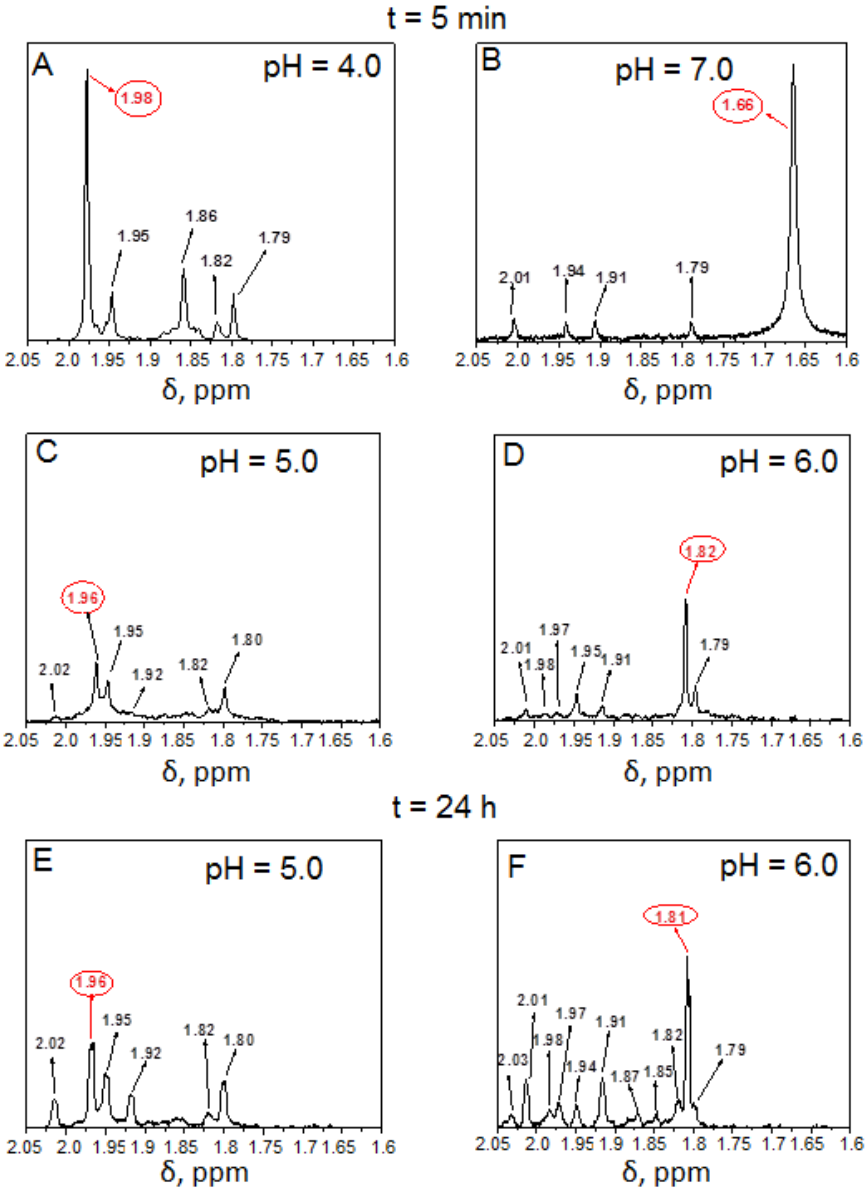

Figure 3.6: ^{1}H-NMR kinetics of Al/NaCaC complex at t=10 min (A, B, C and D) and t=1 day (E and F). C_M=C_L=5.00 × 10^{-3} M, I=0.1 M ($NaClO_4$), pH=4.0, 5.0, 6.0, 7.0 and T=25 °C. Circled chemical shift stands for free cacodylate at every pH.

The broad peak observed at pH 5.0 and 6.0 in the ^{27}Al-NMR experiments (Fig. 3.5A) should be associated to the sum of dimeric, trimeric and other polymeric species coming from the decomposition of the Al_{13} aggregate associated to the broad peak at 60 ppm (Fig. 3.2). In addition, ^{27}Al-NMR spectra recorded at pH 6.0 for $\frac{C_L}{C_M}$= 1, 2 and 3 show constriction of the broad peak, with signal increase at 7.5 ppm (Fig. 3.5B). This behaviour agrees well with further disintegration of the $Al_{13}-$mer in the presence of an excess of cacodylate. As stated above, the ^{1}H-NMR experiments show that the peak at 1.86 ppm, present at pH 4.0, disappears when the solution pH is raised (spectra at pH 5.0 and 6.0 in Figs. 3.6C and 3.6D), while the peaks at 1.95 and 1.80ppm exhibit remarkable intensity. Moreover, a very slow kinetic process is observed, followed by the increase of two peaks at 2.01 and 1.92 ppm, of same intensity (Figs. 3.6E and 3.6F). Therefore, we can surmise that the interaction between aluminium and cacodylate is the overlapping of two reactions. The first one is fast, possibly representing the ligand binding to monomeric or dimeric aluminium species, and the second represents the decomposition of the polymeric $Al_{13}-$mer induced by the interaction of cacodylate to give simpler species, in agreement with the observed disaggregation of Al_{13} induced by ligands with oxygen-containing groups, such as acetate, oxalate and lactate and, more conceivably, by protons [16, 28–30]. In this case, disaggregation seems to be strongly dependent on the pH and less on the ligand.

Furrer et al. [28] state that the disaggregation of $Al_{13}-$mer is driven by the proton concentration. In other words, the only presence of cacodylate does not allow by itself the disaggregation of the aluminium oligomers under the experimental conditions ($\frac{C_L}{C_M} = 1$). However, ^{1}H-NMR spectra (Fig. 3.S4, Supporting Information) show that excess of ligand causes an increase in the peak intensity associated to the complexed cacodylate. Thus, some competition between the inner and outer coordination spheres can be guessed in excess of ligand, where the first one can evolve to simpler forms by disruption of the polymer.

The results at pH 7.0 significantly differ from the trend observed at pH 5.0 and 6.0. A very broad, low intensity, peak centred at 60 ppm is obtained in ^{27}Al-NMR spectra (Fig. 3.5 A), and the ^{1}H-NMR exhibits very small peaks of the complexed forms (Fig. 3.6B), even at same resonance of the peaks at pH 5.0 and 6.0. However, at pH 7.0 no precipitation was observed in the Al/Cac solution, whereas extended precipitation occurs for the free aluminium. Thus, we can envisage occurrence of interaction, even though of different nature compared to that at work at lower pH values.

Stumm [31] suggested that the interaction of an organic ligand with a solid interface can be differentiated between inner (strong bonding) and outer (weak bonding) coordination sphere. In a study of the acetate/aluminium system [32] it has been proposed that the interaction of the acetate ion with Al_2O_3 in suspension involves mainly the outer coordination sphere. We suggest that at pH 7 cacodylate can interact with Al(III) aggregates in the same way as acetate reacts with aluminium oxide suspension. The resulting complex enables aluminium to remain in solution. This is an interesting result because we have verified that cacodylate renders aluminium soluble in near physiological conditions systems (I=0.1 M, pH=7.0 and T=25.0 °C).

3.2.4 Determination of K_{app} of Aluminium/Cacodylate Complexes

The apparent equilibrium constant, K_{app}, for formation of the aluminium/cacodylate (Al/Cac) complexes, was determined from batchwise spectrophotometric titrations performed for different pH values. The apparent reaction is

$$\mathrm{M_f} + \mathrm{L_f} \overset{K_{app}}{\rightleftharpoons} \mathrm{ML_T} \tag{3.5}$$

where $\mathrm{M_f}$ and $\mathrm{L_f}$ are, respectively, the non-complexed free metal and the ligand forms, and $\mathrm{ML_T}$ is the total complex. Most of the experimental data-pairs were obtained with no excess of metal or ligand. The interaction between aluminium species and cacodylate causes a hypochromic effect (Fig. 3.7A).

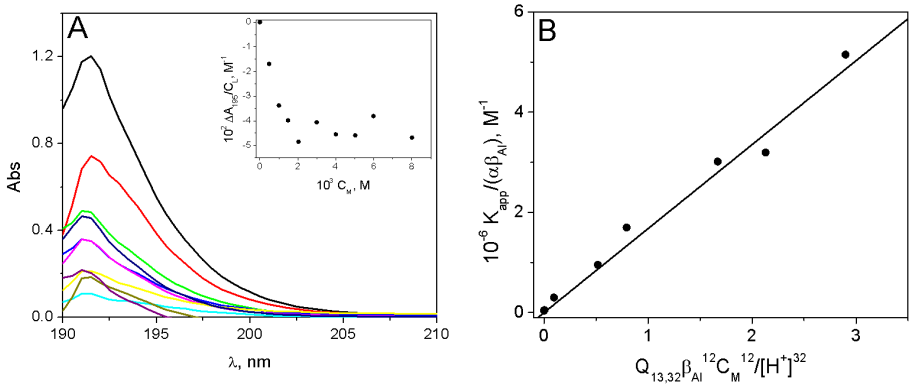

Figure 3.7: (A) Example of spectrophotometric titration of the Al/Cac system. Inset: track at λ=195 nm. C_L=1.0 × 10^{-3} M, I=0.1 M, pH=4.8 and T=25.0 °C. (B) Analysis according to Equation (3.8) of the 4.3<pH<5.0 data.

The data-pairs were analysed according to Equation (3.6):

$$\frac{C_L C_M}{\Delta A} + \frac{\Delta A}{\Delta \epsilon^2} = \frac{C_L + C_M}{\Delta \epsilon} + \frac{1}{K_{app} \Delta \epsilon} \tag{3.6}$$

where C_L and C_M are the analytical ligand and metal concentrations, respectively, $\Delta A = A - \epsilon_L C_L$ and $\Delta \epsilon = \epsilon_{ML} - \epsilon_L$, where ϵ_i is the absorptivity of the i_{th} species.
Different binding isotherms were obtained using absorbance values within 195-205 nm (Fig. 3.7A), a range where aluminium ion displays no absorption, whereas the different dimethylarsinic forms have different absorptivity, ϵ_i. As for the the pK_A measurements of the free cacodylate, the use of different tracks allowed to assure the goodness of our results, in a range where the noise is high. The equilibrium constants obtained (Table 3.1) are averaged values. At pH=2, such evaluation was unfeasible because the change in absorbance was too modest owing to the inhibition of the binding reaction caused by protons, and in agreement with the NMR results.

Table 3.1: *Apparent equilibrium constant for binding of aluminium to cacodylate (K_{app}) at different pH. I=0.1 M ($NaClO_4$) and T=25.0 °C*

pH	K_{app}
3.0	25
4.0	290
4.3	560
4.5	2200
4.7	3400
4.8	4600
4.9	5400
4.95	4800
5.0	6500

The relationship between K_{app}, and $[H^+]$ is expressed by Equation (3.7) (see Appendix 3.B in Supporting Information)

$$\frac{K_{app}}{\alpha\beta_{Al}} = K^I + K^{II}\frac{Q_{1,1}}{[H^+]} + K^{III}\frac{Q_{1,2}}{[H^+]^2} + K^{IV}\frac{Q_{1,3}}{[H^+]^3} + K^{V}\frac{Q_{1,4}}{[H^+]^4} + K^{VI}\frac{Q_{2,2}C_M\beta_{Al}}{[H^+]^2} + K^{VII}\frac{Q_{3,4}C_M^2\beta_{Al}^2}{[H^+]^4} + K^{VIII}\frac{Q_{13,32}C_M^{12}\beta_{Al}^{12}}{[H^+]^{32}} \quad (3.7)$$

where α_L is the molar fraction of the species Cac^-, β_{Al} is the molar fraction of the species Al^{3+}, K_I, K_{II}, K_{III}, K_{IV}, K_V, K_{VI}, K_{VII} and K_{VIII} are the true equilibrium thermodynamic constants for binding of Cac to Al^{3+}, $Al(OH)^{2+}$, $Al(OH)_2{}^+$, $Al(OH)_3$, $Al(OH)_4{}^-$, $Al_2(OH)_2{}^{4+}$, $Al_3(OH)_4{}^{5+}$ and $Al_{13}O_4(OH)_{24}{}^{7+}$, respectively. On the other side, the β values (Fig. 3.3) support simplification of Equation (3.7) to Equation (3.8). Actually, except for the Al^{3+} and $Al_{13}-$mer, all contributions are negligible under the experimental conditions employed, due to the low mole fraction of the other species.

$$\frac{K_{app}}{\alpha\beta_{Al}} = K^I + K^{VIII}\frac{Q_{13,32}C_M^{12}\beta_{Al}^{12}}{[H^+]^{32}} \quad (3.8)$$

Moreover, since formation of the polymeric form is fully attained within a very narrow pH range, two well defined pH ranges can be distinguished; in the first (3.0<pH<4.3) the monomers Al^{3+} and $AlOH^{2+}$ are active, while in the second (4.7<pH<5.0) the $Al_{13}-$mer is active. For pH>4.5, the contribution of K^I to Equation (3.8) is negligible (Fig. 3.7B). In this pH range, $Log\frac{K_{app}}{\alpha_L\beta_{Al}^{13}}$ *versus pH* plots at different C_M (Fig. 3.S5A, Supporting Information), and $Log\frac{K_{app}[H+]^{32}}{\alpha_L\beta_{Al}^{13}}$ *versus* C_M plot (Fig. 3.S5B, Supporting Information) yielded straight lines with slope equal to 32 and 12, respectively, reinforcing the presence of $Al_{13}O_4(OH)_{24}{}^{7+}$ as the reactive species. Analysis according to Equation (3.8) of K_{app} versus pH plots yielded $K_{VIII}=(1.6\pm0.4)\times10^6 M^{-12}$ (Fig. 3.7B). This datum can be used in the 3.0<pH<4.3 region to evaluate the true thermodynamic constant $K_I=(4\pm2)\times10^4 M^{-1}$.

Also, from the NMR data obtained we evaluated the apparent equilibrium constant at $C_L = C_M$ and different pH values (see Appendix 3.A, Supporting Information). The K_{app} values obtained at pH values 4 and 5 (Table 3.S1, Supporting Information) concur well with the spectrophotometric values (Table 3.1). However, the values obtained at pH 6 and 7 are smaller than expected, thus disagreeing with the model proposed by means of UV measurements due to the observed aggregation trend of the Al_{13} units.
^{27}Al-NMR results show that the interaction between metal and ligand yield the AlCac complex and not AlHCac or AlH_2Cac, however no indication is provided as to forming AlCac from Reactions (3.9) or (3.10) written below.

$$Al^{3+} + Cac^{-} \overset{K^I}{\rightleftharpoons} AlCac^{2+} \tag{3.9}$$

Due to the proton ambiguity, Reaction (3.9) cannot be thermodynamically distinguished from the equivalent reaction (3.10), neither by thermodynamic experiments (since the dependence of the conditional equilibrium constant on $[H^+]$ would be the same) nor kinetically (since the formula of the activated complex would be the same).

$$AlOH^{2+} + HCac \overset{K^{I'}}{\rightleftharpoons} AlCac^{2+} \tag{3.10}$$

However some considerations, based on the kinetic behaviour of Al(III) species, will allow us to establish the most probable pathway: being $AlOH^{2+}$ about 10^4-fold more reactive than Al^{3+} aquo ion, as results from comparison of the respective rates of water exchange [33], the first step of the Al(III) binding to a chelating ligand should be about 10^3-fold faster in the case of $AlOH^{2+}$ [34]. Hence, for pH>2 the formation of $AlCac^{2+}$ will involve mainly Reaction (3.10). The equilibrium constant of Reaction (3.10), here denoted as $K^{I'}$, is related to K^I by the relationship $K^{I'} = K^I K_{A,2}/Q_{1,1}$. Its value is $K^{I'}=(8 \pm 4) \times 10^3 M^{-1}$. Only for pH>5 the contribution of the deprotonated Cac^- ion to the binding reaction becomes important. This interpretation differs from that advanced in a previous study were the formation of the 1:1 complex was rationalized assuming that the main process is the reaction of the Al^{3+} ion with the deprotonated form of the ligand, Cac^- [35].

3.2.5 DFT Calculation

By means of the mass spectrometry and NMR data, we have hypothesized possible Al/Cac structures. It can reasonably be assumed that the ligand chelates the metal, as demonstrated for other oxygenated ligands with aluminium [16,32,36]. The suggested structure of the monomer species is shown in Fig. 3.8A (note that water molecules can be replaced by hydroxo groups, and more than one ligand could be present). For the dimer species, the mass spectrometry and NMR data gathered do not clarify the exact structure, so different geometries can be considered. Based on earlier studies on different Al(III) complexes [22, 32], we propose the following structures: two aluminium atoms linked by two oxygen groups (Fig. 3.8B), the interaction of the aluminium complexes is obtained via hydroxo groups (Fig. 3.8C), only one oxygen binds the aluminium complexes, as in the third structure (Fig. 3.8D). Interestingly, a different M_2L structure

is proposed for the aluminium/acetate complex [32]. Since cacodylate exhibits similar structure as the acetate, we proposed similar geometry associated to the most intense signal in the mass spectrometry ($\frac{m}{z} = 121$) and NMR spectra (δ=1.95 and 1.80 ppm) (Fig. 3.8E). As a matter of fact, a *syn-syn* bridging geometry is considered by the experimental results, where the two oxygens bind to both aluminium atoms of the dimeric form. Hence, a double hydroxo- or oxo-bridged geometry is present. For the trimeric and tetrameric species, other more complex structures can be hypothesized with the same bridging geometry.

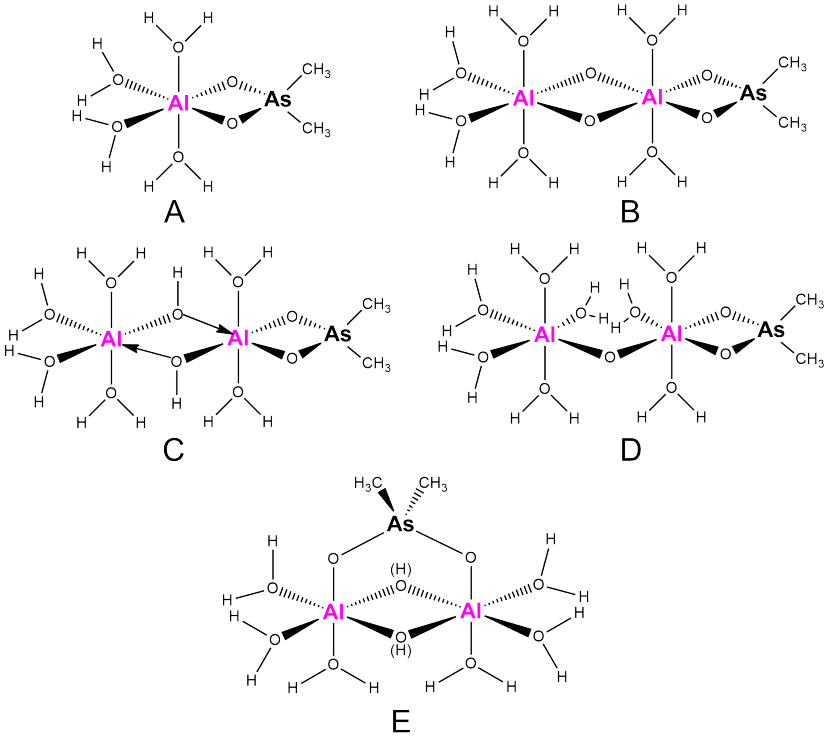

Figure 3.8: (A) 1:1 structure. (B) First 2:1 structure. (C) Second 2:1 structure, (D) Third 2:1 structure (E) Fourth 2:1 structure: syn-syn bridging geometry.

To convincingly justify the hypotheses drawn on the dimeric complexes, we undertook theoretical energy calculations of these complexes.
For the M_2L dimeric system, four different structures were calculated (B, C and two more E structures, with and without bridging oxygens, which will be denoted as E(OH) and E(O), respectively. The two E structures consist of a 2:1 complex, where Cacodylate is bound to only one Al atom via a double O-bridge. B and C structures resemble the E(O) and E(OH) structures, respectively, but with OH bridging ligands between Al atoms, instead of O-bridge, and two more hydroxo ligands.
The stability has been studied in terms of the overall energy (products energy). The DFT optimization of these structures results in the stability sequence, from most stable to less stable (Hartree units), as follows: (B) (-849.660435) > (C)

(-849.651503)> (E(O)) (-849.590124) > (E(OH)) (-849.558751). Thus, the most stable structure involves OH-bridging ligands between Al atoms with cacodylate bound to both metal centres. The optimized structure of (E(OH) is plotted in Fig. 3.9A.

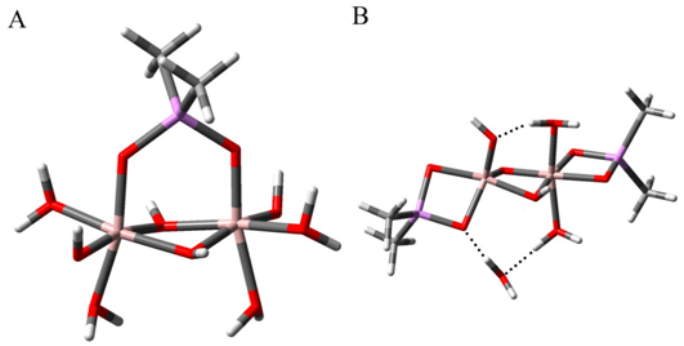

Figure 3.9: (A) DFT optimization of structure E(OH) in water, using B3LYP functional with 6-31G(d) basis set for C (grey), H (white) and O (red) atoms, and LANL2DZ for Al (pink) and As (purple) atoms. (B) DFT optimization of 2:2 linear complex in water, using B3LYP functional with 6-31G(d) basis set for C(grey), H(white) and O(red) atoms, and LANL2DZ for Al (pink), As (purple) atoms and H-bonding interactions (dashed lines).

A non-symmetrical conformation has been obtained (symmetry group C1) with OH groups in the Al-Al plane pointing to cacodylate group. Surprisingly, methyl groups bound to As, adopted eclipsed conformation. Full NBO (Natural Bond Orbital) analysis has revealed that, as expected, the Al and As sites are mainly positively charged. Oxygen atoms in the Al-O-As bonds are significantly more negative than the others due to the charge donating nature of the metals. Thus, the Oxygen site in the OH-bridges between Al atoms are, indeed, more negative than those on the water molecules.
The characterization parameters (bond distance and angle) of the *core* of the molecule (every atom surrounding Al and As atoms) are compiled in Table 3.S2, Supporting Information. The two atom distances and angles containing Al are similar, showing that the core lies in a symmetric environment and the abovementioned asymmetry is due to the slightly asymmetric conformation of the H_2O, OH and CH_3 groups. In addition, DFT optimization and geometry analysis of two 2:2 complex (structures reported in Fig. 3.S7, Supporting Information), has been carried out, whose presence was confirmed by mass spectrometry ($\frac{m}{z}$ = 361). Since the calculations of a double *syn-syn* bridging geometry complex (Fig. 3.S7A) proved to be unstable in water, complex linear geometry (Fig. 3.S7B) has been DFT optimized to a minimum energy state (E= -933.31Hartrees). In the final conformation, one hydrogen atom from a water molecule is lost, and transferred to one of the O-bridging ligand between Al atoms. Moreover, a full water molecule is lost, remaining nearby the 2:2 complex via H-bonding interaction (Fig. 3.9B). These rearrangements, result in a surprisingly differ-

ent conformation for Al atoms, from the initial Al(octhedral)-Al(octahedral) to Al(pyramidal)-Al(octahedral). The stabilization of the pyramidal configuration can be explained by the H-bonding induced by the above mentioned water molecule that falls off the molecule (Table 3.S3, Supporting Information), showing that expected symmetry of the optimized structure is totally lost. The distance and angle values of the Al-O bonds considerably differ from their theoretical mirror image bonds. The dihedral angles show different orientation of the As-O-Al(pyramidal)-O and As-O-Al(octahedral) rings compared to the plane containing Al(1), O(2) and Al(3); the Al(pyramidal) ring is primarily orientated to the yz plane, whereas the Al(octahedral) containing ring, lies in the xz plane. As described for the 2:1 complex, the NBO analysis displays electron donation from metals to oxygen, an effect more intense for the O-bridging ligands between Al atoms. The DFT calculations suggest that the 2:2 complex hypothesized by MS data is an asymmetric system, where the four methyl groups are surrounded by different chemical environments. It follows that they have different chemical shifts. The ^{1}H-NMR at pH=6.0 (Fig. 3.6D) of the Al/Cac system show a lot of peaks that, even if they cannot be specifically associated to each methyl group, could agree with a Al_2Cac_2 asimmetric system. However the peaks are little visible at pH=5.0, even if MS spectra prompts that Al_2Cac_2 is a relevant product even at such a kind of pH. It could be explained by the fact that MS measurements are not performed at $I = 0.1\,\mathrm{M}$, which can affect the process of dimerization. Regarding ^{27}Al-NMR, the broad peak does not allow to obtain information on the presence of this specific complex. However, other studies suggest the presence of penta-coordinated aluminum for oxygenated ligand and mono- and dimeric aluminium [37, 38].

3.3 Conclusion

Thermodynamic experiments of the interaction between Al(III) and dimethylarsinic acid suggest that the apparent binding affinity has a maximum in the 5-6 pH region, whereas at pH 4.0 and pH 7.0 the binding strength is low. Comparison of the MS and NMR data suggests that the main species formed is a 2:1 complex. Thus, the most probable effect is that the 1:1 complex, which forms first, has a high affinity for a second aluminium ion. In particular, the most plausible structure is the dimeric *syn-syn* bridging geometry structure of the cacodylate, interacting with the two aluminium centres (Fig. 3.8E). On the other hand, the different behaviour observed at pH 7.0 respect to that at pH 4-6 is explained assuming the formation of an outer sphere coordination of the ligand to the Al_{13} aggregates at neutral pH, thus avoiding precipitation. On the other hand, at lower pH the polymeric form disintegrates into small molecules, an effect promoted mainly by the proton and, to a lesser extent, by the ligand. Elucidation of the Al/Cac complex, which does not allow aluminium to precipitate, in particular in those conditions named near physiological ($I = 0.1\,\mathrm{M}$, pH=7.0 and 25.0 °C), can be very useful to obtain a system available to study the biological processes and molecular mechanisms that underlie pathological effects induced by aluminium ions.

Bibliography

[1] W. C. Wolsey (1973). *Perchlorate Salts, Their Uses and Alternatives*, Journal of Chemical Educucation 50 (6), A335-A337.

[2] P. A. W. van Hees and U. S. Lundstrom (2000). *Equilibrium Models of Aluminium and Iron Complexation with Different Organic Acids in Soil Solution*, Geoderma, 94 (2), 201-221.

[3] M. Lashkari and M. R. Arshadi (2004). *DFT Studies of Pyridine Corrosion Inhibitors in Electrical Double Layer: Solvent, Substrate, and Electric Field Effects*, Chemical Physics, 299 (1), 131-137.

[4] H. Kawamura, V. Kumar, Q. Sun and Y. Kawazoe (2001). *Bonding Character of Hydrogen in Aluminum Clusters*, Materials Transactions, 42 (11), 2175-2179.

[5] Z. J. Wu and X. F. Ma (2003). *Potential Energy Surface of aAluminum and Tungsten Dimers*, Chemical Physics Letters, 371 (1), 35-39.

[6] X. Jin, W. Yang, Z. Qian, Y. Wanga and S. Bi (2011). *DFT Study on the Interaction between Monomeric Aluminium and Chloride Ion in Aqueous Solution*, Dalton Transactions, 40 (18), 5052-5058.

[7] M. J. Frisch, G. W. Trucks, H. B. Schlegel, G. E. Scuseria, M. A. Robb, J. R. Cheeseman, G. Scalmani, V. Barone, B. Mennucci, G. A. Petersson, H. Nakatsuji, M. Caricato, X. Li, H. P. Hratchian, A. F. Izmaylov, J. Bloino, G. Zheng, J. L. Sonnenberg, M. Hada, M. Ehara, K. Toyota, R. Fukuda, J. Hasegawa, M. Ishida, T. Nakajima, Y. Honda, O. Kitao, H. Nakai, T. Vreven, J. A. Montgomery, J. E. Peralta, F. Ogliaro, M. Bearpark, J. J. Heyd, E. Brothers, K. N. Kudin, V. N. Staroverov, R. Kobayashi, J. Normand, K. Raghavachari, A. Rendell, J. C. Burant, S. S. Iyengar, J. Tomasi, M. Cossi, N. Rega, J. M. Millam, M. Klene, J. E. Knox, J. B. Cross, V. Bakken, C. Adamo, J. Jaramillo, R. Gomperts, R. E. Stratmann, O. Yazyev, A. J. Austin, R. Cammi, C. Pomelli, J. W. Ochterski, R. L. Martin, K. Morokuma, V. G. Zakrzewski, G. A. Voth, P. Salvador, J. J. Dannenberg, S. Dapprich, A. D. Daniels, Farkas, J. B. Foresman, J. V. Ortiz, J. Cioslowski and D. J. Fox (2010). GAUSSIAN REVISION C.01, Inc., Wallingford CT.

[8] K. Yates and H. Wai (1964). *A Redetermination and Extension of the H_0 Scale of Acidity in Aqueous Perchloric Acid*, Journal of the American Chemical Society, 86 (24), 5408-5413.

[9] B. Holmberg (1910). *Uber den Amphoteren Charakter der Kakodylsaure*, Zeitschrift für Physikalische Chemie, 70 (1), 153-57.

[10] M. L. Kilpatrick (1949). *The Basic and the Acid Strength of Cacodylic Acid in Water*, Journal of the American Chemical Society, 71 (8), 2607-2610.

[11] J. Juillard and N. Simonet (1968). *Acids in Mixed Water-Methanol Solvents. I. Determination of Some Thermodynamic Constants of Dissociation*, Bulletin de la Societé Chimique de France, (5), 1883-1894.

[12] K. B. Jacobson, B. D. Sarma and J. B. Murphy (1972). *Reaction of Cacodylic Acid with Organic Thiols*, FEBS Letters, 22 (1), 80-82.

[13] T. W. Shin, K. Kim and I. J. Lee (1997). *Spectrophotometric Determination of the Acid Dissociation Constants for Cacodylic Acid and p-nitrophenol at Elevated Temperatures*, Journal of Solution Chemistry, 26 (4), 379-390.

[14] G. Furrer, C. Ludwig and P. W. Schindler (1992). *On the Chemistry of the Keggin Al_{13} Polymer: I. Acid-Base Properties*, Journal of Colloid and Interface Science, 149 (1), 56-67.

[15] C. Ye, Z. Bi and D. Wang (2013). *Formation of Al_{30} from Aqueous Polyaluminum Chloride under High Temperature: Role of Al_{13} Aggregates*, Colloids and Surfaces A: Physicochemical and Engineering Aspects, 436, 782-786.

[16] W. H. Casey (2006). *Large Aqueous Aluminum Hydroxide Molecules*, Chemical Reviews, 106 (1), 1-16.

[17] C. F. Baes and R. E. Mesmer (1976). *Hydrolysis of Cations*, Ch. 6, pp. 112-123, John Wiley and Sons, New York.

[18] J. W. Eaton, D. Bateman and S. Hauberg (2009). *A High-Level Interactive Language for Numerical Computations*, 3.0.1 Edition, Create Space Independent Publishing Platform.

[19] M. H. Florencio, M. F. Duarte, A. M. M. deBettencourt, M. L. Gomes and L. F. V. Boas (1997). *Electrospray Mass Spectra of Arsenic Compounds*, Rapid Communications in Mass Spectrometry, 11, 469-473.

[20] H. R. Hansen, A. Raab and J. Feldmann (2003). *New Arsenosugar Metabolite Determined in Urine by Parallel Use of HPLC-ICP-MS and HPLC-ESI-MS*, Journal of Analytical Atomic Spectrometry, 18 (5), 474-479.

[21] T. Urabe, M. Tanaka, S. Kumakura and T. Tsugoshi (2007). *Study on Chemical Speciation in Aluminum Chloride Solution by ESI-Q-MS*, Journal of Mass Spectrometry, 42 (5), 591-597.

[22] A. Sarpola, V. Hietapelto, J. Jalonen, J. Jokela, R. S. Laitinen and J. Rämö (2004). *Identification and Fragmentation of Hydrolyzed Aluminum Species by Electrospray Ionization Tandem Mass Spectrometry*, Journal of Mass Spectrometry, 39 (10), 1209-1218.

[23] A. T. Sarpola, V. K. Hietapelto, J. E. Jalonen, J. Jokela and J. H. Rämö (2006). *Comparison of Hydrolysis Products of $AlCl_3 \cdot 6\,H_2O$ in Different Concentrations by Electrospray Ionization Time of Flight Mass Spectrometer (ESI TOF MS)*, International Journal of Environmental and Analytical Chemistry, 86 (13), 1007-1018.

[24] A. Sarpola, V. Hietapelto, J. Jalonen, J. Jokela and R. S. Laitinen (2004). *Identification of the Hydrolysis Products of $AlCl_3 \cdot 6\,H_2O$ by Electrospray Ionization Mass Spectrometry*, Journal of Mass Spectrometry, 39 (4), 423-430.

[25] T. Urabe, T. Tsugoshi and W. Tanaka (2009). *Characterization of Aluminum Species with Nitrate, Perchlorate and Sulfate Ions in the Positive and Negative Ion Mode by Electrospray Ionization Mass Spectrometry*, Journal of Mass Spectrometry, 44 (2), 193-202.

[26] J. W. Akitt and B. E. Mann (1989). *^{27}Al NMR Spectroscopy at 104.2 MHz*, Journal of Magnetic Resonance (1969), 44 (3), 584-589.

[27] J. J. Fitzgerald, L. E. Johnson and J. S. Frye (1989). *Temperature Effects on the ^{27}Al NMR Spectra of Polymeric Aluminum Hydrolysis Species*, Journal of Magnetic Resonance (1969), 84 (1), 121-133.

[28] G. Furrer, M. Gfeller and B. Wehrli (1999). *On the Chemistry of the Keggin Al_{13} Polymer: Kinetics of Proton-Promoted Decomposition*, Geochimica et Cosmochimica Acta, 63 (19), 3069-3076.

[29] A. Masion, F. Thomas, D. Tchoubar, J. Y. Bottero and P. Tekely (1994). *Chemistry and Structure of Al(Oh)/Organic Precipitates-A Small-Angle X-Ray-Scattering Study. 3. Depolymerization of the Al-13 Polycation by Organic-Ligands*, Langmuir, 10 (11), 4353-4356.

[30] A. Amirbahman, M. Gfeller and G. Furrer (2000). *Kinetics and Mechanism of Ligand-Promoted Decomposition of the Keggin Al_{13} Polymer*, Geochimica et Cosmochimica Acta, 64 (5), 911-919.

[31] W. Stumm (1992). *Chemistry of the Solid-Water Interface: Processes at the Mineral-Water and Particle-Water Interface in Natural Systems*, Ch. 1, pp. 4-8, John Wiley and Sons, New York.

[32] P. Persson, M. Karlsson and L. O. Ohman (1998). *Coordination of Acetate to Al(III) in Aqueous Solution and at the Water-Aluminum Hydroxide Interface: A Potentiometric and Attenuated Total Reflectance FTIR Study*, Geochimica et Cosmochimica Acta, 62 (23), 3657-3668.

[33] J. P. Nordin, D. J. Sullivan, B. L. Phillips and W. H. Casey (1998). *An ^{17}O-NMR Study of the Exchange of Water on $AlOH(H_2O)_{5(aq)}{}^{2+}$*, Inorganic Chemistry, 37 (19), 4760-4763.

[34] F. Secco and M. Venturini (1975). *Mechanism of Complex Formation. Reaction between Aluminum and Salicylate Ions*, Inorganic Chemistry, 14 (8), 1978-1981.

[35] P. V. Ioannou (2013). *Dimethylphosphinato and Dimethylarsinato Complexes of Group 13 Metals and their Chemistry*, Monatshefte für Chemie-Chemical Monthly, 144 (6), 793-802.

[36] R. B. Martin (1986). *The Chemistry of Aluminum as Related to Biology and Medicine*, Clinical Chemistry, 32 (10), 1797-1806.

[37] J. F. Stebbins, S. Kroeker, S. K. Lee and T. J. Kiczenski (2000). *Quantification of Five-and Six-Coordinated Aluminum Ions in Aluminosilicate and Fluoride-Containing Glasses by High-Field, High-Resolution ^{27}Al NMR*, Journal of Non-Crystalline Solids, 275 (1), 1-6.

[38] C. H. Lin, B. T. Ko, F. C. Wang, C. C. Lin and C. Y. Kuo (1999). *Electronic and Steric Factors Affecting the Formation of Four or Five-coordinated Aluminum Complexes: Syntheses and Crystal Structures of Some Aluminum Alkoxides*, Journal of Organometallic Chemistry, 575 (1), 67-75.

Supporting Information

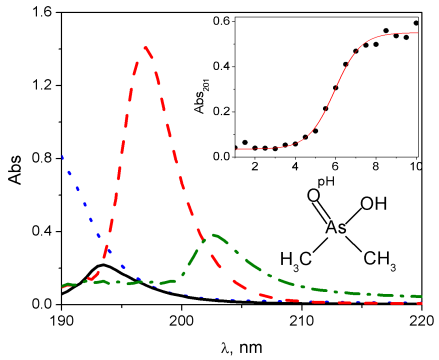

Figure 3.S1: Absorbance spectra of dimethylarsinic acid recorded at different pH: (• • •) 1.0, (—) 3.0, (- - -), 7.0, (- • -) 11.0. C_L=1.0 × 10^3 M, I=0.1 M ($NaClO_4$) and T=25.0 °C. Inset: absorbance variation with pH for the HCac/Cac$^-$ system at λ=201 nm.

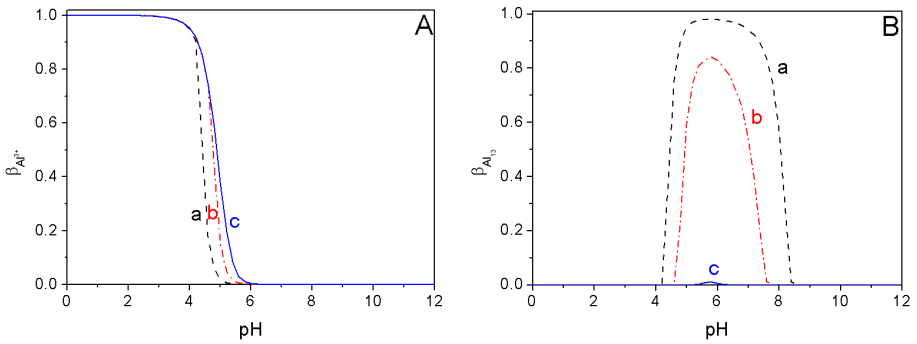

Figure 3.S2: (A) Molar fraction of Al^{3+} (β_{Al}) *versus* pH at different analytical concentration of the metal, C_M. (B) Molar fraction of the polymeric aluminium (β_{Al13}) *versus* pH at different C_M. (a) C_M=1.0 × 10^{-5} M, (b) C_M=1.0 × 10^{-4} M and (c) C_M=1.0 × 10^{-3} M. I=0.1 M and T=25.0 °C.

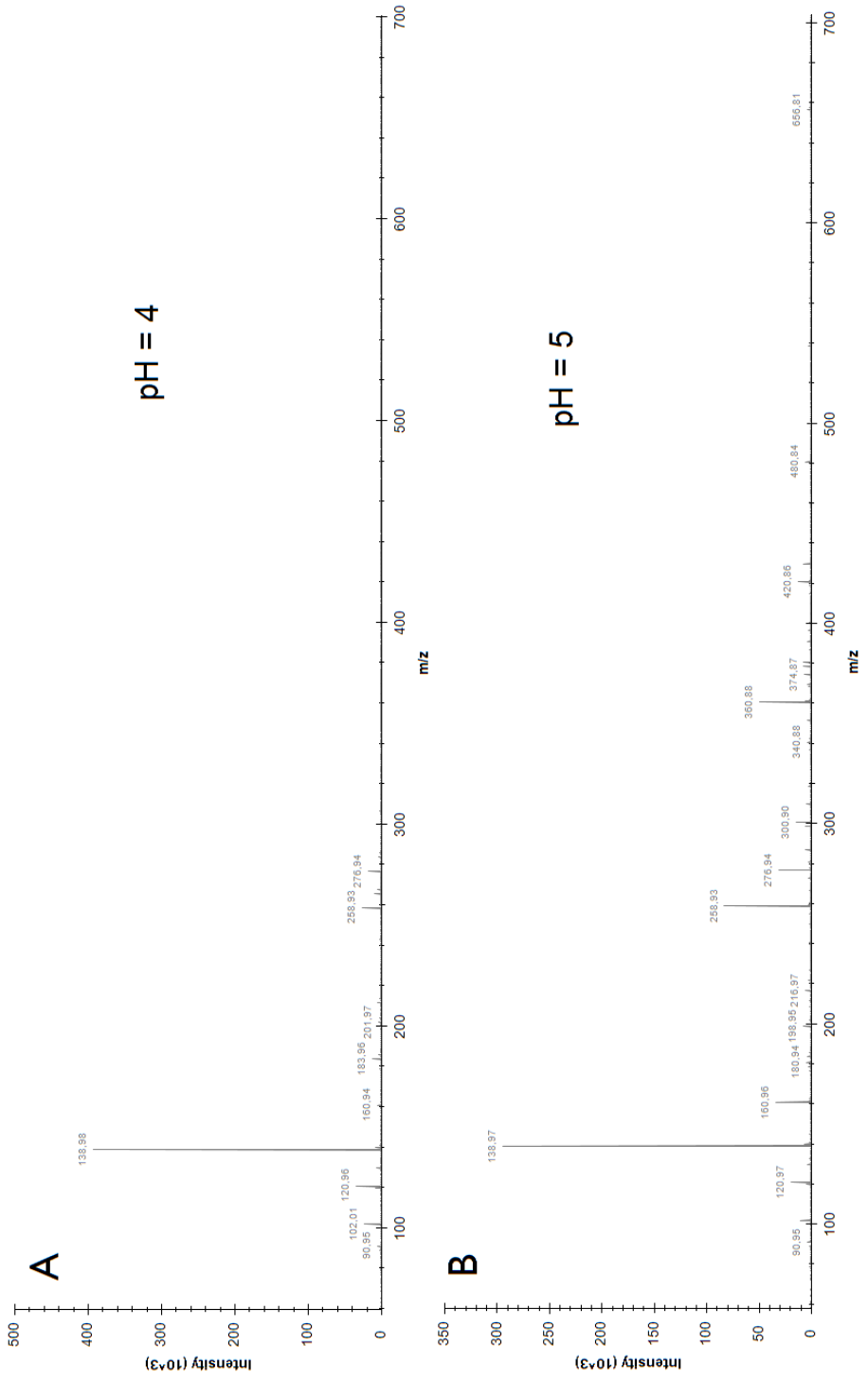

Figure 3.S3: Mass Spectra of Al/Cac solution at pH=4.0 (A) and 5.0 (B). C_M=2.0 × 10^{-4} M, C_L=2.0 × 10^{-4} M, T=25.0 °C.

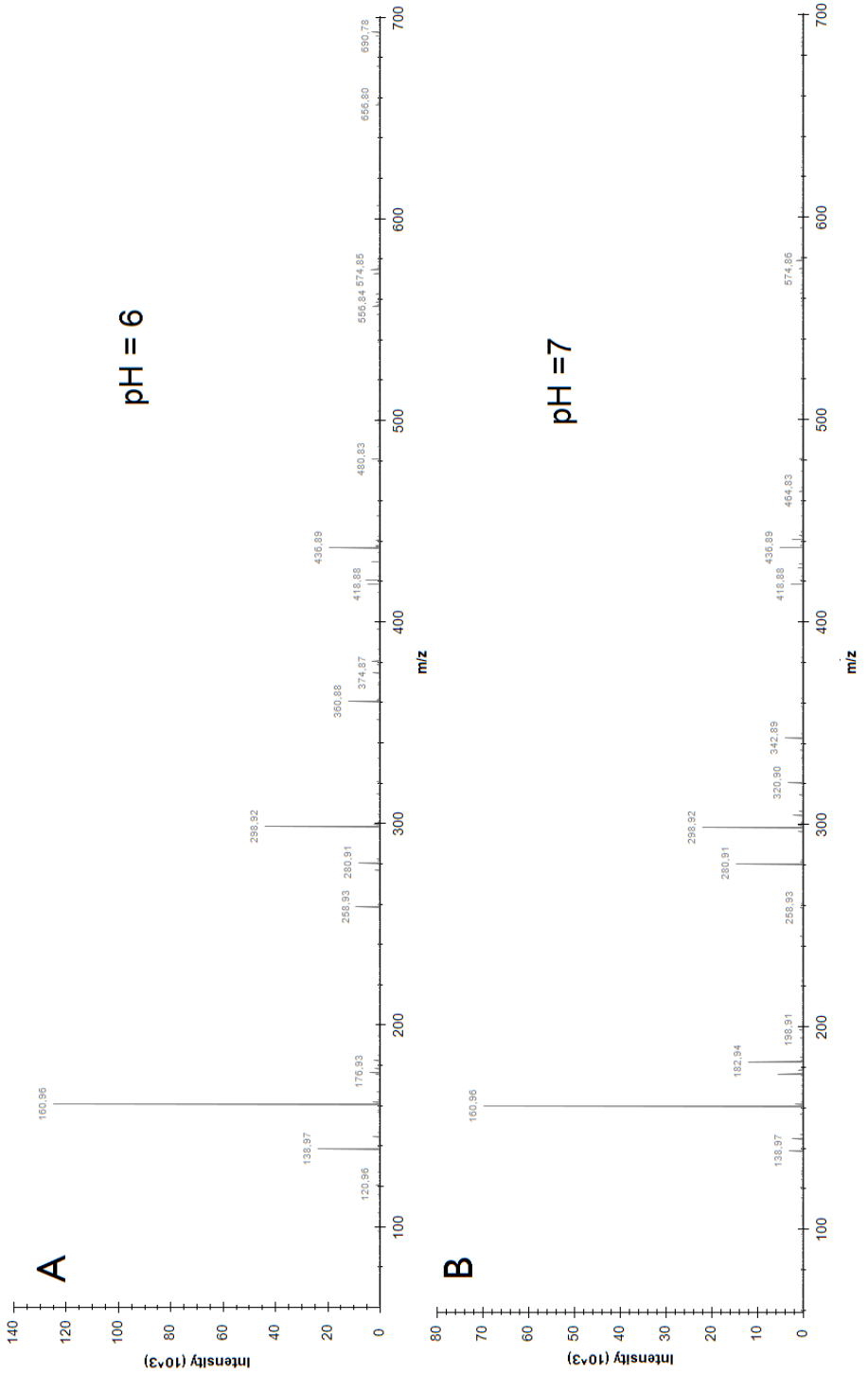

Figure 3.S4: Mass Spectra of Al/Cac solution at pH=6.0 (A) and 7.0 (B). C_M=2.0×10^{-4} M, C_L=2.0×10^{-4} M, T=25.0 °C.

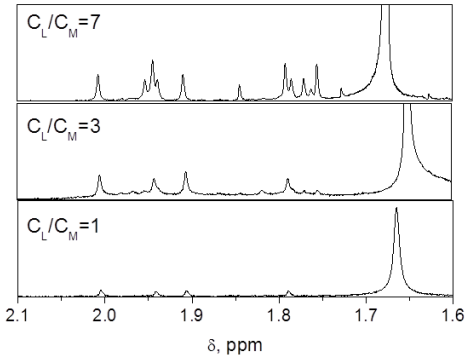

Figure 3.S5: NMR spectra of Al/Cac complexes at different $\frac{C_L}{C_M}$. C_M=5.0 × 10^{-3} M, I=0.1 M ($NaClO_4$), pH=7.0, T=25.0 °C.

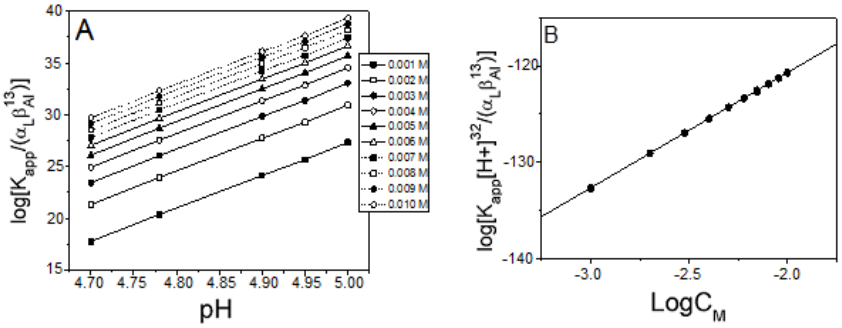

Figure 3.S6: (A) Data treatment of Equation (3.8) as a function of pH at different C_M values; (B) data treatment of Equation (3.8) as a function of $LogC_M$; I=0.1 M and T=25.0 °C.

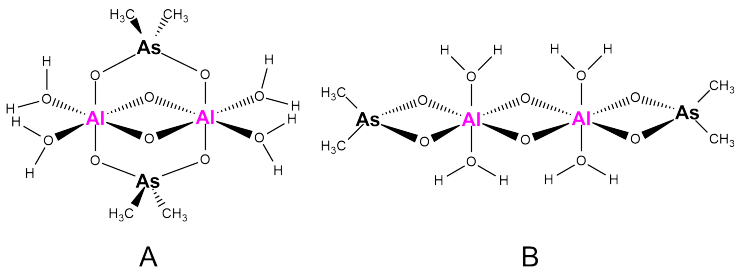

Figure 3.S7: Structures for DFT analysis for the M_2L_2 dimeric system.

Table 3.S1: Formula of Al/Cac complexes by the mass spectrometry data. C_M=C_L=2.0×10^{-4} M; T=25.0 °C.

	Complexes	**v**	**m/z**	1×10^3 **Intensity**			
				pH4	pH5	pH6	pH7
Monomeric	$AlCac(H_2O)_v^{2+}$	1	91	5	3	1	0.5
	$AlOHCac(H_2O)_v^{+}$	0	181	1.5	4		
		1	199	2	8	-	-
		2	217	1	6		
Dimeric	$Al_2O(OH)Cac(H_2O)_v^{2+}$	1	361	40	30	2	1
		2	379	17	3	-	-
	$Al_2O(OH)Cac_2(H_2O)_v^{+}$	0	361		50	13	
		1	379	-	7	1	-
		2	397		2	1	
	$AlOCac_3(H_2O)_v^{+}$	0	481		6	3	0.75
		1	499	-	1	0.5	-
		2	517		0.5	0.3	-
Trimeric	$Al_3O(OH)_3Cac(H_2O)_v^{3+}$	1	107	1	1	1	1
	$Al_3O_3(OH)Cac_2(H_2O)_v^{+}$	0	283		5		
		1	301	-	7	-	-
		2	319		2.5		
	$Al_3O_2(OH)_2Cac_2(H_2O)_v^{+}$	0	421	-	13	5	1
		1	439	-	1	1	-
	$Al_3O(OH)_3Cac_3(H_2O)_v^{+}$	1	577		1.5	-	-
		2	595	-	-	0.5	0.5
		3	613		-	-	0.5
		4	631		-	0.5	-
Tetrameric	$Al_4O_2(OH)_2Cac_3(H_2O)_v^{+}$	1	603		-	-	
		4	657	-	-	1.5	-
		6	693		3	3	
		7	711		-	0.5	

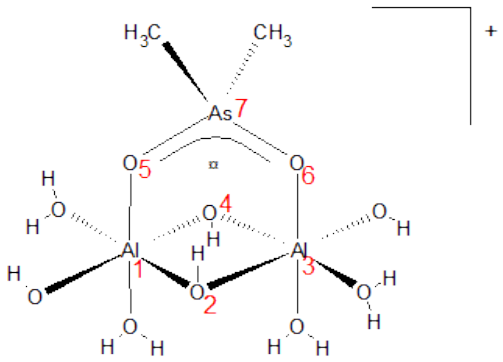

Table 3.S2: Selected parameters, distances (Å) and angles (°), for the 2:1 Al/Cac complex.

Distances, Å		**Angles**, °	
Atoms	Value	Atoms	Value
Al(1)-O(2)	1.92	O(2)-Al(1)-O(4)	74.28
Al(1)-O(4)	1.93	O(2)-Al(1)-O(5)	97.82
Al(1)-O(5)	1.90	O(2)-Al(3)-O(4)	74.28
Al(1)-Al(3)	3.00	O(2)-Al(3)-O(6)	96.14
Al(3)-O(2)	1.93	Al(1)-O(2)-Al(3)	102.65
Al(3)-O(4)	1.92	Al(1)-O(4)-Al(3)	102.79
Al(3)-O(6)	1.90	O(5)-As(7)-O(6)	112.86
As(7)-O(5)	1.70		
As(7)-O(6)	1.70		

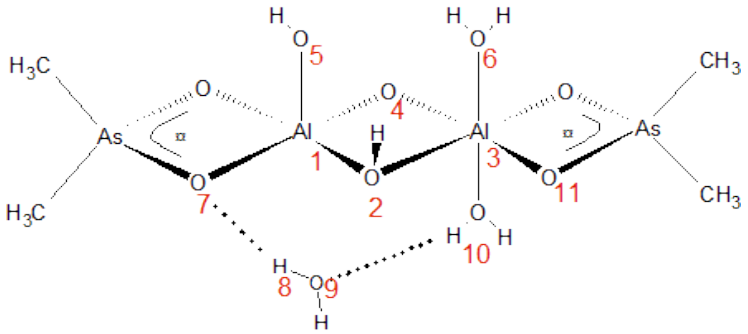

Table 3.S3: Selected parameters, distances (Å), angles (°) and dihedral angles (°) for the 2:2 Al/Cac complex.

Distances, Å		**Angles**, °		**Dihedral Angles**, °	
Atoms	Value	Atoms	Value	Atoms	Value
Al(1)-O(2)	1.98	O(2)-Al(1)-O(4)	84.35	O(7)-Al(1)-O(2)-Al(3)	133.78
Al(1)-O(4)	1.75	O(2)-Al(1)-O(5)	89.26	Al(1)-O(2)-Al(3)-O(11)	164.80
Al(1)-O(5)	1.82	O(2)-Al(3)-O(4)	74.28		
Al(1)-Al(3)	1.95	O(2)-Al(3)-O(6)	84.69		
Al(3)-O(2)	1.94	Al(1)-O(2)-Al(3)	87.87		
Al(3)-O(4)	1.78	Al(1)-O(4)-Al(3)	99.98		
Al(3)-O(6)	2.11	O(7)-Al(1)-O(2)	90.67		
Al(3)-O(10)	1.93				
O(7)-H(8)	1.75				
O(9)-H(10)	1.65				

3.A Determination of the Equilbrium Constant by NMR

To evaluate the apparent equilibrium constant for complex formation (K_{app}) from the NMR data of Fig. 3.S5, quantitative analyses were conducted according to Equation (3.A1), where I_L^n is the normalized peak area of free cacodylate and $I_M^n L$ is the total normalized area of the bound cacodylate

$$K_{app} = \frac{[ML]}{[M][L]} = \frac{I_{ML}^n C_L}{I_L^n C_L (C_M - I_{ML}^n C_L)} \tag{3.A.1}$$

Table 3.S4: *Apparent equilibrium constant for binding of aluminium to cacodylate (K_{app}) at different pH. $I = 0.1$ M ($NaClO_4$) and T=25.0 °C*

pH	$10^{-3} K_{app}$, **M**
4.0	0.2 ± 0.1
5.0	4 ± 2
6.0	1.5 ± 0.5
7.0	0.06 ± 0.02

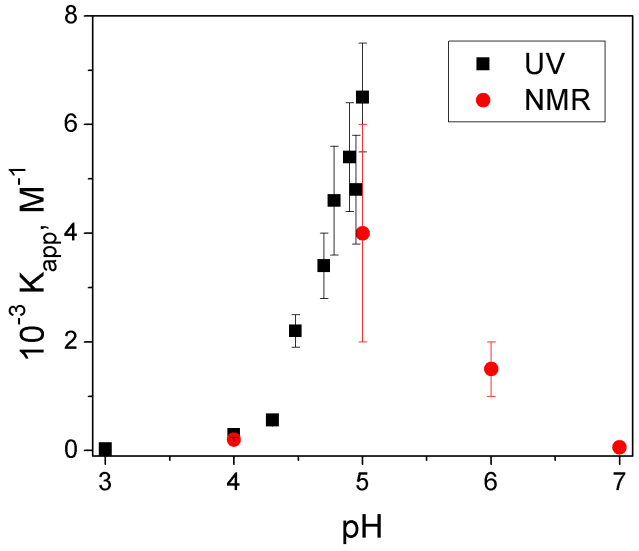

Figure 3.S8: Resume of the values of K_{app} obtained from the UV titrations (■) and the NMR spectra (●). I=0.1 M and T=25.0 °C.

3.B Determination of Equation (3.8)

The apparent constant K_{app} which represents the overall equilibria between the aluminium forms and the cacodylic acid form can be expressed by Equation (3.B.1), where $[i]$, is the concentration at the equilibrium of the *ith* form

$$K_{app} = \frac{[Al^{3+}]}{[Al^{3+}] + [AlOH^{2+}] + [Al(OH)_2^+] + [Al(OH)_3] + [Al(OH)_4^-] + \\ + [Al_2(OH)_2^{4+}] + [Al_3(OH)_4^{5+}] + [Al_{13}O_4(OH)_{24}^{7+}]} \quad (3.B.1)$$

Using the molar fraction of deprotonated cacodylate (α_L) and Al^{3+} (β_{Al})

$$\alpha_L = \frac{[Cac^-]}{[HCac] + [Cac^-]} \quad (3.B.2)$$

$$\beta_{Al^{3+}} = \frac{[AlCac^{2+}] + [Al(OH)Cac^+] + [Al(OH)_2Cac] + \\ + [Al(OH)_3Cac^-] + [Al(OH)_4Cac^{2-}] + [Al_2(OH)_2Cac^{3+}] + \\ + [Al(OH)_3] + [Al(OH)_4^-] + [Al_2(OH)_2^{4+}] + \\ + [Al_3(OH)_4Cac^{4+}] + [Al_{13}O_4(OH)_{24}Cac^{6+}]}{[Al^{3+}] + [AlOH^{2+}] + [Al(OH)_2^+] + \\ + [Al_3(OH)_4^{5+}] + [Al_{13}O_4(OH)_{24}^{7+}]} \quad (3.B.3)$$

Equation (3.B1) turns into Equation (3.B.4) (Note that in Equation (3.B.2) the species H_2CaC^+ has been disregarded since the concentration of this species is negligible in the full range of pH investigated).

$$\frac{K_{app}}{\alpha_L \beta_{Al}} = \frac{[AlCac^{2+}]}{[Al^{3+}][Cac^-]} + \frac{[Al(OH)Cac^+]}{[Al^{3+}][Cac^-]} + \frac{[Al(OH)_2Cac]}{[Al^{3+}][Cac^-]} + \\ + \frac{[Al(OH)_3Cac^-]}{[Al^{3+}][Cac^-]} + \frac{[Al(OH)_4Cac^{2-}]}{[Al^{3+}][Cac^-]} + \frac{[Al_2(OH)_2Cac^{3+}]}{[Al^{3+}][Cac^-]} + \\ + \frac{[Al_3(OH)_4Cac^{4+}]}{[Al^{3+}][Cac^-]} + \frac{[Al_{13}O_4(OH)_{24}Cac^{6+}]}{[Al^{3+}][Cac^-]} \quad (3.B.4)$$

The equilibrium ratio $Q_{x,y}$ for aluminium hydrolysis, defined in [17] of the text are introduced in Equation (3.B.4), to convert $[Al^{3+}]$ into the concentrations of the desired hydrolyzed forms. So, Equation (3.B.5) is obtained.

$$\frac{K_{app}}{\alpha_L \beta_{Al}} = \frac{[AlCac^{2+}]}{[Al^{3+}][Cac^-]} + \frac{[Al(OH)Cac^+]}{[Al(OH)^+][Cac^-]} \frac{Q_{1,1}}{[H^+]} + \frac{[Al(OH)_2Cac]}{[Al(OH)_2^+][Cac^-]} \frac{Q_{1,2}}{[H^+]^2} + \\ + \frac{[Al(OH)_3Cac^-]}{[Al(OH)_3][Cac^-]} \frac{Q_{1,3}}{[H^+]^3} + \frac{[Al(OH)_4Cac^{2-}]}{[Al(OH)_4^-][Cac^-]} \frac{Q_{1,4}}{[H^+]^4} + \\ + \frac{[Al_2(OH)_2Cac^{3+}]}{[Al_2(OH)_2^{4+}][Cac^-]} \frac{Q_{2,2} C_M \beta_{Al}}{[H^+]^2} + \frac{[Al_3(OH)_4Cac^{4+}]}{[Al_3(OH)_4^{5+}][Cac^-]} \frac{Q_{3,4} C_M^2 \beta_{Al}^2}{[H^+]^4} + \\ + \frac{[Al_{13}O_4(OH)_{24}Cac^{6+}]}{[Al_{13}O_4(OH)_{24}^{7+}][Cac^-]} \frac{Q_{13,32} C_M^{12} \beta_{Al}^{12}}{[H^+]^{32}} \quad (3.B.5)$$

The equilibrium constants of the different complexes can be expressed as $K^x = \frac{[ML]}{[M][L]}$. Introduction of this equation in Equation (3.B.5) yields equation Equation (3.B.6).

$$\frac{K_{app}}{\alpha_L \beta_{Al}} = K^I + K^{II}\frac{Q_{1,1}}{[H^+]} + K^{III}\frac{Q_{1,2}}{[H^+]^2} + K^{IV}\frac{Q_{1,3}}{[H^+]^3} + K^V\frac{Q_{1,4}}{[H^+]^4} + \\ + K^{VI}\frac{Q_{2,2}C_M\beta_{Al}}{[H^+]^2} + K^{VII}\frac{Q_{3,4}C_M^2\beta_{Al}^2}{[H^+]^4} + K^{VIII}\frac{Q_{13,32}C_M^{12}\beta_{Al}^{12}}{[H^+]^{32}} \quad (3.B.6)$$

However, since the predominant species are Al^{3+} and Al_{13} in the experimental conditions, the equation can be simplified, resulting the Equation (3.B.7), which corresponds to Equation (3.8) of the text.

$$\frac{K_{app}}{\alpha_L \beta_{Al}} = K^I + K^{VIII}\frac{Q_{13,32}C_M^{12}\beta_{Al}^{12}}{[H^+]^{32}} \quad (3.B.7)$$

Chapter 4

Binding of Al(III) to Synthetic RNA. Metal-Mediated Strand Aggregation

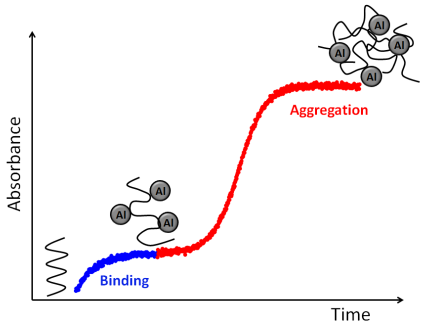

The study carried out in Chapter 3 allowed to keep aluminium ion by complexation with cacodylate anion, even at neutral pH, thus rendering feasible the study with biological molecules. Actually, over the last years, focused interest in aluminium has been heightened by recent studies regarding its health effects. The possible relation with chronic diseases makes it convenient to address more in depth the reactivity of aluminium with biologically relevant molecules. The present work investigates the interaction of aluminium ion with two synthetic RNAs, poly(rA) and poly(rU), through a detailed thermodynamic and kinetic study. The results obtained with spectrophotometry, circular dichroism, viscometry and thermal stability measurements indicate that aluminium strongly interacts with single and duplex RNA structures. The kinetic experiments point up that, even though cacodylate was required to keep the metal in solution, actually it inhibits the reaction of aluminium with RNA as it converts the metal into an unreactive dimer species. Notably, further interaction occurred under excess of aluminium/cacodylate complex, inducing aggregation of single-stranded RNAs. An analysis of the kinetic data has shown that the modes of aggregation of the two RNAs differ and such a difference can be ascribed to the diverse polynucleotide secondary structures. The observed stabilization of multiple-stranded systems by aluminium can be of interest for the use of this metal in the study of non-canonical nucleic acid structures.

4.1 Materials and Methods

4.1.1 Materials

The octahydrate perchlorate ($Al(ClO_4)_3 \cdot 8\,H_2O$, Fluka) was used as the aluminium(III) source. The stock solutions were prepared in doubly distilled water, adding $HClO_4$ acid up to pH=2.0 to avoid precipitation. The standardization of aluminium stock solutions was reported in Chapter 2 (Section 2.1.2). Sodium dimethylarsinate (NaCac, 96 %) was purchased from Carlo Erba and stock solutions were prepared in doubly distilled water; its analytical concentration is denoted as C_L.
Working solutions of the aluminium/cacodylate complex (Al/Cac) were prepared from stock solutions adding doubly distilled water, which was used as reaction medium. The ionic strength was kept at 0.1 M with sodium perchlorate monohydrate salt (Merck), while the desired pH was attained by adding calibrated amounts of NaOH and $HClO_4$.
Adenosine 5'-monophosphate monohydrate (AMP), poly-riboadenylic (poly(rA)) and poly-ribouridylic (poly(rU)) acids were purchased from Sigma as potassium salts and the relevant stock solutions were prepared by dissolving suitable amounts of the solid in water. Standardization of the RNA stock solutions was attained spectrophotometrically to $\epsilon_{257} = 10\,100\,M^{-1}cm^{-1}$ for poly(rA) and $\epsilon_{260} = 8900\,M^{-1}cm^{-1}$ for poly(rU), at $I = 0.1$ M (NaCl), pH=7.0 (NaCac) and T=25.0 °C. The analytical concentration of polynucleotides, C_P, was expressed as the concentration of the phosphate group for single-stranded forms and as the concentration of base pairs for poly(rA) when it is present as double-helix (pH=5). In fact, single stranded poly(rA) dimerizes, yielding $[poly(rA)]_2$ in relatively acidic aqueous media [1, 2].

4.1.2 Methods

The pH value was controlled by means of a Metrohm 713 (Herisau, Switzerland) pH-meter (precision ±0.1), fitted out with a combined glass electrode. Nine buffers in the 1.7-12.5 pH range were required for a proper calibration of the pH-meter required. Scattering of the solutions was evaluated using a LS55 Luminescence Spectrometer (Perkin Elmer), selecting $\lambda_{ex} = \lambda_{em} = 250$ nm and recording the absolute value of the Rayleigh scattering peak. Light scattering experiments were carried out at pH=5.0 and pH=7.0 after one day equilibration. ^{1}H-NMR, ^{31}P-NMR and ^{27}Al-NMR spectra were acquired at 25 °C with a Varian Unity Inova-400 (399.94 MHz for ^{1}H, 161.9 MHz for ^{31}P and 104.21 MHz for ^{27}Al) spectrometer. 1D ^{1}H-NMR spectra were recorded with 32 scans into 32 k data points over 16 ppm spectral width. ^{1}H chemical shifts were referenced internally to TMS using 1,4-dioxane in D_2O ($\delta = 3.75$ ppm). The NMR data were analysed with the MestReNova version 6.1.1 program. Spectrophotometric titrations and kinetic studies were carried out with a double-beam 2450-Spectrophotometer (Shimadzu). Titrations were performed adding increasing amounts of Al/Cac to a cuvette containing the polynucleotide. The kinetic study was performed by adding calibrated amounts of Al/Cac to a cuvette containing the RNA, and absorbance *versus* time curves were recorded. Kinetic experiments were carried out by changing the concentration of the Al/Cac complex, cacodylate ligand

and RNA. The initial rate method was used to estimate the reaction order with respect to each reactant. Denaturation tests were performed with the Shimadzu spectrophotometer, recording one spectral curve every 5 °C and waiting (20 min) for signal stabilization. Solutions of different metal complex-to-RNA ratios were analyzed to observe the possible destabilization/stabilization of the double or multiple-stranded structures. Circular dichroic spectra were recorded with a MOS 450 equipment (BioLogic, Science Instruments) coupled with a water thermostat (25.0 ± 0.1°C). The thermodynamic study was carried out using different solutions at different metal complex-RNA ratios, once the solutions had reached the equilibrium, in a 1 cm path-length cell. The spectra were recorded at $0.5\,\mathrm{nm\,s^{-1}}$ scan rate in the 200-400 nm range. Kinetic data were obtained by recording the time evolution of the dichroic signal at a defined wavelength. An Ubbelhode microviscometer was used to study the dependence of the viscosity of the system on the Al/Cac-RNA ratio. The temperature was kept at 25.0 °C by a water thermostat.

4.2 Results

Firstly, we characterized the aluminium/cacodylate complex, its solubility and stability at pH 5.0 and 7.0 and then we addressed the interaction of the complex with the RNAs.

4.2.1 Properties of Aluminium/Cacodylate System at pH 5.0 and 7.0

In a previous study of the Al/Cac system, we found that for 1:1 Al:Cac ratio and at pH=5.0, the Al_2Cac dimeric form is the dominant species in solution, accompanied by minor amounts of the Al_2Cac_2 dimer, whereas at pH=7.0 formation of remarkable amounts of a Al_{13} oligomer is observed [3]. In the present study, further tests were carried out aimed to individuate optimal species distribution and concentration.

At pH=5.0 no light scattering of aluminium/cacodylate solutions was detected for all the investigated values of the cacodylate concentration, C_L (Fig. 4.S1A, Supporting Information); this finding indicates that neither precipitation nor reactant aggregation occurred. At pH=7.0, however, light scattering was observed (Fig. 4.S1B); the higher the cacodylate concentration, the lower the light dispersion, until the scattering disappeared for $\frac{C_L}{C_{Al}} = 5$.

The ^{1}H-NMR study performed at pH=7.0 agrees with the light scattering measurements. Actually, the signals of the aluminium/cacodylate complexes increased with the concentration of cacodylate (Fig. 4.S2A, Supporting Information). The largest peaks in the 1H-NMR spectra displayed the same chemical shift as the ones found for the aluminium/cacodylate dimeric forms at pH=5.0 [3], hence, we assumed that the main aluminium-containing species, at pH=7.0, in the presence of an excess of cacodylate, are dimeric in nature. Therefore, it follows that an excess of cacodylate promotes disaggregation of the Al_{13} oligomer, forming simpler species. Similar behaviour has been observed for other oxygen functionalized ligands [4]. The extent of complex formation reached a plateau at (roughly) $\frac{C_L}{C_{Al}} = 5.0$, in agreement with the light scattering experiments (see Fig. 4.S2B, Supporting Information).

Based on the above results, the $\frac{C_L}{C_{Al}} = 5.0$ ratio was kept for all experiments in the presence of mono and polynucleotides to maintain the same experimental conditions. This ratio was increased only for the kinetic experiments where C_L was varied. It is reasonable to assume that, under conditions of excess of cacodylate, the concentration of Al_2Cac_2 (M_2L_2) will be higher compared to the conditions of the previous work, where $\frac{C_L}{C_{Al}} = 1.0$. Actually, the kinetic study (described below) has provided evidence for the presence of remarkable amounts of the above dimer. From now on, the analytical concentration of the Al/Cac complex will be denoted as C_{AlCac}.

4.2.2 Binding of Al/Cac to Riboadenosine Monophosphate (AMP)

^{1}H, ^{31}P and ^{27}Al-NMR spectra were recorded for the Al/Cac-AMP system (1:1) at pH 5.0 and 7.0. At pH=5.0 the Al/Cac-AMP system partially precipitated, whereas at pH=7.0 it remained in solution (Fig. 4.S3, Supporting Information). Regarding ^{31}P-NMR spectra, at pH=5.0 the peak of AMP shifted by addition of Al/Cac (Fig. 4.S4A, Supporting Information), suggesting an interaction with the phosphate group. At pH=7.0 no significant variation in chemical shift was observed (Fig. 4.S4B); however, for both pH values, a decrease in the phosphorous band width was noticeable. Little chemical shift variation was observed for the ^{1}H peaks of the adenine (Fig. 4.S4C,D). Moreover, the small shift of the methylene groups adjacent to the phosphorous site (δ = 3.97 ppm at pH=7.0) could suggest interaction with the phosphate group (Fig. 4.S4D). The ^{27}Al-NMR spectra showed a broad peak around 50 ppm for both pH values, advancing a similar structure for the aluminium system (Fig. 4.S4E) and significant shift of the peak respect to the ^{27}Al-NMR spectra of Al/Cac (δ = 7.5 ppm) [3] and a broad peak around 50 ppm for both pH values, suggesting that the structure of the Al/Cac-AMP system is only scarcely affected by pH (Fig. 4.S4E).
Kinetic experiments, carried out under excess of Al/Cac, showed a hypochromic effect of the adenosine band, agreeing with an interaction of Al/Cac with AMP (Fig. 4.S5, Supporting Information).

4.2.3 Binding of Al/Cac to Poly(rA) and Poly(rU)

4.2.3.1 UV Absorption Titrations

Sample spectra for increasing $\frac{C_{AlCac}}{C_P}$ ratios were recorded at pH=5.0 and 7.0, under equilibrium conditions. The behaviour of the systems was complex and the titration curves were biphasic.
Concerning the Al/Cac-$[poly(rA)]_2$ system at pH=5.0, an initial small (but well defined and reproducible) absorbance increase was observed, followed by a decrease in the signal for higher Al/Cac levels, which can be related to formation of a second adduct (Fig. 4.1A). On the other hand, the titration curve of the Al/Cac-poly(rU) system exhibited only a decrease in absorbance (Fig. 4.1B).

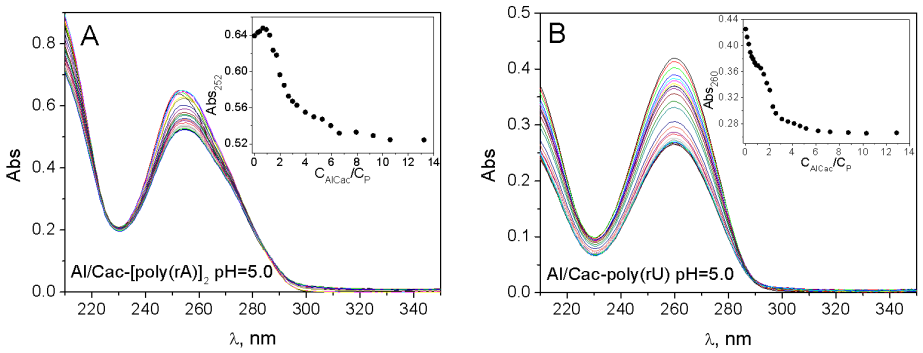

Figure 4.1: Spectrophotometric titrations at pH=5.0. (A) Al/Cac-$[poly(rA)]_2$, C_P=3.8×10^{-5} M; inset: track at 252 nm. (B) Al/Cac-poly(rU), C_P=4.8×10^{-5} M; inset: track at 260 nm. I=0.1 M ($NaClO_4$) and T=25.0 °C.

Concerning the Al/Cac-poly(rA) single stranded system at pH 7.0, the interaction was even more complex. Actually, an initial hyperchromic effect was present and, under excess of Al/Cac, baseline increase and change of the spectrum shape were observed (Fig. 4.2A). The second effect is ascribed to light scattering and most likely it reflects an aggregation of the strands. Fig. 4.S6 in Supporting Information compares the tracks at the maximum of absorbance (257 and 260 nm for poly(rA) and poly(rU), respectively) and at 320 nm, showing a decrease in the absorbance maximum together with baseline enhancement.
On the other hand, the titration of poly(rU) with Al/Cac brought about signal lowering for low $\frac{C_{AlCac}}{C_P}$ values, and light scattering for high $\frac{C_{AlCac}}{C_P}$ ratio, also interpreted as due to aggregation (Fig. 4.2B).

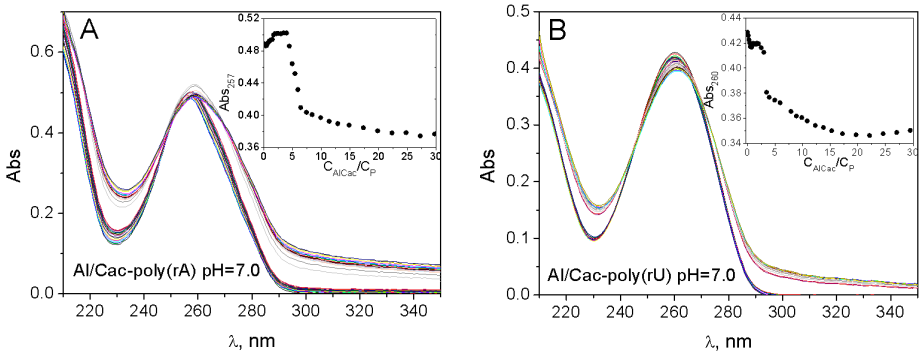

Figure 4.2: Spectrophotometric titrations at pH=7.0. (A) Al/Cac-poly(rA), C_P=5.0×10^{-5} M; inset: track at 257 nm. (B) Al/Cac-poly(rU), C_P=5.0×10^{-5} M; inset: track at 260 nm, the scattering value was subtracted from the maximum absorbance. I=0.1 M ($NaClO_4$), and T=25.0 °C.

4.2.3.2 Circular Dichroism

Al/Cac greatly affected the circular dichroism of poly(rA). At pH=5.0 the dependence of $[\Theta]$ on C_{AlCac} for the Al/Cac-$[poly(rA)]_2$ system, exhibits three

different trends (Fig. 4.3A, inset): (i) for $\frac{C_{AlCac}}{C_P} < 1.0$ a small decrease in the dichroic peak occurred. (ii) In the $1.0 < \frac{C_{AlCac}}{C_P} < 10$ range, the signal displays a sharp fall, indicating precipitation of the Al/Cac-polynucleotide system. (iii) For $\frac{C_{AlCac}}{C_P} > 10$ the Al/Cac-polynucleotide system remains in solution. Note that precipitation was observed at pH 5, also for the Al/Cac-AMP system (Fig. 4.S3, Supporting Information).

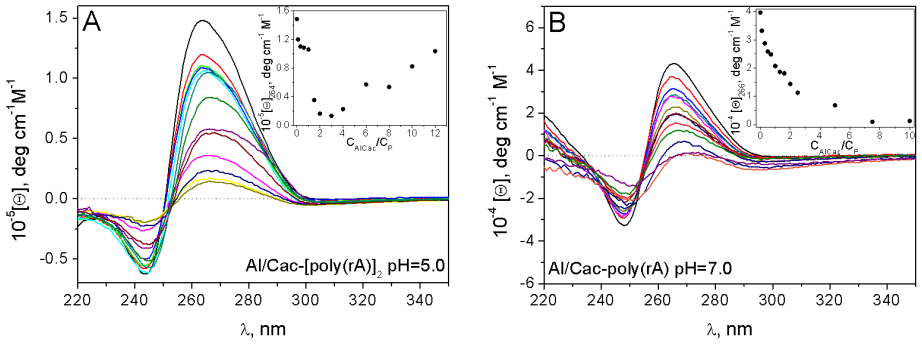

Figure 4.3: CD spectra at increasing $\frac{C_{AlCac}}{C_P}$ ratios. (A) Al/Cac-$[poly(rA)]_2$ at pH=5.0; inset: track at 264 nm. (B) Al/Cac-poly(rA) at pH=7.0; inset: track at 266 nm. C_P=5.0×10^{-5} M, I=0.1 M ($NaClO_4$) and T=25.0 °C.

At pH=7.0, addition of Al/Cac to poly(rA) caused a significant decrease in the CD signals (Fig. 4.3B). The further decrease of the band together with the shift of the minimum (from 248 to 251 nm) and maximum (from 266 to 269 nm) in Al/Cac excess should be ascribed to the aggregation effect observed in the UV experiments (Fig. 4.2A), also in agreement with the CD kinetic experiments described below.
The dichroic signal of poly(rU) is less intense because of its random coil structure [5]; however, further lowering of the signal intensity was found to occur for the Al/Cac-poly(rU) system under both pH conditions (Fig. 4.S7, Supporting Information).

4.2.3.3 Thermal Stability

Thermal denaturation experiments provided valuable information about the effect caused on the polynucleotide stability by addition of Al/Cac.
At pH=5.0, the hyperchromic effect observed for the Al/Cac-$[poly(rA)]_2$ system for small $\frac{C_{AlCac}}{C_P}$ ratio ($\frac{C_{AlCac}}{C_P} < 1$) has been interpreted as due to conversion of the double- to single-stranded poly(rA) (Fig. 4.4A). The presence of Al/Cac caused a reduction in the slope of the melting curve. No melting temperature values could be obtained because the absorbance did not reach a plateau.

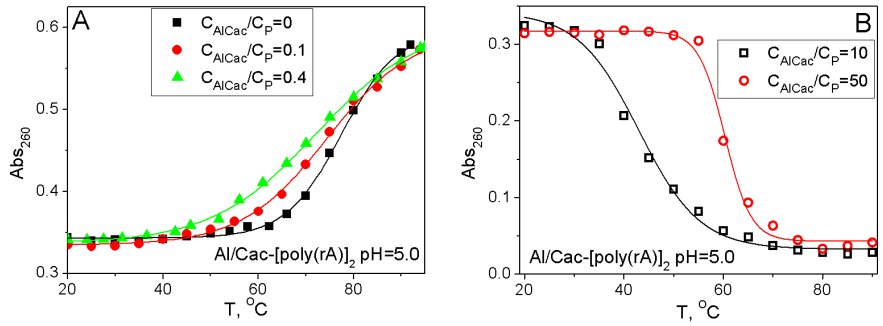

Figure 4.4: Denaturation of $[poly(rA)]_2$ in defect (A) and excess (B) of Al/Cac. C_P=2.5 × 10^{-5} M, I=0.1 M ($NaClO_4$) and pH=5.0.

By contrast, the presence of an excess of Al/Cac, results in hypochromic effect (Fig. 4.4B) and increase of the melting temperature as the $\frac{C_{AlCac}}{C_P}$ ratio is increased. The latter observation agrees with the analysis of the CD spectra, which suggested the formation of a further adduct whose stability is enhanced by increasing the $\frac{C_{AlCac}}{C_P}$ ratio. Temperature increase resulted in reduction of the association extent.
Fig. 4.5 shows the denaturation of the Al/Cac-poly(rA) system at pH=7.0.

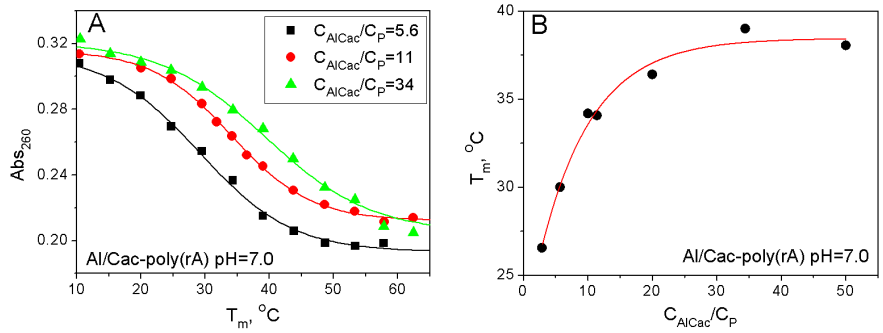

Figure 4.5: Denaturation of the aggregated forms of Al/Cac-poly(rA). (A) Examples of melting curves. (B) Track of T_m at different $\frac{C_{AlCac}}{C_P}$ ratios. C_P=3.4 × 10^{-5} M, I=0.1 M ($NaClO_4$) and pH=7.0.

Since the absorbance value was the sum of the system absorption and the scattering of the solution caused by aggregation, the value of the latter was subtracted. The result was a sigmoidal hypochromic trend, ascribable to breakage of the aggregated form [6] (Fig. 4.5A for Al/Cac-poly(rA) and Fig. 4.S8A, Supporting Information, for Al/Cac-poly(rU)). Rising the metal concentration, the melting temperature increased up to a plateau (Fig. 4.5B for Al/Cac-poly(rA) and Fig. 4.S8B for Al/Cac-poly(rU)).

4.2.3.4 Viscometry

The viscosity values decreased for all the investigated systems upon increasing the aluminium/cacodylate complex content (Fig. 4.6). Precipitation of double-

stranded $[poly(rA)]_2$ occurred at $\frac{C_{AlCac}}{C_P} = 1.0$ ratio. The large viscosity variation observed for poly(rA) and poly(rU) implies major structural changes.

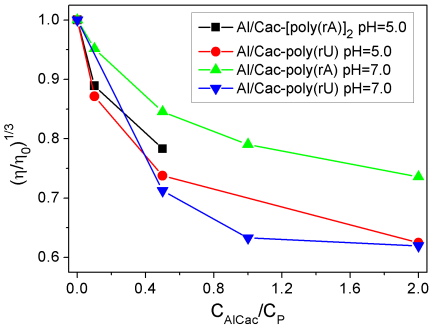

Figure 4.6: Viscometric results for Al/Cac-RNA systems at different $\frac{C_{AlCac}}{C_P}$. C_P=2.0 × 10^{-4} M, I=0.1 M ($NaClO_4$) and T=25.0 °C.

4.2.3.5 Kinetics: Al/Cac-RNA Complex Formation.

The kinetic aspects of the reactions between Al/Cac and the RNAs were investigated by recording the variation of absorbance with time. Figure 4.7 shows examples of the obtained kinetic curves.

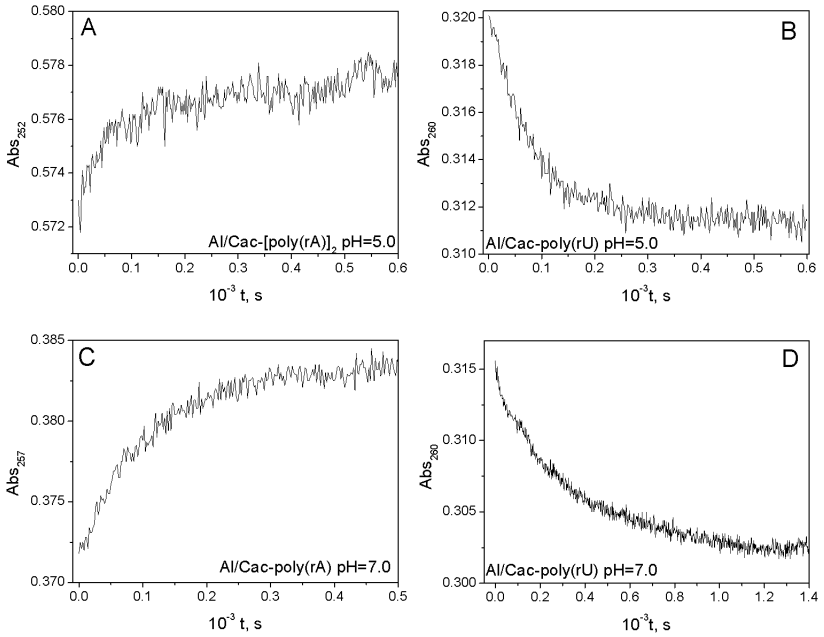

Figure 4.7: Kinetics traces for the interaction between Al/Cac and RNA: (A) $[poly(rA)]_2$ at pH=5.0, track at 252 nm. (B) poly(rU) at pH=5.0, track at 260 nm. (C) poly(rA) at pH=7.0, track at 257 nm. (D) poly(rU) at pH=7.0, track at 260 nm. C_P=3.4 × 10^{-5} M, C_{AlCac}=4.1 × 10^{-4} M, I=0.1 M ($NaClO_4$) and T=25.0 °C.

A hyperchromic signal was visible for poly(rA) (Fig. 4.7A and 4.7C), whereas for poly(rU) a hypochromic effect (Fig. 4.7B and 4.7D) was observed under both pH conditions.
The reaction order with respect to each reactant was derived from the slope of dilogarithmic plots of the initial rate v_i *versus* molar concentration C_i of the *i-th* reactant by means of Equation (4.1), k' being a constant.

$$Logv_i = nLogC + Logk' \tag{4.1}$$

The individual reaction orders are listed in Table 4.1 (see Supporting Information, Figs. 4.S9-4.S12, for details). For the experiments at variable concentration of aluminium, the concentration of cacodylate also had to be varied to maintain $\frac{C_L}{C_{Al}} = 5.0$. Thus, the sum of the individual reaction orders with respect to metal-containing species and free cacodylate (n_{AlCac} and n_L), was obtained. Being n_L known, the value of n_{AlCac} could be obtained straightforwardly.

Table 4.1: *Reaction orders n_i of the reactants for the reaction between Al/Cac and RNA. I=0.1 M, and T=25.0 °C.*

RNA	n_{AlCac}	n_L	n_P
[poly(rA)]$_2$ pH=5.0	1.2	-1.2	0.9
poly(rU) pH=5.0	1.0	-2.0	1.0
poly(rA) pH=7.0	2.0	-2.0	1.0
poly(rU) pH=7.0	2.1	-2.1	1.0

M_2L_2 dissociation is reported in Reactions (4.2) and (4.3), where K_2 and K_1 are the apparent formation constants of the aluminium/cacodylate complex at pH=5.0. Note that Reaction (4.3) involves the formation of two Al(III) ions instead of M_2 because free dimeric aluminium was negligible under the working conditions [7]. On the other hand, the formation of M_2L was observed in our previous work [3].

$$M_2L_2 \overset{1/K_2}{\rightleftharpoons} M_2L + L \tag{4.2}$$

$$M_2L \overset{1/K_1}{\rightleftharpoons} 2\,M + L \tag{4.3}$$

Concerning Al/Cac-poly(rU) at pH=5.0, the reaction orders concur with a model (Equation (4.4)) where two molecules of cacodylate are released upon interaction of the metal complex with the monomeric unit of RNA (see mechanism in Appendix 4.A, Supporting Information). In Equation (4.4), k_1 is the forward kinetic constant for the metal-RNA complex formation.

$$2\,M + P \xrightarrow{k_1} \text{products} \tag{4.4}$$

According to this model the initial rate v_i is given by Equation (4.5).

$$v_i = \frac{k_1}{2K_1K_2}\frac{C_{AlCac}C_P}{C_L^2} \tag{4.5}$$

Two monomeric aluminium ions, from Reaction (4.3), would interact with the polymer, whereas the M_2L and M_2L_2 species do not react directly. The kinetic parameters of the reaction were evaluated from the intercept of the dilogarithmic plots. The values for k_1 obtained from the initial rates of each graph are in good agreement with each other (Table 4.S1, Supporting Information, $\frac{k_1}{2K_1K_2}$=$(7.6 \pm 0.6) \times 10^{-5}\mathrm{s}^{-1}\,\mathrm{M}^2$, Confidence 95 %), reinforcing the goodness of our hypothesis. For the Al/Cac-poly(rA) and Al/Cac-poly(rU) systems at pH=7.0 the partial reaction orders are quite similar, suggesting a similar kinetic mechanism. However, these are significantly different respect to the above cited mechanism found for poly(rU) at pH=5.0. At pH=7.0 the reaction mechanism for both RNAs should involve two M_2L complexes originated from Reaction (4.2) (Appendix 4.B, Supporting Information); under these circumstances the reaction is expressed by Equation (4.6) and the rate law by Equation (4.7) ($\frac{k_2}{4K_2'^2}$=$0.24 \pm 0.10\mathrm{s}^{-1}\,\mathrm{M}^2$ for Al/Cac-poly(rA) and $\frac{k_2'}{4K_2'^2}$=$0.12 \pm 0.01\mathrm{s}^{-1}\,\mathrm{M}^2$ for Al/Cac-poly(rU), where K_2' refers to Reaction (4.2) at pH=7.0 and k_2' to poly(rU)).

$$2\,M_2L + P \xrightarrow{k_2} \text{products} \tag{4.6}$$

$$v_i = \frac{k_2}{4K_2'^2}\frac{C_{AlCac}^2 C_P}{C_L^2} \tag{4.7}$$

To conclude, concerning $[\text{poly(rA)}]_2$ at pH=5.0, the reaction mechanism is given by Equation (4.8) and the relevant initial rate is expressed by Equation (4.9) ($\frac{k_3}{2K_2}$=$(5.0 \pm 0.5) \times 10^{-2}\mathrm{s}^{-1}\mathrm{M}$, Appendix 4.C, Supporting Information). The change of the order of reaction with respect to the ligand implies a change in the reaction mechanism: here, instead of two free Al(III) ions, one molecule of M_2L interacts with a polynucleotide base pair.

$$M_2L + P \xrightarrow{k_3} \text{products} \tag{4.8}$$

$$v_i = \frac{k_3}{2K_2}\frac{C_{AlCac} C_P}{C_L} \tag{4.9}$$

4.2.3.6 Kinetics: Aggregation Reaction

In addition to the effect discussed above, a further kinetic effect was displayed at pH=7.0 by the investigated systems (Fig. 4.8). Actually, an increase in the signal was detected, which is ascribable to the previously observed aggregation effect (Fig. 4.2). Comparison of the kinetic curves recorded at the maximum of absorption of the polynucleotides and at $\lambda = 320\,\mathrm{nm}$, where any RNA absorption is absent, revealed hyperchromic effects in both kinetic curves (Fig. 4.8A). Consequently, the second absorbance enhancement was related to aggregation of the polynucleotides chains, which reflected in an increase of the light scattering process.

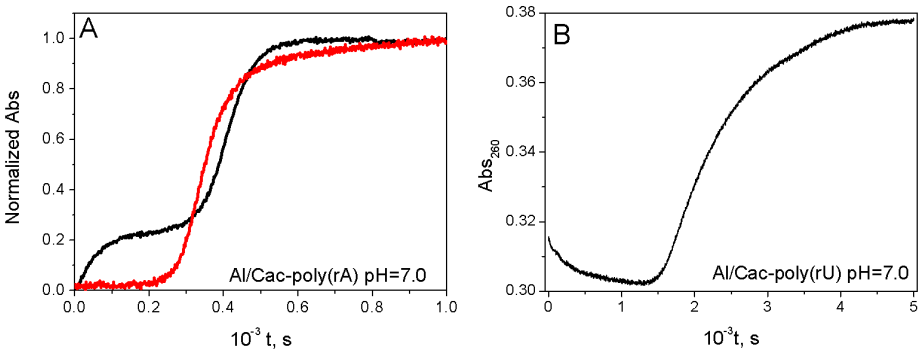

Figure 4.8: Kinetic traces of the reaction between Al/Cac and RNA and subsequent aggregation process. (A) Comparison of the normalized kinetic curves at 257 (black line) and 320 nm (red line) for Al/Cac-poly(rA); (B) Al/Cac-poly(rU), track at 260 nm. C_P=3.4 × 10^{-5} M, C_{AlCac}=4.1 × 10^{-4} M, I=0.1 M ($NaClO_4$), pH=7.0 and T=25.0 °C.

The same effect was clearly visible for the CD signals. In this case, the aggregation caused a signal decrease with time (Fig. 4.9).

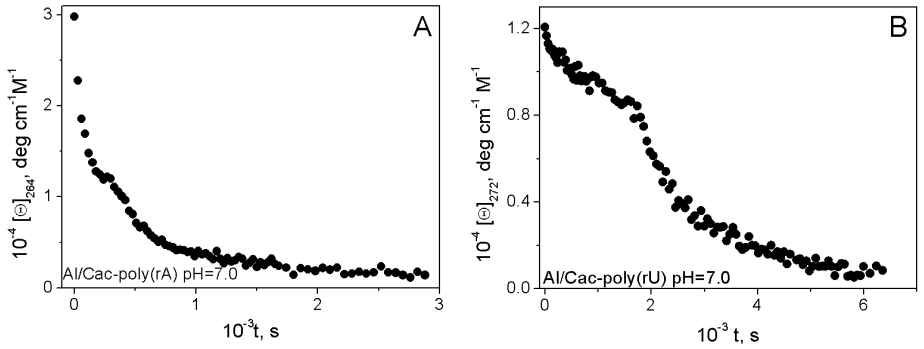

Figure 4.9: Kinetics of the dichroic signal under Al/Cac excess. (A) Al/Cac-poly(rA), track at 264 nm. (B) Al/Cac-poly(rU), track at 272 nm. C_P=5.0 × 10^{-5} M, C_{AlCac}=7.5 × 10^{-4} M, I=0.1 M ($NaClO_4$), pH=7.0 and T=25.0 °C.

The slow kinetic curves were acquired for different concentration of Al/Cac, free ligand and RNA. Figure 4.10 shows some sets of kinetic curves concerning the Al/Cac-poly(rA) system, recorded at 257 nm. From Figures 4.10A-C it was possible to obtain a qualitative trend about the contribution of each reactant to the aggregation effect. By increasing the amount of Al/Cac, the aggregation was faster (Fig. 4.10A), whereas free cacodylate and RNA concentration slowed down the reaction rate (Fig. 4.10B, C).

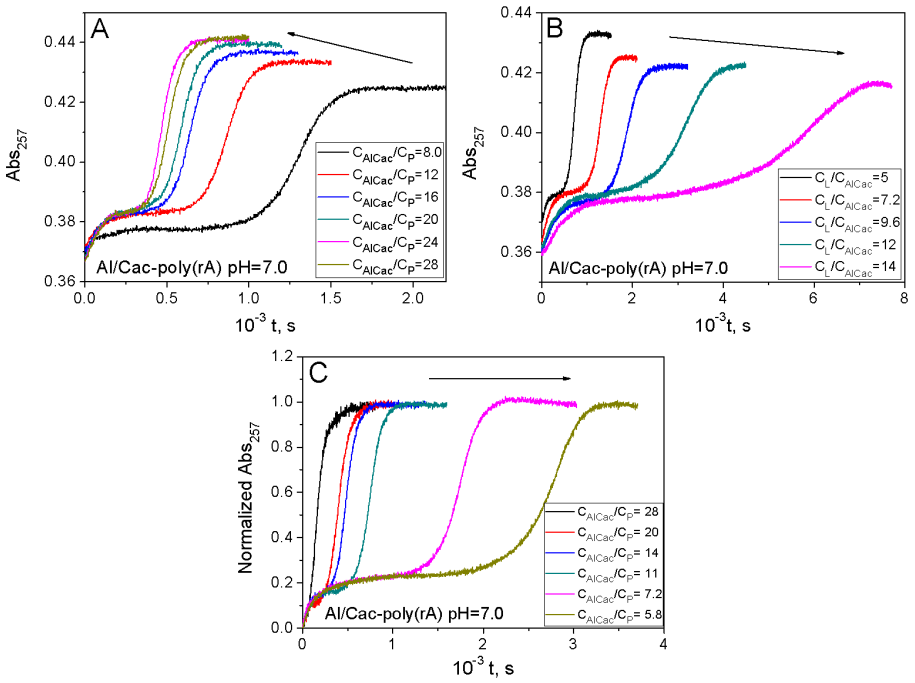

Figure 4.10: Kinetic curves at λ=257 nm of Al/Cac-poly(rA); (A) different C_{AlCac}, C_P=3.4 $\times$ 10^{-5} M; (B) different C_L, C_P=3.4 $\times$ 10^{-5} M (C) different C_P (normalized absorbance values), C_{AlCac}=4.1 $\times$ 10^{-4} M. I=0.1 M ($NaClO_4$), pH=7.0 and T=25.0 °C.

The aggregation kinetics were analysed using Equation (4.10) [8–10]:

$$Abs = A(1 - e^{Bt^m}) \tag{4.10}$$

where A is the curve amplitude, B the time constant and m the parameter that reflects the cooperativity of the aggregation process. From Equation (4.10) the $t_{\frac{1}{2}}$ parameter could be calculated as $t_{\frac{1}{2}} = (ln2/B)^{\frac{1}{m}}$ [11]. Note that the start of the sigmoid curve (t_0) was taken at the end of the first kinetic effect, subtracting the t_0 value from t_{read}, being $t = t_{read} - t_0$ in Equation (4.10). The analysis of the sigmoid curve was carried out at different concentrations of the metal complex and polynucleotide and the results are reported in Table 4.S2 and 4.S3, Supporting Information.

Concerning poly(rA), it was seen that the amplitude was enhanced by increasing C_{AlCac} and C_P, whereas $t_{\frac{1}{2}}$ decreased with Al/Cac concentration (Fig. 4.10A) but it increased with C_P (Fig. 4.10C). At first sight, these results could suggest (wrongly) that the addition of RNA reduces the reaction rate. However, an increase in C_P causes lowering of the $\frac{C_{AlCac}}{C_P}$ ratio, which affects the aggregation. On the other hand, the parameter m seems to depend on the RNA concentration (m increased with C_P up to $m = 4$), but not on the Al/Cac concentration (Table 4.S2 ESI). Al/Cac-poly(rU) behaves similarly as the amplitude and $t_{\frac{1}{2}}$ trends (Table 4.S3). However, the m value did not rise with C_{AlCac} and C_P, being confined between 1.5 and 2.

4.3 Discussion

The affinity of aluminium with AMP and ATP is reported in the literature to be stronger compared to other metal ions [12]. Although interaction of aluminium with adenine group has been reported, the interaction with phosphate group seems to be preferred [13, 14]. The preliminary study of the Al/Cac-AMP by ^{1}H and ^{31}P-NMR would confirm that, under equimolar conditions ($\frac{C_{AlCac}}{C_P} = 1$), the interaction involves the phosphate group.
However, the study with single-stranded nucleic acids reveals alterations to the secondary structure that can hardly be related only to interaction with the phosphate, which generally induces small modifications. Actually, the study of the binding of Al/Cac to polynucleotides, using different techniques, has revealed the occurrence of changes in the nature of the interaction depending on the amount of aluminium present in the reaction medium.
Concerning single-stranded poly(rA) at pH=7.0, the initial hyperchromic effect displayed by the absorbance measurements (Fig. 4.2A) and the strong decrease in the dichroic maximum (Fig. 4.3B) suggest involvement of nitrogen containing base to the coordination process. Actually, the results obtained here concur with the transition from the ordered poly(rA) structure to a random coil one; the unwinding of the single helix agrees with interaction of the metal with the adenine, promoting unstacking of the bases [15]. In addition, unwinding of the partially ordered poly(rA) structure leads to a viscosity decrease [16], as observed in the presence of Al/Cac (Fig. 4.6). Hence, from the NMR data and the results obtained from the various techniques employed, one can conclude that two different coordination sites are available for the Al/Cac complex: the phosphate group and the nitrogenous base. A dual mode of binding has been advanced for other trivalent cations like Terbium(III) [17]. The results shown in Fig. 4.2 reveal that, under excess of Al/Cac, strand aggregation occurs. Poly(rA) aggregation induced by Mg^{2+} was spectrophotometrically detected also by Kankia [18], an effect that causes the baseline to increase and a hypochromic effect, as well. The observation that the same effect is induced by Al/Cac both in poly(rA) and poly(rU) implies that the aggregation is not promoted by a particular base pair, but rather it starts up when an adequate excess of metal (or metal complex) is present at the appropriate concentration level ($\frac{C_{AlCac}}{C_P}$ about 4.0 for both systems). Moreover, the thermal experiments performed in the present study have shown that relatively large levels of complex do stabilize the aggregate solutions (Fig. 4.5 and Fig. 4.S8, Supporting Information).
It should be noted that aggregation effects are promoted by aluminium in several proteins [19]. For instance, a deal of interest has been addressed to aggregation of the β-amyloid proteins, which is observed in relation to Alzheimer's disease, for the in vitro formation of plaques [20]. Hence, our results point up that such behaviour is not only exclusive to proteins, but also nucleic acids can undergo aggregation in the presence of aluminium. Such a discovery can be of interest to the effects of aluminium with other biologically relevant macromolecules.
On the other hand, at pH=5.0, the behaviour of $[poly(rA)]_2$ is different. For $\frac{C_{AlCac}}{C_P} < 1$, the small variation in the circular dichroism (Fig. 4.3A) could suggest an interaction with the phosphate group, in agreement with the NMR results obtained for Al/Cac-AMP. The broadening of the sigmoid curve observed in thermal denaturation concurs with the presence of unbound $[poly(rA)]_2$ and bound Al/Cac-$[poly(rA)]_2$ systems, ensuing the overlapping of the sigmoidal tracks, to

give a final broad curve (Fig. 4.4A). Broad sigmoid curves are observed for DNA in the presence of aluminium, as well, and an analogue explanation has been proposed [21]. Destabilization of the $[\text{poly(rA)}]_2$ double-helix is verified for many metal ions (even though a strong stabilization effect has recently been reported due to ammonium ion [22]). As the double-helix is stabilized by hydrogen bonds involving the phosphate and the base nitrogen, the interaction of the metal with these coordination sites promotes the transition to single-stranded RNA [15].
The precipitation of the Al/Cac-$[\text{poly(rA)}]_2$ system at higher aluminium concentration observed by viscometry (Fig. 4.6) and circular dichroism (Fig. 4.3A) concurs with neutralization of the negative charge of phosphate group, which reduces the solubility of the system. However, a further excess of aluminium renders the system soluble again, probably because of electrostatic interaction on the poly surface that promotes solubilization of the systems. The sigmoidal track obtained in the thermal denaturation experiments (Fig. 4.4B) would suggest association between the double-strands, forming a positively charged aggregated. Heating of the solution causes breakage of such a linkage; the larger the aluminium concentration, the more stable becomes the strand association.
Concerning poly(rU), the high variation of viscosity shown in Fig. 4.6 is to be ascribed to formation of a more ordered and compact form, also in agreement with the observed decrease in the system absorbance (Fig. 4.1B and 4.2B). Viscosity decrease is reported for poly(rU) with temperature decrease and in the presence of various salts, which are accounted to provoke folding of the single-strand to form intramolecular double-helix [23, 24]. A similar behaviour could be tought for the Al/Cac-poly(rU) system, as well. Interestingly, the aggregation effect occurs only at pH 7.0, suggesting that the mechanism of action of the Al/Cac complex changes by changing the pH of the medium.
Regarding the kinetic study, the negative reaction order with respect to cacodylate ($n_L = -2$) at both pH 5.0 and 7.0 indicates that, under the experimental conditions employed, the main species present in solution is the M_2L_2 dimer, which does not react directly with the polynucleotides. However, the data analyses indicate that the dimer dissociates partially to give simpler species able to interact directly with the RNAs. At pH=5.0 the reacting species is Al^{3+} (and/or $AlOH^{2+}$), whereas at pH=7.0 the reacting species is M_2L. This behaviour is explained by the fact that at pH=5.0 the cacodylate anion is more than 90 % protonated ($pK_A = 6.2$ [3]) and, under these circumstances, the ligand dissociation from the metal coordination shell is favoured.
Concerning the Al/Cac-poly(rA) system at neutral pH, thermodynamic data suggest interaction with phosphate and nitrogen containing bases, agreeing with a kinetic model involving reaction of two M_2L molecules. On the other hand, the mechanism derived for the Al/Cac-$[\text{poly(rA)}]_2$ system involves only one M_2L molecule. Note that adenine is partially protonated at pH=5.0 and it could inhibit the attack of a second molecule of M_2L to the double strand. The features of the Al/Cac-AMP ^{31}P-NMR spectrum at pH=5.0 (Fig. 4.S4A, Supporting Information) suggest that the interaction of Al/Cac with the phosphate of AMP plays the main role in the binding process and this could apply to $[\text{poly(rA)}]_2$ as well. A similar result has been reported also for Terbium, whose interaction with the guanine moiety of poly(dG) is inhibited by protonation of N_7 ($pH \leq 2$, $I = 0.02\,\text{M}$) [17].
The kinetics of the aggregation process were analysed using the Avrami equation, which has been successfully applied to polymeric systems [11]. The observed

differences in the values of the reaction parameters show that differences are present in the aggregation mechanism of the two RNAs. In particular, the difference in the m parameter means that, although the aluminium ion plays a chief role in both RNAs, the mechanisms of the aggregation processes follow different pathways, which depend on the structures of the two nucleic acids. Our results agree with a picture where the more ordered poly(rA) is able to develop an aggregation mechanism characterized by a higher degree of cooperativity and efficiency, as shown by the higher m and lower $t_{\frac{1}{2}}$ values.

4.4 Conclusion

Aluminium strongly binds to single-stranded poly(rA) and poly(rU) in acidic and neutral pH, interacting with the phosphate and the base nitrogen groups, thus inducing a notable alteration of the polynucleotides secondary structure. However, the interaction with phosphate seems to prevail in the case of double-stranded $[\text{poly(rA)}]_2$. Kinetic studies indicate that cacodylate inhibits the interaction of the metal with the RNAs since it converts the aluminium reactive forms into the inert dimer Al_2Cac_2 form.
A RNA aggregation process is induced by appropriate amounts of Al/Cac complex, the aggregation being more extended in the case of poly(rA). The kinetic studies confirm that the ordered poly(rA) structure undergoes aggregation at faster rate and with higher cooperativity degree than poly(rU), which displays a random coil structure. The extent of aggregation can be tuned by calibrating the level of added Al/Cac complex. Hence, the results of this investigation reveal that the Al/Cac-poly(rA) and poly(rU) systems can be used as a model for future studies, as they provide a useful tool for the study of the interaction of biomolecules with those metals which, due to hydrolysis, polymerization or poor solubility, could not be employed under physiological pH conditions. The ability of aluminium to stabilize multiple nucleic acid strands could be of interest for the study of non-conventional forms of polynucleotides. Lastly, since aluminium-promoted protein aggregation have been indicated in many chronic diseases, the finding that aluminum can promote aggregation also in nucleic acids can prompt further studies on the effects of aluminium towards other biologically relevant macromolecules.

Bibliography

[1] J. R. Fresco and P. Doty (1957). *Polynucleotides I. Molecular Properties and Configurations of Polyriboadenilic Acid in Solution*, Journal of the American Chemical Society, 79 (14), 3928-3929.

[2] T. N. Holcomb and I. Jr. Tinoco (1965). *Conformation of Polyriboadenylic Acid: pH and Temperature Dependence*, Biopolymers, 3 (2), 121-133.

[3] M. Lari, H. J. Lozano, N. Busto, T. Biver, J. M. Leal, S. Ibeas, J. A. Platts, F. Secco and B. García (2015). *Stabilization of Al(III) Solutions by Complexation with Cacodylic Acid: Speciation and Binding Features*, Physical Chemistry Chemical Physics, 17 (44), 29803-29813.

[4] A. Amirbahman, M. Gfeller and G. Furrer (2000). *Kinetics and Mechanism of Ligand-Promoted Decomposition of the Keggin Al_{13} Polymer*, Geochimica et Cosmochimica Acta, 64 (5), 911-919.

[5] K. Imahori and K. Watanabe (1970). *Circular Dichroism of Polynucleotides in Relation to Their Conformation*, in Journal of Polymer Science, C Polymer Symposia, Vol. 30, pp. 633-656, Wiley Subscription Services, Inc., A Wiley Company.

[6] T. Biver, N. Busto, B. García, J. M. Leal, L. Menichetti, F. Secco and M. Venturini (2015). *Mg(II) and Ni(II) Induce Aggregation of Poly(rA)Poly(rU) to either Tetra-Aggregate or Triplex Depending on the Metal Ion Concentration*, Journal of Inorganic Biochemistry, 151, 115-122.

[7] C. F. Baes and R. E. Mesmer (1976). *Hydrolysis of Cations*, Ch. 6, pp. 112-123, John Wiley and Sons, New York.

[8] M. Avrami (1939). *Kinetics of Phase Change. I General Theory*, The Journal of Chemical Physics, 7 (12), 1103-1112.

[9] M. Avrami (1940). *Kinetics of Phase Change. II Transformation-Time Relations for Random Distribution of Nuclei*, The Journal of Chemical Physics, 8 (2), 212-224.

[10] M. Avrami (1941). *Granulation, Phase change, and Microstructure Kinetics of Phase Change. III*, The Journal of Chemical Physics, 9 (2), 177-184.

[11] M. Kodaka (2004). *Requirements for Generating Sigmoidal Time–Course Aggregation in Nucleation-Dependent Polymerization Model*, Biophysical Chemistry, 107 (3), 243-253.

[12] T. Kiss, P. Zatta and B. Corain (1996). *Interaction of Aluminium(III) with Phosphate-Binding Sites: Biological Aspects and Implications*, Coordination Chemistry Reviews, 149, 329-346.

[13] T. Kiss, I. Sovago and R. B. Martin (1991). *Al^{3+} binding by Adenosine 5'-Phosphates: AMP, ADP, and ATP*, Inorganic Chemistry, 30 (9), 2130-2132.

[14] S. J. Karlik, G. A. Elgavish and G. L. Eichhorn (1983). *Multinuclear NMR Studies on Al(III) Complexes of ATP and Related Compounds*, Journal of the American Chemical Society, 105 (3), 602-609.

[15] Y. A. Shin, J. M. Heim and G. L. Eichhorn (1972). *Interactions of Metal Ions with Polynucleotides and Related Compounds. XX. Control of the Conformation Polyriboadenylic Acid by Divalent Metal Ions*, Bioinorganic Chemistry, 1 (2), 149-163.

[16] H. Eisenberg and G. Felsenfeld (1967). *Studies of the Temperature-Dependent Conformation and Phase Separation of Polyriboadenylic Acid Solutions at Neutral pH*, Journal of Molecular Biology, 30 (1), 17-37.

[17] D. S. Gross and H. Simpkins (1981). *Evidence for Two-Site Binding in the Terbium(III)-Nucleic Acid Interaction*, Journal of Biological Chemistry, 256 (18), 9593-9598.

[18] B. I. Kankia (2004). *Inner-Sphere Complexes of Divalent Cations with Single-Stranded Poly(rA) and Poly(rU)*, Biopolymers, 74 (3), 232-239.

[19] X. Long, C. Zhang, J. Cheng and S. Bi (2008). *A Novel Method for Study of the Aggregation of Protein Induced by Metal Ion Aluminum(III) Using Resonance Rayleigh Scattering Technique*, Spectrochimica Acta Part A: Molecular and Biomolecular Spectroscopy, 69 (1), 71-77.

[20] P. W. Mantyh, J. R. Ghilardi, S. Rogers, E. DeMaster, C. J. Allen, E. R. Stimson and J. E. Maggio (1993). *Aluminum, Iron, and Zinc Ions Promote Aggregation of Physiological Concentrations of β-Amyloid Peptide*, Journal of Neurochemistry, 61 (3), 1171-1174.

[21] S. J. Karlik and G. L. Eichhorn (1989). *Polynucleotide Cross-Linking by Aluminum*, Journal of Inorganic Biochemistry, 37 (4), 259-269.

[22] N. Safaee, A. M. Noronha, D. Rodionov, G. Kozlov, C, J. Wilds, G. M. Sheldrick and K. Gehring (2013). *Structure of the Parallel Duplex of Poly(A) RNA: Evaluation of a 50 Year-Old Prediction*, Angewandte Chemie International Edition, 52 (39), 10370-10373.

[23] M. N. Lipsett (1960). *Evidence for Helical Structure in Polyuridylic Acid*, Proceedings of the National Academy of Sciences, 46 (4), 445-446.

[24] D. Bode, M. Heinecke and U. Schernau (1973). *An IR-Investigation of the Helix-Coil Conversion of Poly U*, Biochemical and Biophysical Research Communications, 52 (4), 1234-1240.

Supporting Information

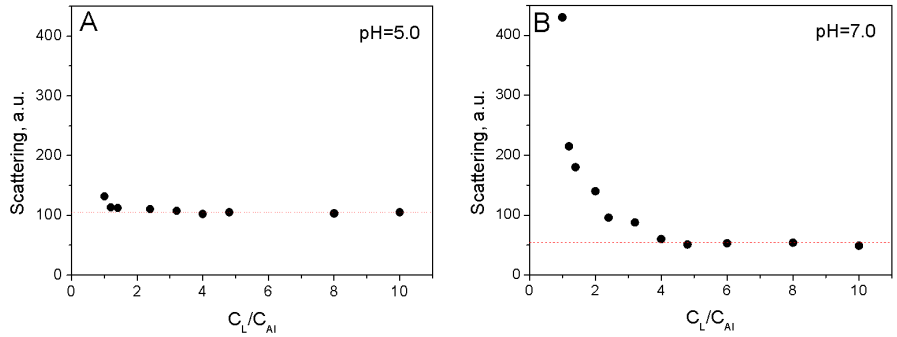

Figure 4.S1: Scattering of the aluminium/cacodylate solutions for increasing $\frac{C_L}{C_{Al}}$ ratios at (A) pH=5.0 and (B) pH=7.0. The dotted line is the solvent background. C_{Al}=2.5 × 10^{-3} M, I=0.1 M, λ_{ex}=λ_{em}=250 nm and T=25.0 °C.

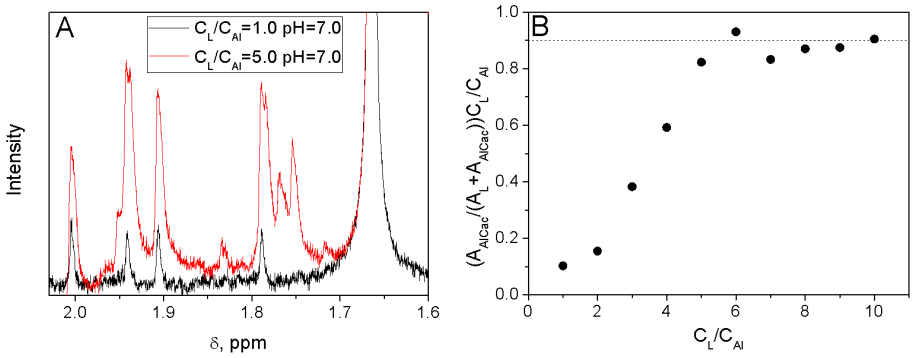

Figure 4.S2: (A) ^{1}H-NMR spectra at $\frac{C_L}{C_{Al}}$=1.0 and $\frac{C_L}{C_{Al}}$=5.0 at pH=7.0. (B) Normalized area of AlCac peaks at pH=7.0 by the equation $A_{norm} = \frac{A_{AlCac}}{A_L+A_{AlCac}} \frac{C_L}{C_{Al}}$, where A_{AlCac} is the area of the complex peaks and A_L the area of the free ligand. $\frac{A_{AlCac}}{A_L+A_{AlCac}}$ is the relative area of the bound cacodylate. Multiplication of the relative area by C_L yields the absolute concentration of the bound cacodylate and, dividing by C_{Al}, it yields the ratio between the ligand and the metal in the complex when the extent of the complex formation reaches the plateau. I=0.1 M ($NaClO_4$) and T=25.0 °C.

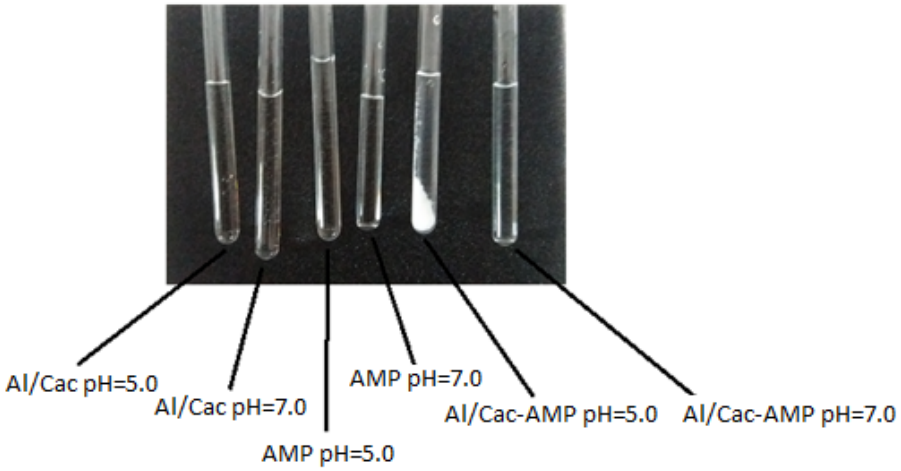

Figure 4.S3: Photo of the NMR solutions of the Al/Cac-AMP experiments. C_{AlCac}=5.0 $\times$ 10^{-3} M, C_P=5.0 $\times$ 10^{-3} M and I=0.1 M ($NaClO_4$).

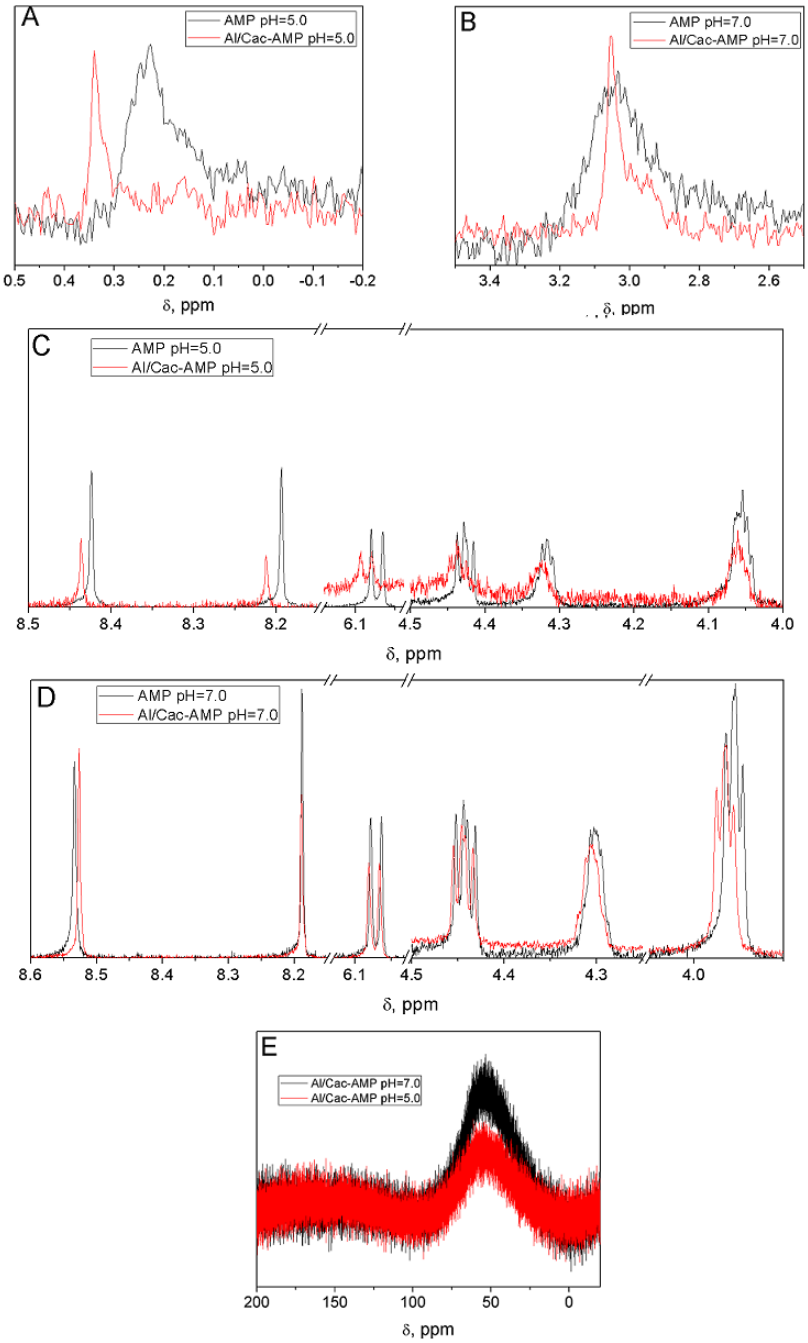

Figure 4.S4: NMR spectra of Al/Cac and AMP solutions. (A) ^{31}P-NMR of AMP and Al/Cac-AMP at pH=5.0. (B) ^{31}P-NMR of AMP and Al/Cac-AMP at pH=7.0. (C) ^{1}H-NMR of AMP and Al/Cac-AMP at pH=5.0. (D) ^{1}H-NMR of AMP and Al/Cac-AMP at pH=7.0. (E) ^{27}Al-NMR of Al/Cac-AMP at pH=7.0 and 5.0. C_{AlCac}=5.0 $\times$ 10^{-3} M, C_P=5.0 $\times$ 10^{-3} M. I=0.1 M ($NaClO_4$) and T=25.0 °C.

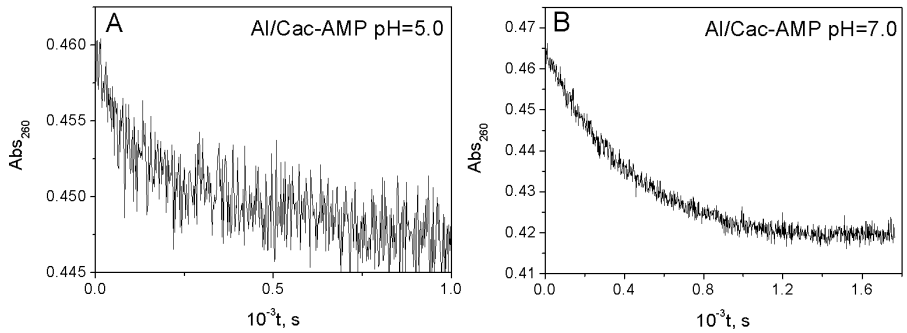

Figure 4.S5: Kinetic curve of the Al/Cac-AMP system in excess of aluminium. (A) Al/Cac-AMP at pH=5.0 (B) Al/Cac-AMP at pH=7.0. C_P=3.0 × 10^{-5} M, $\frac{C_{AlCac}}{C_P}$=10, I=0.1 M ($NaClO_4$) and T=25.0 °C.

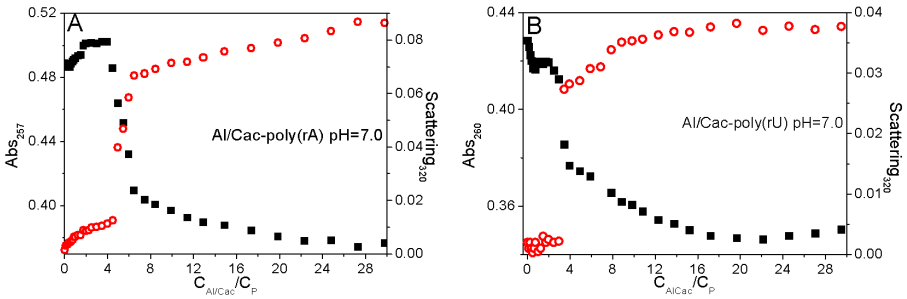

Figure 4.S6: Comparison of the track at the absorbance maximum and 320 nm for (A) Al/Cac-poly(rA) and (B) Al/Cac-poly(rU). Absorbance maximum (full square) 257 nm for poly(rA) and 260 nm for poly(rU); Scattering at 320 nm (open circle). The scattering value was subtracted from the absorbance maximum. C_P=5.0 × 10^{-5} M, I=0.1 M ($NaClO_4$), pH=7.0 and T=25.0 °C.

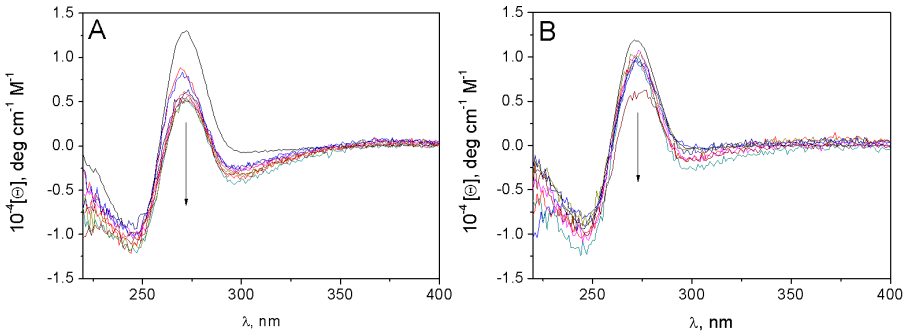

Figure 4.S7: Circular dichroism of poly(rU) for increasing concentration of Al/Cac, at (A) pH=5.0 and (B) pH=7.0. C_P=5.0 × 10^{-5} M, C_{AlCac}=0-5.0 × 10^{-4} M I=0.1 M ($NaClO_4$) and T=25.0 °C.

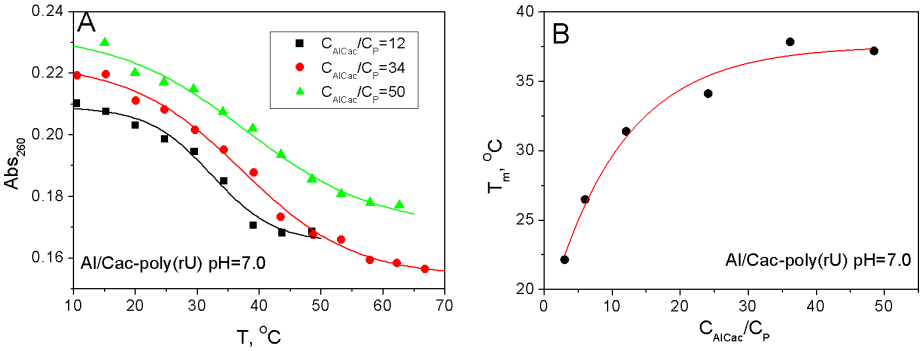

Figure 4.S8: Denaturation proofs of the aggregated forms of Al/Cac-poly(rU). (A) Examples of melting curves. (B) Track of T_m for different $\frac{C_{AlCac}}{C_P}$ ratios. C_P=3.4 × 10^{-5} M, I=0.1 M ($NaClO_4$) and pH=7.0.

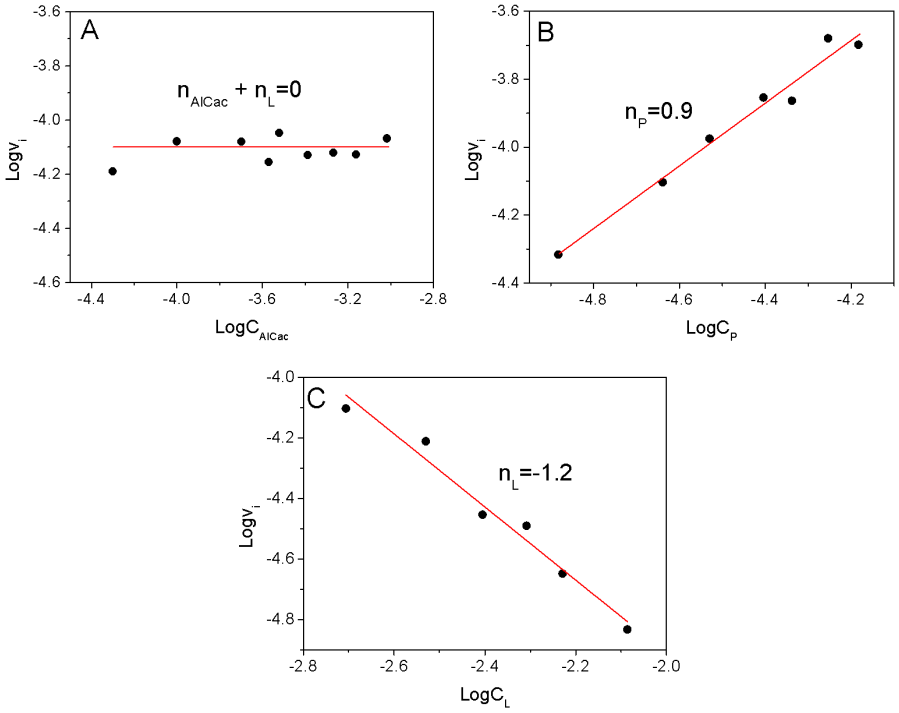

Figure 4.S9: Dilogarithmic plots of initial rates *versus* (A) C_{AlCac}, (B) C_P and (C) C_L for Al/Cac-$[poly(rA)]_2$ at pH=5.0. I=0.1 M ($NaClO_4$) and T=25.0 °C.

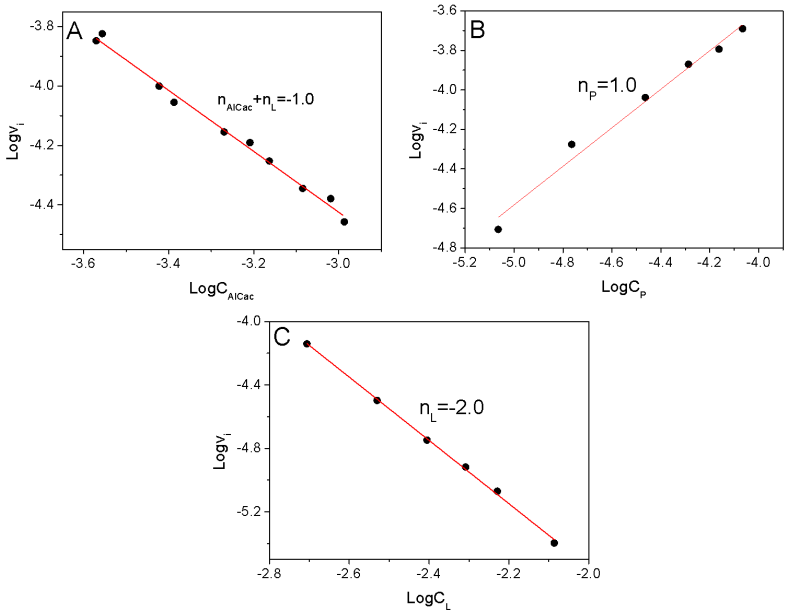

Figure 4.S10: Dilogarithmic plots of initial rates *versus* (A) C_{AlCac}, (B) C_P and (C) C_L for Al/Cac-poly(rU) at pH=5.0. I=0.1 M ($NaClO_4$) and T=25.0 °C.

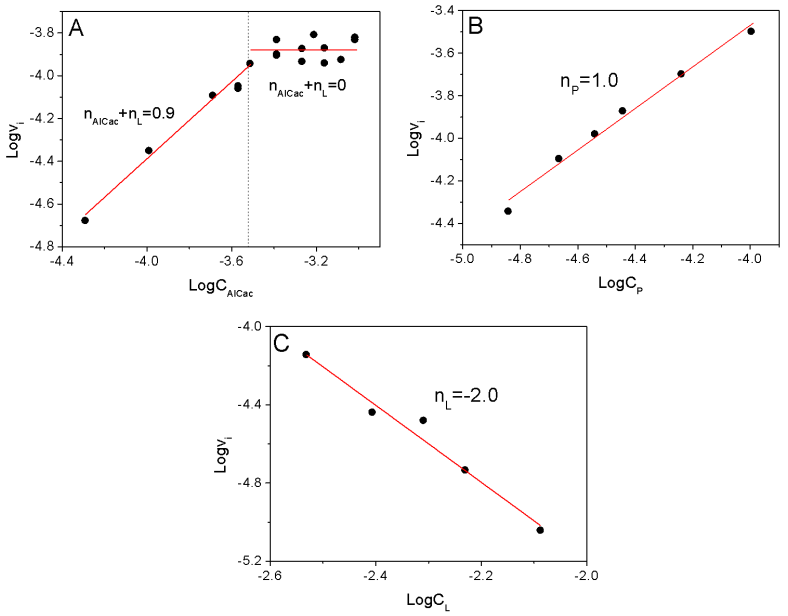

Figure 4.S11: Dilogarithmic plots of initial rates *versus* (A) C_{AlCac}, (B) C_P and (C) C_L for Al/Cac-poly(rA) at pH=7.0. I=0.1 M ($NaClO_4$) and T=25.0 °C. The change in the reaction orders at the lower Al/Cac concentration was due to formation of noticeable amounts of M_2L.

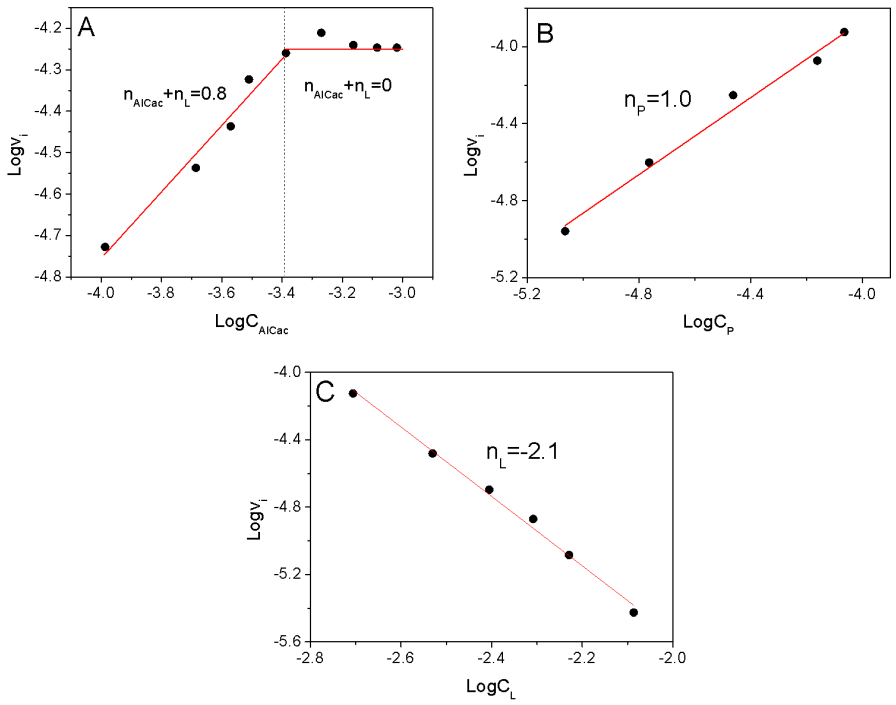

Figure 4.S12: Dilogarithmic plots of initial rates *versus* (A) C_{AlCac}, (B) C_P and (C) C_L for Al/Cac-poly(rU) at pH=7.0. I=0.1 M ($NaClO_4$) and T=25.0 °C. The change in the reaction orders at the lower Al/Cac concentration was due to formation of noticeable amounts of M_2L.

Table 4.S1: *Kinetic constants obtained from plots of the initial rate equations. I=0.1 M, and T=25.0 °C.*

Parameter	$\mathbf{[poly(rA)]_2}$ pH=5.0 $10^2\frac{k_3}{2K_2}$ $s^{-1}\,M$	**poly(rU)** pH=5.0 $10^5\frac{k_1}{2K_1K_2}$ $s^{-1}\,M^2$	**poly(rA)** pH=7.0 $10\frac{k_2}{4K_2'^2}$ $s^{-1}\,M^2$	**poly(rU)** pH=7.0 $10\frac{k_2'}{4K_2'^2}$ $s^{-1}\,M^2$
C_L	3.0	7.8	3.4	1.2
C_P	7.4	8.1	2.3	1.2
C_{AlCac}	5.0	7.6	1.7	1.0
Mean Value	5	7.6	2.4	1.1
Conf. 95 %	2.5	0.6	1.0	0.1

Table 4.S2: *Avrami parameters obtained for Al/Cac-poly(rA) aggregation. I=0.1 M, pH=7.0 and T=25.0 °C. A, is the amplitude, $t_{\frac{1}{2}}$ is the time corresponding to 50 % of aggregation process, m is the cooperativity parameter. In brackets the uncertainty in the last digit.*

$C_P = 3.4 \times 10^{-5}$ M, fixed				$C_{AlCac} = 4.1 \times 10^{-4}$ M, fixed			
$10^4 C_{AlCac}$ M	$10^2 A$	$10^{-2} t_{\frac{1}{2}}$ s	m	$10^5 C_P$ M	$10^2 A$	$10^{-2} t_{\frac{1}{2}}$ s	m
2.7	4.8(1)	6.4(5)	4.1(1)	1.1	2.2(1)	1.6(3)	2.0(1)
4.1	5.0(1)	4.6(4)	4.4(1)	1.4	2.5(1)	1.1(2)	1.7(1)
5.4	5.3(3)	3.6(5)	4.2(1)	2.2	3.6(1)	2.7(3)	2.9(1)
6.9	5.5(1)	3.4(4)	4.3(1)	2.9	4.8(1)	3.1(3)	3.5(1)
8.2	5.8(1)	2.6(3)	4.1(1)	3.6	5.6(1)	4.8(2)	4.4(1)
9.6	5.8(1)	2.9(4)	4.0(1)	5.7	6.8(1)	8.6(2)	4.1(1)
				7.2	7.8(1)	13(2)	3.8(1)

Table 4.S3: *Avrami parameters obtained for Al/Cac-poly(rU) aggregation. I=0.1 M, pH=7.0 and T=25.0 °C. A, is the amplitude, $t_{\frac{1}{2}}$ is the time corresponding to 50 % of aggregation process, m is the cooperativity parameter. In brackets the uncertainty in the last digit.*

$C_P = 3.4 \times 10^{-5}$ M, fixed				$C_{AlCac} = 4.1 \times 10^{-4}$ M, fixed			
$10^4 C_{AlCac}$ M	$10^2 A$	$10^{-2} t_{\frac{1}{2}}$ s	m	$10^5 C_P$ M	$10^2 A$	$10^{-2} t_{\frac{1}{2}}$ s	m
2.7	5.8(1)	18(2)	2.0(1)	0.9	2.5(1)	6.7(8)	1.5(1)
4.1	7.8(1)	12(1)	1.8(1)	1.7	4.9(1)	5.6(7)	1.4(1)
5.4	8.0(3)	9(1)	1.8(1)	3.4	7.9(1)	9(1)	1.5(1)
6.9	7.4(1)	9(1)	1.8(1)				
8.2	7.9(1)	8(1)	1.5(1)				
9.6	6.2(1)	9(1)	2.1(1)				
10.3	7.5(1)	9(1)	1.4(1)				

4.A Determination of the Initial Rate Equation for the Al/Cac-Poly(rU) System at pH=5.0

For Al/Cac-poly(rU) at pH=5.0 the hypothesized model is

$$\mathrm{M_2L_2} \overset{1/K_2}{\longleftrightarrow} \mathrm{M_2L} + \mathrm{L} \tag{4.A.1}$$

$$\mathrm{M_2L} \overset{1/K_1}{\longleftrightarrow} 2\,\mathrm{M} + \mathrm{L} \tag{4.A.2}$$

$$2\,\mathrm{M} + \mathrm{P} \xrightarrow{k_1} \text{products} \tag{4.A.3}$$

where M is the free metal, L the free ligand, P is the RNA monomeric unit, $\mathrm{M_2L_2}$ and $\mathrm{M_2L}$ are the metal/ligand complexes. The apparent constants K_1 and K_2 of the metal/ligand complex at pH=5.0 are given by (4.A.4) and (4.A.5) with $[M]$, $[L]$, $[M_2L]$ and $[M_2L_2]$ the molar concentration of the free metal, the free ligand and the complexes at the equilibrium, respectively, whereas k_1 is the kinetic constant of the direct reaction.

$$K_1 = \frac{[M_2L]}{[M]^2[L]} \tag{4.A.4}$$

$$K_2 = \frac{[M_2L_2]}{[M_2L][L]} \tag{4.A.5}$$

The initial rate of the reaction is given by Equation (4.A.6)

$$v_i = k_1[M]^2[P] \tag{4.A.6}$$

Analytical concentration of the RNA (C_P) and metal (C_{AlCac}) are expressed by equation (4.A.7) and (4.A.8)

$$C_P = [P] + [products] \tag{4.A.7}$$

$$C_{AlCac} = [M] + 2[M_2L_2] + 2[M_2L] + [products] \tag{4.A.8}$$

In the initial stage of the reaction, the concentration of the products is negligible with respect to the reactant concentrations. So, it can be excluded from (4.A.7) and (4.A.8). The reaction order with respect L is $n_L = -2$ which indicates that large amounts of $\mathrm{M_2L_2}$ are formed. Hence $C_{AlCac} \cong 2[M_2L_2]$. In addition, as we work in excess of cacodylate, it follows that $[L] \cong C_L$.
From (4.A.4) and (4.A.5) one obtains (4.A.9)

$$[M]^2 = \frac{C_{AlCac}}{2K_1K_2C_L^2} \tag{4.A.9}$$

and, then, equation (4.A.10) for the initial reaction rate, provided that reaction (4.A.1) and (4.A.2) are fast compared to reaction (4.A.3).

$$v_i = \frac{k_1}{2K_1K_2}\frac{C_{AlCac}C_P}{C_L^2} \tag{4.A.10}$$

4.B Determination of the Initial Rate Equation for the Al/Cac-Poly(rA) and the Al/Cac-Poly(rU) Systems at pH=7.0

For Al/Cac-poly(rU) and Al/Cac-poly(rA) at pH=7.0 the hypothesized model is

$$\mathrm{M_2L_2} \overset{1/K_2'}{\longleftrightarrow} \mathrm{M_2L + L} \tag{4.B.1}$$

$$2\,\mathrm{M_2L + P} \xrightarrow{k_2} \text{products} \tag{4.B.2}$$

where L is the free ligand, P is the RNA monomeric unit, M_2L_2 and M_2L are the metal/ligand complexes. The apparent equilibrium constant K_2' of the metal/ligand complex at pH=7.0 is given by (4.B.3) with $[L]$, $[M_2L_2]$ and $[M_2L]$ the molar concentration of the free ligands and the complexes at the equilibrium, respectively, whereas k_2 and k_2' are the kinetic constants of the forward reaction for the Al/Cac-poly(rA) and Al/Cac-poly(rU) systems, respectively.

$$K_2' = \frac{[M_2L_2]}{[M_2L][L]} \tag{4.B.3}$$

The initial rate of the reaction is:

$$v_i = k_2[M_2L]^2[P] \tag{4.B.4}$$

Analytical concentration of the RNA (C_P) and metal (C_{AlCac}) are expressed by Equations (4.B.5) and (4.B.6)

$$C_P = [P] + [products] \tag{4.B.5}$$

$$C_{AlCac} = 2[M_2L_2] + 2[M_2L] + [products] \tag{4.B.6}$$

For the reasons given in Appendix 4.A it turns out that for this system as well $C_{AlCac} \cong 2[M_2L_2]$ and $[L] \cong C_L$.
Rearranging (4.B.3) one obtains (4.B.7)

$$[M_2L]^2 = \frac{C_{AlCac}^2}{4K_2'^2C_L^2} \tag{4.B.7}$$

which, introduced in (4.B.4), yields the expression (4.B.8) for the initial reaction rate.

$$v_i = \frac{k_2}{4K_2'^2}\frac{C_{AlCac}^2 C_P}{C_L^2} \tag{4.B.8}$$

4.C Determination of the Initial Rate Equation for the Al/Cac-[Poly(rA)]$_2$ System at pH=5.0

For Al/Cac-[poly(rA)]$_2$ at pH=5.0 the proposed model is

$$\mathrm{M_2L_2} \overset{1/K_2}{\longleftrightarrow} \mathrm{M_2L + L} \tag{4.C.1}$$

$$\mathrm{M_2L + P} \xrightarrow{k_3} \text{products} \tag{4.C.2}$$

where L is the free ligand, P is the RNA monomeric unit, M_2L and M_2L_2 are the metal/ligand complexes. The apparent constant K_2 of the metal/ligand complex is given by (4.C.3), being $[L]$, $[M_2L]$ and $[M_2L_2]$ the molar concentration of the free ligand and of the metal/ligand complexes at the equilibrium, respectively, whereas k_3 is the kinetic constant of the direct reaction.

$$K_2' = \frac{[M_2L_2]}{[M_2L][L]} \tag{4.C.3}$$

The initial rate of the slow reaction is:

$$v_i = k_3[M_2L][P] \tag{4.C.4}$$

Analytical concentration of the RNA (C_P) and metal (C_{AlCac}) are expressed by Equation (4.C.5) and (4.C.6)

$$C_P = [P] + [products] \tag{4.C.5}$$

$$C_{AlCac} = 2[M_2L_2] + 2[M_2L] + [products] \tag{4.C.6}$$

For the reasons given in Appendix 4.A it results that $C_{AlCac} \cong 2[M_2L_2]$ and $[L] \cong C_L$. From (4.C.3) one obtains (4.C.7)

$$[M_2L] = \frac{C_{AlCac}}{2K_2C_L} \tag{4.C.7}$$

which, introduced in (4.C.4), yields the initial reaction rate (4.C.8)

$$v_i = \frac{k_3}{2K_2}\frac{C_{AlCac}C_P}{C_L} \tag{4.C.8}$$

Part II

Metal Complexes: Interaction with DNA and Photoreactivity

The second part of the Thesis has been centered on the study of the interaction between metal complexes of Ruthenium, Iridium and Rhodium with different conformations of DNA. In particular, a deep study of the photoreactivity of the selected classes of metal complexes has been carried out, in order to observe the optimal properties of a metal drug for the Photodynamic Therapy. The metal complexes taken into account are the η^6-arene and biscyclometalated complexes. The examined arene complex was the [(*p*−cymene)Ru(L−1)(SCN)] with **HL-1** = 2-(2'-hydroxyphenyl)benzothiazole. The work is inserted in the study of a new family of arene ruthenium complexes developed in collaboration with the Inorganic Chemistry Laboratory of the Universidad de Burgos. This complex was chosen because of its interesting cytotoxic activity, which results higher respect to the free **HL-1** ligand. Initially, the physico-chemical properties of **HL-1** and the ruthenium complex were studied, together with the pK_A values and the aquation process by means of UV-vis spectrophotometry and fluorimetry. Then, the interaction of the ligand and the complex with different types of DNA was analysed by different techniques (fluorimetry, circular dichroism, viscometry, DSC). In addition, the product derived from the irradiation of the metal complex was analysed using UV-vis absorption, NMR and mass spectrometry and the photoreactivity was evaluated in the presence of plasmid pUC18 DNA. Then, in Chapter 6 and 7 our interest was focused on to bicyclometalated complexes of iridium (Ir) and rhodium (Rh).

In Chapter 6 we proposed two newly synthesized cyclometalated complexes, which differ from the metal centre, Ir(III) and Rh(III), with CN = 2-phenylpyridynate and NN = 2-(2'pyridyl)benzoxazole, [**Ir-1**]Cl and [**Rh-1**]Cl, prepared by Dr. Martinez Alonso of the Inorganic Chemistry group. Interaction in dark condition with CT-DNA was studied by means of UV-vis absorption titrations, ITC, fluorescence steady-state, fluorescence decays, DSC and viscometry. Photocleavage of plasmid pUC18 in the presence of the complexes was conducted under different conditions in order to elucidate the mechanism of action of the irradiated drugs. Finally MTT proofs with SW480 cell lines were performed by Dr. Busto, in the dark and under irradiation, to prove the obtained results from the photocleavage study.

From the results obtained in Chapter 6 we decided to synthesize eight new biscyclometalated complexes, which are the topic of Chapter 7. In this case we changed not only the nature of the metal centre (again Iridium and Rhodium), but also the CN (2-phenylpyridyine and 2-phenylisoquinoline) and the NN ancillary ligands (2-(2'-pyridyl)benzothiazole and 2-(2'-quinolinyl)benzothiazole). The resulting complexes ([**Ir-2**]Cl, [**Ir-3**]Cl, [**Ir-4**]Cl and [**Ir-5**]Cl Ir complexes and [**Rh-2**]Cl, [**Rh-4**]Cl and [**Rh-5**]Cl Rh complexes) were fully characterized by NMR, mass spectrometry, IR and elemental microanalysis in order to assure the structure and the purity of the products. UV-vis absorption and luminescence properties were also studied. Then, two different studies were carried out: the photoreactivity and the interaction towards G-Quadruplex DNA. Part of this work was developed in collaboration with Dr. Ilse Manet from the Istituto per la Sintesi Organic e la Fotoreattività, of the National Research Center of Bologna, Italy. Concerning the photoreactivity, photocleavage of DNA was checked at different irradiation wavelengths, from the ultraviolet to visible region. Again, MTT proofs of the irradiated and non-irradiated species with SW480 cancer cell line were performed by Dr. Busto. On the other side, the study of the interaction with G-Quadruplex and duplex oligonucleotides was conducted

using various techniques (UV-vis absorption titrations, UV and visible circular dichroism, fluorescence steady-state and fluorescence decay). These proofs were integrated by stabilisation proofs of different G4 structures in the presence of the metal complexes, performed by Dr. Busto.

Chapter 5

Ruthenium Arene Complex with Arylazole Ligand: Two-Step Binding to DNA and Photoreactivity

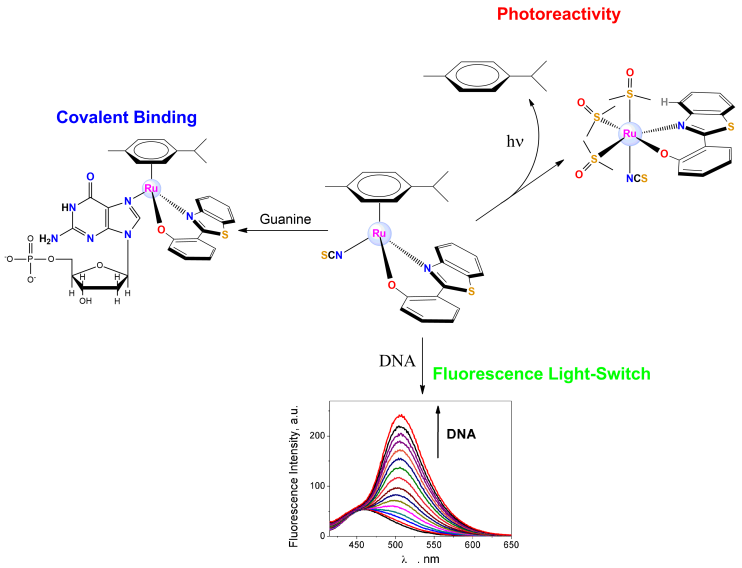

The interaction with DNA of a ruthenium arene complex was tested, namely the [(*p*−cym)Ru(L−1)(SCN)] complex. This complex suffers aquation in buffer solution (I=6.5 mM and pH=7.0). First of all, interaction towards *d*GMP was found, which was accounted to a covalent binding to the guanine moiety. Irreversible interaction with guanine was observed in the presence of DNA, as well. Interestingly, a further interaction was hinted for DNA by the kinetic study and confirmed by fluorimetric titrations. Actually, a light-switch behaviour was

displayed and proofs with different DNA sequences showed that the highest fluorescence enhancement was observed in the presence of poly$(dAdT)_2$, suggesting a weak binding on the minor groove. Proofs with the **HL-1** ligand showed a similar fluorescence enhancement. Consequently, a dual mode of binding of the arene complex with DNA has been advanced: a covalent binding to the guanine, which is governed by the leaving group (H_2O) and a minor groove binding, ruled by the ancillary chelating ligand.
Furthermore, photoirradiation of the ruthenium complex provoked the release of the η^6-arene ligand, and a certain photocleavage activity with plasmid DNA was diplayed, which seems to follow an oxygen-independent pathway.

5.1 Materials and Methods

5.1.1 Materials

Lyophilized Calf Thymus (CT) DNA sodium salt was purchased from Sigma Aldrich and prepared according to Chapter 2 (Section 2.1.2). The poly(deoxyadenylic-deoxythymidylic) (p$(dAdT)_2$), and the poly(deoxyguanylic-deoxycytidylic) (p$(dGdC)_2$) acid sodium salts were purchased from Sigma and the concentrations were checked by UV-vis spectra, using $\epsilon = 13\,400\,\mathrm{cm^{-1}M^{-1}}$ in base pairs (bp) at $\lambda_{irr} = 260\,\mathrm{nm}$ for p$(dAdT)_2$ and $\epsilon = 16\,600\,\mathrm{cm^{-1}M^{-1}}$ in bp at $\lambda = 254\,\mathrm{nm}$ for p$(dGdC)_2$, $I = 0.1\,\mathrm{M}$ (NaCl), pH=7.0 and T=25.0 °C [1]. Plasmid pUC18 (2686 bp) for the photocleavage study was extracted from bacteria and purified by means of a HP Plasmid Midi Kit (OMEGA Bio-tek, VWR). The concentration of the polynucleotides is expressed in molarity of the nitrogenous bases and denoted as C_P. 2'-Deoxyguanosine-5'-Monophosphate (dGMP), was purchased from Sigma Aldrich (purity of 99 %) and used without further purification.
[($p-$cym)Ru(L−1)SCN] (where **HL-1**=2-(2'-hydroxyphenyl)benzothiazole), defined as **[Ru-1]**, was prepared by Dr. Martinez-Alonso of Inorganic Chemistry group, and it was previously characterized. The structure of the complex is reported in Figure 5.1.

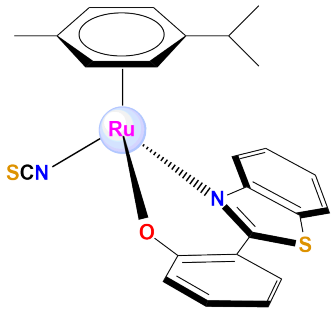

Figure 5.1: Molecular structure of **[Ru-1]**.

All the experiments between **[Ru-1]** and mono- and polynucleotides were carried out in double distilled water, at a fixed ionic strength (I) and pH. Work solutions had I=6.5 mM ($NaClO_4$) and pH=7.0.

5.1.2 Methods

Desired pH of work solutions was reached adding small aliquots of concentrated solution of $HClO_4$ and NaOH, using a Metrohm 16 DMS Titrin pH meter, with a glass electrode containing a solution of KCl 3 M. UV-vis absorption spectra were recorded by means of a Hewlett Packard 8453 A spectrophotometer (Agilent Technologies), with diode-array detector and coupled with a computer-assisted temperature-control system. Kinetic absorption studies of the interaction between **[Ru-1]** with *d*GMP and CT-DNA were performed recording the spectra at a defined time lapse and a kinetic curve was treated at a specific wavelength. Circular dichroic spectra were recorded with a MOS-450 Bio-Logic dichrograph (Claix, France), at different $\frac{C_D}{C_P}$ or $\frac{C_L}{C_P}$ ($C_P = 5.0 \times 10^{-5}$ M), where C_L, C_D and C_P are the analytical concentration of the ligand L, the complex and the polynucleotide, respectively. The spectra were recorded from 200 to 600 nm, with an acquisition rate of 0.5 nm s^{-1}. The elapsed time of 1 mL of DNA solution passing through a capillar was measured in a microviscometer Ubbelhode. The measurement of the viscosity allows to determine the elongation of the DNA through Eq. (2.20) (Chapter 2, Section 2.2.7). The temperature was kept at 25.0 °C by means of an external water thermostat. Thermal denaturation study was carried out by means of a Nano-DSC (TA Instruments). The working solutions (solutions at different $\frac{C_D}{C_P}$, $C_P = 4.0 \times 10^{-4}$ M) were degassed before injection in the equipment. The system was pressurized at 3 atm and the solutions were heated from 20 to 110 °C at 1 °C min^{-1} scan rate. NMR samples were prepared under a N_2 atmosphere by dissolving the suitable amount of compound in 0.5 mL of the respective oxygen-free deuterated solvent, and the spectra were recorded at 298 K on a Varian Unity Inova-400 (399.94 MHz for ^{1}H; 161.9 MHz for ^{31}P). Typically, 1D ^{1}H-NMR spectra were acquired with 32 scans into 32 K data points over a spectral width of 16 ppm. ^{1}H chemical shifts were internally referenced to tetramethylsilane *via* 1,4-dioxane in D_2O (δ=3.75 ppm). Chemical shift values are reported in ppm and coupling constants (J) in hertz. All NMR data processing was carried out using MestReNova v10.0.2-15465. FAB mass spectra (position of the peaks in Da) were recorded with an Autospec spectrometer. Study of photo-dissociation was carried out by means of the illuminator explained in Chapter 2 (Section 2.2.10), in which was described also the cleavage assay (Section 2.2.11).

5.2 Results and Discussion

5.2.1 Physico-Chemical Properties

5.2.1.1 HL-1 Luminescence

A comparison between the physico-chemical properties and the reactivity of **HL-1** and **[Ru-1]** was conducted to observe the role played by the ligand in the reactivity of the metal complex.

HL-1 ligand was poorly soluble in the buffer solution (micromolar concentrations in I=6.5 mM, $NaClO_4$, pH=7.0 in 2 % DMSO:H_2O (v:v)). Its photo-properties have been largely studied in scientific literature [2, 3]. The UV-vis spectrum displays two maxima at 288 and 327 nm, and a band at 460 nm is visible in the emission spectra, corresponding to the solvated tautomer enol-imine form [4].

Hence, **HL-1** displays a large Stokes shift of the emission peak ($\Delta\lambda$=135 nm, Figure 5.2).

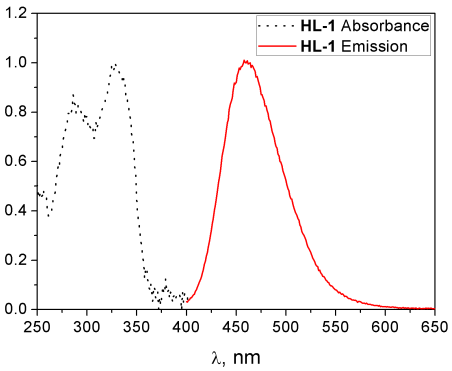

Figure 5.2: Absorption and emission spectra of **HL-1**. C_L=2.5 µM, 2 % DMSO, I=6.5 mM ($NaClO_4$), pH=7.0 (NaCac), λ_{ex}=325 nm and T=25.0 °C.

Interestingly, variation with time of the absorption and fluorescence spectra was observed, for concentrations above C_L>3 µM, C_L being the molar concentration of **HL-1**. A kinetic process was recorded both in absorbance and fluorescence modes (Figure 5.3). The well-defined isosbestic points at 272 and 343 nm in the spectral curves denote two species in equilibrium (Figure 5.3A). Figure 5.3B shows the change with time undergone by the fluorescence spectra. The band at 460 nm gradually vanishes, producing a shoulder, while a new band emerges at 508 nm.

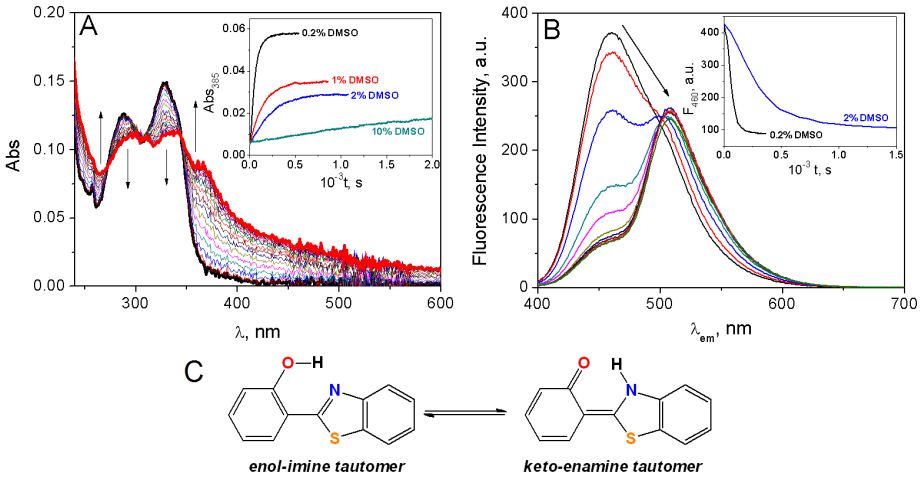

Figure 5.3: Kinetics of **HL-1** in buffer solution. (A) Absorbance *versus* time for the experiment at 0.2 % DMSO; inset: track at 385 nm for different DMSO contents. (B) Fluorescence *versus* time example; inset: track at 460 nm for different DMSO contents. C_L=10 µM, I=6.5 mM ($NaClO_4$), pH=7.0 (NaCac), λ_{ex}=325 nm and T=25.0 °C. (C) Tautomeric equilibrium for **HL-1**.

According to literature [4], the fluorescence spectrum of the keto-enamine tautomer shows a strong emission band at ≈535 nm and a weak shoulder at 456 nm. This finding demonstrates that the illustrated process in Figure 5.3 corresponds to the enol-imine to keto-enamine transformation by ESIPT (Excited State Intramolecular Proton Transfer) effect. It follows that a dual emission occurs from mixtures, with the keto-enamine form emitting at longer wavelength. The contribution of the isomers primarily depends on the solvent. Actually, the tracks at 385 nm in the UV-vis absorption spectra (Figure 5.3A, inset) and at 460 nm in the emission spectra (Figure 5.3B, inset) reveal that the reaction rate diminishes when the DMSO content increases, and becomes very slow above 10 % DMSO. The rate constants obtained from fitting of a monoexponential function to the kinetic tracks recorded are shown in Table 5.1.

Table 5.1: *Rate constants of the observed kinetics for **HL-1** at different DMSO concentration.* C_L=10 µM, I=6.5 mM, pH=7.0 *and* T=25.0 °C.

DMSO, %	$10^3 \frac{1}{\tau}$, s^{-1}
1	6.8
2	4.3
10	0.66

Therefore, it is conceivable that under the conditions utilized the enol-imine form of the ligand is present in the early stages, evolving afterwards to the keto-enamine taumer form. As we always used freshly prepared solutions of the ligand and under suitable DMSO concentration (2-5 % depending on the technique employed) it can be assumed that, under the working conditions, the ligand was preferentially in the enol form.
On the other hand, for very low DMSO concentration (0.2 %), the monoexponential function could not fit properly the kinetic trace, suggesting aggregation, as many dyes are prone to aggregation in water [5, 6]. Actually, aggregation has been observed previously for high **HL-1** concentration (20 µM, 2 % DMSO [4]) and for similar molecules, as 2-(2'-hydroxyphenyl)benzoxazole [7].

5.2.1.2 Aquation of [Ru-1]

Regarding the low-fluorescent complex **[Ru-1]**, this is soluble in DMSO and, for $C_D \leq 50$ µM, at neutral pH buffer, as well; in the presence of CT-DNA, the solubility increased, rendering viable the study at higher concentrations.
Exchange kinetics of SCN^- with dimethylsulfoxide was not observed. However, the recorded UV-vis spectra in aqueous solution at neutral pH as a function of time (Figure 5.4) shows SCN^- release and substitution by a H_2O molecule, according to Reaction 5.1, forming the $[(p\text{−cym})\text{Ru}(\text{L}-1)(\text{OH}_2)]^+$ species, which, from now on, will be denoted as **aquo-[Ru-1]**.

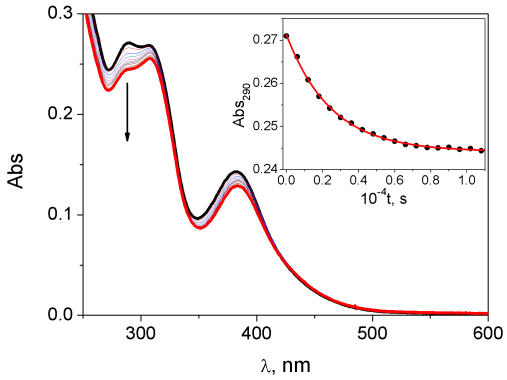

Figure 5.4: Kinetic of aquation of [**Ru-1**] complex. Inset: track at λ=290 nm fitted by a monoexponential curve (red line). C_D=18 µM, 2 % DMSO, I=6.5 mM, pH=7.0 and T=25.0 °C.

Fitting of the monoexponential function to the recorded data-pairs leads to the rate constant k=4.0 × 10^{-4} s^{-1}. This value resembles aquation processes of many chlorido ruthenium complexes [8].

$$(p\text{−cym})\text{Ru(L1)(SCN)} + \text{H}_2\text{O} \xrightarrow{k} (p\text{−cym})\text{Ru(L1)(OH}_2)^+ + \text{SCN}^- \qquad (5.1)$$

Since aqua-complexes are generally more reactive species than their chlorido precursors [9], the experiments were carried out after finishing the aquation process of [**Ru-1**].

5.2.1.3 Acid Base Behaviour

Regarding pH, fluorescence enhancement of **HL-1** was visualized for increasing pH values (Figure 5.5A).

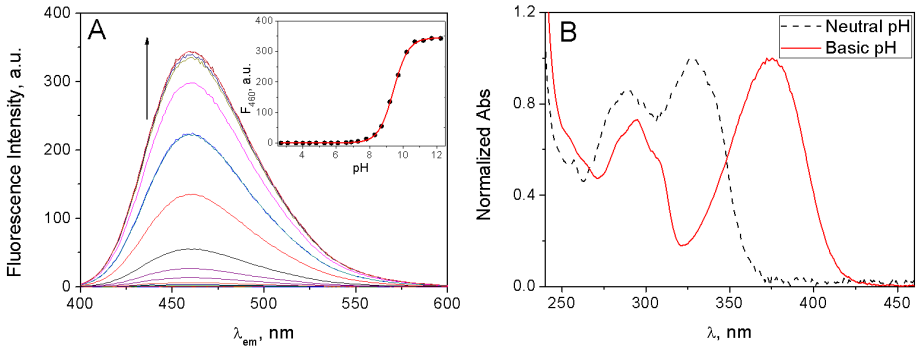

Figure 5.5: (A) Fluorescence spectra of **HL-1** for different pHs. Inset: track at λ_{em}=460 nm. C_L=2.5 µM, λ_{ex}=380 nm. (B) Normalized absorbance of the neutral **HL-1** (dashed line) and the deprotonated **L-1** species (red line). 2 % DMSO, I=6.5 mM and T=25.0 °C.

In addition, notable variations of the absorption spectra were recorded for basic pH, as well (Figure 5.5B). The pK_A values obtained by means of the Henderson-Hasselbach equation [10], 9.4 ± 0.1, refers to deprotonation of the phenol group (Reaction (5.2)). This value concurs with pK_A obtained for other (hydroxyphenyl)benzothiazoles (for example, for 2-(3'-hydroxyphenyl)benzothiazole, pK_A=9.5 and, for 2-(4'-hydroxyphenyl)benzothiazole, pK_A=8.8 [11]).

$$\mathrm{HL1} + \mathrm{OH^-} \overset{K_A}{\rightleftharpoons} \mathrm{L1^-} + \mathrm{H_2O} \tag{5.2}$$

Related to **aquo-[Ru-1]**, the spectra recorded for increasing pH values show changes and two isosbestic points at 290 and 330 nm (Figure 5.6).

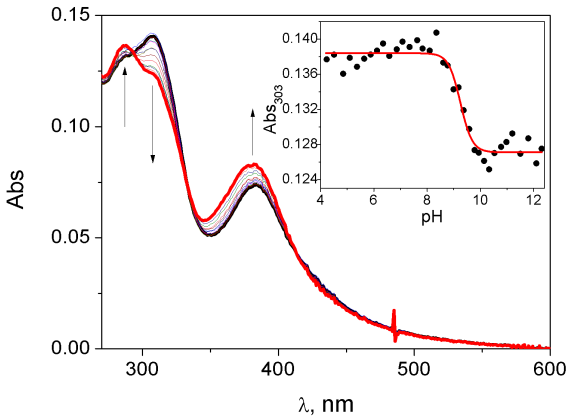

Figure 5.6: UV-vis absorption spectra of the **aquo-[Ru-1]** complex for different pH values. C_D=10 µM, 2 % DMSO, I=6.5 mM and T=25.0 °C.

Such spectral variations are ascribable to formation of the hydroxo-compound [(*p*−cym)Ru(L−1)(OH)], according to Reaction 5.3.

$$[(p\text{−cym})\mathrm{Ru(L1)(H_2O)}]^+ + \mathrm{OH^-} \overset{K'_A}{\rightleftharpoons} [(p\text{−cym})\mathrm{Ru(L1)(OH)}] + \mathrm{H_2O} \tag{5.3}$$

From the track at 303 nm (Figure 5.6, inset) we obtain pK'_A=9.2 ± 0.1 indicating that at neutral pH the complex is present in the aqua form. Similar K_A values have been reported for the formation of some ruthenium hydroxo-compounds [8]. Note that, even though the pK_A values for **HL-1** and the complex are similar, the acid-base equilibria are definitively related to different functional groups, the hydroxo group and the water leaving group for **HL-1** and **[Ru-1]**, respectively, because of the different structure of the compounds. For high pH values, a slow kinetic effect (data not shown) was observed for **aquo-[Ru-1]** and, as the new peaks formed are the same as those of the ligand anion form, we assumed that highly basic conditions can disrupt the binding between the metal and the **L-1** ancillary ligand.

5.2.2 Interaction of aquo-[Ru-1] with *d*GMP

Prior to the study of the interaction of DNA with **aquo-[Ru-1]**, kinetic proofs by means of absorption measurements were performed in the presence of deoxyadenosine-5'-monophosphate (*d*AMP) and deoxyguanosine-5'-monophosphate (*d*GMP) in excess of nucleotides. No signal variation was detected for **aquo-[Ru-1]** with *d*AMP, whereas for the **aquo-[Ru-1]**/*d*GMP system a slow kinetic was perceptible. The reaction caused hypochromism at 383 nm and a hyperchromic effect at 340 nm of the **aquo-[Ru-1]** absorption spectra, with an isosbestic point at 353 nm (Figure 5.7A).

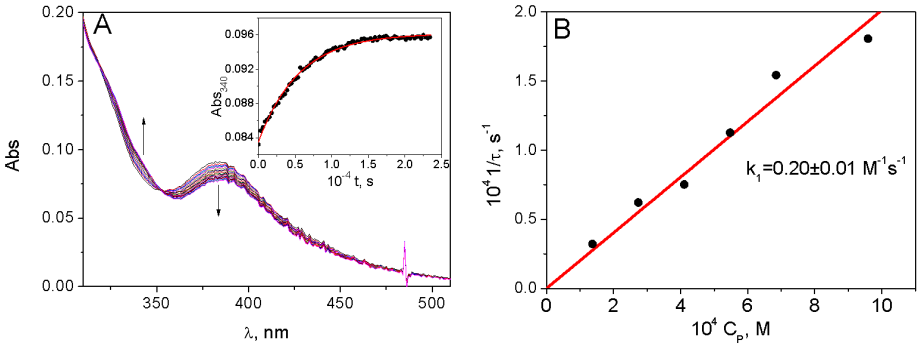

Figure 5.7: (A) Example of kinetic spectra for the interaction between the **aquo-[Ru-1]** complex and *d*GMP system, C_D=14 µM, $\frac{C_P}{C_D}$=50; inset: track at λ=340 nm and fitting (red line) by monoexponential function. (B) Fitting of the rate constants by the $\frac{1}{\tau} = k_1 C_P$ equation (red line). 2 % DMSO, I=6.5 mM, pH=7.0 and T=25.0 °C.

Interactions of metal complexes with the phosphate group are generally fast, whereas covalent binding to the nitrogenous bases are slower. Actually, various ruthenium arene complexes have been reported to bind guanine through the N_7 by substitution of their leaving group [12, 13].
The time constants ($\frac{1}{\tau}$) increased linearly with the increase in the *d*GMP concentration (C_P) (Figure 5.7B). In addition, the plotting shows close to zero intercept, indicating that an irreversible reaction between **aquo-[Ru-1]** and *d*GMP to give a **[Ru-1]**/*d*GMP complex is at work (Equation 5.4). The slope value provides the reaction rate constant k_1=0.20 ± 0.01 $M^{-1}s^{-1}$.

$$\text{aquo}-[\text{Ru}-1] + d\text{GMP} \xrightarrow{k_1} [\text{Ru}-1]d\text{GMP} + \text{H}_2\text{O} \tag{5.4}$$

This type of interaction was also studied by means of ^{1}H-NMR and ^{31}P{^{1}H}-NMR spectroscopy. New sets of peaks emerged in the presence of 9-MeG (data not shown) and *d*GMP. In particular, for the **[Ru-1]**/*d*GMP system, a new set of proton peaks was detected after three days (Figure 5.8), suggesting a slow reaction between the complex and *d*GMP. In addition, a small signal in the ^{31}P{^{1}H}-NMR spectrum appeared for **[Ru-1]**/*d*GMP (Figure 5.9).

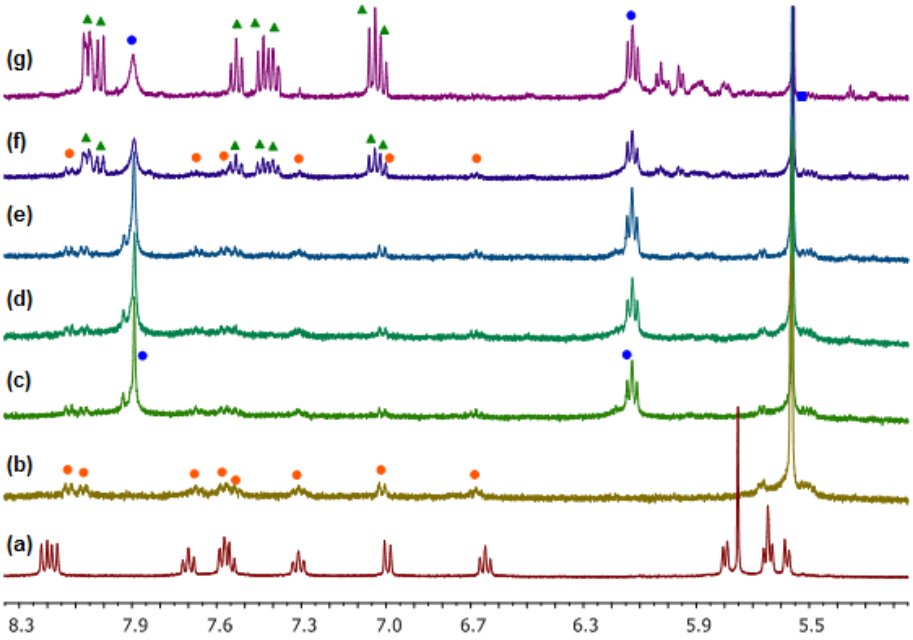

Figure 5.8: ^{1}H-NMR: evolution of the aromatic region of [**Ru-1**] with *d*GMP in DMSO−d_6/D_2O (5:2) at 25 °C. ● [**Ru-1**], ● free *d*GMP and ▲[**Ru-1**]/*d*GMP product. (a) Spectrum in DMSO−d_6, (b) after addition of D_2O at t=0 and after addition of *d*GMP at (c) *t*=5 min, (d) 20 min, (e) 55 min, (f) 72 h and (g) 1 week.

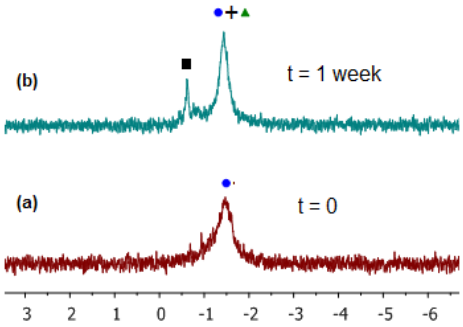

Figure 5.9: ^{31}P{^{1}H}-NMR spectra for the reaction between *d*GMP and [**Ru-1**] complex recorded after one week. ● free *d*GMP, ▲ [**Ru-1**]/*d*GMP majority product and ■ [**Ru-1**]/*d*GMP minority product.

Hence, we can hypothesize the presence of a minor species in which the ruthenium is bound to the phosphate group. Moreover, a second more intense peak is attributed to the major Ru-N species. This signal undergoes no significant shift in the ^{31}P{H}-NMR spectrum, and exhibits intense peaks in the ^{1}H-NMR.

5.2.3 Interaction of HL-1 and aquo-[Ru-1] with CT-DNA

First of all, the interaction between the **HL-1** ligand and CT-DNA was studied. Fluorescence titrations of polynucleotides with **HL-1** were performed; note that, under the working conditions (low **HL-1** concentration, DMSO 2 % and freshly prepared solutions), the species present in solution is the enol-imine tautomer, as demonstrates by the emission spectra of the ligand (Figure 5.2B).
The presence of CT-DNA and poly(dG−dC)$_2$ caused a strong red shift in the emission of **HL-1** ($\Delta\lambda_{em}$=55 nm) and in the presence of poly(dA−dT)$_2$ a sudden fluorescence enhancement was also observed (Fig. 5.10A). Figure 5.10B shows that fluorescence enhancement is much higher in the presence of the poly(dA−dT)$_2$ sequence than in the presence of poly(dG−dC)$_2$ or CT-DNA.

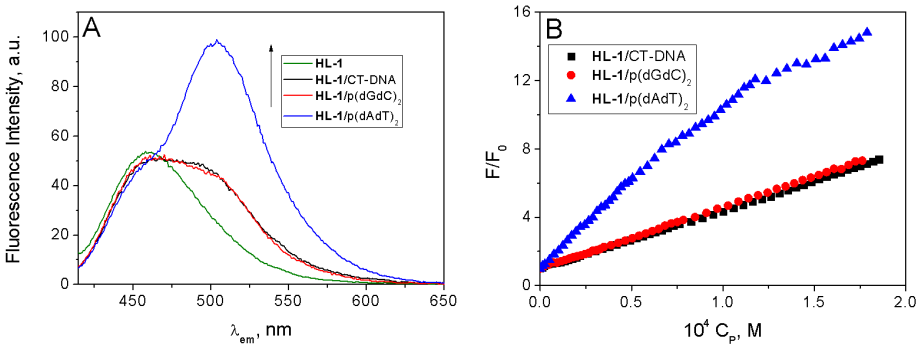

Figure 5.10: (A) Comparison of the fluorescence spectra of the titration of **HL-1** with different polynucleotides at $\frac{C_P}{C_L}$=10. (B) Titration track at λ_{em}=500 nm for the **HL-1**/p(dAdT)$_2$, **HL-1**/CT−DNA and **HL-1**/p(dGdC)$_2$ systems; the fluorescence intensity F is normalized for the value at λ_{em}=500 nm of the free ligand, F_0. C_L=2.5 µM, C_P=0-180 µM, 2 % DMSO, I=6.5 mM ($NaClO_4$), pH=7.0 (NaCac), λ_{ex}=355 nm and T=25.0 °C.

This result points up that **HL-1** displays selectivity towards AT base pairs, concurring with binding on the minor groove [14, 15].
Results provided by fluorimetric titrations are endorsed by further employed techniques. Actually, the **HL-1**/CT-DNA system exhibited slight decrease of circular dichroism (Figure 5.11A) and viscosity (Figure 5.11C). In addition, **HL-1** did not alter the melting temperature of the DNA double-stranded conformation (Figure 5.11D). All these results agree with a non-intercalative binding. Most minor groove binders (netropsin, distamycin, Hoechst 33258, berenil, 40,6-diamidino-2-phenylindole, and SN-6999) are prone to interact with AT-rich sequences, bringing about only a slight distortion of the double helix [16]. Indeed, first of all the GC grooves are sterically hindered by the H bond between the NH_2 functional group at C_2 of the guanine and the carbonyl group at C_2 of the cytosine. Therefore, the electrostatic potential is larger in the AT sequences than in the GC-rich regions. Both characteristics render poly(dA−dT)$_2$ suitable for the external interaction with groove binders [17].

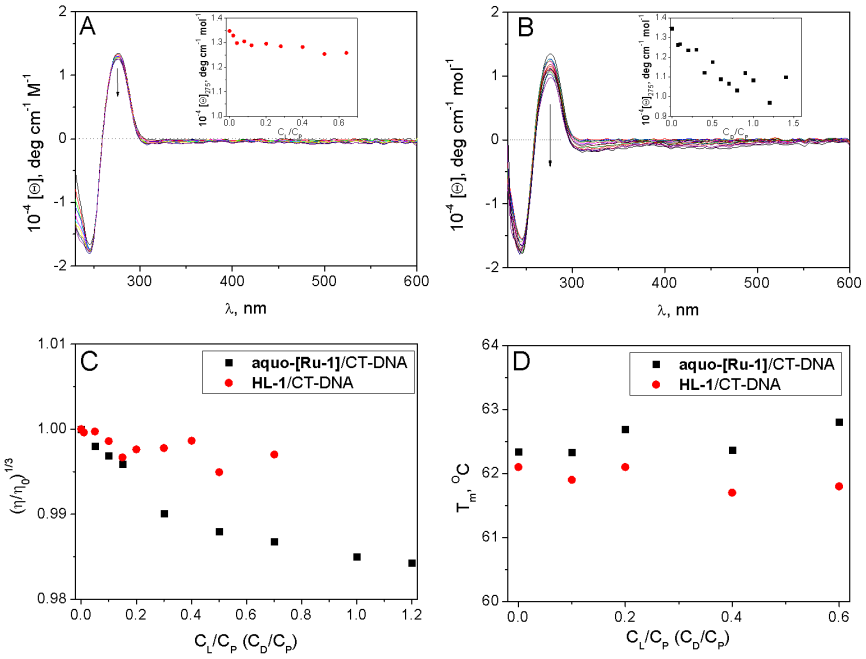

Figure 5.11: Thermodynamic study of the interaction between **HL-1** and **aquo-[Ru-1]** with CT-DNA. (A) Circular dichroism of **HL-1**/CT-DNA system, $\frac{C_L}{C_P}$=0-0.65 (arrow sense) and (B) circular dichroism of **aquo-[Ru-1]**/CT-DNA system, $\frac{C_D}{C_P}$=0-1.2 (arrow sense); C_P=50 µM, 4 % DMSO and T=25.0 °C. (C) Viscometry; C_P=200 µM, 5 % DMSO and T=25.0 °C. (D) T_m *versus* $\frac{C_D}{C_P}$ experiments; C_P=400 µM, 5 % DMSO. Square: **aquo-[Ru-1]**/CT-DNA, Circle: **HL-1**/CT-DNA. I=6.5 × 10^{-3} M, and pH=7.0.

Concerning the **aquo-[Ru-1]** system, variation of the absorption spectra with time was observed also in the presence of CT-DNA (Figure 5.12).

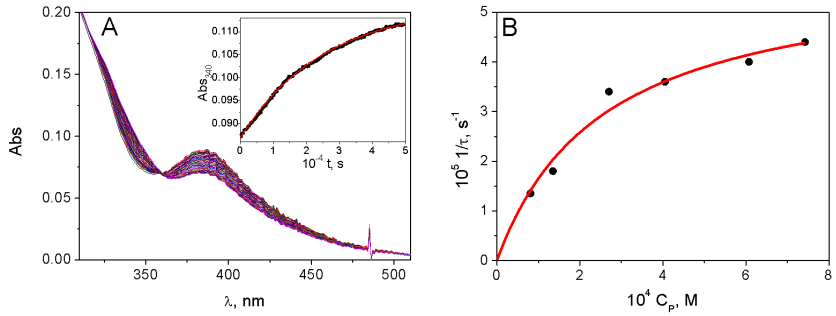

Figure 5.12: (A) Example of kinetics of the **aquo-[Ru-1]**/CT-DNA system. C_D=14 µM, $\frac{C_P}{C_D}$=45; inset: track at 340 nm. (B) Fitting of the rate constants by Equation (5.6). I=6.5 mM ($NaClO_4$), pH=7.0 (NaCac), T=25.0 °C.

Figure 5.12A shows the kinetic spectral curves for the **aquo-[Ru-1]**/CT-DNA

system (with an isosbestic point at 359 nm) and the inset shows the absorbance-time track at 340 nm. The spectral changes are similar to those observed for the **aquo-[Ru-1]**/*d*GMP system (Figure 5.7A), hence, similar interaction with the guanine moiety can be assumed. In this case, however, the increase of the rate constant versus C_P (C_P being the CT-DNA concentration, Figure 5.12B) is nonlinear as the one observed with *d*GMP (Figure 5.7B). This kinetic behavior agrees with a pre-association mechanism of the metal complex to the nucleic acid *via* a noncovalent binding, which modulates the kinetic rate of the covalent binding to the guanine [18]. Therefore, we can assume: (i) the **aquo-[Ru-1]** species reacts quickly with CT-DNA to form the PD complex, K_1 being the equilibrium constant of this step, and (ii) the PD complex converts to PD* in a second unimolecular, irreversible step, k_2 being the rate-determining constant (Reaction (5.5)).
On this basis, Equation (5.6) was fitted to the $\frac{1}{\tau}$ *versus* C_P data-pairs (see Appendix 5.A, Supporting Information). Table 5.2 collects the values obtained for the equilibrium (K_1) and rate (k_2) constants.

$$\mathrm{D} + \mathrm{P} \underset{fast}{\overset{K_1}{\rightleftharpoons}} \mathrm{PD} \xrightarrow[slow]{k_2} \mathrm{PD}^* \tag{5.5}$$

$$\frac{1}{\tau} = k_2 \frac{K_1 C_P}{1 + K_1 C_P} \tag{5.6}$$

Table 5.2: *Thermodynamic and kinetic parameters obtained by fitting of the kinetic curves from the reactions of* ***aquo-[Ru-1]*** *with dGMP and CT−DNA.*

	k_1, $\mathrm{M^{-1}s^{-1}}$	$10^{-3}K_1$, $\mathrm{M^{-1}}$	$10^5 k_2$, $\mathrm{s^{-1}}$
*d*GMP	0.20 ± 0.01		
CT-DNA		4 ± 1	5.8 ± 0.5

The fluorimetric titration of **aquo-[Ru-1]** with CT-DNA (Fig. 5.13) caused a similar fluorescence light-switch and shifted the maximum emission to a wavelength longer than that observed for the **HL-1**/CT-DNA system (Fig. 5.10). The signal did not reach a plateau, and rose for increasing DNA concentration. Note that, since the covalent binding is a very slow process, we can assume that this interaction does not affect the fluorimetric titration. Actually, the time elapsed to perform the titration (about one hour) ensured that, under such conditions, formation of the covalent binding is minority (for example, considering the end of the titration proof, at $C_P = 120\,\mu\mathrm{M}$, the total amount of covalent binding will be some 10 %). The increase in the emission (or light-switch) in the presence of DNA is verified for other ruthenium complexes [19, 20]. Light switch is usually considered a proof for intercalation; however, it is verified that other interactions, such as groove binding, can induce light switch as well, as seen for $[(\mathrm{bpy})_2\mathrm{Ru(tpphz)Ru(bpy)_2}]^{4+}$ [21] and $\mathrm{Ru(phen)_2(Hcdpq)(ClO_4)_2}$ [22]. Performed experiments with $\mathrm{p(dAdT)_2}$ and $\mathrm{p(dGdC)_2}$ exhibit preference for AT base-pairs, as observed for the **HL-1** ligand. It was not possible to obtain an equilibrium constant from the fluorimetric titrations because the plateau was not reached.

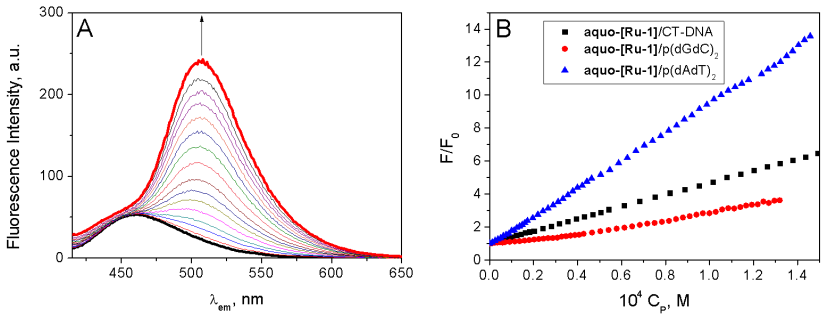

Figure 5.13: (A) Fluorescence titration of **aquo-[Ru-1]** by addition of increasing amount of CT-DNA. (B) Titration track at λ_{em} = 500 nm for the **aquo-[Ru-1]**/p(dAdT)$_2$, **aquo-[Ru-1]**/CT−DNA and **aquo[Ru-1]**/p(dGdC)$_2$; the fluorescence intensity F is normalized for the value at λ_{em}=500 nm of the free complex, F_0. C_D=2.5 µM, C_P=0-150 µM, 2 % DMSO, I=6.5 mM, pH=7.0, λ_{ex}=355 nm and T=25.0 °C.

Weak groove binding is verified for other ruthenium arene complexes [23]. In the same way, few modifications were observed by circular dichroism, viscometry and melting temperature, agreeing with minor groove binding hypothesis (Figures 5.11B to D).

The results indicate that the fast interaction observed for **aquo-[Ru-1]** is governed by the ancillary ligand. Although the highest light switch effect is observed for the p(dAdT)$_2$, as for **HL-1**, certain preference is observed for CT-DNA respect to p(dGdC)$_2$ polymer. Since **aquo-[Ru-1]** is singly charged while the ligand is neutral, change in the nature of binding can occur, influencing the interaction and, consequently, the binding preference.

In conclusion, a dual mode of binding of **aquo-[Ru-1]** towards CT-DNA was observed: covalent binding to guanine moiety and the minor groove binding, with preference towards AT base pairs. Covalent binding is governed by the leaving group (the water molecule), while the interaction to the groove is governed by the ancillary chelating ligand (**HL-1**). Recently, our group reported a stable bifunctional interaction (covalent and partially intercalated) between the $[(p-\text{cymene})\text{Ru}(\kappa^2-\text{NN}-2-\text{pydaT})]^{2+}$ fragment and CT-DNA, where both interactions are present concurrently [24]. In the case of **aquo-[Ru-1]**, however, the obtained results did not clear about the possibility of a bifunctional group or a two-step mode of binding. The geometrical structure of the compound and the nature of the interactions would exclude a bifunctional interaction, but, rather, the groove binding would promote the association of the metal complex to the nucleic acid and, then, the covalent interaction to guanine occurs, resulting in a two-step mechanism. However, the nature of the sequences of nitrogenous base-pairs inside the DNA could influence one of the ways of interaction, obtaining a different mode of action along the polynucleotidic chain.

5.2.4 Photoreactivity and Plasmid Photocleavage

Irradiation of deoxygenated solutions of **aquo-[Ru-1]** showed important changes in its absorption spectra, suggesting alterations in its structure. Furthermore,

the kinetic rate is faster in DMSO (Fig. 5.14A) respect to buffer solution (Fig. 5.14B), under the same experimental conditions.

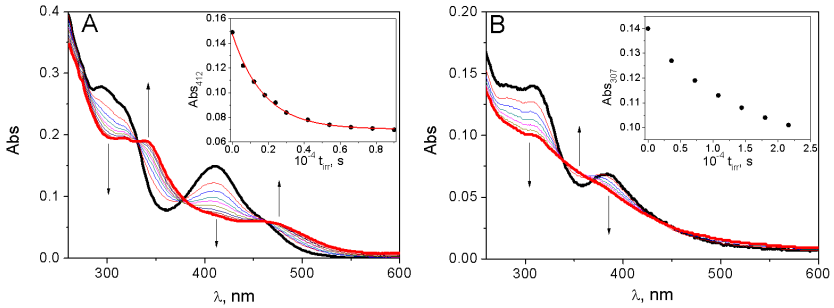

Figure 5.14: UV-vis absorption kinetic of photorelease of *p*-cymene from [**Ru-1**] in (A) DMSO (Inset: track at 412 nm fitted by a monoexponential curve, $\frac{1}{\tau}$=5.7 × 10^{-4} s^{-1}) and (B) buffer solution (2 % DMSO), I=6.5 mM ($NaClO_4$) and pH=7.0 (NaCac) (Inset: track at 383 nm). C_D=20 µM, λ_{irr}=325 nm, and T=25.0 °C.

Thus, the stability of [**Ru-1**] in DMSO−d_6 was studied by ^{1}H-NMR for 3 months under exposure to ambient light and N_2 atmosphere at room temperature. No significant change was observed after 24 h. However, after 3 months signals for free *p*-cymene and a new set of peaks for a new species, denoted as [**Ru-1***], were detected along with the resonances of [**Ru-1**], which reveals a slow decomposition process that involves arene loss. Moreover, irradiation of a [**Ru-1**] sample in DMSO−d_6 with an arc lamp source set at λ_{irr} = 325 nm speeds up the process, in such a way that degradation was completed after 29 h (Figure 5.15).

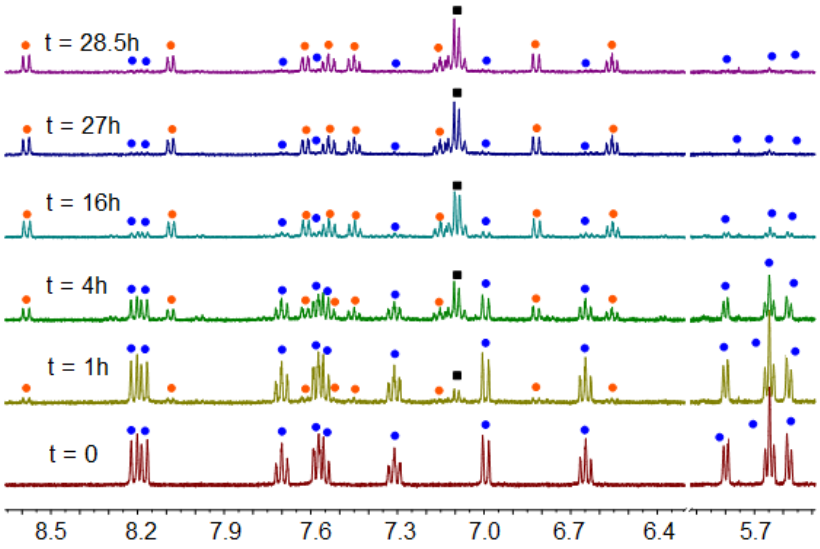

Figure 5.15: ^{1}H-NMR spectra of an irradiated solution of [**Ru-1**] in DMSO−d_6. ● [**Ru-1**] complex; ● [**Ru-1***] complex; ■ free *p*-cymene.

Again, resonances for free *p*-cymene (labeled with black squares in Figure 5.15), and a new Ru(II) complex bearing **L-1** (**[Ru-1*]**, orange circles) were recorded by ^{1}H-NMR in the final mixture.
The molecular structure of **[Ru-1*]** (Figure 5.16) was elucidated by FAB-MS experiments. In particular, the resulting peaks indicate that *p*-cymene was replaced by three DMSO molecules: 470 [**Ru-1***$-2\,\mathrm{DMSO}-\mathrm{d}_6]^+$, 496 [**Ru-1***$-\mathrm{NCS}-\mathrm{DMSO}-\mathrm{d}_6]^+$, 554 [**Ru-1***$-\mathrm{DMSO}-\mathrm{d}_6]^+$, 580 [**Ru-1***$-\mathrm{NCS}]^+$, 638 ([**Ru-1***$]^+$) Da (See spectra in Figure 5.S1-5.S3, Supporting Information). Release of *p*-cymene from ruthenium arene complexes has been reported in other studies [25, 26].

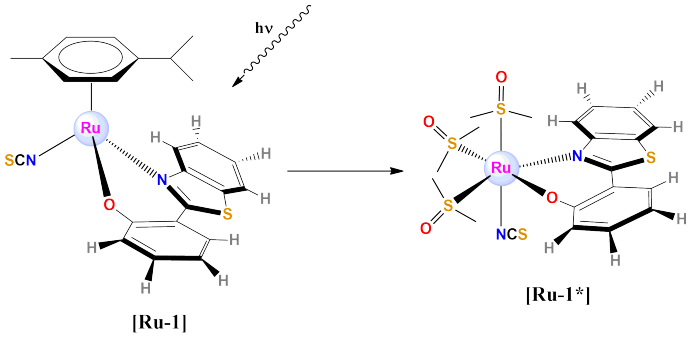

Figure 5.16: Proposed photoreaction found in DMSO involving the release of the *p*-cymene ligand.

Photoreactivity of the **aquo-[Ru-1]** ruthenium complex was evaluated by cleavage of plasmid pUC18 DNA (Figure 5.17).

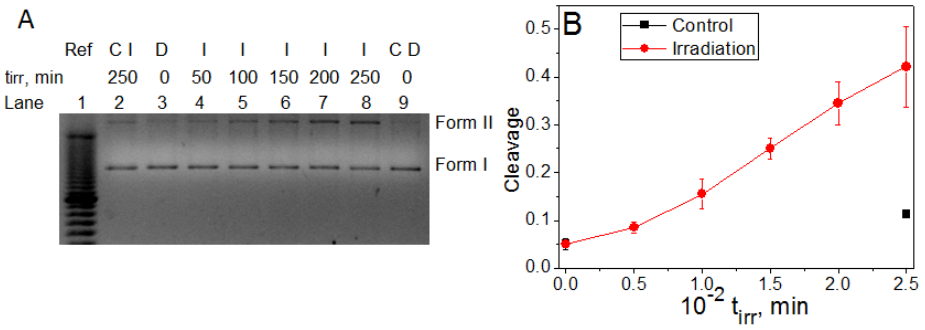

Figure 5.17: (A) Irradiated **aquo-[Ru-1]**/pUC18 samples. Lane 1: Molecular weight marker. Lane 2: Irradiated control (C I), t_{irr}=250 min. Lanes 3-8: **aquo-[Ru-1]**/pUC18 (I), t_{irr}=0 (D), 50, 100, 150, 200, 250 min. Lane 9: Dark Control (CD). C_D=20 µM, C_P=20 µM, [$NaClO_4$]=4.0 mM, [NaCac]=2.5 mM, pH=7.0 and λ_{irr}=325 nm. Incubation at T=37 °C, overnight. (B) Quantification of the cleavage by Equation (2.31).

The photocleavage was quantified by the conversion of the plasmidic native supercoiled form (Form I) to the circular form (Form II), by means of Equation

(2.31) (See Chapter 2, Section 2.2.11). The separation of the different forms was achieved by means of electrophoresis (Figure 5.17A), adding ethidium bromide as probe of the different nucleic acid forms. Figure 5.17B shows certain degree of cleavage of plasmid DNA, and it increased with enhancement of the irradiation time.
Photocleavage proofs in the presence of scavengers of oxygenated radicals and singlet oxygen would confirm the oxygen-independent pathway of reaction. Actually, no decrease of the cleavage was found in the samples containing L-Histidine (for $^1O_2$), DMSO (for OH·) and Superoxide dismutase (SOD, for O_2^{-}·) (Figure 5.S4, Supporting Information). An analogue independence from oxygen of the photocleavage of plasmid DNA has been reported by Magennis et al. in the presence of a ruthenium complex which releases the arene under nitrogen atmosphere, as well [27].

5.2.5 Cytotoxic activity

MTT assays were performed by the group of Prof. Dominguez of the University of Santiago de Compostela and Dr. Busto from our group in the University of Burgos.
The difference in the type of the complexes formed with DNA, groove binding for **HL-1** ligand and bifunctional covalent-groove binding for **aquo-[Ru-1]**, could justify the difference in cytotoxicity towards A2780 cell culture. Actually, the IC_{50} values (Table 5.3) indicate that, whereas the ligand is not cytotoxic, the complex shows strong cytotoxicity, 26 µM. In other words, the metal plays a key role regarding the biological behaviour due to its ability to bind covalently with the guanine N_7 site.

Table 5.3: *IC_{50} (µM) of the metal complexes in different cancer cell lines.*

Compound	A2780 (96h)	A549 (24h)
HL-1	> 100	-
[Ru-1]	26 ± 1	65
[Ru-1*]	-	37
Cisplatin	0.54 ± 0.01	25

In addition, the IC_{50} value of **[Ru-1*]** in the A549 cancer cell line resulted 2-fold lower respect to the value obtained for **[Ru-1]** (Table 5.3), demonstrating that the obtained product from photo-irradiation of **[Ru-1]** is more cytotoxic.

5.3 Conclusions

The **aquo-[Ru-1]** complex displays a dual mode of binding towards DNA, showing a covalent binding to the guanine and a weak binding on the minor groove of the helix, switching on its fluorescence. A two-step mechanism of action has been advanced for **aquo-[Ru-1]**, with a fast pre-association, the groove

binding and, then, the irreversible binding to the guanine. Proof with the 2-(2'-hydroxyphenyl)benzothiazole ligand clearly indicates that the ancillary ligand plays the main role in the interaction with the groove, whereas the interaction with the guanine depends on the release of the leaving group. The two-step mode of binding could be accountable to the higher cytotoxic activity of the drug respect to the cytotoxic activity of the free **HL-1** ligand. The possibility to tune the properties of the complex modifying the arylbenzazoles or adding new ancillary ligands that can promote further interactions could be of interest for new syntheses. In addition, photo-induced arene loss and photocleavage of the plasmid DNA caused by ruthenium arene complex add interest towards such class of complexes for the PDT strategy.

Bibliography

[1] A. M. Brun and A. Harriman (1994). *Energy- and Electron-Transfer Processes Involving Palladium Porphyrins Bound to DNA*, Journal of the American Chemical Society, 116 (23), 10383-10393.

[2] P. F. Barbara, L. E. Brus and P. M. Rentzepis (1980). *Intramolecular Proton Transfer and Excited-State Relaxation in 2-(2-hydroxyphenyl)benzothiazole*, Journal of the American Chemical Society, 102 (17), 5631-5635.

[3] F. Laermer, T. Elsaesser and W. Kaiser (1988). *Femtosecond Spectroscopy of Excited-State Proton Transfer in 2-(2'-hydroxyphenyl)benzothiazole*, Chemical Physics Letters, 148 (2-3), 119-124.

[4] T. I. Kim, H. J. Kang, G. Han, S. J. Chung and Y. Kim (2009). *A Highly Selective Fluorescent ESIPT Probe for the Dual Specificity Phosphatase MKP-6*, Chemical Communications, (39), 5895-5897.

[5] T. D. Slavnova, A. K. Chibisov and H. Görner (2005). *Kinetics of Salt-Induced J-Aggregation of Cyanine Dyes*, The Journal of Physical Chemistry A, 109 (21), 4758-4765.

[6] W. West and S. Pearce (1965). *The Dimeric State of Cyanine Dyes*, The Journal of Physical Chemistry, 69 (6), 1894-1903.

[7] J. Huang, A. Peng, H. Fu, Y. Ma, T. Zhai and J. Yao (2006). *Temperature-Dependent Ratiometric Fluorescence from an Organic Aggregates System*, The Journal of Physical Chemistry A, 110 (29), 9079-9083.

[8] M. Martínez-Alonso, N, Busto, F. A. Jalón, B. R. Manzano, J. M. Leal, A. M. Rodríguez, B. García and G. Espino (2014). *Derivation of Structure–Activity Relationships from the Anticancer Properties of Ruthenium(II) Arene Complexes with 2-Aryldiazole Ligands*, Inorganic Chemistry, 53 (20), 11274–11288.

[9] F. Y. Wang, A. Habtemariam, E. P. L. van der Geer, R. Fernandez, M. Melchart, R. J. Deeth, R. Aird, S. Guichard, F. P. A. Fabbiani, P. Lozano-Casal, I. D. H. Oswald, D. I. Jodrell, S. Parsons and P. J. Sadler (2005). *Controlling Ligand Substitution Reactions of Organometallic Complexes: Tuning Cancer Cell Cytotoxicity*, Proceedings of the National Academy of Sciences of the United States of America, 102 (51), 18269-18274.

[10] H. N. Po and N. M. Senozan (2001). *The Henderson-Hasselbalch Equation: its History and Limitations*, Journal of Chemical Education, 78 (11), 1499-1503.

[11] J. Dey and S. K. Dogra (1991). *Electronic Absorption and Fluorescence Spectra of 2-phenyl-substituted Benzothiazoles: Study of Excited-State Proton Transfer Reactions*, Canadian Journal of Chemistry, 69 (10), 1539-1547.

[12] H. M. Chen, J. A. Parkinson, S. Parsons, R. A. Coxall, R. O. Gould and P. J. Sadler (2002). *Organometallic Ruthenium(II) Diamine Anticancer Complexes: Arene-Nucleobase Stacking and Stereospecific Hydrogen-Bonding in Guanine Adducts*, Journal of the American Chemical Society, 124 (12), 3064-3082.

[13] Y. K. Yan, M. Melchart, A. Habtemariam and P. J. Sadler (2005). *Organometallic Chemistry, Biology and Medicine: Ruthenium Arene Anticancer Complexes*, Chemical Communications, (38), 4764-4776.

[14] J. S. Ren and J. B. Chaires (1999). *Sequence and Structural Selectivity of Nucleic Acid Binding Ligands*, Biochemistry, 38 (49), 16067-16075

[15] S. Neidle (2001). *DNA Minor-Groove Recognition by Small Molecules*, Natural Product Reports, 18 (3), 291-309.

[16] B. Suter, G. Schnappauf and F. Thoma (2000). *Poly(dA · dT) Sequences Exist as Rigid DNA Structures in Nucleosome-Free Yeast Promoters in Vivo*, Nucleic Acids Research, 28 (21), 4083-4089.

[17] C. Bailly and J. B. Chaires (1998). *Sequence-Specific DNA Minor Groove Binders. Design and Synthesis of Netropsin and Distamycin Analogues*, Bioconjugate Chemistry, 9 (5), 513-538.

[18] F. R. Keene, J. A. Smith and J. G. Collins (2009). *Metal Complexes as Structure-Selective Binding Agents for Nucleic Acids*, Coordination Chemistry Reviews, 253 (15), 2021-2035.

[19] A. E. Friedman, J.-C. Chambers, J.-P. Sauvage, N. J. Turro and J. K. and Barton (1990). *A Molecular Light Switch for DNA: $Ru(bpy)_2(dppz)^{2+}$*, Journal of the American Chemical Society, 112 (12), 4960-4962.

[20] Y. Sun, D. A. Lutterman and C. Turro (2008). *Role of Electronic Structure on DNA Light-Switch Behavior of Ru(II) Intercalators*, Inorganic Chemistry, 47 (14), 6427-6434.

[21] D. A. Lutterman, A. Chouai, Y. Liu, Y. Sun, C. D. Stewart, K. R. Dunbar and C. Turro (2008). *Intercalation Is not Required for DNA Light-Switch Behavior*, Journal of the American Chemical Society, 130 (4), 1163-1170.

[22] A. G. Zhang, Y. Z. Zhang, Z. M. Duan, K. Z. Wang, H. B. Wei, Z. Q. Bian, C. H. Huang (2011). *Dual Molecular Light Switches for pH and DNA Based on a Novel Ru(II) Complex. A Non-Intercalating Ru(II) Complex for DNA Molecular Light Switch*, Inorganic Chemistry, 50 (14), 6425-6436.

[23] G. S. Yellol, A. Donaire, J. G. Yellol, V. Vasylyeva, C. Janiak and J. Ruiz (2013). *On the Antitumor Properties of Novel Cyclometalated Benzimidazole Ru(II), Ir(III) and Rh(III) Complexes*, Chemical Communications, 49 (98), 11533-11535.

[24] N. Busto, J. Valladolid, M. Martínez-Alonso, H. J. Lozano, F. A. Jalón, B. R. Manzano, A. M. Rodríguez, M. C. Carrión, T. Biver, J. M. Leal, G. Espino and B. García (2013). *Anticancer Activity and DNA Binding of a Bifunctional Ru(II) Arene Aqua-Complex with the 2,4-Diamino-6-(2-Pyridyl)-1,3,5-Triazine Ligand*, Inorganic Chemistry, 52 (17), 9962–9974.

[25] W. Weber and P. C. Ford (1986). *Photosubstitution Reactions of the Ruthenium(II) Arene Complexes Ru($\eta^6-arene$)L_3^{2+} (L=NH_3 or H_2O) in Aqueous Solution*, Inorganic Chemistry, 25 (8), 1088-1092.

[26] F. Barragán, P. López-Senín, L. Salassa, S. Betanzos-Lara, A. Habtemariam, V. Moreno, P. J. Sadler and V. J. Marchán, (2011). *Photocontrolled DNA Binding of a Receptor-Targeted Organometallic Ruthenium(II) Complex*, Journal of the American Chemical Society, 133 (35), 14098–14108.

[27] S. W. Magennis, A. Habtemariam, O. Novakova, J. B. Henry, S. Meier, S. Parsons, I. D. H. Oswald, V. Brabec and P. J. Sadler (2007). *Dual Triggering of DNA Binding and Fluorescence via Photoactivation of a Dinuclear Ruthenium(II) Arene Complex*, Inorganic Chemistry, 46 (12), 5059-5068.

Supporting Information

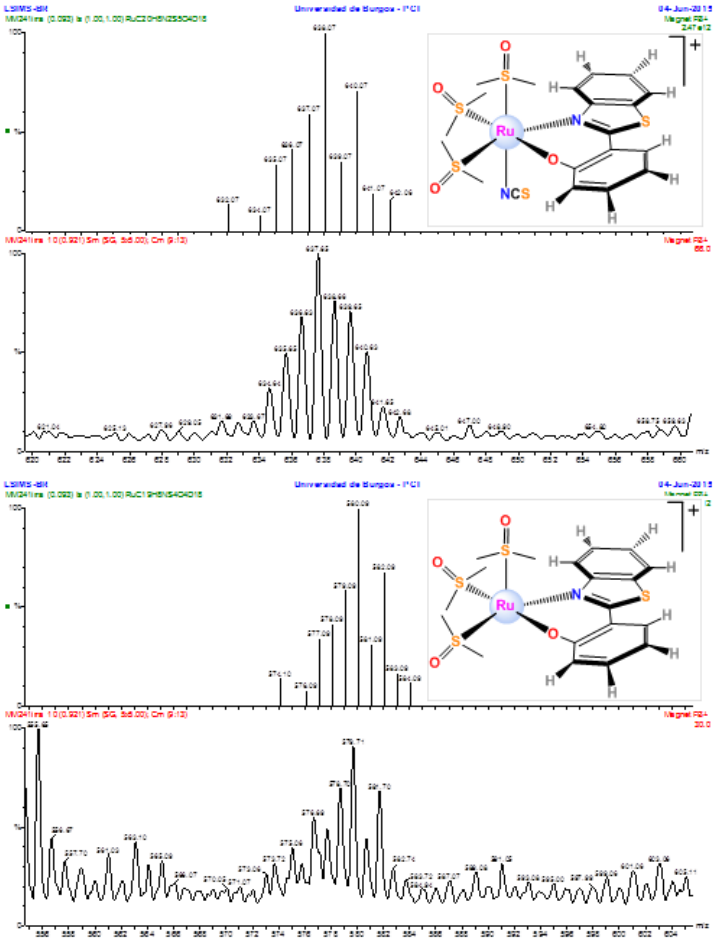

Figure 5.S1: FAB-MS of [**Ru-1***]. Theoretical and experimental spectrum of the observed fragments. m/z=580 ([**Ru-1***−NCS]$^+$), 638 ([**Ru-1**−(p−cym)$^+$3DMSO$_d$6]$^+$ = [**Ru-1***]$^+$).

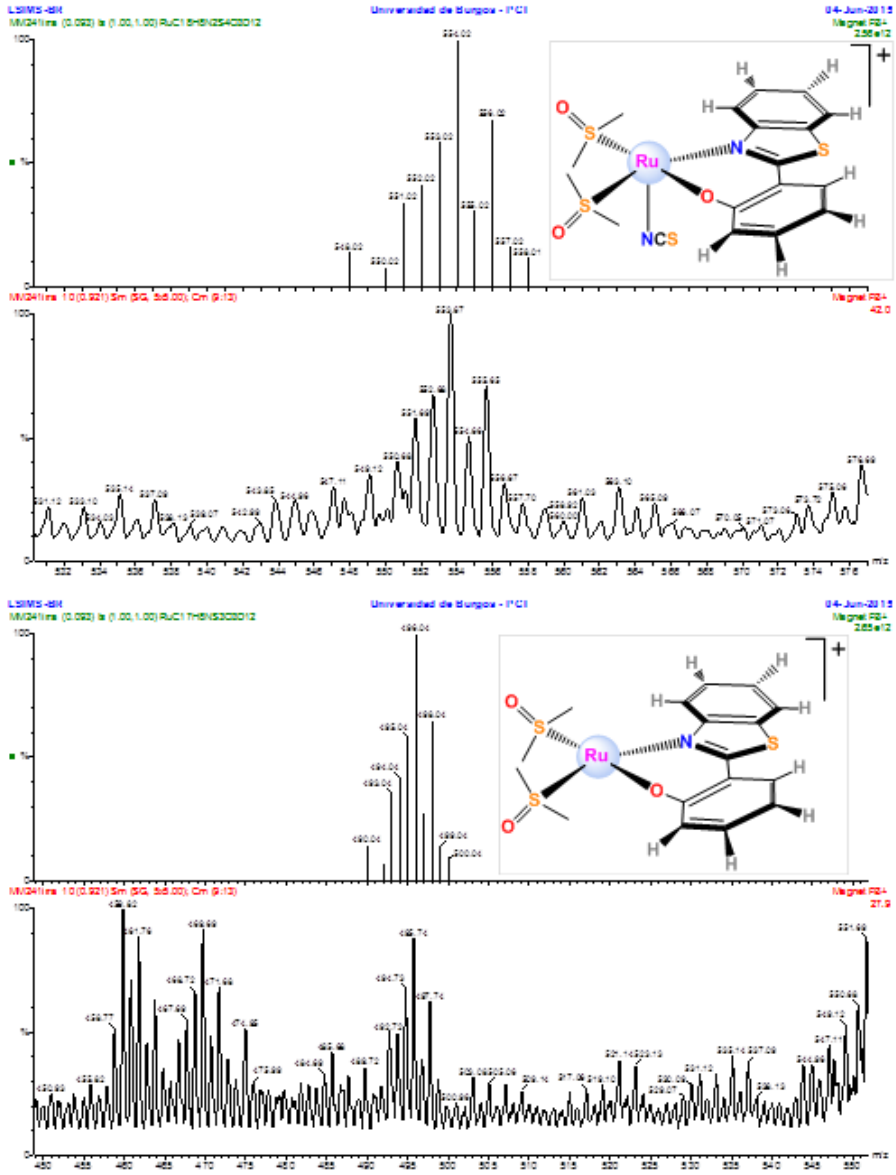

Figure 5.S2: FAB-MS of [**Ru-1***]. Theoretical and experimental spectrum of the observed fragments. m/z=496 ([**Ru-1***−NCS−DMSO−d_6]$^+$), 554 ([**Ru-1***−DMSO−d_6]$^+$).

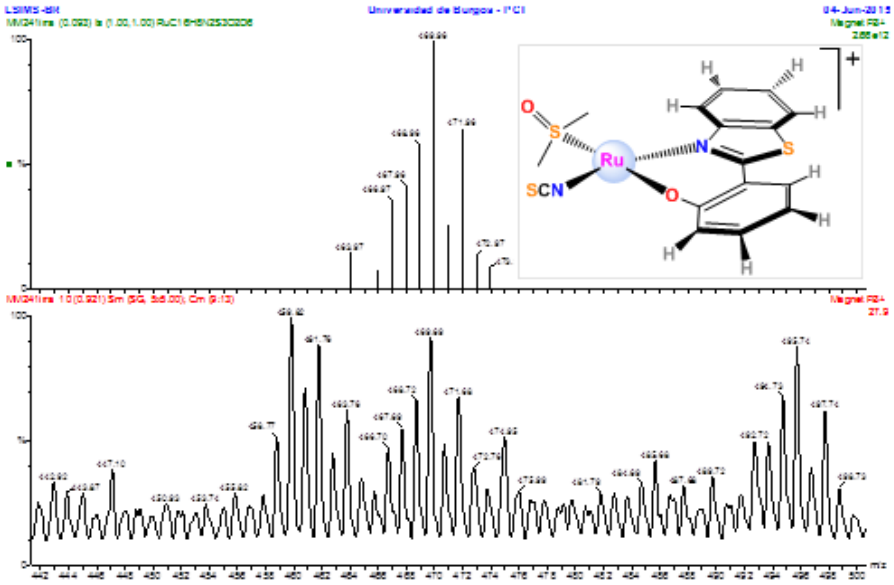

Figure 5.S3: FAB-MS of [**Ru-1***]. Theoretical and experimental spectrum of the observed fragments. m/z=470 ([**Ru-1***−2DMSO−d_6]$^+$).

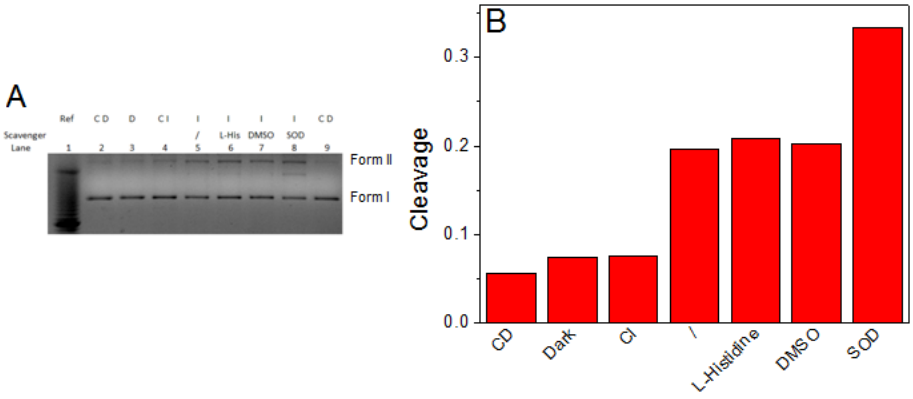

Figure 5.S4: (A) Electrophoresis of the irradiated **aquo[Ru-1]**/pUC18 system in presence of scavengers. Lane 1: Molecular weight marker. Lane 2: Dark control. Lane 3: **aquo[Ru-1]**/pUC18 in the dark. Lane 4: Irradiated control. Lane 5: Irradiated **aquo[Ru-1]**/pUC18. Lane 6: Irradiated **aquo[Ru-1]**/pUC18 + [L-His]=1.2 mM. Lane 8: Irradiated **aquo[Ru-1]**/pUC18 + [DMSO]=200 mM. Lane 9: Irradiated **aquo[Ru-1]**/pUC18+ [SOD]=1000 Uml^{-1}. Lane 9: Dark control. C_D=20 µM, C_P=20 µM; [$NaClO_4$]=4.0×10^{-3} M; [NaCac]=2.5×10^{-3} M, pH=7.0. Irradiation: λ_{irr}=325 nm and t_{irr}=140 min. Incubation at T=37 °C, overnight. (B) Quantification of the cleavage in the presence of scavengers.

5.A Determination of Equation (5.6)

Considering the Reaction (5.A.1) between a dye D and a monomeric unit P.

$$\mathrm{P} + \mathrm{D} \underset{}{\overset{K_1}{\rightleftarrows}} \mathrm{PD} \underset{k_{-2}}{\overset{k_2}{\rightleftarrows}} \mathrm{PD}^* \tag{5.A.1}$$

where K_1 is the equilibrium of the fast preliminary reaction defined in Equation (5.A.2), being $[P]$, $[D]$ and $[PD]$ the concentration of the free P, the free D and the PD complex

$$K_1 = \frac{[PD]}{[P][D]} \tag{5.A.2}$$

The variation of $[PD^*]$ with time is given by Equation (5.A.3)

$$\frac{d[PD]}{dt} = k_2[PD] - k_{-2}[PD^*] \tag{5.A.3}$$

where k_1 and k_{-1} are the kinetic constants of the direct and the inverse reaction of formation of the second adduct, respectively, being $[PD^*]$ its concentration. In a very short δt time the formula is converted into

$$\frac{d\delta PD^*}{dt} = k_2\delta PD - k_{-2}\delta PD^* \tag{5.A.4}$$

The anaytical concentration C_D of the dye D and C_P of the P unit, are given by Eqs. (5.A.5) and (5.A.6)

$$C_D = [D] + [PD] + [PD^*] \tag{5.A.5}$$

$$C_P = [P] + [PD] + [PD^*] \tag{5.A.6}$$

Considering that we worked in an excess of P, it follows that $C_P \approx [P]$ and, expressing $[D]$ in the (5.A.5) using Equation (5.A.2), we obtain

$$C_D = \frac{[PD]}{K_1 C_P} + [PD] + [PD^*] \tag{5.A.7}$$

In a δt time the Equation (5.A.8) is given

$$0 = \frac{\delta PD}{K_1 C_P} + \delta PD + \delta PD^* \Rightarrow \delta PD = -\frac{K_1 C_P}{1 + K_1 C_P}\delta PD^* \tag{5.A.8}$$

Inserting the (5.A.8) in the Equation (5.A.4) we obtain the (5.A.9)

$$\frac{d\delta PD^*}{dt} = -k_2\frac{K_1 C_P}{1 + K_1 C_P}\delta PD^* - k_{-2}\delta PD^* \tag{5.A.9}$$

Expressing $-\frac{d\delta PD^*}{\delta PD^* dt} = \frac{1}{\tau}$, the rate constant results by the Equation (5.A.10)

$$\frac{1}{\tau} = k_2\frac{K_1 C_P}{1 + K_1 C_P} + k_{-2} \tag{5.A.10}$$

If the reaction is irreversible, $k_{-1} = 0$ and the final Equation (5.A.11) will be

$$\frac{1}{\tau} = k_2\frac{K_1 C_P}{1 + K_1 C_P} \tag{5.A.11}$$

Chapter 6

Biscyclometalated Iridium and Rhodium Complexes. DNA Binding and Photoreactivity

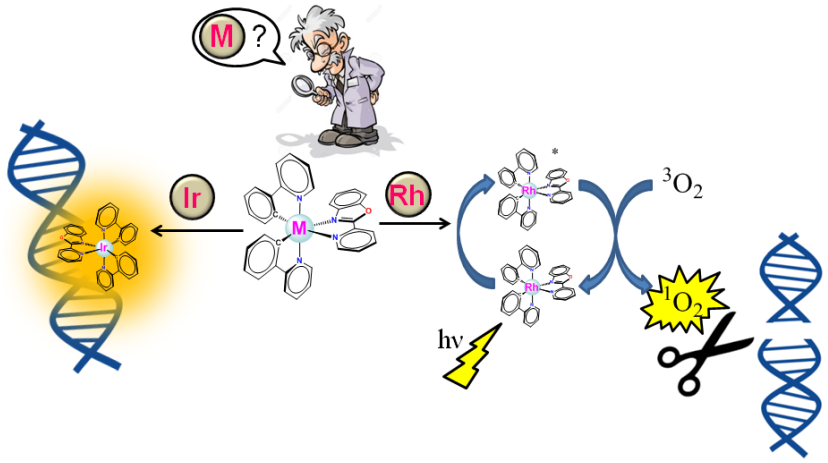

The interaction of the ruthenium arene complex towards DNA summarized in Chapter 5 showed an interesting dual binding mode. However, low photocleavage of plasmid DNA was found, and only at high irradiation energy (325 nm).
For this reason we took into account a new class of metal complexes: the biscyclometalated ones. Here in Chapter 6, we treat two new biscyclometalated systems, differing only by the metal center, the $[Ir(ppy)_2(pyboz)]Cl$ (**[Ir-1]**Cl) and the $[Rh(ppy)_2(pyboz)]Cl$ (**[Rh-1]**Cl) complexes. Our study was focused on the reactivity differences of such compounds in the absence of irradiation and photoirradiated. Proofs in the dark regarded the interaction with CT-DNA, whereas photocleavage was evaluated in the presence of plasmid pUC18.

In the absence of a source of irradiation, the interaction of the iridium and the rhodium complexes with CT-DNA was quite similar. Interestingly, the iridium complex displayed increase of the fluorescence, whereas emission decrease was visualized for [**Rh-1**]Cl, ascribable to the different nature of the electronic states of the metal complexes.
Moreover, irradiation of the rhodium complex at 365 nm provoked an extensive cleavage of DNA; on the other side, the iridium complex exhibited very low photoactivity. Studies in the presence of scavengers demonstrated that singlet oxygen is involved in the mechanism of reaction, confirmed also by singlet oxygen detection experiments. In addition, a minority effect provoked the photodissociation of the ancillary ligand and the resulting product was seen to bind covalently to 9-MeG through an oxygen-independent pathway. MTT proofs showed an increase of cytotoxicity for the rhodium complex under irradiation, in agreement with the photocleavage study.
Such work reveals the importance of the metal center in the biscyclometalated complexes. Further study on the contribution of the ligands in the reactivity of such a class of compounds towards nucleic acids and their photoreactivity is treated in Chapter 7.

6.1 Materials and Methods

6.1.1 Materials

The examined iridium and rhodium complexes are the $[Ir(ppy)_2(pyboz)]Cl$ and the $[Rh(ppy)_2(pyboz)]Cl$ complexes, named as [**Ir-1**]Cl and [**Rh-1**]Cl, respectively, whose structures are drawn in Figure 6.1.

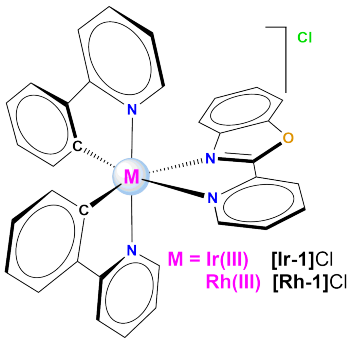

Figure 6.1: Molecular structure of [**Ir-1**]Cl and [**Rh-1**]Cl.

The complexes have been synthesized by Dr. Martinez-Alonso from Inorganic Chemistry Laboratory of the Universidad de Burgos and they have been previously fully characterized. Stock solutions of [**Ir-1**]Cl and [**Rh-1**]Cl were prepared in water, which resulted stable over weeks by checking the absorption spectra. Calf Thymus DNA sodium salt was purchased from Sigma Aldrich and prepared according to Chapter 2. Working solution were prepared in [NaCl]=4.0 mM and [NaCac]=2.5 mM buffer (I=6.5 mM and pH=7.0). Ionic strength was attained by concentrated solutions of NaCl, whereas suitable pH was reached by addition

of concentrated solutions of NaOH and HCl.

6.1.2 Methods

UV-vis absorption titrations were carried out with an Evolution 300 UV-VIS double beam spectrophotometer (Thermo Scientific), adding increasing concentration of CT-DNA to the reference and to the sample, in order to subtract the contribution of the DNA to the spectra. Fluorescence steady-state and lifetime measurements were performed in a FLS980 (Edinburgh Instruments) fluorimeter. Lifetime study was performed using a laser as excitation source ($\lambda_{exc} = 375\,\text{nm}$), preparing solutions at different $\frac{C_D}{C_P}$ and recording the decay, C_D and C_P being the analytical concentration of the complex and the DNA in basepairs, respectively. Analysis of the lifetime data was performed by Global Analysis with FStat program, selecting the numbers of lifetime involved in the interaction. Circular dichroic spectra were recorded with a MOS-450 (Bio-Logic Science Instruments), equipped with a Xenon Arc Lamp. It is coupled with a Julabo F30 thermostat (precision of 0.1 °C). The experiments were carried out adding the metal complex to a solution of CT-DNA and recording the spectra in the 200-600 nm, scan rate $0.5\,\text{nm}\,\text{s}^{-1}$. DSC experiments were performed for different $\frac{C_D}{C_P}$ ($C_P = 3.0 \times 10^{-4}\,\text{M}$), using a NanoDSC (TA Instrument) and scanning the sample from 20 to 100 °C at 3 atm (scan rate $1\,^{\circ}\text{C}\,\text{min}^{-1}$). Isothermal Titration Calorimetry technique was employed using a NanoITC, degassing the solution with a TA Degassing Station (2×15 min). A solution of CT-DNA was inserted in the sample cell and the metal complex was added to the cell by means of a syringe under stirring (25 additions of 2 µL, waiting 5 min after each addition). Analysis of the titration was obtained by the NanoAnalyze program. Viscometry measurements were performed with a Ubbelhode Microviscometer for different $\frac{C_D}{C_P}$ ratios and analysed by Equation (2.20) (Chapter 2, Section 2.2.7). NMR samples were prepared under a N_2 atmosphere in the respective oxygen-free deuterated solvent, and the spectra were recorded at 298 K on a Varian Unity Inova-400 (399.94 MHz for ^{1}H). 1D ^{1}H-NMR spectra were acquired with 32 scans into 32 K data points over a spectral width of 16 ppm and the chemical shifts were internally referenced to tetramethylsilane via 1,4-dioxane in D_2O (δ=3.75 ppm). All NMR data processing was carried out using MestReNova v10.0.2-15465. Mass spectrometry samples were analysed by an Agilent Instrument, equipped with a TOF mass analyzer. Photoirradiation and cleavage study were performed according to Chapter 2, Sections 2.10 and 2.11.

6.2 Results and Discussion

6.2.1 Metal Complex Properties

Various absorption peaks result from the biscycometalated complex spectra, which can be related to different transitions [1]: bands with high extinction molar coefficient ($>30\,000\,\text{M}^{-1}\text{cm}^{-1}$) are ascribable to spin-allowed ligand centered transitions (^{1}LC), whereas above 350 nm, the lower peaks are associated to spin forbidden LC and spin allowed MLCT transitions. Then, above 400 nm, very low absorption is perceptible for iridium complex, which is related to the spin forbidden MLCT transition.

The luminescence properties are listed in Table 6.1. Fluorescence of the complexes are quite different: iridium complex has a broad and unstructured emission peak and exhibits large stoke shift; on the other hand, rhodium complex has a structured peak and emits at shorter wavelengths than iridium does. Both complexes exhibit low quantum yield fluorescence in air equilibrated water, calculated by comparison with the $Ru(bpy)_3{}^{2+}$ quantum yield ($\Phi = 0.028$ in water) [2]. Interestingly, the rhodium species has a long lifetime in comparison with the iridium one.

Table 6.1: *Emission parameters in water. Φ is the fluorescence quantum yield and τ is the lifetime (in brackets the fractional intensity for each τ).*

Complex	λ_{ex}^{max}, nm	λ_{em}^{max}, nm	Φ	τ, ns
[**Ir-1**]Cl	310	625	0.0013	10.3 (0.90), 217 (0.10)
[**Rh-1**]Cl	303	542	0.0021	540

The analysis of the luminescent properties of rhodium and iridium complexes is quite present in literature and important differences are reported [3, 4]. In addition, large efforts were carried out in the study of the excited states of iridium and rhodium cyclometalated complexes [5–10]. For biscyclometalated complexes, structured peaks as the one observed for the rhodium complex are associated to ^{3}LC transitions, whereas unstructured peaks are generally due to ^{3}MLCT. Actually, a recent paper [11] reports TD-DFT calculation for the new synthesized [**Ir-1**]PF_6 complex, which demonstrates that the lowest T_1 triplet excited state has a mixing ^{3}MLCT-^{3}LLCT nature.
The absorption spectra of the compounds did not change by varying the pH of the solutions in the pH=2-11 range, in agreement with the absence of acid/base behaviour. However, a decomposition process occurred for basic conditions (pH>12, Figure 6.2). In addition, no dimerization or aggregation effect was detected by absorption under the experimental conditions (Figure 6.S1).

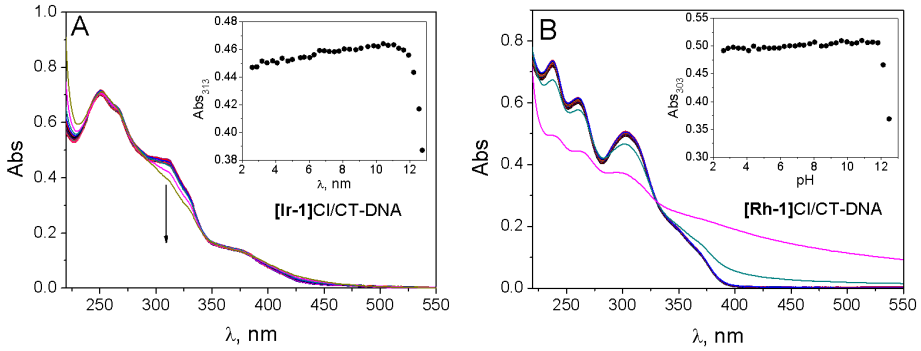

Figure 6.2: UV-vis absorption spectra at different pH values. (A) [**Ir-1**]Cl, inset: track at 313 nm. (B) [**Rh-1**]Cl, inset: track at 303 nm. C_D=20 µM I=6.5 mM (NaCl), T=25.0 °C.

6.2.2 Interaction with CT-DNA

6.2.2.1 UV-vis Absorption Titration

Preliminary tests by means of spectrophotometry proved that no slow interaction is present for the complexes in the presence of CT-DNA and *d*GMP monomeric unit (data not shown). Consequently, we assumed a fast interaction between the metal complexes and DNA.
UV-vis titrations with CT-DNA caused hypochromism of the bands for both metal complexes, reported in Figure 6.3 (8 % for **[Ir-1]**Cl and 11 % for **[Rh-1]**Cl).

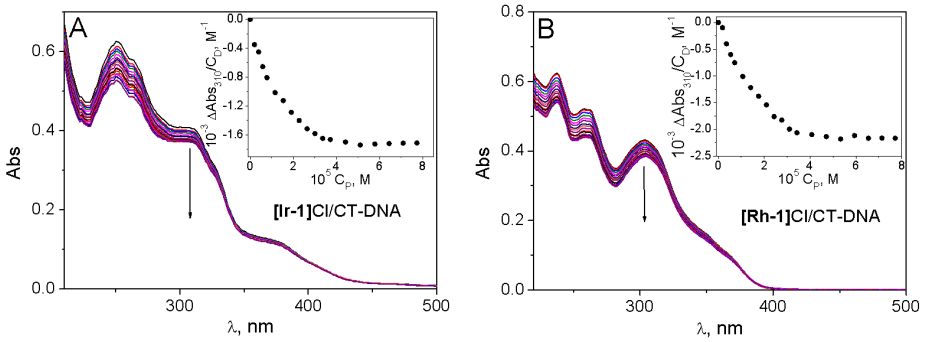

Figure 6.3: (A) **[Ir-1]**Cl/CT-DNA UV-vis titration. Inset: track at 310 nm. (B) **[Rh-1]**Cl/CT-DNA UV-vis titration. Inset: track at 310 nm. C_D=20 µM, I=6.5 mM (NaCl), pH=7.0 (NaCac), T=25.0 °C.

Data treatment by means of Equation (2.46) and Scatchard Plot (Equation (2.55), Figure 6.S2, [12]) allows to determine a constant (K) and a dimension site (n, using the McGhee and von Hippel correction, Equation (2.58) [13]). The obtained values are very similar: for the **[Ir-1]**Cl/CT-DNA system, K=$(5 \pm 1) \times 10^5 \mathrm{M}^{-1}$ and n=1.1 ± 1; for the **[Rh-1]**Cl/CT-DNA system, K=$(6 \pm 1) \times 10^5 \mathrm{M}^{-1}$ and n=1.2 ± 0.1. This result suggests the same kind of interaction to DNA for both compounds.

6.2.2.2 ITC

The titrations of CT-DNA with increasing amounts of the metal complexes reveal two effects for both systems by isothermal titration calorimetry (Figure 6.4), differently from the absorption titrations, where only one effect was observed (Figure 6.3). As the blank proofs did not show any effect, the observed tracks were related to the direct interaction of the CT-DNA with the metal complexes. The data were plotted by means of the *multiple site* model provided by the NanoAnalyze program.
Consequently, we can hypothesize two different modes of binding, whose contributions to the overall interaction of the metal to DNA depend on the $\frac{C_D}{C_P}$ ratio.

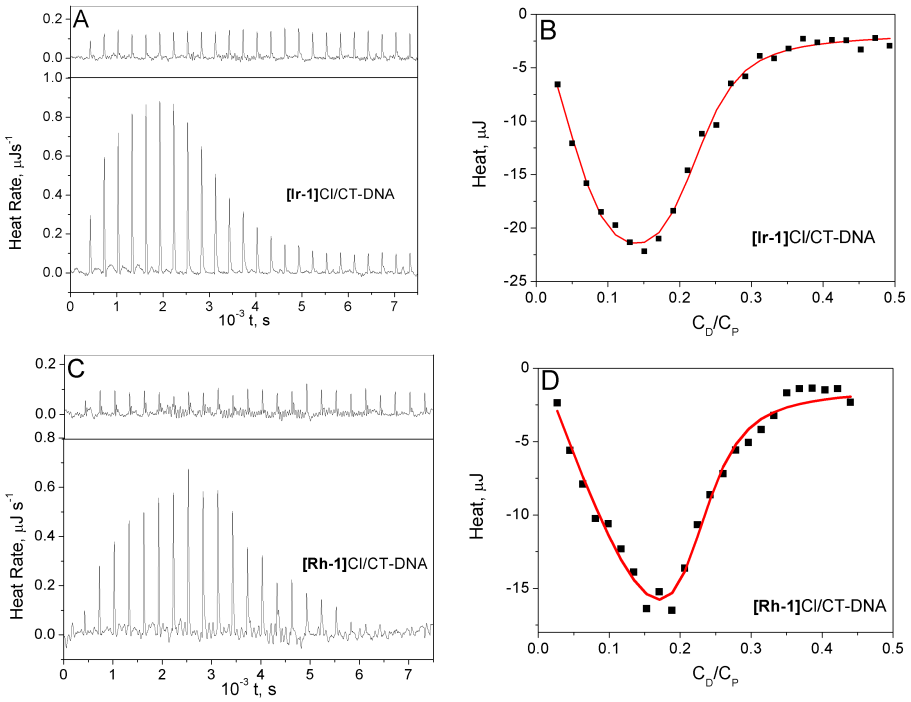

Figure 6.4: Isothermal Titration Calorimetry. (A) [**Ir-1**]Cl/CT-DNA titration; C_P^0=5.0 × 10^{-4} M. (B) [**Ir-1**]Cl/CT-DNA proposed model; straight line: theoretical data; dots: experimental data. (C) [**Rh-1**]Cl/CT-DNA titration; C_P^0=5.0 × 10^{-4} M. (D) [**Rh-1**]Cl/CT-DNA proposed model; straight line: theoretical data; dots: experimental data. I=6.5 mM (NaCl), pH=7.0 (NaCac), T=25.0 °C

In literature, a biphasic behaviour, in particular an exothermic process followed by an endothermic reaction, has been observed in the interaction of some octahedral metal complexes with CT-DNA [14, 15], and it is ascribed to a dual mode of binding of the complex, due to a canted and a central intercalation of the ancillary ligand, respectively. The thermodynamic values obtained by the [**Ir-1**]Cl/CT-DNA and [**Rh-1**]Cl/CT-DNA titrations are listed in Table 6.2.

Table 6.2: *Thermodynamic values obtained from the plotting of the ITC titrations of the [**Ir-1**]Cl/CT-DNA and [**Rh-1**]Cl/CT-DNA systems. K is the equilibrium constant and ΔH the enthalpy of the reaction. Confidence interval* 95 %.

Parameters	[**Ir-1**]Cl/CT-DNA	[**Rh-1**]Cl/CT-DNA
K_1, M^{-1}	$(9 \pm 6) \times 10^5$	$(9 \pm 6) \times 10^5$
K_2, M^{-1}	$(3 \pm 1) \times 10^5$	$(4 \pm 2) \times 10^5$
ΔH_1, kJ mol^{-1}	1.3 ± 0.7	1.8 ± 0.3
ΔH_2, kJ mol^{-1}	-4.0 ± 0.7	-4.0 ± 0.3

The obtained values are quite similar, as we observed by means of the absorp-

tion titrations; it means that the metal center does not influence the reversible interaction with DNA. The result makes sense for the reason that iridium and rhodium exhibit the same oxidation number and the electronic density of the molecule most likely is the same.

6.2.2.3 Fluorimetric Titration

Titrations were performed in fluorimetry, as well (Figure 6.5).

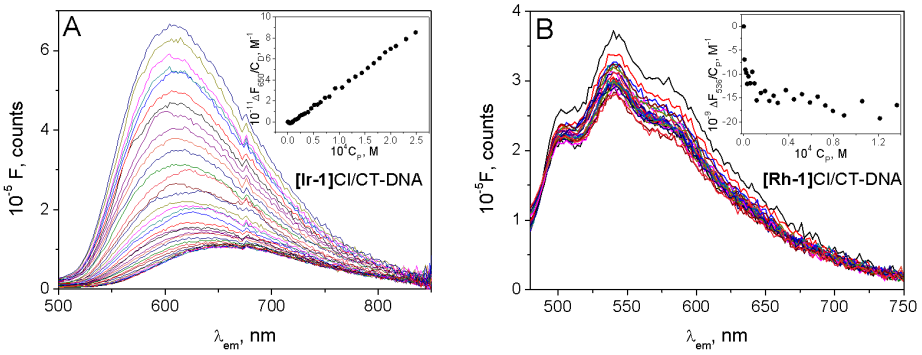

Figure 6.5: Fluorimetric titration of the metal complex with CT-DNA. (A) **[Ir-1]**Cl/CT-DNA, λ_{ex}=335 nm; inset at λ_{em}=650 nm. (B) **[Rh-1]**Cl/CT-DNA, λ_{ex}=340 nm; inset at λ_{em}=538 nm. C_D=5.0 µM, I=6.5 mM (NaCl), pH=7.0 (NaCac) T=25.0 °C.

Initially, a decrease of the fluorescence was observed for both systems, which can be ascribable to the initial hypochromism seen in the absorption (Figure 6.3). However, for **[Ir-1]**Cl/CT-DNA a linear increase of the fluorescence was detected, which did not reach the plateaux, together with a blue shift of the signal from 640 nm to 602 nm. This effect was reported for other metal complexes [16, 17] in the presence of CT-DNA. It is likely due to the fact that the aqueous environment quenches the emission of the fluorophore, whereas the addition of a polynucleotide allows the metal complex to be shielded from the water molecules, which yields to a fluorescence switch-on [18]. For **[Rh-1]**Cl it was possible to obtain the equilibrium constant from the fluorescence decrease (Figure 6.S3), and the obtained value is $K=(4 \pm 1) \times 10^5 \mathrm{M}^{-1}$, concurring well with the ones obtained by UV-vis absorption and calorimetry titrations.
The effect of CT-DNA on the fluorescence lifetime of the biscyclometalated systems was also monitored. Notably, for **[Ir-1]**Cl a relevant increase of the fluorescence lifetime was observed (Figure 6.6A). In particular, the decrease of the $\tau_1 = 10.1$ ns contribution and the appearance of a new lifetime, $\tau_3 = 235$ ns (Figure 6.6C), was noticed, increasing the average lifetime of the species (Figure 6.6B). The average lifetime reached a plateau at $\frac{C_D}{C_P} = 1$, in agreement with the size site observed by the absorbance titration (Figure 6.S2).
On the other side, low variation of the rhodium lifetime was recorded by addition of DNA (Figure 6.7A).

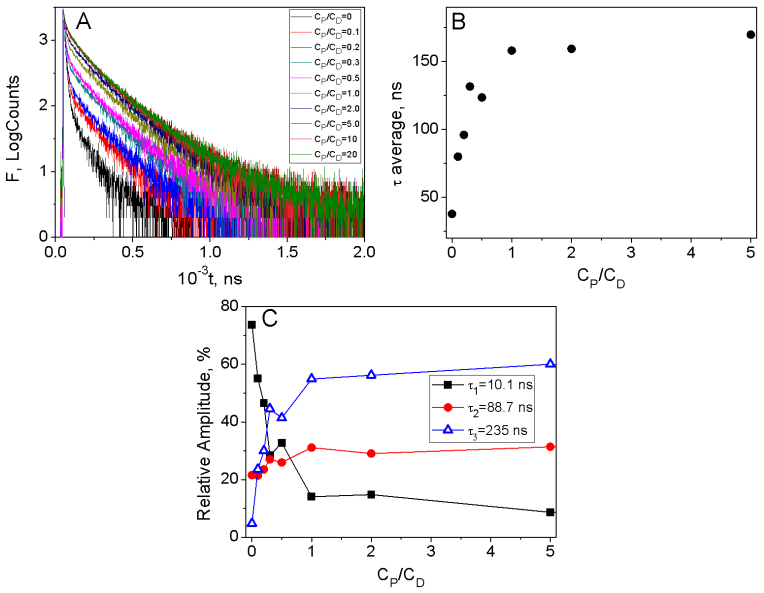

Figure 6.6: Fluorescence lifetime study of the **[Ir-1]**Cl/CT-DNA system for different $\frac{C_P}{C_D}$ ratios. (A) Fluorescence decays. (B) Average lifetimes. (C) Relative amplitudes of the lifetimes. I=6.5 mM (NaCl), pH=7.0 (NaCac), λ_{ex}=375 nm, λ_{em}=610 nm and T=25.0 °C.

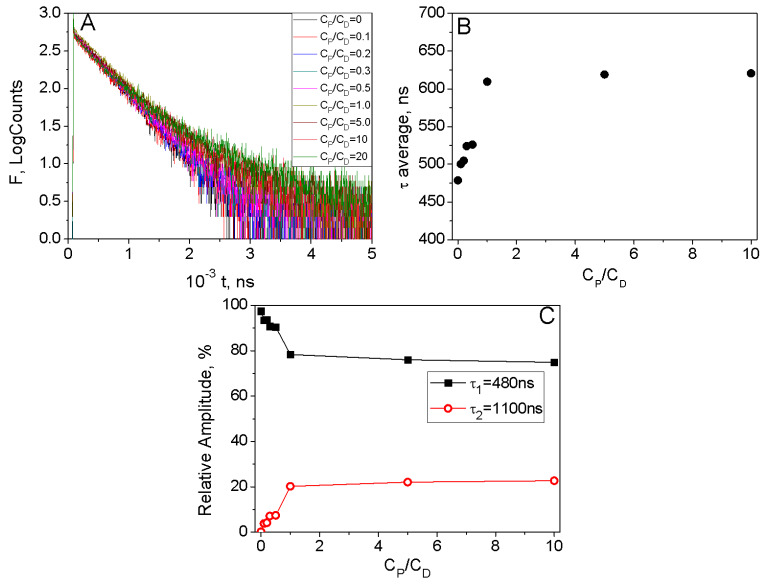

Figure 6.7: Fluorescence lifetime study of the **[Rh-1]**Cl/CT-DNA system for different $\frac{C_P}{C_D}$ ratios. (A) Fluorescence decays. (B) Average lifetimes. (C) Relative amplitudes of the lifetimes. I=6.5 mM (NaCl), pH=7.0 (NaCac), λ_{ex}=375 nm, λ_{em}=542 nm and T=25.0 °C.

In fact, another lifetime appears, but it has a low relative amplitude (Figure 6.7C) and does not remarkably influence the average lifetime (Figure 6.7B).
To sum up: on the one hand, calorimetric and UV-vis absorption titrations suggest an analogue interaction of [**Ir-1**]Cl and [**Rh-1**]Cl to CT-DNA. On the other hand, both steady-state and lifetime fluorimetric titrations reveal important differences. Diversity in the excited state of rhodium and iridium complexes can explain such behaviour. It is important to recall here that rhodium biscyclometalated complexes have ^{3}LC as lowest excited state and iridium complexes a ^{3}LC/^{3}MLCT mixing state. Hence, we have a molecule, the [**Ir-1**]Cl, whose fluorescence is highly sensitive to external variation; differently, [**Rh-1**]Cl excited state is only little modified by the environment [19].
As we have previously pointed out, an increase in the fluorescence intensity and lifetime means that the molecule is shielded from the quenching because of the interaction with DNA. This evidence hints an insertion of the molecule inside the DNA structure. Consequently, the most reasonably interaction is the intercalation of the ancillary ligand, which is observed for many octahedral compounds with aromatic ligands. However, the low aromatic extension of 2-(2'-pyridyl)benzoxazole probably does not allow a full intercalation of the ligand. In agreement to this, the found equilibrium constants by the different techniques are lower in comparison with the values obtained for other octahedral complexes whose ancillary ligands intercalate inside the basepairs, considering also that we worked at low ionic strength (I = 6.5 mM). For instance, 1.3×10^6, 1.1×10^6 and 1×10^6 M^{-1} equilibrium constant values have been observed for Δ−[Ru(bpy)$_2$(dppz)]$^{2+}$, Δ−[Ru(phen)$_2$(dppz)]$^{2+}$ [15] and [Ru(tpy)(py)(dppz)]$^{2+}$ (dppz=dipyrido[3,2-a:2',3'-c]phenazine) [14] at I=0.15 M.

6.2.2.4 Circular dichroism

Addition of metal complex to a DNA solution provoked the decrease of the dichroic maxima of CT-DNA, as it can be observed in Figure 6.8.

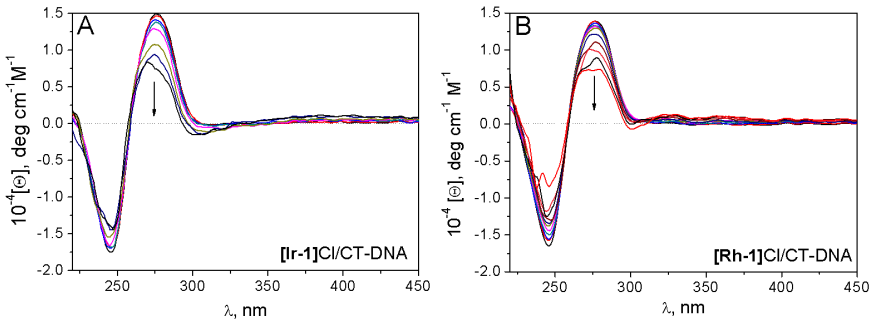

Figure 6.8: Dichroic spectra of CT-DNA for different $\frac{C_D}{C_P}$ ratios. (A) [**Ir-1**]Cl and (B) [**Rh-1**]Cl. C_P=5.0 × 10^{-5} M, $\frac{C_D}{C_P}$=0-1.0, I=6.5 mM (NaCl), pH=7.0 (NaCac), T=25.0 °C.

In addition, small peaks seem to appear above 300 nm, which could be accountable to a weak induced dichroism proportioned by the nucleic acid to the metal

complexes, once they interacted with the polynucleotide.

6.2.2.5 Viscometry

A remarkable decrease of $(\frac{\eta}{\eta_0})^{\frac{1}{3}}$ was visualized for increasing value of the metal complexes (Figure 6.9). This effect excludes classical intercalation. However, partial intercalation, which kinks the secondary structure of the nucleic acid, could explain a decrease of the chain elongation and, consequently, the viscometric data [20].

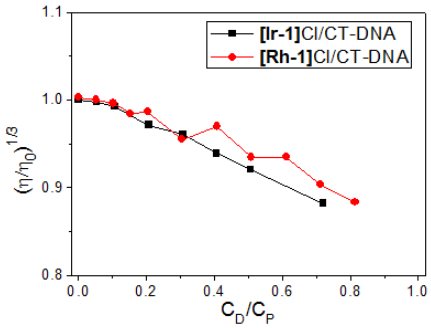

Figure 6.9: Viscometric data for the **[Ir-1]**Cl/CT-DNA and **[Rh-1]**Cl/CT-DNA systems for different $\frac{C_D}{C_P}$ ratios. C_P=2.0 $\times$ 10^{-4} M, I=6.5 mM and T=25.0 °C.

6.2.2.6 DSC

Figure 6.10 reports a slight increase of the melting temperature for increasing $\frac{C_D}{C_P}$ values, so a little stabilization of the double-helix structure is provided by the presence of the metal complexes.

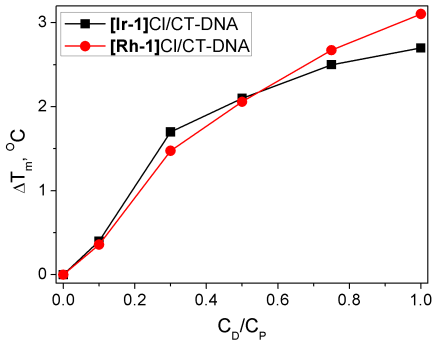

Figure 6.10: Melting temperature of CT-DNA for increasing $\frac{C_D}{C_P}$ for the **[Ir-1]**Cl/CT-DNA and **[Rh-1]**Cl/CT-DNA systems. C_P=3.0 $\times$ 10^{-4} M, I=6.5 mM and pH=7.0.

The resulting melting temperature enhancement (ΔT=2.5-3 °C) is not so high as to be associable to a full intercalation of the system, but, rather, to a partial intercalation, in agreement with the previous results.

6.2.3 Photoreactivity

6.2.3.1 Irradiation Study

First of all, proofs of irradiation of a complex solution were carried out and the effect of light was checked by absorbance and NMR (Figure 6.11 and 6.12).

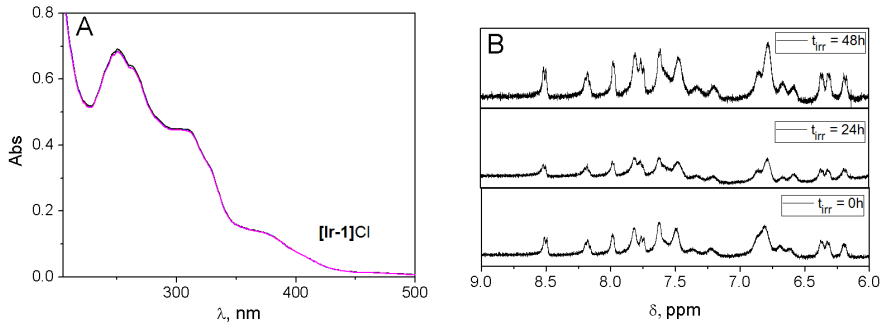

Figure 6.11: Irradiation of [**Ir-1**]Cl in deoxygenated solutions. (A) UV-vis absorption spectra for different irradiation times (t_{irr}=0-200 min); C_D=30 µM, I=6.5 mM (NaCl), pH=7.0. (B) ^{1}H-NMR in D_2O, C_D=3.7 mM. λ_{irr}=365 nm and T=25.0 °C.

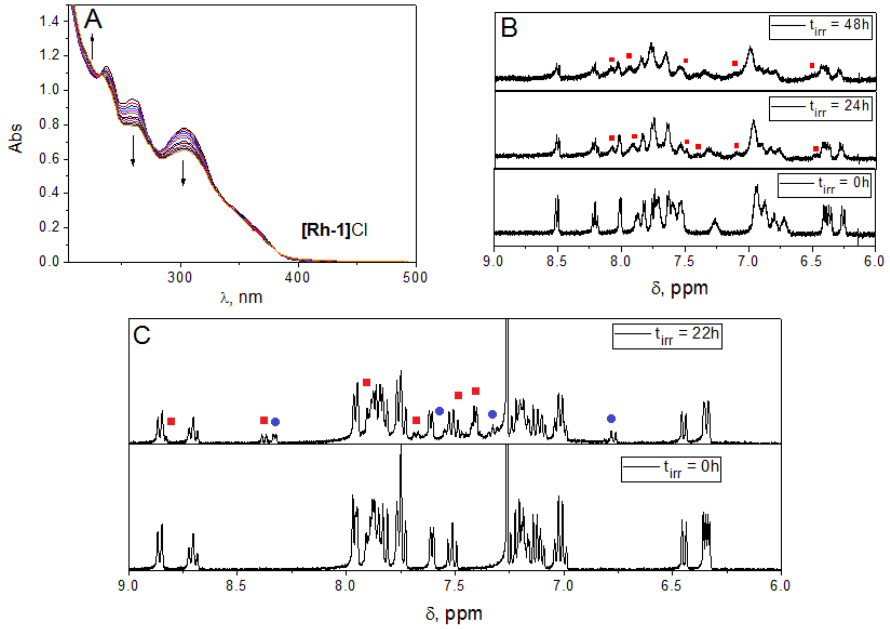

Figure 6.12: Irradiation of [**Rh-1**]Cl in deoxygenated solutions. (A) UV-vis absorption spectra for different irradiation times (t_{irr}=0-300 min); C_D=30 µM, I=6.5 mM (NaCl), pH=7.0. (B) ^{1}H-NMR in D_2O, ■ new formed peaks; C_D=3.7 mM. (C) Irradiation in $CDCl_3$−d: ■ free pyboz; • shifted Rh(ppy)$_2$ signals; C_D=5.0 mM. λ_{irr}=365 nm and T=25.0 °C.

No significant variation of the iridium complex absorption spectra was obtained at 365 nm (Figure 6.11A). Differently, the rhodium complex spectra changed after irradiation in the UV region (Figure 6.12A).
The NMR analysis confirms that new signals appeared for [**Rh-1**]Cl, whereas [**Ir-1**]Cl did not change upon irradiation (Figure 6.11B and 6.12B). Note that no peak variation was observed for [**Rh-1**]Cl left in the dark after 24 h (Figure 6.S4). The irradiation of [**Rh-1**]Cl in chloroform demonstrated that the ancillary ligand is released upon irradiation by comparison with the spectra of the free ligand [21]. As all the proofs were performed under deoxygenated conditions, the photorelease of the ligand is oxygen independent.

6.2.3.2 Photocleavage of plasmid DNA

Photocleavage proofs with pUC18 at 365 nm revealed a low photocleavaging activity by the iridium complexes (Figure 6.13), which increased only at high irradiation time (t_{irr}). On the other hand, high photocleavage of plasmid DNA was achieved in the presence of [**Rh-1**]Cl. Photocleavage increased with the rhodium concentration (Figure 6.S5) and significant amount of linear form appeared at higher irradiation time.

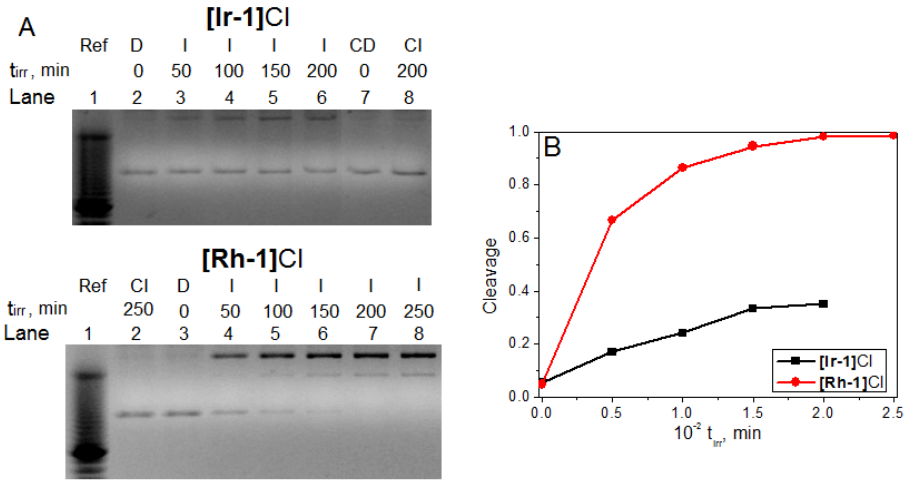

Figure 6.13: (A) Top: [**Ir-1**]Cl/pUC18 photocleavage at 365 nm. Lane 1: Molecular weight marker. Lane 2-6: Irradiated samples at t_{irr}=0, 50, 100, 150, 200 min. Lane 7: Dark Control. Lane 8: Irradiated control, t_{irr}=200 min. Bottom: [**Rh-1**]Cl/pUC18 photocleavage at 365 nm. Lane 1: Molecular weight marker. Lane 2: Irradiated control, t_{irr}=250 min. Lane 3-8: Irradiated samples at t_{irr}=0, 50, 100, 150, 200, 250 min. (B) Quantification of the cleavage by Eq. (2.31), Chapter 2. C_P=20 µM, C_D=20 µM, [NaCl]=4.0 mM, [NaCac]=2.5 mM, pH=7.0. Incubation: T_{inc}=37.0 °C, overnight.

In order to get some information about the reaction mechanism, proofs were carried out in the presence of scavengers of oxygenated radicals. Cleavage of the [**Rh-1**]Cl/pUC18 system at λ_{irr} = 365 nm significantly decreased in the presence of NaN_3 and L−His, scavengers of singlet oxygen, and, to a lesser extent, in the presence of superoxide dismutase, scavenger of superoxide anion (Figure 6.14). Cleavage did not change in the presence of DMSO, scavenger of

the hydroxyl radical.

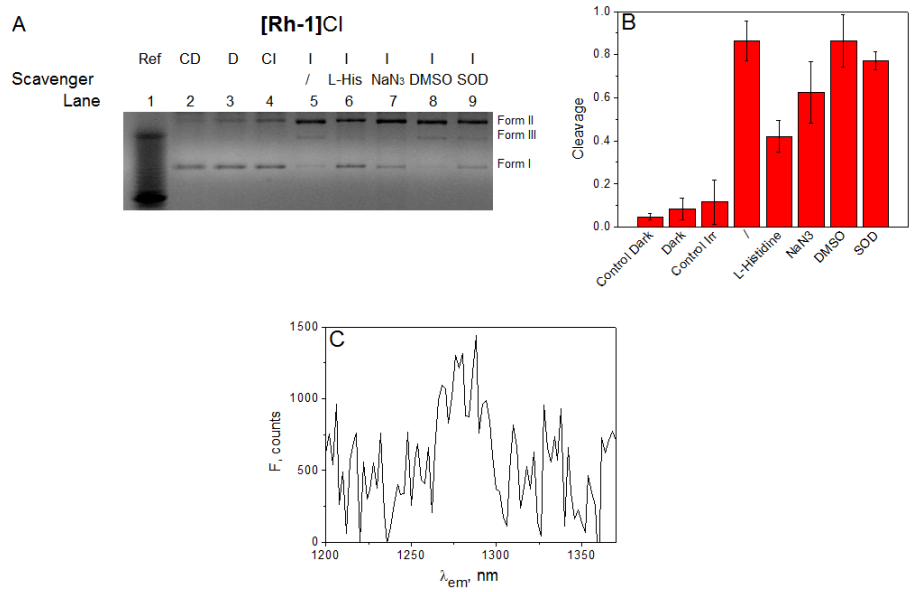

Figure 6.14: (A) Electrophoresis of **[Rh-1]**Cl/pUC18 in the presence of scavengers. Lane 1: Molecular weight marker. Lane 2: Dark Control. Lane 3: Sample left in the dark. Lane 4: Irradiated control. Lane 5: Irradiated sample. Lane 6: Irradiated sample + [L−His]=1.2 mM. Lane 7: Irradiated sample + [NaN_3]=10 mM. Lane 8: Irradiated sample + [DMSO]=200 mM. Lane 9: Irradiated sample + [SOD]=1000 UmL^{-1}. C_D=20 µM, C_P=20 µM, [NaCl]=4.0 mM, [NaCac]=2.5 mM, pH=7.0, t_{irr}=100 min, λ_{irr}=365 nm. Incubation: T_{inc}=37 °C, overnight. (B) Quantification of the cleavage (mean value of three independent experiments). (C) Phosphorescence of the singlet oxygen produced by a solution of **[Rh-1]**Cl in D_2O, irradiated at λ_{irr} = 325 nm.

Consequently, a conceivable mechanism of action would involve the excitation of the rhodium complex, which transfers its energy to oxygen by collisions. Hence, oxygen is excited from the triplet ground state to the singlet excited state, which provokes DNA cleavage. Singlet oxygen was also observed by its phosphorescence at 1270 nm by irradiation of a **[Rh-1]**Cl solution with a HeCd laser at 325 nm in D_2O (Figure 6.14C). Comparison with singlet oxygen production by phenalenone under the same experimental conditions gave us the singlet oxygen quantum yield value, which is $\Phi_{^1\Delta_g} = 0.10$ for the rhodium complex [22].
To confirm the result, proofs with deoxygenated samples, obtained by bubbling argon for 15 min, were performed. An important lowering of the cleavage was detected in comparison with the air-equilibrated samples (Figure 6.15). It follows that the main pathway of photoreaction of the rhodium complex is oxygen-dependent (Type II Mechanism).

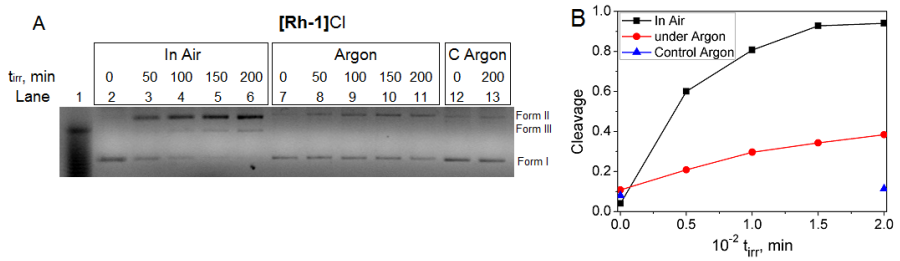

Figure 6.15: (A) Electrophoresis of [**Rh-1**]Cl/pUC18 with deoxygenated samples. Lane 1: Molecular weight marker. Lanes 2-6: Irradiated samples at t_{irr}=0, 50, 100, 150, 200 min in air. Lanes 7-11: Irradiated deoxygenated samples at t_{irr}=0, 50, 100, 150, 200 min. Lane 12: Deoxygenated dark control. Lane 13: Deoxygenated irradiated control (t_{irr}=200 min). C_D=20 µM, C_P = 20 µM, [NaCl]=4.0 mM, [NaCac]=2.5 mM, pH=7.0, λ_{irr}=365 nm. (B) Quantification of the cleavage.

6.2.3.3 Photoadduction to Guanine

From the collected results, we have verified that irradiation of [**Rh-1**]Cl is the cause of (i) singlet oxygen production and (ii) release of the ancillary ligand, being this an oxygen-independent mechanism. So, excitation of the metal complex seems to have three different pathways: emission, non-radiative energy transfer to triplet oxygen and slow photodissociation. The photoproduct, which reasonably is the $Rh(ppy)_2^+$ because of the observed release of the ancillary ligand in ^{1}H-NMR (Figure 6.12C), could be accountable of part of the photoreactivity.
To verify it, solutions of [**Rh-1**]Cl in the presence of 9-methylguanine (9-MeG) were prepared and irradiated at 365 nm for different irradiation times. Then, the solutions were analysed by means of a high-resolution mass spectrometry to detect the exact formula of the photoproducts. Little decomposition was observed for the complex, even though two new peaks can be related to the formation of adducts between the rhodium complex and 9-MeG. The signal at 576 m/z (Figure 6.16) is due to the release of the ancillary ligand and the formation of the covalent binding with the guanine moiety, reasonably to N_7 position.

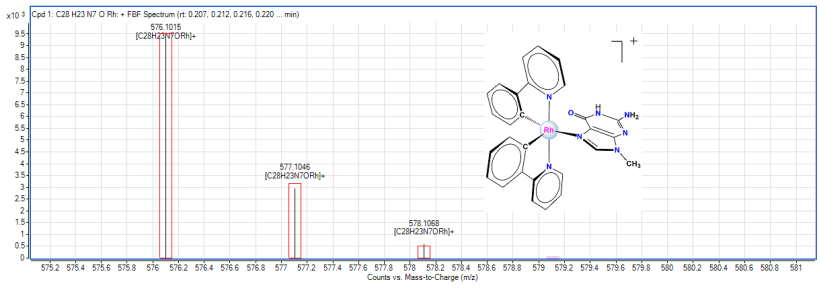

Figure 6.16: Experimental peaks of the $Rh(ppy)_2$/9-MeG adduct and theoretical value (squared).

Reported studies in literature with dirhodium complexes containing photolabile ligands prove that they can form covalent binding with DNA *via* oxygen-independent mechanism [23, 24]. Unlike the previous studies found in scientific literature, which use a monodentate photolabile ligand, the release of the chelating ancillary ligand from the **[Rh-1]**Cl system makes two coordination sites available, which could increase the affinity strength of the metal complex to guanine. Moreover, the release of the benzoxazole in solution could further increase the cytotoxicity, as it is seen that many benzoxazole compounds display anticancer activity by its own [25, 26].
The list of the relevant observed peaks by mass spectrometry is reported in Table 6.3.

Table 6.3: *Intensity of the observed peaks for irradiated **[Rh-1]**Cl/9-MeG solutions.*

m/z	**Formula**	**t=0**	**t=3h**	**t=6h**
166	$[9\,\mathrm{MeG}^{+}\mathrm{H}]^{+}$	1.3×10^5	1.2×10^5	1.0×10^5
607	$[\mathrm{Rh(ppy)_2(pyboz)}]^{+}$	7×10^5	6×10^5	5×10^5
411	$[\mathrm{Rh(ppy)_2}]^{+}$	1×10^5	9×10^4	7×10^4
788	$[\mathrm{Rh(ppy)_2(pyboz)} + 9\,\mathrm{MeG} + \mathrm{O}]^{+}$	/	5×10^3	1.2×10^4
576	$[\mathrm{Rh(ppy)_2} + 9\,\mathrm{MeG}]^{+}$	1×10^2	8×10^2	1.0×10^3

Thus, a further mechanism of photoreaction seems to be present for the rhodium complex, even though it is minority respect to the oxygen-dependent pathway. As we have previously reported, the photorelease has been observed under nitrogenous atmosphere; it means that the photoadduction to the guanine moiety is an oxygen-independent mechanism.
More than that, another peak was found to increase with the irradiation time, which is the peak at 788 m/z, corresponding to $[\mathrm{Rh(ppy)_2(pyboz)} + 9\,\mathrm{MeG} + \mathrm{O}]^{+}$. In this case no release of the ligand occurs but a 9-MeG species is coordinated to the complex, which has a new oxygen atom. Such species could be accountable to the 8-oxoguanine form, which coordinates to the rhodium. 8-oxoguanine is generally formed by the interaction of singlet oxygen with the guanine moiety, which provokes the oxidation at C_8 position. On the other hand, the ancillary ligand would be coordinated to only a nitrogenous atom.

6.2.4 Cytotoxic Activity in the Dark and under Irradiation

MTT proofs were performed by Dr. Busto from our Physical-Chemical Group, testing **[Ir-1]**Cl and **[Rh-1]**Cl with the SW480 human colon cancer cell line, in the dark and upon irradiation (20 min at 365 nm). No variation of the cytotoxic activity was observed for the iridium complex. On the other hand, a five-fold increase of the cytotoxic activity of $[\mathrm{Rh(ppy)_2(pyboz)}]\mathrm{Cl}$ was found upon irradiation (Photoindex value $PI = 5$, Figure 6.17), in agreement with the cleavage study.

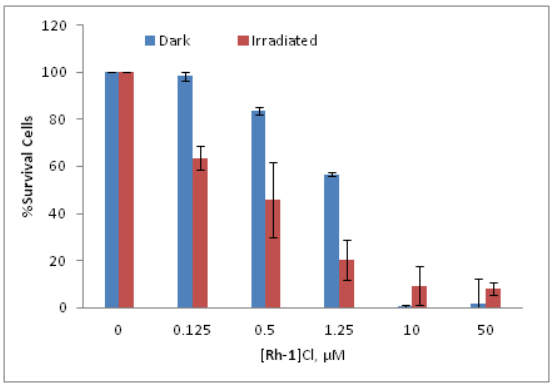

Figure 6.17: Percentage of SW480 cell viability for different concentrations of **[Rh-1]**Cl, in the dark and irradiating at 365 nm for 20 min. Incubation time: 24 h.

The obtained IC_{50} are collected in Table 6.4.

Table 6.4: *Cytotoxic activity of the metal complexes in the dark ($IC_{50}DARK$) and upon irradiation ($IC_{50}IRR$) for* 20 min *at* 365 nm *(*20 mWcm^{-1}*) and Photoindex value (PI).* 1×10^4 cells, *incubation time:* 24 h.

Compound	$IC_{50}DARK$, µM	$IC_{50}IRR$, µM	PI
[Ir-1]Cl	0.3 ± 0.1	0.4 ± 0.1	1
[Rh-1]Cl	1.6 ± 0.7	0.3 ± 0.1	5

The cytotoxic activity results very high in the dark, as well. Even though the results show that the complexes has not the optimal features for the PDT, they can be useful for future synthesis of biscyclometalated complexes. In addition, further proofs could be performed with different cell lines, in order to observe variations of the cytotoxicity in dark conditions.

6.3 Conclusion

Two biscyclometalated complexes having iridium and rhodium as metal centers exhibit a very similar interaction towards CT-DNA in dark conditions. The results obtained from the different techniques suggest a partial intercalation of the complex inside the basepairs. However, interesting differences are observed exciting the complexes. First of all, the **[Ir-1]**Cl iridium complex switches on its fluorescence in the presence of the polynucleotide, together with a notable increase of the lifetime, whereas the **[Rh-1]**Cl rhodium complex did not. On the other hand, the rhodium complex exhibits good cleavaging activity under irradiation at 365 nm, whereas iridium poorly breaks plasmid DNA. The mechanism of action mainly involves singlet oxygen production, although an oxygen-independent pathway cannot be discarded, as the formation of a new reactive species provoked by the release of the ancillary ligand was observed,

even in deoxygenated conditions. Our work could be useful for the synthesis of new complexes having similar skeleton structure, but improving singlet oxygen production and interaction with nucleic acids by addition of new ligands.

Bibliography

[1] K. P Zanoni, B. K. Kariyazaki, A. Ito, M. K. Brennaman, T. J. Meyer and N. Y. Murakami Iha (2014). *Blue-Green Iridium(III) Emitter and Comprehensive Photophysical Elucidation of Heteroleptic Cyclometalated Iridium(III) Complexes*, Inorganic Chemistry, 53 (8), 4089-4099.

[2] G. A. Crosby and J. N. Demas (1971). *Measurement of Photoluminescence Quantum Yields. Review*, The Journal of Physical Chemistry, 75 (8), 991-1024.

[3] R. D. Costa, E. Ortí, H. J. Bolink, F. Monti, G. Accorsi and N. Armaroli (2012). *Luminescent Ionic Transition-Metal Complexes for Light-Emitting Electrochemical Cells*, Angewandte Chemie International Edition, 51 (33), 8178-8211.

[4] S. Pal, S. Joy, H. Paul, S. Banerjee, A. Maji, E. Zangrando, and P. Chattopadhyay (2017). *Understanding the Difference in Photophysical Properties of Cyclometalated Iridium(III) and Rhodium(III) Complexes by Detailed TDDFT and FMO Supports*, The Journal of Physical Chemistry C, 10.1021/acs.jpcc.7b01573.

[5] K. A. King and R. J. Watts (1987). *Dual Emission from an Ortho-Metalated Iridium(III) Complex*, Journal of the American Chemical Society, 109 (5), 1589-1590.

[6] Y. Ohsawa, S. Sprouse, K. A. King, M. K. DeArmond, K. W. Hanck and R. J. Watts (1987). *Electrochemistry and Spectroscopy of Ortho-Metalated Complexes of Iridium(III) and Rhodium(III)*, Journal of Physical Chemistry, 91 (5), 1047-1054.

[7] M. G. Colombo and H. U. Güdel (1993). *Synthesis and High-Resolution Optical Spectroscopy of Bis[2-(2-thienyl)pyridinato-C^3,N'](2,2'-bipyridine)Iridium(III)*, Inorganic Chemistry, 32 (14), 3081-3087.

[8] M. G. Colombo, A. Hauser and H. U. Güdel (1993). *Evidence for Strong Mixing between the LC and MLCT Excited States in Bis(2-phenylpyridinato-C^2,N')(2,2'-bipyridine)Iridium(III)*, Inorganic Chemistry, 32 (14), 3088-3092.

[9] M. G. Colombo, A. Hauser and H. U. Güdel (1994). *Competition between Ligand Centered and Charge Transfer Lowest Excited States in Bis Cyclometalated Rh^{3+} and Ir^{3+} Complexes*, in Electronic and Vibronic

Spectra of Transition Metal Complexes I, pp. 143-171, Springer Berlin Heidelberg.

[10] P. J. Hay (2002). *Theoretical Studies of the Ground and Excited Electronic States in Cyclometalated Phenylpyridine Ir(III) Complexes Using Density Functional Theory*, The Journal of Physical Chemistry A, 106 (8), 1634-1641.

[11] C. D. Ertl, C. Momblona, A. Pertegás, J. M. Junquera-Hernández, M. G. La-Placa, A. Prescimone, E. Ortí, C. E. Housecroft, E. C. Constable and H. J. Bolink (2017). *Highly Stable Red-Light-Emitting Electrochemical Cells*, Journal of the American Chemical Society, 139 (8), 3237-3248.

[12] G. Scatchard (1949). *The Attractions of Proteins for Small Molecules and Ions*, Annals of the New York Academy of Sciences, 51 (4), 660-672.

[13] J. D. McGhee and P. H. von Hippel (1974). *Theoretical Aspects of DNA-Protein Interactions: Co-operative and Non-Co-operative Binding of Large Ligands to a One-Dimensional Homogeneous Lattice*, Journal of Molecular Biology, 86 (2), 469-489.

[14] J. Andersson, L. H. Fornander, M. Abrahamsson, E. Tuite, P. Nordell and P. Lincoln (2012). *Lifetime Heterogeneity of DNA-Bound dppz Complexes Originates from Distinct Intercalation Geometries Determined by Complex–Complex Interactions*, Inorganic Chemistry, 52 (2), 1151-1159.

[15] A. K. F. Mårtensson and P. Lincoln (2015). *Binding of Ru(terpyridine)(pyridine)dipyridophenazine to DNA Studied with Polarized Spectroscopy and Calorimetry*, Dalton Transactions, 44 (8), 3604-3613.

[16] Y. Chen, W. Lei, G. Jiang, Q. Zhou, Y. Hou, C. Li, B. Zhang and X. Wang (2013). *A Ruthenium(II) Arene Complex Showing Emission Enhancement and Photocleavage Activity towards DNA from Singlet and Triplet Excited States Respectively*, Dalton Transactions, 42 (16), 5924-5931.

[17] A. G. Zhang, Y. Z. Zhang, Z. M. Duan, K. Z. Wang, H. B. Wei, Z. Q. Bian and C. H. Huang (2011). *Dual Molecular Light Switches for pH and DNA Based on a Novel Ru(II) Complex. A Non-Intercalating Ru(II) complex for DNA Molecular Light Switch*, Inorganic Chemistry, 50 (14), 6425-6436.

[18] K. J. Castor, K. L. Metera, U. M. Tefashe, C. J. Serpell, J. Mauzeroll and H. F. Sleiman (2015). *Cyclometalated Iridium(III) Imidazole Phenanthroline Complexes as Luminescent and Electrochemiluminescent G-Quadruplex DNA Binders*, Inorganic Chemistry, 54 (14), 6958-6967.

[19] L. Flamigni, A. Barbieri, C. Sabatini, B. Ventura and F. Barigelletti (2007). *Photochemistry and Photophysics of Coordination Compounds: Iridium*, in Photochemistry and Photophysics of Coordination Compounds II, pp. 143-203, Springer-Verlag Berlin Heidelberg.

[20] Y. J. Liu, C. H. Zeng, H. L. Huang, L. X. He and F. H. Wu (2010). *Synthesis, DNA-Binding, Photocleavage, Cytotoxicity and Antioxidant Activity of Ruthenium(II) Polypyridyl Complexes*, European Journal of Medicinal Chemistry, 45, 564-571.

[21] R. Gao, L. Xiao, X. Hao, W. H. Sun and F. Wang (2008). *Synthesis of Benzoxazolylpyridine Nickel Complexes and Their Efficient Dimerization of Ethylene to α-Butene*, Dalton Transactions, (41), 5645-5651.

[22] R. Schmidt, C. Tanielian, R. Dunsbach and C. Wolff (1994). *Phenalenone, a Universal Reference Compound for the Determination of Quantum Yields of Singlet Oxygen O_2 ($\Phi_{^1\Delta_g}$) sensitization*, Journal of Photochemistry and Photobiology A: Chemistry, 79 (1), 11-17.

[23] P. K. L. Fu, P. M. Bradley and C. Turro (2001). *DNA Cleavage by Photogenerated $Rh_2(O_2CCH_3)_4(H_2O)^{2+}$*, Inorganic Chemistry, 40 (11), 2476-2477.

[24] D. A. Lutterman, P. K. L. Fu and C. Turro (2006). *cis-$[Rh_2(\mu-O_2CCH_3)_2(CH_3CN)_6]^{2+}$ as a Photoactivated Cisplatin Analog*, Journal of the American Chemical Society, 128 (3), 738-739.

[25] D. Kumar, M. R. Jacob, M. B. Reynolds and S. M. Kerwin (2002). *Synthesis and Evaluation of Anticancer Benzoxazoles and Benzimidazoles Related to UK-1*, Bioorganic & Medicinal Chemistry, 10 (12), 3997-4004.

[26] S. M. Rida, F. A. Ashour, S. A. El-Hawash, M. M. ElSemary, M. H. Badr, and M. A. Shalaby (2005). *Synthesis of Some Novel Benzoxazole Derivatives as Anticancer, Anti-HIV-1 and Antimicrobial Agents*, European Journal of Medicinal Chemistry, 40 (9), 949-959.

Supporting Information

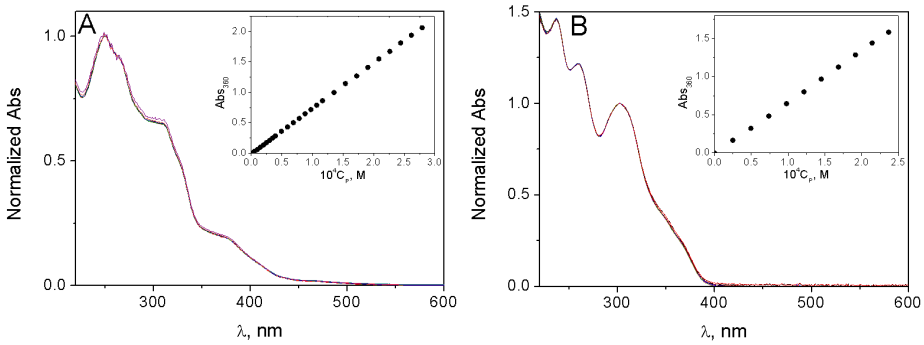

Figure 6.S1: Normalized spectra at different C_D. (A) **[Ir-1]**Cl/CT-DNA. Inset: track at 360 nm. **[Rh-1]**Cl/CT-DNA. Inset: track at 360 nm. I=6.5 mM (NaCl), pH=7.0 (NaCac), T=25.0 °C.

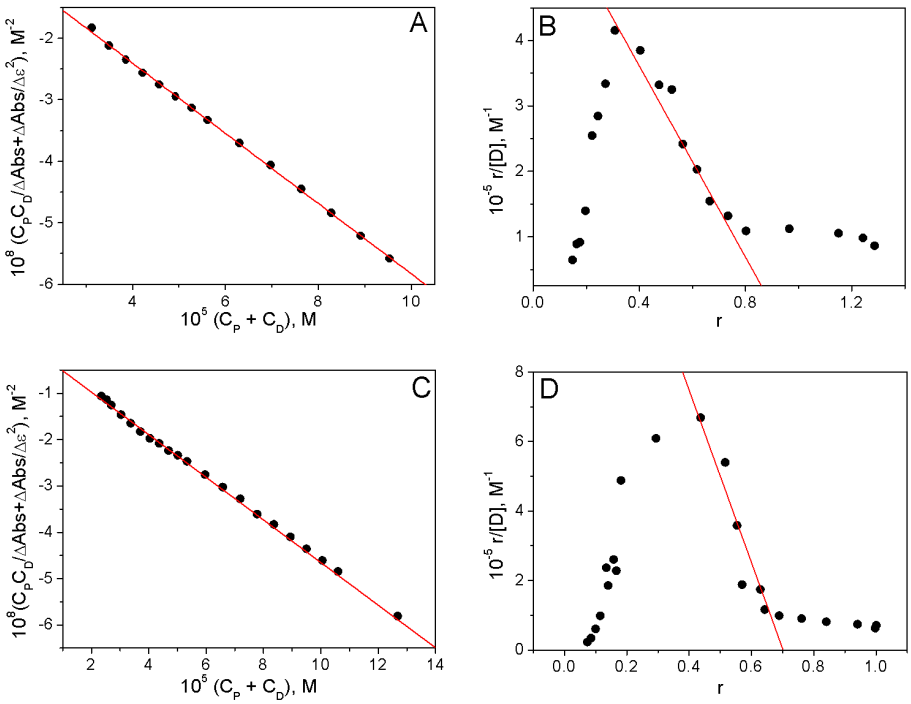

Figure 6.S2: Data treatment of the Uv-Vis Titration. **[Ir-1]**Cl/CT-DNA (A) Data Treatment by Equation (2.48); (B) Scatchard Plot (Equation (2.55)). **[Rh-1]**Cl/CT-DNA (A) Data Treatment by Equation (2.48); (B) Scatchard Plot (Equation (2.55)). C_D=20 µM, I=6.5 mM (NaCl), pH=7.0 (NaCac), T=25.0 °C.

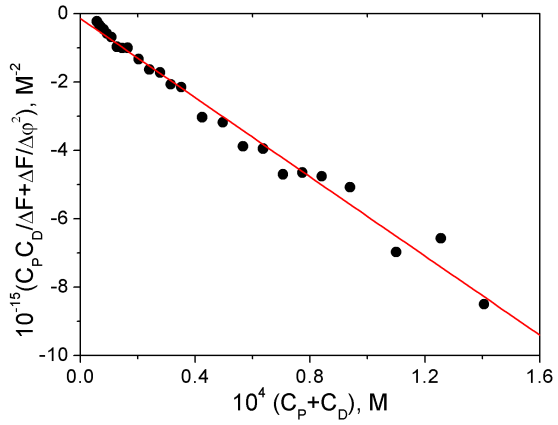

Figure 6.S3: Data treatment of the fluorescence titration for the **[Rh-1]**Cl/CT-DNA system. C_D=5.0 µM, I=6.5 mM (NaCl), pH=7.0 (NaCac), T=25.0 °C.

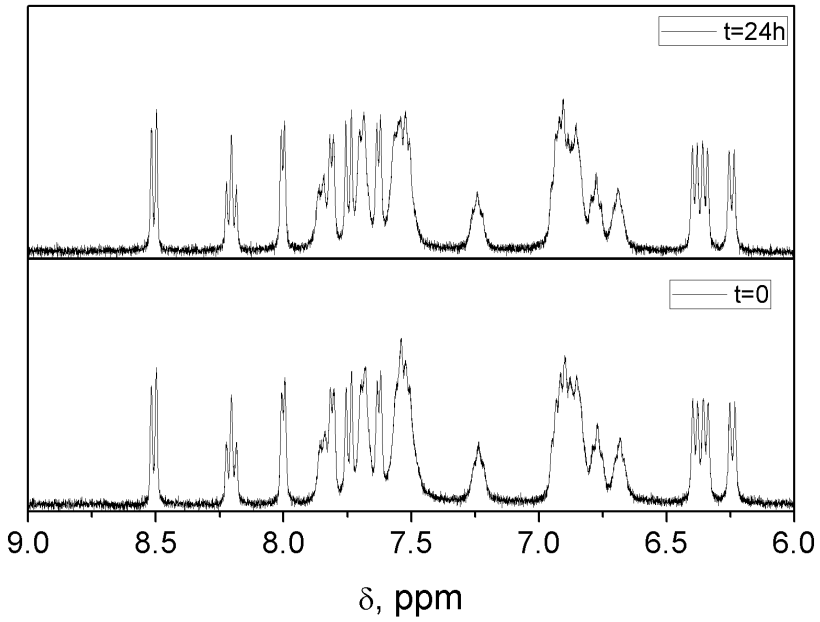

Figure 6.S4: ^{1}H-NMR spectra of [**Rh-1**]Cl left in the dark in D_2O. C_D=5.0 mM and T=25.0 °C

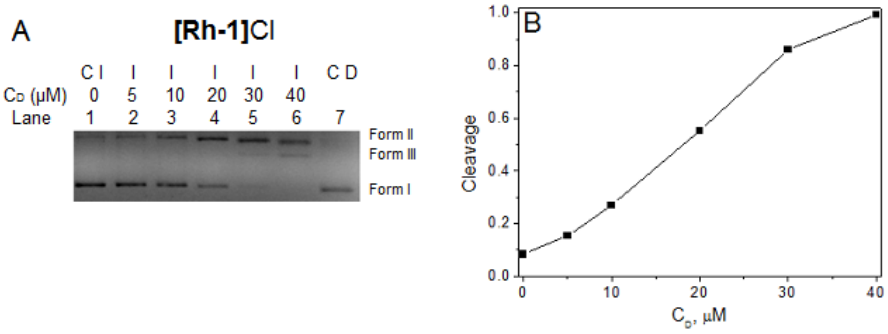

Figure 6.S5: (A) Photocleavage of the [**Rh-1**]Cl/pUC18 system at different metal concentration. Lane 1-6: Irradiated system at C_D=0, 5, 10, 20, 30, 40 µM. Lane 7: Dark control. (B) Quantification of the cleavage. C_P=20 µM, [NaCl]=4.0 mM, [NaCac]=2.5 mM, pH=7.0, λ_{irr}=365 nm, t_{irr}=90 min. Incubation: T_{inc}=37.0 °C, overnight.

Chapter 7

Biscyclometalated Iridium and Rhodium Complexes. Photoreactivity and Selective Binding to G-Quadruplex

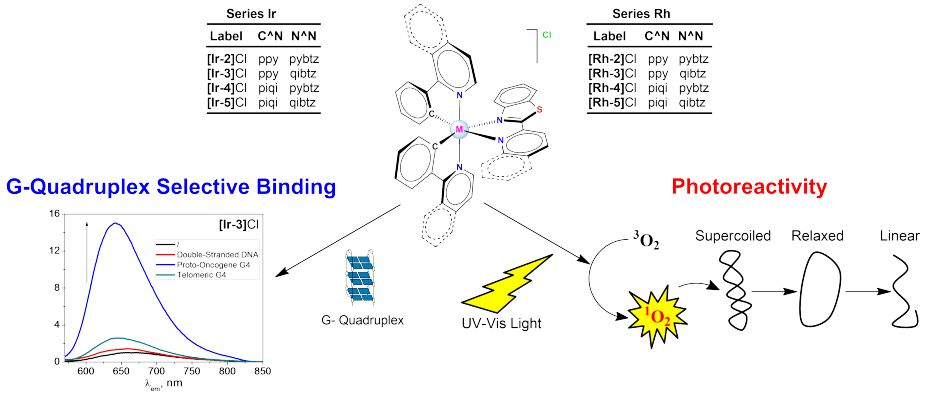

In Chapter 6 we observed that the Rh biscyclometalated [**Rh-1**]Cl complex exhibits good photocleavaging activity upon irradiation in the UV region, whereas the [**Ir-1**]Cl Ir complex, having the same CN and NN ligands, does not.
However, the main disadvantage of Rh complexes is their high absorption energy, an unfavorable condition for PDT. Differently, cyclometalated Ir complexes exhibit lower absorption energy because of the presence of a peak in the 400-500 nm region, which could allow photoactivation in a less-damaging and better tissue penetrating wavelength region.
Hence, further investigation was addressed to observe the effect of the ligands on the photoreactivity of cyclometalated complexes of Ir and Rh. Seven new biscy-

clometalated complexes have been synthesized and fully characterized, varying the NN and the CN ligands and the metal center.
Photoreactivity was tested with plasmid pUC18 DNA irradiating in the ultraviolet and visible region. Then, MTT assays on SW480 cancer cells were performed in the dark and upon irradiation. High photocleavage yields were observed for the Rh complexes, but only the Ir complexes could reach longer wavelength of photoactivation ($\lambda_{irr} = 500\,\text{nm}$). The increase of the aromatic size of the ligands resulted in an extension of the absorption in the visible region and, consequently, their photoactivity was tested in this wavelength region.
In addition, focus was given to the interaction with oligonucleotides. In particular, we tested the interaction towards various G-Quadruplex (G4) structures, in order to detect possible binding selectivity, depending on the ligand type. Titrations were carried out with the Ir complexes and three different oligonucleotides: double-stranded DNA of self-complementary 26-mer (52B), G4 c-myc (Pu22) and human telomere (Tel22) sequences in potassium salt excess. The affinity of the complex towards DNA was evaluated by means of Uv-vis absorption, circular dichroism in the UV visible region, steady-state and time-resolved fluorescence. The obtained equilibrium constants hinted at selectivity of the complex towards the quadruplex moieties, in particular for c-myc proto-oncogene quadruplex. FRET assays showed stabilization of such structures, with the highest effect observed upon increase of the aromatic extension of the ligand.

7.1 Materials and Methods

7.1.1 Materials

$IrCl_3 \cdot xH_2O$ and $RhCl_3 \cdot xH_2O$ have been purchased from Johnson Matthey. Organic compounds phenylpyridyne, phenylboronic acid and 1-bromoisoquinoline were from ACROS, while 2-pyridylcarbaldheyde 2-quinolinylcarbaldheyde and 2-aminothiophenol were from Sigma-Aldrich and used without further purification. Seven new complexes have been prepared, namely the [**Ir-2**]Cl, [**Ir-3**]Cl, [**Ir-4**]Cl and [**Ir-5**]Cl Ir complexes and the [**Rh-2**]Cl, [**Rh-4**]Cl and [**Rh-5**]Cl Rh complexes. The synthesis procedure is presented in Section 7.2.1 and the characterization data are listed in Section 7.4. Stock solutions of the complexes were prepared in bidistilled water, whereas working solutions in two different buffer media: (i) I=6.5 mM (NaCl) and pH = 7.0 (NaCac); this buffer was used in the study of the photoreactivity, and (ii) I=0.1 M (KCl) and potassium phosphate buffer at pH=7.0 for the titrations with oligonucleotides. Stock solutions of oligonucleotides were prepared in KCl buffer (I = 0.1 M, pH = 7.0), heating the solution above the melting temperature of the quadruplex or duplex structures, and waiting overnight the solution to return to room temperature. The solutions were spectrophotometrically standardized.

7.1.2 Methods

All synthetic manipulations were carried out under an atmosphere of dry, O-free N_2 using standard Schlenk techniques, as explained in Chapter 2, Section 2.1. The solvents were distilled from the appropriate drying agents and degassed

before use. Elemental analyses were performed with a LECO CHNS-932 microanalyzer. IR spectra were recorded on a Nicolet Impact 410 (within the frequency range 4000-400 cm^{-1}), and in a Jasco FT/IR-4200 spectrophotometers.
NMR samples were prepared under a N_2 atmosphere by dissolving the suitable amount of compound in 0.5 mL of the respective oxygen-free deuterated solvent, and the spectra were recorded at 298 K on a Varian Unity Inova-400 (399.94 MHz for ^1H and 100.6 MHz for ^{13}C). Typically, 1D ^1H-NMR spectra were acquired with 32 scans into 32 K data points over a spectral width of 16 ppm. ^1H and ^{13}C chemical shifts were internally referenced to tetramethylsilane via the residual ^1H and ^{13}C signals of the corresponding solvents, according to the values reported by Fulmer et al. [1]. 2D NMR spectra such as ^1H-^1H gCOSY, ^1H-^1H NOESY, ^1H-^{13}C gHSQC, and ^1H-^{13}C gHMBC were recorded using standard pulse sequences. The probe temperature (±1 K) was controlled by a standard unit calibrated with methanol as a reference. All NMR data processing was carried out using MestReNova v10.0.2-15465.
Singlet oxygen emission was detected by means of an Edinburgh Fluorimeter equipped with a Hamamatsu RC5509-72 detector, using a CW HeCd Laser as light source ($\lambda_{ex} = 325$ nm). To ensure that no interfering light arrived at the detector, two filters were inserted in the emission path, namely the 850 nm and the 1000 nm cut-off filters. Photoirradiation and cleavage study was performed according to Chapter 2, Sections 2.10 and 2.11.
Titrations of the metal complex with oligonucleotides were performed preparing solutions of constant metal complex concentration (C_D) and increasing DNA concentration (C_P), analysing the mixtures with different techniques. Absorption spectra were recorded with a Perkin Elmer Lambda 650 spectrophotometer in the 200-800 nm range. UV and visible circular dichroism spectra were recorded by means of a Jasco J-715. For the oligonucleotide region (220-305 nm), 1 cm and 2 mm path length quartz cuvettes were used, whereas for the visible region (310-500 nm), a 2 cm path length quartz cuvette was used. For all the dichroic spectra, 4 accumulations of the signal were averaged out. Corrected steady-state fluorescence spectra were acquired in 1 cm quartz cuvettes with an Edinburgh F980 fluorimeter using right angle geometry. Fluorescence decays were measured in air-equilibrated solutions for excitation at 331 nm and 465 nm (Horiba led) and 407 nm (Hamamatsu pulsed laser with 1 MHz repetition rate) using a time-correlated single-photon counting system (TCSPC) (IBH Consultants Ltd., Glasgow, UK) with a resolution of 55 ps and 1.755 ns per channel. Photons were detected in right angle configuration with a cut-off filter. Fluorescence decay profiles were analysed with a least-squares method, using multiexponential decay functions (Equation 7.1) and deconvolution of the instrumental response function. The software package was provided by IBH Consultants Ltd.
The fitting equation used is the (7.1), where a_j is the pre-exponential of τ_j.

$$I(t) = b + \sum_j a_j e^{-\frac{t}{\tau_j}} \tag{7.1}$$

The relative amplitude f_i, also known as the fractional intensity, and the average fluorescence lifetime τ_{av} are calculated according to the following Equations (7.2) and (7.3).

$$f_i = \frac{a_i \tau_1}{\sum_j a_j \tau_j} \tag{7.2}$$

$$\tau_{av} = \sum_j f_j \tau_j \tag{7.3}$$

Multiwavelength global analysis of the titrations was performed by REACTLAB program, choosing a 1:1 or a 2:1 metal complex:oligonucleotide model.
Stabilization study of G-Quadruplex was performed in a 7500 Real Time PCR System (Applied Biosystems), setting $\lambda_{ex} = 492\,\text{nm}$ and $\lambda_{em} = 516\,\text{nm}$. For our study, 0.2 µM oligonucleotide covalently linked to a donor (fluorescein) and an acceptor (TAMRA, a rhodamine) was heated in the presence of an excess of metal complex (10 µM), with a temperature ramp rate of $1\,^{\circ}\text{C}\,\text{min}^{-1}$ ($I = 0.11\,\text{M}$ ([LiCl] = 90 mM, [KCl] = 10 mM, [LiCac] = 10 mM), pH = 7.2).

7.2 Results and Discussion

7.2.1 Synthesis Procedure

The synthesis of the complexes was carried out under the supervision of Prof. Espino of the Inorganic Chemistry Lab. (Universidad de Burgos). Eight different complexes of general formula $[M(CN)_2(NN)]Cl$ have been planned, the **[Ir-2]**Cl, **[Ir-3]**Cl, **[Ir-4]**Cl and **[Ir-5]**Cl Ir complexes and the **[Rh-2]**Cl, **[Rh-3]**Cl, **[Rh-4]**Cl and **[Rh-5]**Cl Rh complexes (Figure 7.1).

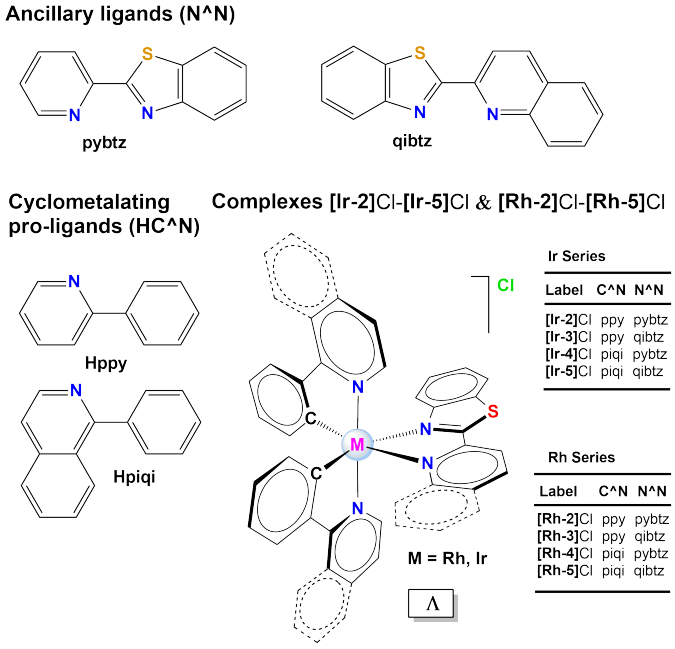

Figure 7.1: The eight planned biscyclometalated complexes and their ligands. NN ancillary ligands: pybtz = 2-(2'-pyridyl)benzothiazole, qibtz = 2-(2'-quinolinyl)benzothiazole. HCN proligands: ppy = 2-phenylpyridine, piqi = 2-phenyilisoquinoline.

The scheme of the synthesis is reported in Figure 7.2.

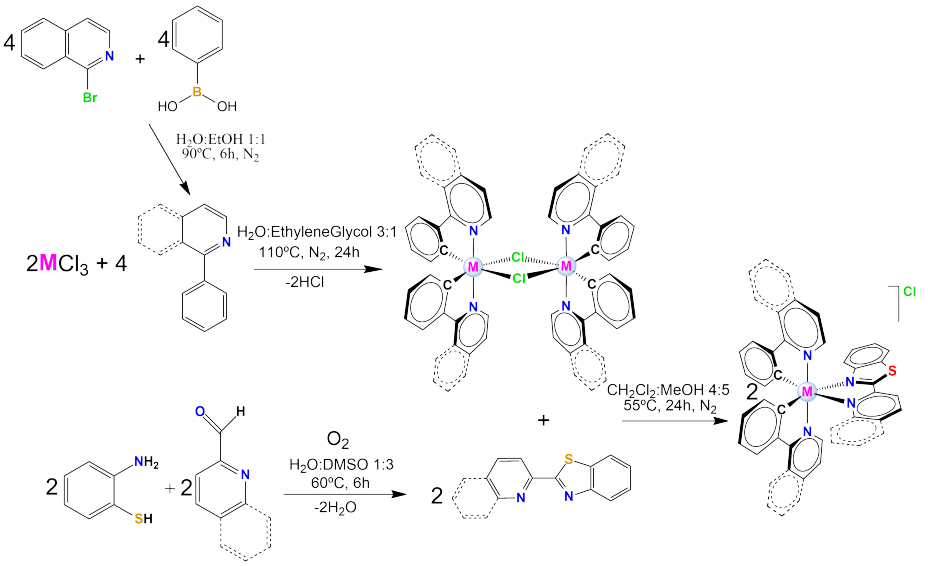

Figure 7.2: Scheme of the biscyclometalated complexes synthesis.

The new-synthesized Ir and Rh compounds differ by the aromatic size of the CN and NN ligands. On the one hand, aromaticity enhancement of both CN and NN ligands should favour the π-stacking interaction towards nucleic acids, increasing the affinity between the reactants [2]. In addition, aromatic extension should shift the absorption spectra to longer wavelengths, allowing more achievable wavelengths for PDT. For an analogue reason, we changed the oxygen (present in the NN benzoxazole ligand, in Chapter 6) for the S heteroatom, which theoretically stabilizes the LUMO, obtaining low absorption energy [3].
First of all, an important consideration concerns the structural conformation of the complexes. Actually, a biscyclometalated metal complex contains 2 CN ligands and a NN ancillary ligand and this theoretically implies the presence of *cis-trans* isomerism. Three isomers are possible: the *trans*-N,N *cis*-C,C, the *trans*-C,C *cis*-N,N and the *cis*-N,N *cis*-C,C (Figure 7.3).

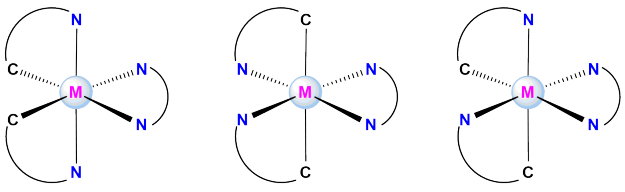

Figure 7.3: Possible *cis-* *trans-* isomers of biscycometalated compounds.

However, as the M-C bonds display strong *trans* effect, the *trans*-C,C conformation is impeded because of the high electronic density which would be provided to the same *d* orbital of the metal center. So, the most thermodinamically stable

isomer results to be the *trans*-N,N *cis*-C,C one, where M-C groups can supply electronic density to the NN ancillary ligand by the *trans* effect.
The complexes depicted were prepared following the classical two-steps procedure reported by Nonoyama [4]. In the first step, $RhCl_3 \cdot xH_2O$ or $IrCl_3 \cdot xH_2O$ were reacted with the proligands HCN to produce the respective chlorido-bridged dimeric Rh and Ir complexes $[M(\mu{-}Cl)(CN)_2]_2$ (M = Rh or Ir).
The spatial disposition of the ligands along the dimer complex can be different (Figure 7.4).

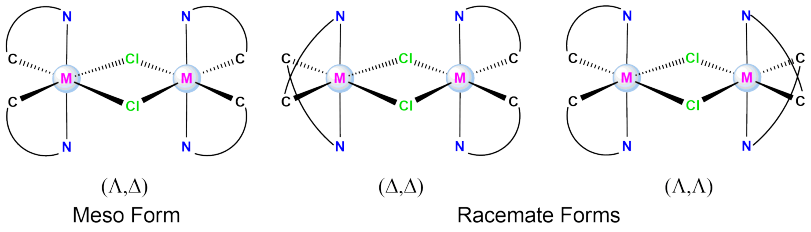

Figure 7.4: Diastereoisomeric forms of the dimeric complexes.

Four different forms can be obtained, which are (Δ,Δ), (Λ,Λ), (Λ,Δ) and (Δ,Λ) complexes. For steric reasons the (Δ,Λ) and (Λ,Δ) meso forms are disadvantaged due to the fact that the hydrogens of the CN ligands are sterically hindered, namely the H in C_6 and C_{10} of ppy and piqi ligands, respectively. Hence, the most favourable forms are the (Δ,Δ) and (Λ,Λ) racemate forms [5].
Afterwards, the appropriate ancillary ligand, NN, was reacted with the desired Rh(III) or Ir(III) starting material to obtain the chloride salts of new derivatives with general formula $[M(CN)_2(NN)]Cl$ (M = Ir, Rj; NN = pybtz, qibtz; CN = ppy, piqi) through a bridge splitting reaction. The ancillary ligands were prepared by reaction of the 2-aminothiophenol and 2-pyridylcarboxaldehyde or 2-quinolinylcarboxaldehyde in the presence of oxygen [6]. The reaction evolves to a first imine intermediate, then cyclization of the chain occurs followed by a further oxydation which brings to 2-pyridylbenzothiazole (pybtz) and 2-quinolinylbenzothiazole (qibtz). Purification is needed for the separation of subproducts, using a silica gel column (eluent AcOEt:Hexane).
The reaction between the dimer and the ancillary ligand yields two molecules of monomeric compound (Figure 7.5).

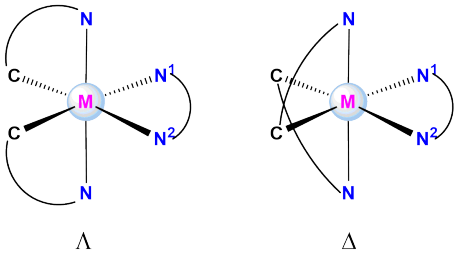

Figure 7.5: Enantiomeric Δ and Λ forms of a $[M(CN)_2(NN)]^+$ complex.

The complexes were isolated as racemic mixtures (Δ and Λ) of yellow to red

solids with good yield and purity according to analytical and spectroscopic data. Moreover, they are soluble in common organic solvents, such as EtOH, CH_3CN and CH_2Cl_2 and slightly soluble in water and methanol.
The synthesis work led to seven complexes from the eight planned compounds. We did not obtain [**Rh-3**]Cl with acceptable purity degree, so it was not further characterized.

7.2.2 Characterization

All the characterization data are reported in Section 7.4.
We cleared the structures up by means of various techniques. First of all, high-resolution mass spectrometry allows the identification of the exact formula of the compound, checking the experimental molecular weight and the isotopic distribution with the theoretical one. Then, bidimensional NMRs were employed to obtain structural information of the complex. With the COSY technique we assembled the protons of each aromatic group. Note that the CN ligands are surrounded by different chemical environments; this means that the protons are not equivalent and two sets of signals can be detected. With the NOESY we were able to visualize the geometric distribution of the ligands around the metal. For example, the NOESY spectra for [**Rh-4**]Cl complex is reported in Figure 7.6.

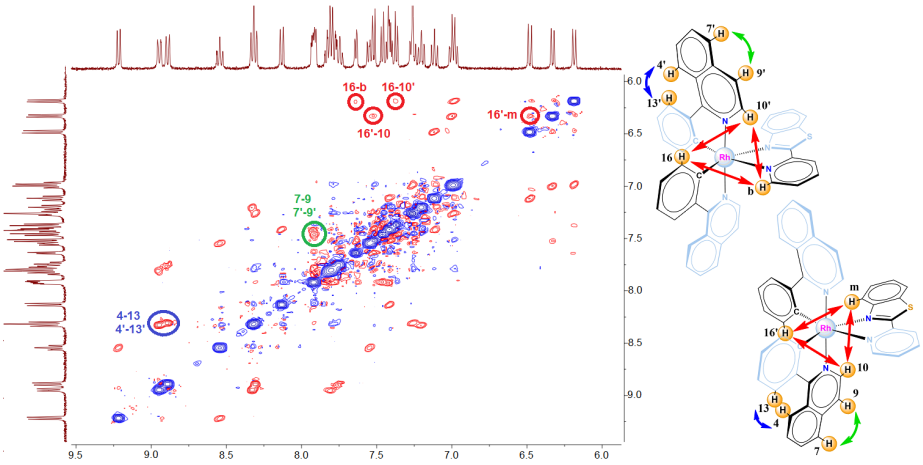

Figure 7.6: Example of assignment of the spatially correlated peaks by the NOESY bidimensional spectra.

For biscyclometalated complexes it is possible to individuate two triangular interactions between the protons of the ancillary ligand and the protons of the CN ligands. For example, the triangular interactions in the [**Rh-4**]Cl structure can be found for the 16-10'-b and for the 16'-10-m protons. In addition, for the 2-phenylisoquinoline CN ligand we can observe two signals between 4-13 and 7-9 atoms which allows to distinguish the signals of the aromatic groups from each CN ligand. From these data we drew the structure up.

7.2.2.1 Crystal Structure by X-ray Diffraction

Single crystals of [**Ir-5**]$PF_6 \cdot CH_2Cl_2$ and [**Rh-2**]$PF_6 \cdot CH_3OH$ suitable for X-ray diffraction analysis were obtained by slow diffusion of a saturated NH_4PF_6 solution in methanol into a solution of [**Ir-5**]Cl and [**Rh-2**]Cl in dichloromethane. For [**Rh-2**]Cl, two drops of H_2O were also added. The acquired data are reported in Table 7.S1, Supporting Information. Both [**Ir-5**]$PF_6 \cdot CH_2Cl_2$ and [**Rh-2**]$PF_6 \cdot CH_3OH$ crystallize in the monoclinic space group $P2_1/n$. The corresponding unit cells show two pairs of the enantiomers (Δ) and (Λ) resulting from helical chirality inherent to trischelate octahedral metal complexes, along with four PF_6^- counterions, four CH_2Cl_2 and four CH_3OH molecules for [**Ir-5**] and [**Rh-2**], respectively. For the [**Ir-5**] structure, both PF_6^- counterion and the ancillary ligand display positional disorder (see Figure 7.S1, Supporting Information). The Ir center displays a slightly distorted octahedral coordination geometry with the expected cis-C,C and trans-N,N mutual disposition for the piqi ligands, whereas for the Rh center such a distortion is less evident. The ORTEP diagrams for (Δ)-[**Ir-5**]$^+$ and (Δ)-[**Rh-2**]$^+$ are depicted in Figure 7.7.

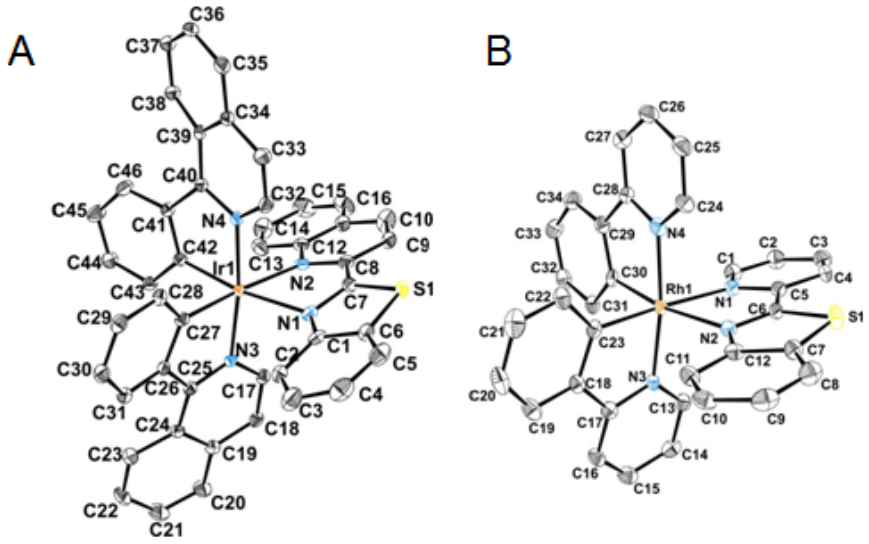

Figure 7.7: ORTEP diagram for (A) (Δ)-[**Ir-5**]$^+$ and (B) (Δ)-[**Rh-2**]$^+$ forming the asymmetric unit of racemic [**Ir-5**]$PF_6 \cdot CH_2Cl_2$ and [**Rh-2**]$PF_6 \cdot CH_3OH$, respectively. Thermal ellipsoids are shown at the 30 % probability level. The counterion (PF_6^-) and solvent molecules (CH_2Cl_2 and CH_3OH) have been omitted for the sake of clarity

Selected bond lengths and angles with estimated standard deviations (in brackets) are gathered in Table 7.1 and Table 7.2.

Table 7.1: Selected parameters, distances (Å) and angles (°) for the X-Ray structure of [**Ir-5**] complex. Standard deviations in brackets.

Distances		**Angles**	
Atoms	Value	Atoms	Value
Ir(1)-C(27)	1.997(5)	C(27)-Ir(1)-C(42)	82.62(17)
Ir(1)-C(42)	2.005(4)	C(27)-Ir(1)-N(4)	94.13(17)
Ir(1)-N(4)	2.059(4)	C(42)-Ir(1)-N(4)	79.44(16)
Ir(1)-N(3)	2.052(4)	C(27)-Ir(1)-N(3)	79.71(17)
Ir(1)-N(1)	2.221(3)	C(42)-Ir(1)-N(3)	96.01(16)
Ir(1)-N(2)	2.232(2)	N(4)-Ir(1)-N(3)	172.82(14)
		C(27)-Ir(1)-N(1)	101.81(15)
		C(42)-Ir(1)-N(1)	170.98(15)
		N(4)-Ir(1)-N(1)	92.34(13)
		N(3)-Ir(1)-N(1)	92.53(13)
		C(27)-Ir(1)-N(2)	175.99(15)
		C(42)-Ir(1)-N(2)	100.95(14)
		N(4)-Ir(1)-N(2)	88.36(12)
		N(3)-Ir(1)-N(2)	98.00(13)
		N(1)-Ir(1)-N(2)	74.91(11)

Table 7.2: Selected parameters, distances (Å) and angles (°) for the X-Ray structure of [**Rh-2**] complex. Standard deviations in brackets.

Distances		**Angles**	
Atoms	Value	Atoms	Value
Rh(1)-C(23)	1.994(4)	C(23)-Rh(1)-C(30)	87.89(14)
Rh(1)-C(30)	1.995(4)	C(23)-Rh(1)-N(3)	81.48(14)
Rh(1)-N(3)	2.032(3)	C(30)-Rh(1)-N(3)	92.75(14)
Rh(1)-N(4)	2.042(3)	C(23)-Rh(1)-N(4)	93.55(14)
Rh(1)-N(1)	2.180(3)	C(30)-Rh(1)-N(4)	81.26(14)
Rh(1)-N(2)	2.196(3)	N(3)-Rh(1)-N(4)	172.39(12)
		C(23)-Rh(1)-N(1)	176.50(14)
		C(30)-Rh(1)-N(1)	95.04(13)
		N(3)-Rh(1)-N(1)	96.45(12)
		N(4)-Rh(1)-N(1)	88.79(12)
		C(23)-Rh(1)-N(2)	101.03(13)
		C(30)-Rh(1)-N(2)	169.72(13)
		N(3)-Rh(1)-N(2)	93.62(12)
		N(4)-Rh(1)-N(2)	92.98(12)
		N(1)-Rh(1)-N(2)	76.23(12)

Intermolecular distances were measured by MERCURY 3.0 program. Concerning the [**Ir-5**] structure, the Ir−C_{piqi} and Ir−N_{piqi} bond distances lie in

the expected ranges for phenylpyridanate type ligands, that is, very close to 2 Å [7, 8]. The bond lengths for the ancillary ligand are significantly longer due to the strong trans influence attributed to the C atoms of the CN ligands, Ir(1)-N(1) = 2.221(3) Å and Ir(1)-N(2) = 2.232(2) Å [9, 10]. The bite angle for the NN ligand, N(1)-Ir(1)-N(2) = 74.91(11)°, is comparable to those previously reported for five-membered N-Ir-N iridacycles in analogous derivatives, whereas the C-Ir-N bite angles for the CN ligands, C(27)-Ir(1)-N(3) and C(42)-Ir(1)-N(4), are also standard (79.71° and 79.44° respectively) [11]. The 3D crystal packing is hold down by intermolecular hydrogen bonds, (C(51)-H(51A)—F(3), C(37)-H(37)—F(4) and C(5)-H(5)—F(4)), anion-π (PF_6^- and quinoline ring) and CH-π (C(30)-H(30)—isoquinolinyl) contacts and offset $\pi - \pi$ stacking interactions between isoquinolinyl and benzothiazolyl units (see Tables 7.S2-7.S5, Supporting Information).
Regarding the **[Rh-2]** crystal structure, similar lengths of the bonds between the metal and the ligands were found (Rh−C_{ppy} Rh−N_{ppy} close to 2 Å, whereas Rh(1)-N(1) = 2.180(3) Å and Rh(1)-N(2) = 2.196(2) Å). The same consideration can be advanced for the angles (for the ancillary ligand N(1)-Rh(1)-N(2) = 76.23(12)°, and for the CN ligands C(23)-Rh(1)-N(3) = 81.48(12)° and C(30)-Rh(1)-N(4) = 81.26(14)°). Differently from the iridium structure, no relevant π-π stacking and CH-π interaction have been found, probably because the lower aromatic extension, which does not provide strong intermolecular interactions between the metal complexes. However, intermolecular hydrogen bonds (C(15)-H(15)—F(2), C(16)-H(16)—F(2), C(2)-H(2)—F(6) and C(13)-H(13)—O(1)) and anion-π contacts (PF_6^--ppy) are found and they are listed in Tables 7.S6 and 7.S7, Supporting Information.

7.2.3 UV-vis Absorption Spectra

Photophysical properties of the complexes were analysed in water. The absorption spectra of the complexes are drawn in Figure 7.8.

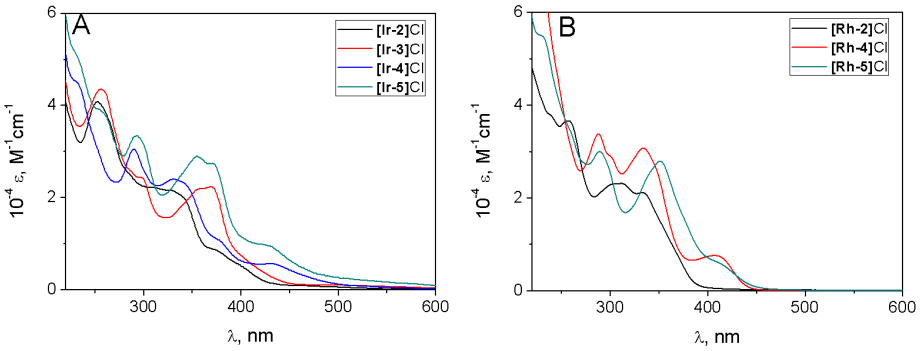

Figure 7.8: UV-vis absorption spectra of the metal complexes in water. (A) Ir complexes. (B) Rh complexes.

The main peaks of the absorption spectra are reported in Table 7.3.

Table 7.3: *Wavelengths of the absorption maxima of the metal complexes; the corresponding molar absorption are reported in brackets. sh=shoulder, t=tail.*

Complex	λ, nm ($10^{-4}\epsilon$, $M^{-1}cm^{-1}$)
[Ir-2]Cl	253 (4.0), 324 (2.1), 373sh (0.8), 463t (0.1)
[Ir-3]Cl	256 (4.4), 298(2.5), 359(2.2), 369(2.3), 488t (0.1)
[Ir-4]Cl	233 (4.6), 290 (3.1), 331 (2.5), 373sh (1.2), 429 (0.6), 525t (0.1)
[Ir-5]Cl	258 (3.9), 297 (3.2), 354 (2.9), 370 (2.7), 420sh (1.0), 530t (0.2)
[Rh-2]Cl	257 (3.7), 312 (2.3), 334 (2.1)
[Rh-4]Cl	230sh (6.4), 288 (3.4), 334 (3.1), 408 (0.8)
[Rh-5]Cl	230 (5.6), 289 (3.0), 350 (2.9), 405sh (0.7)

As we reported in Chapter 6, biscyclometalated complexes exhibit different peaks associated to different electronic transitions [12]. Bands having molar absorption coefficients higher than 30 000 $M^{-1}cm^{-1}$ at $\lambda < 300$ nm are related to high energy spin allowed ^{1}LC transitions, whereas peaks at $\lambda > 300$ nm are due to spin allowed ^{1}MLCT and spin forbidden ^{3}LC. For longer wavelength a very small and broad tail is visible for the iridium complexes ($\lambda > 450$ nm), which is related to the spin forbidden ^{3}MLCT band. For rhodium complexes no ^{3}MLCT tail is visible above 450 nm and it is in agreement with the fact that ^{3}LC is in general the lowest state of Rh complexes, whereas Ir complexes exhibit a mixing of both ^{3}MLCT and ^{3}LC transitions [13]. From the collected data, the CN piqi and NN qibtz ligands have the absorption spectra shifted to longer wavelengths, due to the extension of the aromaticity of the system.

7.2.4 Luminescence

Normalized emission spectra are reported in Figure 7.9.

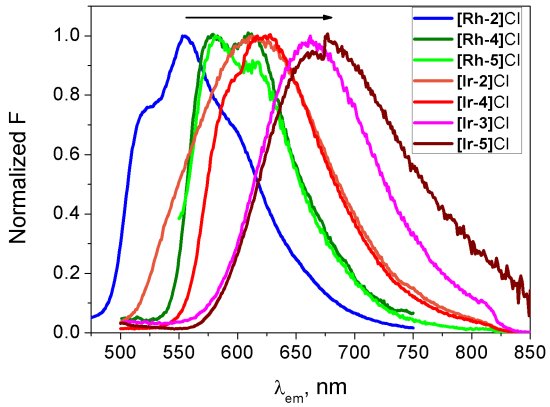

Figure 7.9: Emission spectra of the metal complexes in water. λ_{ex}=340 nm **[Ir-2]**Cl, 369 nm **[Ir-3]**Cl, 365 nm **[Ir-4]**Cl, 360 nm **[Ir-5]**Cl, 340 nm **[Rh-2]**Cl, 370 nm **[Rh-4]**Cl, 390 nm **[Rh-5]**Cl.

Concerning the emissive properties, they are listed in Table 7.4

Table 7.4: *Luminescence properties of metal complexes in water. Φ is the fluorescence quantum yield, τ is the fluorescence lifetime (in brackets the fractional intensity calculated according to Equation (7.2)). For the lifetime measurements, λ_{exc}=331 nm for **[Ir-2]**Cl, **[Ir-4]**Cl, **[Rh-2]**Cl and **[Rh-4]**Cl; λ_{exc}=373 nm for **[Ir-3]**Cl and **[Ir-5]**Cl.*

Complex	λ_{ex}, nm	λ_{em}, nm	Φ	τ, ns
[**Ir-2**]Cl	335	620	0.0023	13.1 (0.72), 320 (0.28)
[**Ir-3**]Cl	357, 369	665	0.0010	15.9 (0.92), 130 (0.08)
[**Ir-4**]Cl	335	625	0.0028	31.1 (0.79), 389 (0.21)
[**Ir-5**]Cl	358	675	0.0023	15.5 (0.90), 172 (0.10)
[**Rh-2**]Cl	312, 332	556	0.0048	1470
[**Rh-4**]Cl	335	578, 613	0.0026	2150
[**Rh-5**]Cl	350	585, 614	0.0004	n.d.

Changing the metal centre, the CN cyclometalated ligand and the NN ancillary ligand allows tuning the emission maximum of the complexes from 540 to 675 nm. In particular, Ir complexes exhibit fluorescence at longer wavelengths. Comparing the spectra of [**Ir-2**]Cl, [**Ir-3**]Cl, [**Ir-4**]Cl and [**Ir-5**]Cl, qibtz ligand shifts the fluorescence at longer wavelengths compared to pybtz. It agrees with the increase of the electron-acceptor character of the NN ligand. Actually the increase of the aromaticity of the ancillary ligand can better delocalize the electron in the MLCT transition, diminishing the energy of the excited state, as recently observed for other iridium complexes [14]. Interestingly, from our data set, the NN ancillary ligand has stronger influence on the fluorescence of the Ir complex compared to the cyclometalated ligand. On the contrary, the CN ligand mostly affects the shift of emission peak for the Rh complexes. This result agrees with literature data, where a large effect is observed for rhodium complexes changing the CN ligand [15] and low modification is obtained varying the ancillary NN moiety [16, 17]. So, the ancillary ligand plays an important role in the excited state of the Ir complexes, whereas the CN ligand influences the excited state of the Rh species. In addition, Rh complexes exhibit structured peaks, whereas Ir complexes have a broad band.
All these differences support the diversity in the excited states for the Ir and Rh centers. Actually, the metal center greatly influences the excited state of an organometallic complex: the different nature of the metal and its intrinsic properties (oxidation number and orbital size) mainly determines the lowest excited state (MC or MLCT) [18]. Mutually, ligands can also influence the excited state of a species, concurring to the splitting Δ of the metal orbitals (Figure 7.10A), following the spectrochemical series. Hence, the ligand can influence the MC or the MLCT states, or promote other transitions, such as the LLCT and LC ones. Figure 7.10 outlines the excitation and emission pathways of a metal complex.

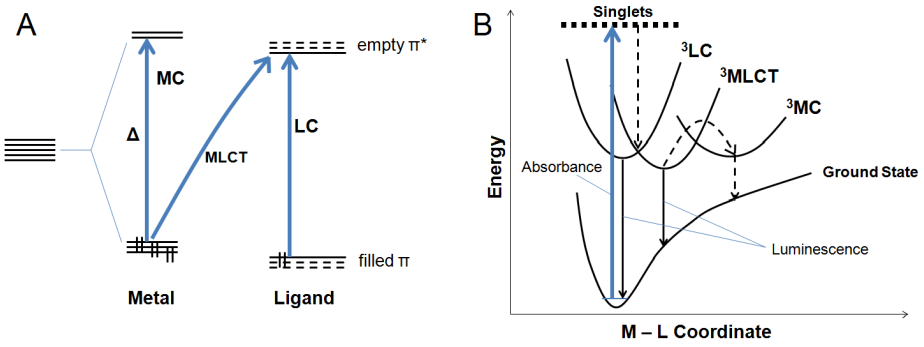

Figure 7.10: Possible absorption and emission mechanisms of a metal complex.

Structured peaks are typical of spin forbidden ^{3}LC transition, and broad bands of ^{3}MLCT transition. So, for the Rh complexes the lowest excited state seems to be a ^{3}LC transition, as generally observed for the cyclometalated Rh species [19]. For Ir complexes, a ^{3}MLCT process is hypothesized to be the lowest energy transition. Actually, a recent published work reports that the new synthesized [**Ir-2**]PF_6 complex has ^{3}MLCT/^{3}LLCT as lowest excited state [3].
The fluorescence quantum yield was determined by comparison with the emission of a reference ($Ru(bpy)_3^{2+}$, $\Phi = 0.028$) under the same experimental conditions. Quantum yield in air-equilibrated water is low for all the complexes (Table 7.4). Interestingly lifetime data of the complexes show that a different trend occurs for Rh and Ir complexes: the Rh [**Rh-2**]Cl and [**Rh-4**]Cl complexes exhibited the longest lifetimes. Notably, the change of the heteroatom from oxygen to sulphur greatly influences the lifetime, being $\tau = 540$ ns for [**Rh-1**]Cl (from Chapter 6) and $\tau = 1470$ ns for [**Rh-2**]Cl.
Another found difference is the variation of the lifetime in different solvents. For Ir complexes, an increase of the lifetime occurs following the trend H_2O < CH_3CN < CH_2Cl_2 (Figure 7.11A). On the other hand, Rh complexes display an opposite behaviour (Figure 7.11B).

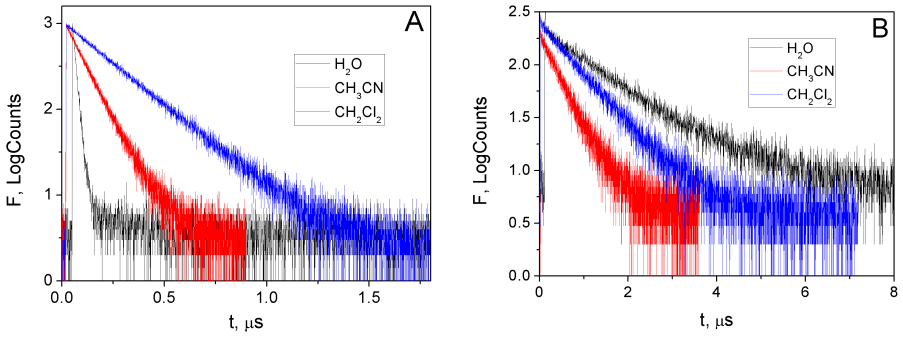

Figure 7.11: Examples of fluorescence decays in different solvents. (A) [**Ir-3**]Cl. (B) [**Rh-2**]Cl.

Table 7.5 reports the lifetimes of the metal complexes in different solvents.

Table 7.5: *Fluorescence lifetimes of the metal complexes in different solvents (τ,* ns*; in brackets the fractional intensity calculated according to Equation (7.2)).* λ_{exc}=331 nm *for **[Ir-1]**Cl, **[Ir-2]**Cl, **[Ir-4]**Cl, **[Rh-1]**Cl, **[Rh-2]**Cl and **[Rh-4]**Cl;* λ_{exc}=373 nm *for **[Ir-3]**Cl and **[Ir-5]**Cl.*

Complex	H_2O	CH_3CN	CH_2Cl_2
[Ir-1]Cl(1)	10.3 (0.90), 217 (0.10)	42.3	110
[Ir-2]Cl	13.1 (0.72), 320 (0.28)	58.5 (0.79), 303 (0.21)	170
[Ir-3]Cl	15.9 (0.92), 130 (0.08)	91	222
[Ir-4]Cl	31.1 (0.79), 389 (0.21)	89	185
[Ir-5]Cl	15.5 (0.90), 172 (0.10)	81.2	198
[Rh-1]Cl(1)	540	165	155
[Rh-2]Cl	1470	480	870
[Rh-4]Cl	2150	338	874

(1) from Chapter 6

These results concur well with the nature of the lowest electronic states of the complexes, as fluorescence lifetimes from ligand centered transitions increase with the solvent polarity, and lifetimes from CT transitions decrease with solvent polarity [20]. In addition, emission spectra of Ir complexes are less broad in apolar solvents, whereas the Rh species have little changes in the structured peaks and they do not change their broadness (Figure 7.S2).
An important point is the dual emission observed for Ir complexes. The Ir dual emission can hardly be associated to impurity. First of all because dual emission is lost in organic solvent (it is still present only for **[Ir-2]**Cl in CH_3CN). Another indication that impurity can be ruled out is the unchanging of excitation spectra varying the emission wavelength (an example is reported in Figure 7.S3 for **[Ir-4]**Cl) [21]. Two lifetimes could be accountable to an aggregation effect in water, but absorption study excludes it at low concentration (see Section 7.2.6). Dual emission of cyclometalated complexes is a controversial theme in literature: two lifetimes for Ir biscyclometalated complexes and only one for Rh complexes are often reported in literature [22,23], but total agreement cannot be found [13,24,25]. However, in the last years several articles have been published reporting dual phosphorescence of Ir complexes [21,26]. Dual emission seems to occur for the very close energy of the ^{3}LC and ^{3}MLCT states [21]. The energy difference between the states strongly depends on the solvent, and changing it can provoke a variation of the energy of the LC and MLCT excited electronic states [27,28]. In effect, our results show two lifetimes having one order of magnitude difference, and it has been reported in literature that the relaxation of ^{3}LC is approximately ten-fold slower than the relaxation of ^{3}MLCT [29].

7.2.5 Singlet Oxygen Production

Detection of singlet oxygen was carried out in the ISOF center of Bologna, under the supervision of Dr. Ilse Manet. Singlet oxygen production was estimated by detection of phosphorescence at 1270 nm in D_2O, irradiating the metal complex solutions at 325 nm (HeCd laser). The absorption was 0.30 at 325 nm for the

samples and the reference (phenalonone, whose singlet oxygen quantum yield is $\Phi_{^1\Delta_g} = 1.0$ [30]), ensuring an equal amount of absorbed photon. For **[Rh-5]**Cl it was not possible to obtain any spectra because of its low solubility in water, while for **[Ir-5]**Cl it was not measured. The highest $\Phi_{^1\Delta_g}$ values were obtained for **[Rh-2]**Cl and **[Rh-4]**Cl (Figure 7.12A and Table 7.6), while for iridium complexes the signal was lower or absent.

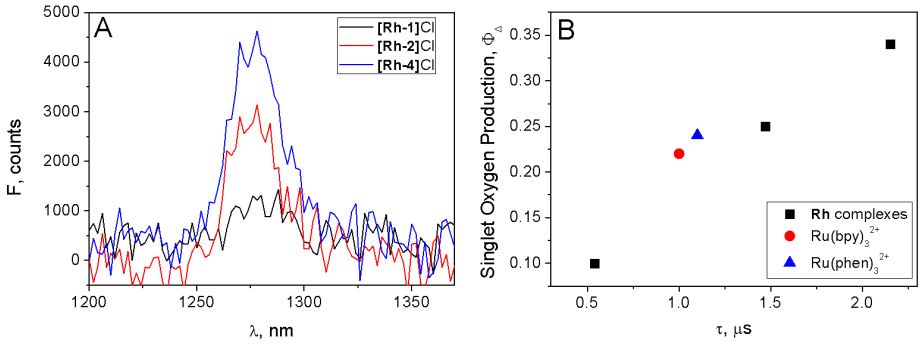

Figure 7.12: (A) Singlet oxygen phosphorescence in the presence of rhodium metal complexes in D_2O. (B) Correlation between fluorescence lifetime and singlet oxygen production; $\Phi_{^1\Delta_g}$ value of **[Rh-1]**Cl is taken from Chapter 6, $Ru(bpy)_3^{2+}$ and $Ru(phen)_3^{2+}$ $\Phi_{^1\Delta_g}$ values are taken from [31].

Table 7.6: *Singlet oxygen quantum yield for the rhodium complexes in D_2O.*

Complex	$\Phi_{^1\Delta_g}$
[Rh-1]Cl**(1)**	0.10
[Rh-2]Cl	0.25
[Rh-4]Cl	0.34

(1) from Chapter 6

This result is noteworthy for the reason that the highest values of singlet oxygen quantum yield are obtained for the complexes displaying the largest lifetime in the set (see Table 7.4). In effect, a linear correspondence between the lifetime and the $\Phi_{^1\Delta_g}$ was found (Figure 7.12B), agreeing well, also, with the singlet oxygen production of two well known compounds, namely $Ru(bpy)_3^{2+}$ ($\Phi_{^1\Delta_g} = 0.22$ with $\tau = 1.0\,\mu s$) and $Ru(phen)_3^{2+}$ ($\Phi_{^1\Delta_g} = 0.24$ with $\tau = 1.1\,\mu s$) in the same solvent (D_2O) [31]. Note that a long lifetime means an enhancement of the probability that the metal complex strikes an oxygen molecule in its excited state.

7.2.6 Dimerization

Dimerization tests in buffer were carried out to observe the presence of possible dimer/aggregate for high complex concentrations. At $I = 6.5\,mM$ no deviation

in the absorbance linearity or in the shape of the absorption spectra was detected for [**Ir-2**]Cl, [**Ir-3**]Cl and [**Rh-2**]Cl (Figure 7.S4) and small variations were observed for [**Ir-4**]Cl and [**Rh-4**]Cl. However, important variations in the spectra appeared for the [**Ir-5**]Cl and [**Rh-5**]Cl complexes for increasing C_D, and the data treatment by means of Equation (2.67) revealed a dimerization process (Figure 7.S5). In effect, X-Ray structure showed stacking interactions between the aromatic rings for [**Ir-5**]Cl (see Table 7.S2), whereas, such interaction was not observed for [**Rh-2**]Cl. Although direct relationship between crystalline and solute states cannot be advanced, this result could confirm the tendency of larger aromatic compounds to associate to give dimeric systems.
Data treatment was performed by means of the dimerization equation derived in Chapter 2, Section 2.2.16, considering the Reaction (7.4).

$$2\,\mathrm{D} \overset{K_{agg}}{\rightleftharpoons} \mathrm{D}_2 \tag{7.4}$$

Table 7.7 reports the obtained dimerization constants (K_{agg}).

Table 7.7: *Dimerization constants of the complexes obtained by Equation (2.67), Chapter 2 (Section 2.2.16). I=6.5 mM, pH=7.0, T=25.0 °C.*

Complex	$10^{-4}K_{agg}$ M^{-1}
[**Ir-2**]Cl	-
[**Ir-3**]Cl	-
[**Ir-4**]Cl	0.3
[**Ir-5**]Cl	3.3
[**Rh-2**]Cl	-
[**Rh-4**]Cl	0.5
[**Rh-5**]Cl	5.4

High dimerization constants were obtained for the [**Ir-5**]Cl and [**Rh-5**]Cl, which are one order higher respect to the K_{agg} of [**Ir-4**]Cl and [**Rh-4**]Cl. However, the low concentrations employed in the photoreactivity experiments and in the titrations guarantee that the predominant species in solution are the monomeric forms.

7.2.7 Photoreactivity

7.2.7.1 Photocleavage of pUC18 Plasmid DNA

The photoreactivity of the metal complexes was evaluated by the conversion of the supercoiled natural form (Form I) of plasmid pUC18 DNA to the circular (Form II) and linear (Form III) forms, detected by electrophoresis. Irradiation was carried out at 365 nm (UV region, Figure 7.13), 435 nm (visible blue region, Figure 7.14) and 500 nm (visible cyano-green region, Figure 7.15) and t_{irr} = 100 min ($\frac{C_D}{C_P} = 1$, with $C_P = 20\,\mu$M in nitrogenous bases). The quantification of the cleavage by means of Equation (2.31), Chapter 2, is reported in Figure 7.16. Two independent electrophoretic assays were performed at every irradiation wavelength and a mean value is reported.

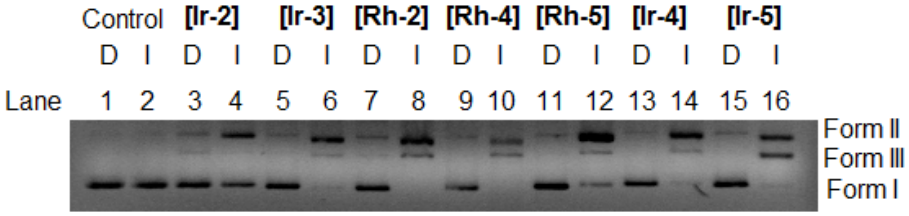

Figure 7.13: Photocleavage of the metal complexes/pUC18 systems in the dark (D) and irradiated (I) at $\lambda = 365\,\text{nm}$ and $t_{irr} = 100\,\text{min}$. Lane 1: Control in the dark. Lane 2: Irradiated control. Lane 3-4: [**Ir-2**]Cl. Lane 5-6: [**Ir-3**]Cl. Lane 7-8: [**Rh-2**]Cl. Lane 9-10: [**Rh-4**]Cl. Lane 11-12: [**Rh-5**]Cl. Lane 13-14: [**Ir-4**]Cl. Lane 15-16: [**Ir-5**]Cl. C_D=20 µM; C_P=20 µM; [NaCl]=4.0 mM; [NaCac]=2.5 mM.

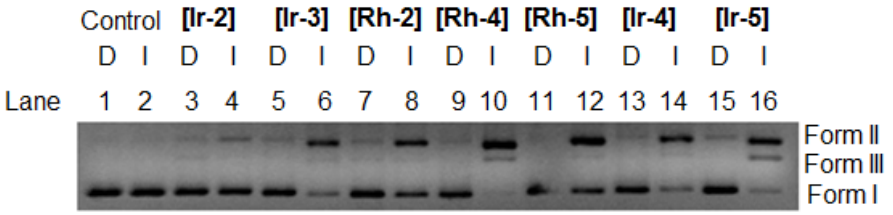

Figure 7.14: Photocleavage of the metal complexes/pUC18 systems in the dark (D) and irradiated (I) at $\lambda = 435\,\text{nm}$ and $t_{irr} = 100\,\text{min}$. Lane 1: Control in the dark. Lane 2: Irradiated control. Lane 3-4: [**Ir-2**]Cl. Lane 5-6: [**Ir-3**]Cl. Lane 7-8: [**Rh-2**]Cl. Lane 9-10: [**Rh-4**]Cl. Lane 11-12: [**Rh-5**]Cl. Lane 13-14: [**Ir-4**]Cl. Lane 15-16: [**Ir-5**]Cl. C_D=20 µM; C_P=20 µM; [NaCl]=4.0 mM; [NaCac]=2.5 mM.

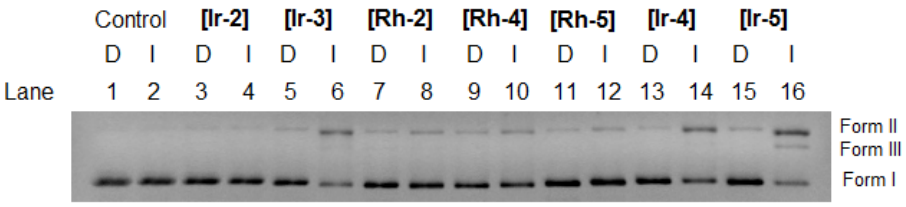

Figure 7.15: Photocleavage of the metal complexes/pUC18 systems in the dark (D) and irradiated (I) at $\lambda = 500\,\text{nm}$ and $t_{irr} = 100\,\text{min}$. Lane 1: Control in the dark. Lane 2: Irradiated control. Lane 3-4: [**Ir-2**]Cl. Lane 5-6: [**Ir-3**]Cl. Lane 7-8: [**Rh-2**]Cl. Lane 9-10: [**Rh-4**]Cl. Lane 11-12: [**Rh-5**]Cl. Lane 13-14: [**Ir-4**]Cl. Lane 15-16: [**Ir-5**]Cl. C_D=20 µM; C_P=20 µM; [NaCl]=4.0 mM; [NaCac]=2.5 mM.

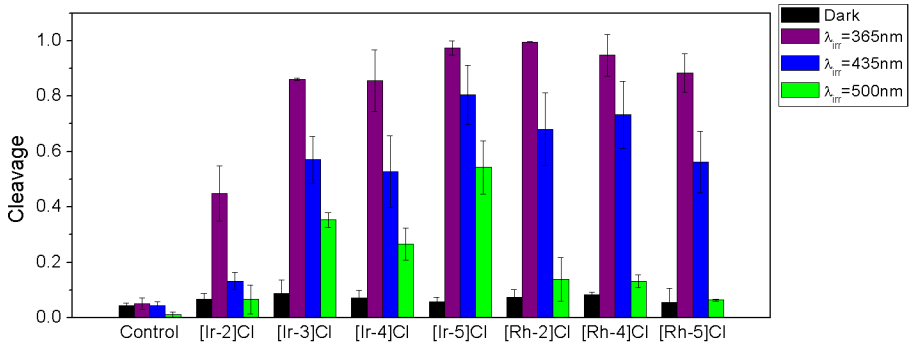

Figure 7.16: Quantification of the cleavage at λ_{irr}=365 nm, 435 nm and 500 nm, t_{irr}=100 min. C_D=20 µM; C_P=20 µM; [NaCl]=4.0 mM; [NaCac]=2.5 mM.

From the collected experiments, we found that:

- at 365 nm high cleavage was observed in the presence of all the complexes except for the [**Ir-2**]Cl iridium complexes. In particular, high cleavage was observed for all the Rh complexes, with significant formation of Form III of plasmid DNA. It concurs well with the fact that we found the highest singlet-oxygen production. High cleavage was obtained also in the presence of [**Ir-5**]Cl, with a very high formation of Form III;
- at 435 nm significant cleavage of plasmid DNA is still present for both Ir and Rh species;
- at 500 nm the decrease of the cleavage is relevant for samples containing the Rh complexes, whereas for the solutions with Ir complexes significant cleavage is still present. Activation in the green visible region is possible thanks to the presence of the above mentioned tail in the absorption spectra of the Ir complexes, in the 500 nm region (Figure 7.8A).

Hence, despite the Rh complexes displayed the highest values of singlet oxygen quantum yield, their absorption spectra is not compatible with photoactivation above $\lambda = 450$ nm. On the contrary, for Ir complexes the singlet oxygen quantum yield is lower, but the higher molar absorption coefficient associated to the ^{3}MLCT transition, allows the activation in the green region, more interesting for PDT.

7.2.7.2 Photoreactivity with Cell Line and Cellular Uptake

The complexes have been tested with the SW480 cancer cell line under irradiation in the ultraviolet region with a lamp (maximum around 365 nm), while the control consisted of treated cell kept in the dark. The proofs were performed by Dr. Natalia Busto from the Physical Chemistry laboratory of Universidad de Burgos. An increase in the cytotoxic effect was observed upon irradiation for the majority of the complexes, in particular for the [**Ir-3**]Cl and [**Rh-4**]Cl (Table 7.8). However, the IC_{50} values are also low in dark conditions, an undesirable property for a photosensitizer.

Table 7.8: *Cytotoxic activity of the metal complexes in the dark ($IC_{50}DARK$) and upon irradiation ($IC_{50}IRR$) for* 20 min *at* 365 nm *(*20 mWcm^{-1}*) and Photoindex value (PI).* 1×10^4 cells*, incubation* 24 h.

Compound	$IC_{50}DARK$, µM	$IC_{50}IRR$, µM	PI
[**Ir-2**]Cl	1.6 ± 0.2	0.5 ± 0.1	3
[**Ir-3**]Cl	1.4 ± 0.2	0.3 ± 0.1	5
[**Ir-4**]Cl	1.8 ± 0.1	0.5 ± 0.3	3
[**Ir-5**]Cl	1.2 ± 0.3	pending	-
[**Rh-1**]Cl	2.5 ± 0.3	0.7 ± 0.2	4
[**Rh-4**]Cl	1.8 ± 0.2	0.4 ± 0.1	5
[**Rh-5**]Cl	2.2 ± 0.6	1.2 ± 0.5	2

Finally, cellular uptake was monitored by means of fluorescence. The clearest images are obtained for the iridium complexes, which exhibited orange fluorescence. From the comparison of the reported images (phase contrast, orange emission and their overlay) in Figure 7.17 and 7.18 we verified that iridium complexes enter inside the cell, even though it seems that they predominantly remains outside the nucleus, because of the low fluorescence intensity in this region.

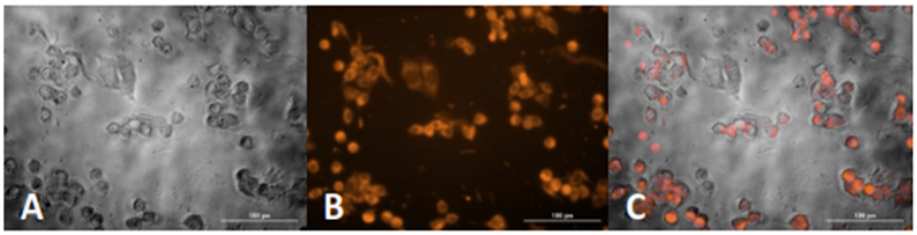

Figure 7.17: Image of SW480 cells treated with 50 µM of [**Ir-2**]Cl after 30 min incubation. (A) Phase contrast, (B) orange emission ($\lambda_{ex} = 469$ nm and $\lambda_{em} = 647$ nm) and (C) overlay.

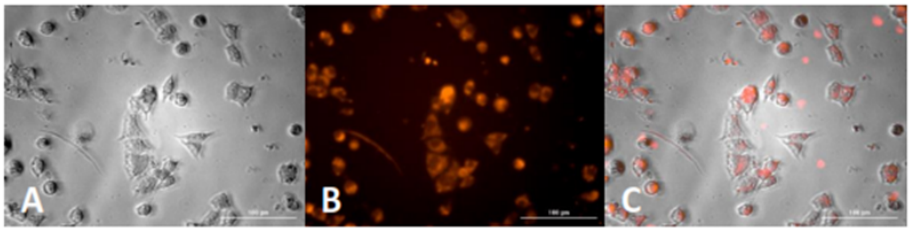

Figure 7.18: Image of SW480 cells treated with 50 µM of [**Ir-3**]Cl after 30 min incubation. (A) Phase contrast, (B) orange emission ($\lambda_{ex} = 469$ nm and $\lambda_{em} = 647$ nm) and (C) overlay.

It is noteworthy to point out that such a method only allows to verify that the metal drugs enter inside the cell, but we cannot obtain reliabale information about the amount of drugs that passes through the membrane or where it is placed.

7.2.8 Binding study to G-Quadruplexes

7.2.8.1 Titrations with Oligonucleotides

Following the photoreactivity tests on our complexes, we completed their study addressing the affinity of the metal complexes for G-Quadruplexes of G-rich DNA. Regarding the polynucleotides, double-stranded DNA of self-complementary 26-mer (52B), G4 c-myc (Pu22) and human telomere (Tel22) sequences were used. Titrations were performed in the ISOF center, in Bologna, under the supervision of Dr. Ilse Manet.
We checked the interaction of three Ir complexes ([**Ir-2**]Cl, [**Ir-3**]Cl and [**Ir-4**]Cl). Since the chosen iridium species are different for the ancillary and the cyclometalating ligand, we can try to associate the difference in the affinity with the structure of the cyclometalated metal complex.
Why we tested the Ir complexes and not the Rh ones?:

- as observed in Chapter 6, the presence of a polynucleotide switched the fluorescence of the [**Ir-1**]Cl complex on, whereas no important variation was observed for [**Rh-1**]Cl. To verify if such result was a general behaviour of our complex family, we checked the fluorescence in the presence of an excess of CT-DNA. What we found agrees with our hypothesis: light switch on behaviour was displayed for all the Ir complexes, whereas for the Rh systems either decrease or very small increase of the fluorescence intensity was observed (Figure 7.19).

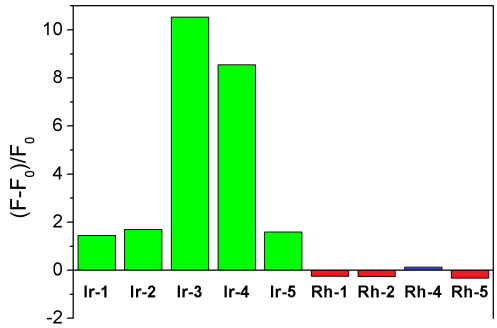

Figure 7.19: Light-switch on behaviour in the presence of an excess of CT-DNA. C_D=5.0 × 10^{-6} M, C_P=1.0 × 10^{-4} M (in basepairs), I=6.5 mM (NaCl), pH=7.0 (NaCac) and T=25.0 °C.

This result likely is related to the nature of the excited states, which behave differently once the molecules interact with the nucleic acids; as to the

Rh complexes the LC excited states are expected to be better electron acceptors than the ground state, and independently of the nature of the ligand all complexes may be quenched by electron transfer from the DNA to ligand in the complex. We observe different *turn on* efficiencies for the Ir complexes in line with the emitting state being a MLCT state. In the presence of DNA emission from the MLCT state depends not only on the nature of the ligand, but also on the involvement or not of the ligand in the binding process.

- the previous reported results of cellular uptake show that iridium complexes can be observed inside the cell, whereas no image has been obtained for the rhodium ones. Consequently, the most interesting species seem to be the iridium complexes;
- finally, the previous proofs with **[Ir-1]**Cl and **[Rh-1]**Cl (Chapter 6) verified similar mode of binding to DNA and, as the oligonucleotides are rather expensive, we focused only on one metal center.

UV-vis absorption, circular dichroism in the ultraviolet and visible region, excitation profiles, fluorescence steady-state and fluorescence decays have been employed to study the interaction of the metal compounds towards the oligo.
The results of the titrations between the iridium complexes and the oligonucleotides are reported in Supporting Information (Figure 7.S6-7.S14).
Regarding the UV-vis titrations (Figures A in 7.S6-7.S14), the interaction of double-stranded (ds) DNA and the metal complexes provoked small changes in the spectra of the metal compounds. In particular, no remarkable hypochromic effect and/or red shift of the bands is visualized, ruling out intercalation as a possible mechanism of interaction. On the other side, variations of the spectra are more evident in the interaction with G4 structures.
The circular dichroism of the duplex and quadruplex structure were not greatly affected by the binding of the metal complexes (Figures B in 7.S6-7.S14), even though decrease of the band intensity is observed for some systems, in particular for the c-myc G4 dichroic signals once interacting with **[Ir-3]**Cl and **[Ir-4]**Cl. It should mean that the binders did not significantly modify the native quadruplex structures.
The binding of the metal complex provoked in some cases weak induced CD signal in the visible region due to the Ir complex. In Figures 7.S6-7.S14 we show the visible CD of the Ir-complexes that are endowed with a signal upon DNA binding.
But the most interesting results are obtained with the fluorescence titrations. Actually, a fluorescence intensity increase was visualized for all the metal complexes (Figure 7.20). Interestingly, for some systems this variation was not high (2-fold), while a more than 30-fold fluorescence intensity increase was observed for others. In particular, the lowest light-switch on was visualized for the interaction with ds DNA for all the complexes in the data set.
From the experimental data, we observed that

- **[Ir-2]**Cl: the interaction with ds DNA and telomere G4 increased the fluorescence of 2-fold in the presence of excess DNA. On the other hand, a nine-fold increase was obtained in the presence of the c-myc G4. For **[Ir-2]**Cl the plots suggest the formation of only one adduct with the oligonucleotides with 1:1 stoichiometry;

- [**Ir-3**]Cl: slight fluorescence increase was obtained in the presence ds DNA and telomere G4 and the results suggest the formation of a 1:1 adduct. On the other hand the interaction with c-myc G4 caused a 15-fold fluorescence intensity increase. In addition induced dichroism, steady-state fluorescence and lifetime study suggest two different modes of binding, the first one obtained in defect of oligonucleotides (maybe a 2:1 adduct) and the second one in equimolar conditions (1:1 adduct);

- [**Ir-4**]Cl: a relevant fluorescence light-switch is obtained in the presence of all the oligonucleotides, with the highest increase displayed by the [**Ir-4**]Cl/c-myc G4 system, showing a 32-fold fluorescence enhancement. A plausible reason may be the breakdown of complex dimers by the DNA with the amount of monomeric complexes increasing together with the upset of the adduct in solution. For [**Ir-4**]Cl the interactions with all the oligonucleotides seem to involve two types of adducts, the 2:1 and the 1:1 ones.

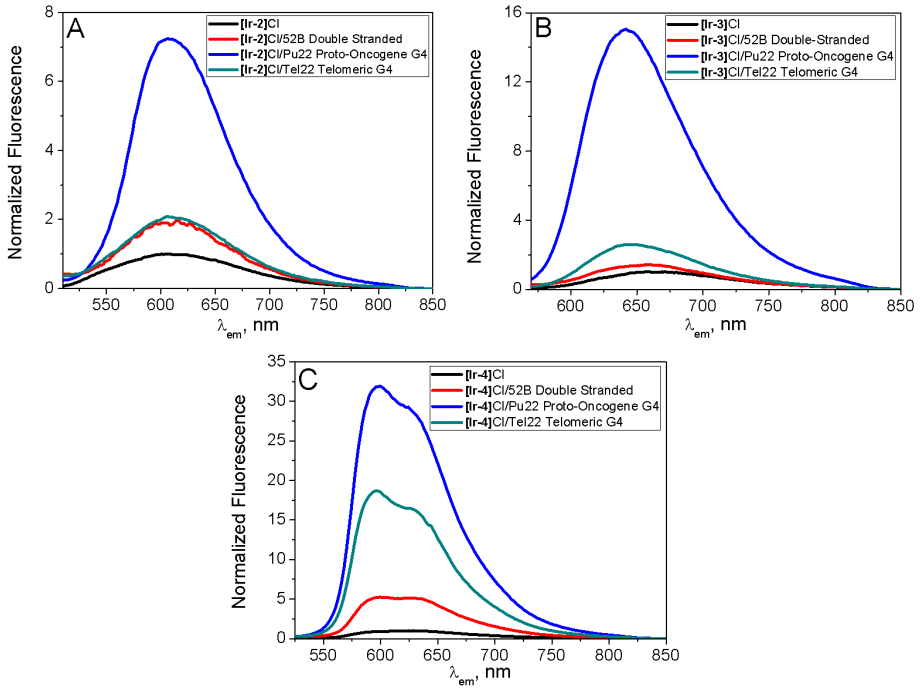

Figure 7.20: Fluorescence enhancement in the presence of oligonucleotides. (A) [**Ir-2**]Cl. (B) [**Ir-3**]Cl. (C) [**Ir-4**]Cl. C_D=7.5 × 10^{-6} M, C_P=2.2 × 10^{-5} M, I=0.1 M (KCl), pH=7.0 (phosphate buffer) and T=25.0 °C.

Fluorescence enhancement has been previously reported by Castor et al. for other Ir biscylometalated complexes interacting with quadruplex structures [32]. In fact, many compounds display a fluorescence light switch together with a blue shift of the maximum by interaction with G-Quadruplexes, as we observed [33, 34]. This behaviour was ascribed to the shielding of the metal complex by

the oligonucleotide, placing the complex from a polar aqueous environment to an apolar surrounding. Interestingly, direct correlation between the maximum blue shift ($\Delta\lambda_{max}$) and fluorescence enhancement has been recently reported [34], in agreement with our results.
Differently, Castor et al. observed the highest fluorescence switch-on in the presence of telomeric G4 structure and a minor increase in the presence of the c-myc moiety. In our case we observed the opposite results, with the highest fluorescence enhancement observed in the presence of the c-myc G4. Such result is probably due to the different folding of the G-Quadruplex structures (c-myc G4 has a parallel conformation [35,36], whereas telomere G4 has hybrid structure in potassium aqueous medium [37]).
Note that the same explanation can be advanced for the lifetime measurements [38], as a correlation between fluorescence enhancement and increase in the fluorescence lifetime was found. The cited values are listed in Table 7.9.

Table 7.9: *Obtained parameter of the luminescence of the interaction between the biscyclometalated complexes with the oligonucleotides.*

Complex	**Oligo**	$\frac{F}{F_0}$	$\Delta\lambda_{em}^{max}$, nm	τ_{adduct}, ns
[Ir-2]Cl	52B	2	0	128 (1:1)
	Pu22	7	−4 nm	109 (1:1)
	Tel22	2	−2 nm	85 (1:1)
[Ir-3]Cl	52B	1.5	−3 nm	57 (1:1)
	Pu22	15	−20 nm	109 (2:1),377 (1:1)
	Tel22	3	−10 nm	74 (1:1)
[Ir-4]Cl	52B	5	−20 nm	120 (2:1)
	Pu22	32	−25 nm	133 (2:1), 1732 (1:1)
	Tel22	16	−25 nm	140 (1:1), 1430 (2:1)

Concerning the interaction of a small molecule with G-Quadruplex, various modes of binding are viable (external, groove/loop binding, intercalation, end stacking) [39–41]. For many octahedral compounds the end-stacking interaction has been proposed [32,34]. However, for part of the examined systems two types of adduct have been hypothesized from the experimental tracks in fluorescence and the appearance of two very different new lifetimes. A dual mode of binding was observed for other cyclometalated complexes towards interaction with DNA by means of calorimetry and/or lifetime measurements [42,43]. Interestingly, for the systems exhibiting two modes of binding, at the first point of the titration the prevailing complex (which reasonably is a 2:1 complex) has a faster lifetime respect to the species prevailing at higher concentration of oligonucleotide (1:1 complex). It could agree with the fact that the presence of more than one metal complex bound to the same oligonucleotide can provoke mutual quenching of the fluorescence, with a decrease of the lifetime. However, in equimolar conditions of metal complex/oligonucleotide, all the metal complexes can insert inside the G-Quadruplex structure and the resulting species will have a longer lifetime because it will be shielded more efficiently by the solvent molecules and it is free from intermolecular interactions between other metal complexes.

Multiwavelength global analysis of the titration data was carried out by means of the REACTLAB program. REACTLAB calculates the equilibrium constant of adducts between the metal complex and the oligonucleotides as well as the spectra of the adducts with the different stoichiometries. The program requires as input all spectra, total concentration of complex (C_D) and DNA (C_P) in all mixtures and a binding model. Analysing the data, different models have been used, with a single adduct having 1:1 or 2:1 stoichiometry (complex:DNA) or two adducts forming contemporarily with 1:1 or 2:1 stoichiometry. Statistical parameters are indicative of the goodness of the fitting model.
The choice of the binding model (1:1) or (2:1) was further compared with the lifetime measurements. When the lifetime measurements suggested the presence of more than one adduct, we fitted the spectra including the formation of two adducts (Reactions (7.5) and (7.6)), being M the oligonucleotide and L the metal complex.

$$\mathrm{M} + \mathrm{L} \overset{K_1}{\rightleftarrows} \mathrm{ML} \tag{7.5}$$

$$\mathrm{M} + 2\,\mathrm{L} \overset{K_1 K_2}{\rightleftarrows} \mathrm{ML_2} \tag{7.6}$$

Table 7.10 reports the equilibrium constants obtained by REACTLAB analysis from the different employed techniques. The obtained equilibrium constants demonstrate a selectivity towards G-Quadruplex; in particular a strong interaction with the c-myc G4 was found for all the complexes, having the highest equilibrium constants in the titrations set.

Table 7.10: *Logarithmic values of the equilibrium constants (K_1 for 1:1 stoichiometry and K_1K_2 for 2:1 stoichiometry) of the interaction between the metal complexes and the oligonucleotides. I=0.1 M (KCl), pH=7.0 (phosphate buffer). Kinetic constants obtained from (1) fluorescence titrations; (2) induced circular dichroism of the complex.*

Complex	ds DNA	c-myc G4	telomeric G4
[**Ir-2**]Cl	$4.5(1:1)^{(1)}$ $4.4(1:1)^{(2)}$	$5.3(1:1)^{(1)}$ $5.1(1:1)^{(2)}$	$4.3(1:1)^{(1)}$
[**Ir-3**]Cl	-	$6.4(1:1)$, $11.5(2:1)^{(1)}$ $6.6(1:1)$, $11.4(2:1)^{(2)}$	$4.2(1:1)^{(1)}$
[**Ir-4**]Cl	Not Calculated	$6.3(1:1)$, $11.4(2:1)^{(1)}$ $5.5(1:1), 10.3(2:1)^{(2)}$	$4.5(1:1)$, $10.4(2:1)^{(1)}$ $4.4(1:1)$, $10.0(2:1)^{(2)}$

7.2.8.2 FRET Analysis

Stabilization proofs of oligonucleotides secondary structures were performed by means of FRET analysis. Excess of metal complex (50-fold, saturation condition) was used in the presence of different oligonucleotides covalently linked by a fluorophore (Fluorescein, F) and an acceptor (TAMRA, T) at both terminals of the chain. Proofs were performed in I = 0.11 M and pH = 7.2 ([LiCl] =

90 mM, [KCl] = 10 mM, [LiCac] = 10 mM); in such a condition the studied oligonucleotides fold to form different Quadruplex structures, which are listed in Table 7.11 [44]. In addition, an intramolecular duplex structure (FdxT) was tested, as well.

Table 7.11: *Oligonucleotides covalently linked to fluorescein (F) and TAMRA (T). Primary and secondary structures formed in the experimental conditions and melting temperature [44]. [LiCl]*=90 mM, *[KCl]*=10 mM, I=0.1 M, *pH*=7.2.

Oligonucleotide	**Sequence**	T_m, °C
F21T	mayor human hybrid-telomeric DNA GGG TTA GGG TTA GGG TTA GGG	53.1
F21RT	human parallel-telomeric RNA GGG UUA GGG UUA GGG UUA GGG	59
F25CebT	human-parallel DNA mini satellite with large loop A GGG T GGG TGT AAGTGT GGG T GGG T	68.7
F21CTAT	human parallel telomeric DNA GGG CTA GGG CTA GGG CTA GGG	57.9
FmycT	parallel proto-oncogene TTGA GGG T GGG TA GGG T GGG TAA	65.5
FBom17T	2tetrads of Bombix-antiparallel telomeric DNA GG TTA GG TTA GG TTA GG	48.8
FTBAT	trombin binding aptamer-2antiparallel tetrads GG TT GG TGT GG TT GG	51.6
FdxT	duplex intramolecular TATAGCTAT-hexaetilenglycol-TATAGCTATA	66.1

Concerning Ir complexes, increase of the melting temperature of the G4 structures was observed in the presence of all complexes (Figure 7.21).

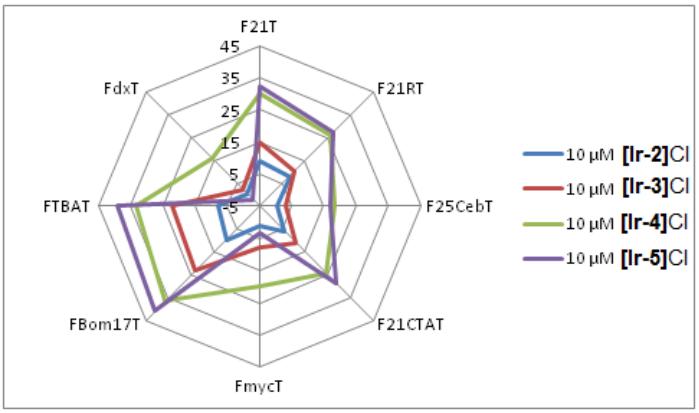

Figure 7.21: ΔT_m increase for quadruplex and duplex structures in the presence of Ir complexes. C_P=0.2 µM, C_D=10 µM, [LiCl]=90 mM, [KCl]=10 mM, [LiCac]=10 mM, I=0.11 M, pH=7.2.

In particular, the stabilization effect increased with the aromatic extension of the CN and the NN ligands, ensuing the following order: [**Ir-5**]Cl ≈ [**Ir-4**]Cl > [**Ir-3**]Cl > [**Ir-2**]Cl. Although the stabilization effect provided by the [**Ir-5**]Cl and [**Ir-4**]Cl complexes was similar, [**Ir-5**]Cl did not stabilize the ds DNA, whereas [**Ir-4**]Cl did.
High values of thermal stabilization were detected for the telomeric F21T, F21RT and F21CTAT quadruplexes, and for FBom17T and FTBAT, whereas less stabilization was reached for c-myc structure. However, it should be pointed out that telomeric structures exhibit lower melting temperature respect to c-myc structure, which has high T_m even in the absence of the metal drug under the employed experimental conditions (see Table 7.11).
Proofs were performed with the Rh complexes, as well (Figure 7.22). [**Rh-2**]Cl and [**Rh-4**]Cl complexes show very similar results compared to their [**Ir-2**]Cl and [**Ir-4**]Cl analogues. On the other hand, low stabilization effect is observed in the presence of the [**Rh-5**]Cl complex.

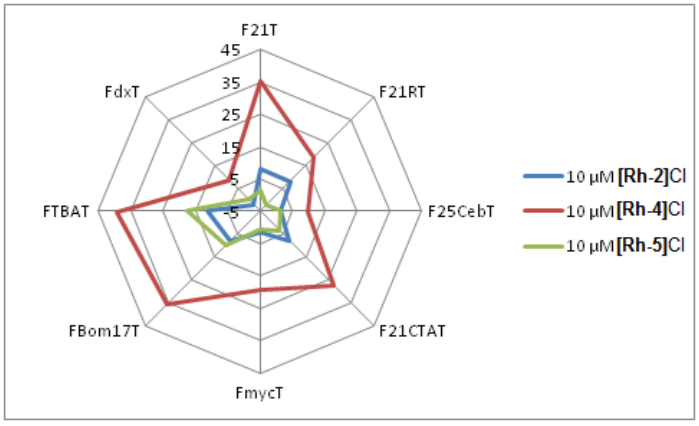

Figure 7.22: ΔT_m increase for quadruplex and duplex structures in the presence of Rh complexes. C_P=0.2 µM, C_D=10 µM, [LiCl]=90 mM, [KCl]=10 mM, [LiCac]=10 mM, I=0.11 M, pH=7.2.

It is noteworthy to recall here that the proofs performed with the FRET analysis were in a large excess of metal complex. Further studies will be addressed to stabilization tests for lower $\frac{C_D}{C_P}$ ratios. In addition, competition proofs in the presence of quadruplex and duplex could be useful in order to observe if the complexes are able to selectively stabilize the G4 forms, even in the presence of ds structures.

7.3 Conclusions

From Chapter 6 we found interesting differences between two biscyclometalated complexes, differing only by the metal center (iridium and rhodium). In Chapter 7 we planned the synthesis of new complexes to observe how such differences can be tuned varying the ligands. More than that, in this Chapter we wanted to go one step further, and a study on the selectivity towards different DNA structures, namely G-Quadruplex structures and ds DNA, was carried out. Our study

showed that Rh complexes had the highest singlet oxygen quantum yield, a property which we related to the longest lifetime, in agreement with literature data, but they absorb only below 450 nm. The absorption bands at longer wavelength found for the Ir complex make them more attractive as photosensitizer because, even if they exhibit lower singlet oxygen production, they can be activated in a more appropriate region for PDT. In this context, the ligands play an important role, shifting the absorption to red region. In addition, Ir complexes exhibited emission switch on, whereas Rh complexes did not, in agreement with our result in Chapter 6. Such fluorescence allowed to observe the Ir complexes inside the cell. Our results also showed that ligands not only influence the photoproperties of the biscylometalated complexes, but we verified that they are decisive for the affinity towards DNA. In particular, higher affinity for G-Quadruplex was revealed by different techniques. Interestingly the highest fluorescence switch on was observed in the presence of c-myc G-Quadruplex. Stabilization of the G4 was found in the presence of both Ir and Rh species, corroborating the results of recent papers reporting that even octahedral compounds are able to stabilize G-Quadruplex structures.

7.4 Synthesis and Characterization Data

7.4.1 2-(2'-pyridyl)benzothiazole (pybtz)

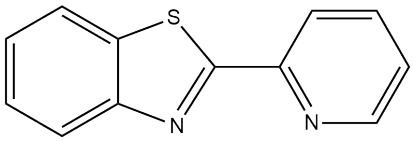

2-aminothiophenol (0.250 g, 2.00 mmol) and 2-pyridylcarboxaldheyde (0.228 mL, 0.257 g, 2.40 mmol) were inserted in a schlank with DMSO (7 mL), and the mixture was stirred at 60 °C for 6 h under air atmosphere. H_2O was added (7 mL) and the product was extracted with ethylacetate (AcOEt, 3×20 mL). Then, $MgSO_4$ was added and the solution was filtered and evaporated under vacuum. The purification of the product was achieved by means of a silica gel column; the eluting phase was AcOEt:Hexane 1:1. The aliquots of the product were collected, added $MgSO_4$, filtered and evaporated in vacuum. The resulting white solid was dried under vacuum. Yield: 111.0 mg (0.523 mmol, 26.2 %).
^{1}H-NMR (400 MHz**, DMSO−$\mathbf{d_6}$,** 25.0 °C): δ 8.74 (d, J = 4.7 Hz, 1H), 8.34 (d, J = 7.9 Hz, 1H), 8.18 (d, J = 8.0 Hz, 1H), 8.11 (d, J = 8.1 Hz, 1H), 8.05 (t, J = 7.7 Hz, 1H), 7.63–7.55 (m, 2H), 7.51 (t, J = 8.0 Hz, 1H) ppm.

7.4.2 2-(2'-quinolinyl)benzothiazole (qibtz)

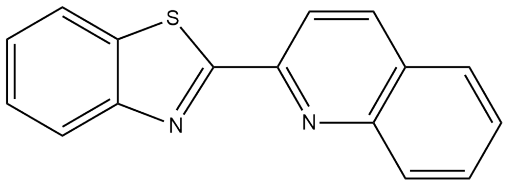

2-aminothiophenol (0.250 g, 2.00 mmol) and 2-quinolinylcarboxaldheyde (0.381 g, 2.42 mmol) were inserted in a schlank with DMSO (6 mL), and the mixture was stirred at 60 °C for 6 h under air atmosphere. H_2O was added (6 mL) and the product was extracted with ethylacetate (AcOEt, 3×20 mL). Then, $MgSO_4$ was added and the solution was filtered and evaporated under vacuum. The purification of the product was achieved by means of a silica gel column; the eluting phase was AcOEt:Hexane 1:1. The aliquots of the product were collected, added $MgSO_4$, filtered and evaporated in vacuum. The resulting yellowish solid was dried under vacuum. Yield: 264.4 mg (0.101 mmol, 51 %).
^{1}H-NMR (400 MHz**, $CDCl_3$−d,** 25.0 °C): δ 8.51 (d, J = 8.5 Hz, 1H), 8.32 (d, J = 8.5 Hz, 1H), 8.21 (d, J = 8.5 Hz, 1H), 8.15 (d, J = 8.1 Hz, 1H), 8.00 (d, J = 8.0 Hz, 1H), 7.88 (d, J = 8.3 Hz, 1H), 7.81–7.76 (t, 1H), 7.64–7.58 (t, 1H), 7.56–7.51 (t, 1H), 7.48–7.43 (t, 1H) ppm.

7.4.3 2-phenylisoquinoline (piqi)

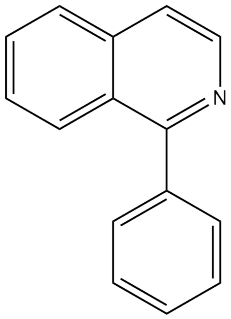

1-bromoisoquinoline (0.500 g, 2.403 mmol) was added in a schlenk in the presence of a solution of phenylboronic acid (0.352 g, 2.88 mmol), K_2CO_3 (0.795 g, 4.81 mmol) and 2.2 mg $PdCl_2$ (catalyst) with 10 mL of EtOH and 10 mL of H_2O (EtOH:H_2O 1:1). The solution was stirred and heated at 90 °C for 6 h under nitrogen atmosphere. A saturated solution of NaCl (60 mL) was added and the complex was extracted with diethylether (3×20 mL). The resulting solution was washed with 20 mL of water and dried with $MgSO_4$. The solvent was evaporated and, then, hexane was added. The solution was passed through a silica gel column (AcOEt:Hexane 30:70), collected the aliquots, dried again with $MgSO_4$, filtered and the solvent was evaporated under vacuum. Yield: 274.8 mg (1.67 mmol, 58 %).

^{1}H-NMR (400 MHz, **$CDCl_3$–d,** 25.0 °C): δ 8.62 (d, J = 5.6 Hz, 1H), 8.11 (d, J = 8.4 Hz, 1H), 7.89 (d, J = 8.3 Hz, 1H), 7.73–7.68 (m, 3H), 7.66 (d, J = 5.8 Hz, 7H), 7.57–7.46 (m, 4H) ppm.

7.4.4 $Ir_2(ppy)_4Cl_2$

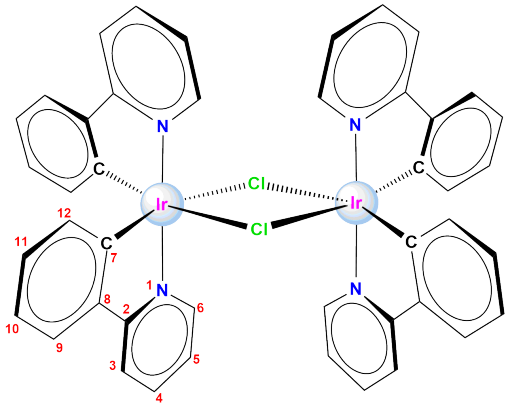

2-phenylpyridine (1.00 mL, 1.09 g, 7.01 mmol) was added to a solution of $IrCl_3 \cdot 3\,H_2O$ (1.00 g, 2.83 mmol) in a schlank with 20 mL of ethoxyethanol and 6.7 mL of H_2O, and the mixture was stirred at 110 °C for 24 h under a nitrogen atmosphere. The product was washed with diethyl ether, filtered and washed with a solution EtOH (3 mL) and acetone (3 mL). The resulting yellow powder was dried under vacuum. Yield: 1188.7 mg (1.109 mmol, 78 %).
^{1}H-NMR (400 MHz, **$CDCl_3$–d,** 25.0 °C) δ 9.24 (d, J = 5.7 Hz, 4H), 7.87 (d, J = 7.7 Hz, 4H), 7.73 (t, J = 7.6 Hz, 4H), 7.48 (d, J = 7.9 Hz, 4H), 6.87–6.68 (m, 8H), 6.56 (t, J = 7.5 Hz, 4H), 5.93 (d, J = 7.8 Hz, 4H) ppm.

7.4.5 $Rh_2(ppy)_4Cl_2$

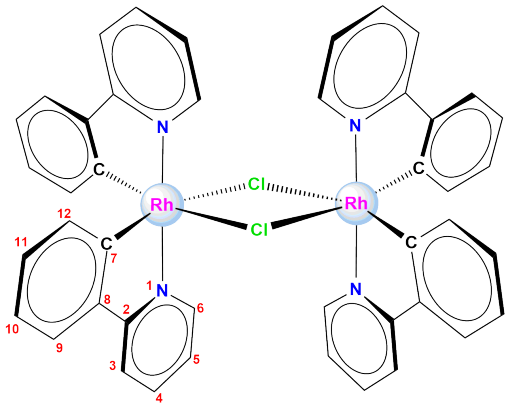

2-phenylpyridyne (2.82 mL, 3.07 g, 19.8 mmol) was added to a solution of $RhCl_3 \cdot 3\,H_2O$ (2.09 g, 7.90 mmol) in a schlank with 15 mL of 2-methoxyethanol and 2.5 mL of H_2O, and the mixture was stirred at 110 °C for 24 h under a nitrogen atmosphere. The product was washed with diethyl ether, filtered and washed with a solution EtOH (3×3 mL) and acetone (3×3 mL). The resulting yellow powder was dried under vacuum. Yield: 2991.0 mg (3.348 mmol, 88 %).
^{1}H-NMR (400 MHz, **$CDCl_3$–d,** 25.0 °C) δ 9.24 (d, $J = 5.7$ Hz, 4H), 7.87 (d, $J = 7.7$ Hz, 4H), 7.73 (t, $J = 7.6$ Hz, 4H), 7.48 (d, $J = 7.9$ Hz, 4H), 6.87–6.68 (m, 8H), 6.56 (t, $J = 7.5$ Hz, 4H), 5.93 (d, $J = 7.8$ Hz, 4H) ppm.

7.4.6 $Ir_2(piqi)_4Cl_2$

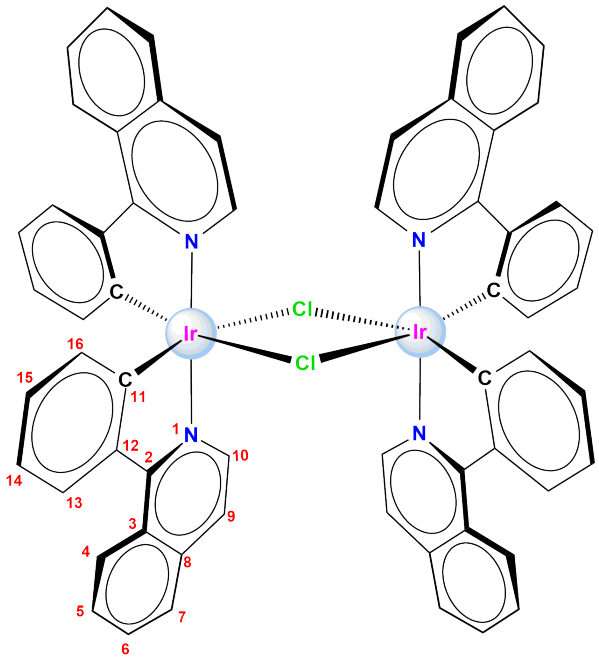

2-phenylisoquinoline (0.264 g, 1.285 mmol) was added to a solution of $IrCl_3 \cdot 3\,H_2O$ (0.189 g, 0.537 mmol) in a schlank with 15 mL of ethoxyethanol and 5 mL H_2O, and the mixture was stirred at 110 °C for 24 h under a nitrogen atmosphere. 15 mL of water were added and the solvent was filtered, the powder was washed with 4 mL of Acetone, 4 mL of EtOH and 4 mL of Et_2O. The resulting red powder was dried under vacuum. Yield: 216.3 mg (0.170 mmol, 63 %).
^{1}H-NMR (400 MHz, **$CDCl_3$–d,** 25.0 °C): δ 9.05 (d, $J = 6.4$ Hz, 4H), 8.97 (d, $J = 8.1$ Hz, 4H), 8.12 (d, $J = 8.0$ Hz, 4H), 7.83 (m, $J = 8.7$ Hz, 8H), 7.79–7.69 (t, 4H), 6.81 (t, $J = 8.1$ Hz, 4H), 6.55 (d, $J = 6.5$ Hz, 4H), 6.50 (t, $J = 7.5$ Hz, 4H), 6.03 (d, $J = 7.8$ Hz, 4H) ppm.

7.4.7 $Rh_2(piqi)_4Cl_2$

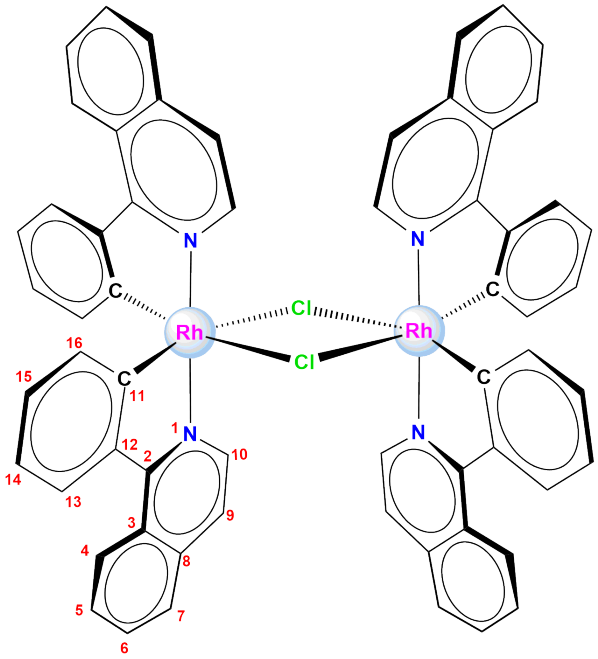

2-phenylisoquinoline (0.275 g, 1.34 mmol) was added to a solution of $RhCl_3 \cdot 3\,H_2O$ (0.117 g, 0.4466 mmol) in a schlank with 15 mL of 2-methoxyethanol and 2.5 mL H_2O, and the mixture was stirred at 120 °C for 24 h under a nitrogen atmosphere. The product was washed with ethanol (2×4 mL) and diethyl ether (2×4 mL) and filtered. The resulting green powder was dried under vacuum. Yield: 127.6 mg (0.117 mmol, 52 %).
^{1}H-NMR (400 MHz, **$CDCl_3$−d,** 25.0 °C): δ 9.16 (d, J = 6.2 Hz, 4H, H^{10}), 8.96 (d, J = 8.6 Hz, 4H, H^4), 8.16 (d, J = 7.4 Hz, 4H, H^{13}), 7.91–7.81 (m, 8H, H^6,H^7), 7.74 (ddd, J = 8.2, 5.9, 2.3 Hz, 4H, H^5), 6.88 (t, J = 7.6 Hz, 4H, H^{14}), 6.72 (d, J = 6.4 Hz, 4H, H^9), 6.60 (t, J = 6.8 Hz, 4H, H^{15}), 5.98 (d, J = 7.9 Hz, 4H, H^{16}) ppm. **^{13}C-NMR** (101 MHz, **$CDCl_3$−d,** 25.0 °C) δ 169.85 (d, 4C, C^{11}), 165.95 (s, 4C, C^2), 145.72 (s, 4C, C^{12}), 144.52 (s, 4C, C^{10}), 137.09 (s, 4C, C^8), 132.84 (s, 4C, C^{16}), 130.75 (s, 4C, C^6), 129.33 (s, 4C, C^{13}), 128.82 (s, 4C, C^{15}), 127.81 (s, 4C, C^5), 127.42 (s, 4C, C^7), 127.12 (s, 4C, C^4), 126.27 (s, 4C, C^3), 122.11 (s, 4C, C^{14}), 119.43 (s, 4C, C^9) ppm. **Mass Spectrometry (ESI-MS)**: $\frac{m}{z}$ = 511 (100) $[(M-2Cl)]^{2+}$, 1057 (6) $[M-Cl]^+$

7.4.8 [Ir-2]Cl ([Ir(ppy)$_2$(pybtz)]Cl)

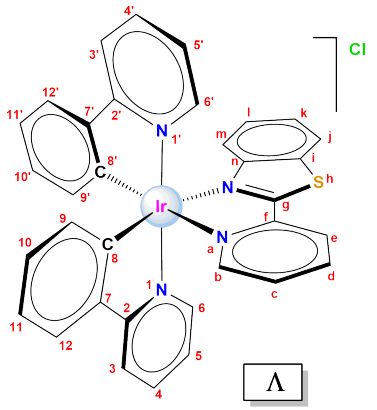

2-(2'-pyridyl)benzothiazole (0.0424 g, 0.200 mmol) was added to a solution of $Ir_2(ppy)_4Cl_2$ (0.1006 g, 0.0938 mmol) in CH_2Cl_2:MeOH (4:5, 18 mL), and the mixture was stirred at 60 °C overnight under a nitrogen atmosphere. The solvent was completely evaporated under vacuum and n-hexane (10 mL) was added to produce a crude solid that was washed with diethyl ether (2×5 mL). The resulting orange powder was dried under vacuum. Yield: 91.5 mg (0.122 mmol, 65 %). **^{1}H-NMR** (400 MHz, **DMSO−d_6,** 25.0 °C) δ 8.82 (d, J = 7.7 Hz, 1H, H^e), 8.40 (d, J = 8.2 Hz, 1H, H^j), 8.358.27 (m, 2H, H^k, H$^{3'}$), 8.22 (d, J = 7.9 Hz, 1H, H^3), 7.97-7.91 (m, 3H, H$^{4'}$,H^9, H$^{9'}$), 7.91–7.83 (m, 2H, H^4, H^b), 7.79–7.75 (m, 2H, H^6, H^c), 7.64 (d, J = 5.8 Hz, 1H,H$^{6'}$), 7.58–7.53 (t, 1H,H^k), 7.22 (t, J = 7.7 Hz, 1H, H^l), 7.17–7.03 (m, 4H, H$^{5'}$, H^5, H$^{10'}$, H^{10}), 6.99–6.90 (m, 2H, H$^{11'}$, H^{11}), 6.79 (d, J = 8.5 Hz, 1H, H^m), 6.27 (d, J = 7.5 Hz, 1H, H$^{12'}$), 6.12 (d, J = 7.3 Hz, 1H, H^{12}) ppm. **^{13}C-NMR** (101 MHz, **DMSO−d_6,** 25.0 °C) δ 170.59 (s, 1C, H^g), 166.88 (s, 1C, C$^{2'}$), 166.29 (s, 1C, C^2), 151.13 (s, 1C, C^f), 150.17 (s, 1C, C$^{6'}$), 150.02 (s, 1C, C^n), 149.97 (s, 1C, C^b), 149.24 (s, 1C, C^6), 147.62 (s, 1C, C$^{7'}$), 147.57 (s, 1C, C^7), 144.36 (s, 1C, C$^{8'}$), 143.76 (s, 1C, C^8), 140.25 (s, 1C, C^d), 138.86 (s, 1C, C^4), 138.82 (s, 1C, C$^{4'}$), 134.38 (s, 1C, C^i), 131.62 (s, 1C, C$^{12'}$), 130.47 (s, 1C, C^{12}), 130.36 (s, 1C, C^{11}), 129.99 (s, 1C, C$^{11'}$), 129.91 (s, 1C, C^c), 128.16 (s, 1C, C^l), 127.90 (s, 1C, C^k), 127.10 (s, 1C, C^e), 125.13 (s, 1C, C^9), 125.10 (s, 1C, C$^{9'}$), 124.35 (s, 1C, C^j), 124.24 (s, 1C, C$^{5'}$), 123.92 (s, 1C, C^5), 122.67 (s, 1C, C^{10}), 122.44 (s, 1C, C$^{10'}$), 121.20 (s, 1C, C^m), 120.13 (s, 1C, C$^{3'}$), 119.81 (s, 1C, C^3) ppm. **Anal. Calcd for $C_{34}H_{24}N_4SClIr(CH_2Cl_2)_{0.6}$**: C 51.99, H 3.18, N 7.01, S 4.01; **Found**: C 51.59, H 3.27, N 6.86, S 4.52. **ATR-IR** (solid powder, cm^{-1}) selected bands: 1605 1581-1560-1477-1437 ($\nu_{C=C}$+$\nu_{C=N}$) 1417, 1322 (ν_{C-N}) 1268, 1161 (ν_{C-C}), 1063-1029 (m, δ_{C-Hip}) 1008, 759-730 (δ_{C-Hoop}+ν_{C-S}). **Mass Spectrometry (ESI-MS)**: $\frac{m}{z}$ = 711 (100) [M−Cl]$^+$. **Molar Conductivity** (CH_3CN): 115.4 Scm^{2}mol^{-1}. **Solubility**: soluble in DMSO, CH_3CN, CH_2Cl_2, EtOH, partially soluble in MeOH, H_2O, insoluble in Et_2O and hexane.

7.4.9 [Ir-3]Cl ([Ir(ppy)$_2$(qibtz)]Cl)

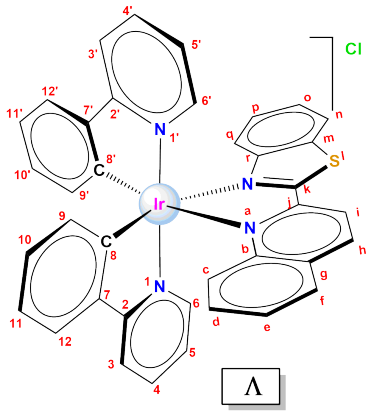

2-(2'-quinolinyl)benzothiazole (0.0526 g, 0.200 mmol) was added to a solution of $Ir_2(ppy)_4Cl_2$ (0.1006 g, 0.0938 mmol) in CH_2Cl_2:MeOH (4:5 18 mL), and the mixture was stirred at 60 °C overnight under a nitrogen atmosphere. The solvents were completely evaporated under vacuum and n-hexane (10 mL) was added to produce a crude solid that was washed with diethyl ether (2×5 mL). The resulting dark red powder was dried under vacuum. Yield: 111.8 mg (0.140 mmol, 75 %). **^{1}H-NMR** (400 MHz, **DMSO-d6,** 25.0 °C) δ 8.97 (d, J = 8.6 Hz, 1H, H^{h}), 8.82 (d, J = 8.6 Hz, 1H, H^{i}), 8.45 (d, J = 8.2 Hz, 1H, H^{n}), 8.29 (d, J = 8.6 Hz, 1H, H^{3}), 8.20 (d, J = 8.5 Hz, 1H,H^{f}), 8.17 (d, J = 8.7 Hz, 1H, H$^{3'}$), 7.97 (d, J = 8.1 Hz, 2H, H^{9}, C^{c}), 7.92 (t, J = 5.8 Hz, 1H, H^{4}), 7.91–7.86 (m, 2H, H$^{9'}$, H^{6}), 7.82 (t, J = 7.8 Hz, 1H, H$^{4'}$), 7.69 (d, J = 6.0 Hz, 1H, H$^{6'}$), 7.66 (t, 1H, H^{e}), 7.56 (t, J = 7.7 Hz, 1H, H^{o}), 7.25 (t, 1H, H^{d}), 7.17 (t, 1H, H^{p}), 7.12 (t, 1H, H$^{10'}$), 7.10-7.03 (m, 3H, H^{10},H^{5},H$^{5'}$), 6.98 (t, J = 7.4 Hz, 1H, H^{11}), 6.94 (t, J = 7.5 Hz, 1H, H$^{11'}$), 6.59 (d, J = 8.6 Hz, 1H, H^{q}), 6.22 (d, J = 7.5 Hz, 1H, H^{12}), 6.12 (d, J = 7.6 Hz, 1H, H$^{12'}$) ppm. **^{13}C-NMR** (101 MHz, **DMSO-d$_6$,** 25.0 °C) δ 172.45 (s, 1C, C^{k}), 166.58 (s, 1C, C$^{2'}$), 166.26 (s, 1C, C^{2}), 153.15 (s, 1C, C^{j}), 150.83 (s, 1C, C^{6}), 150.60 (s, 1C, C^{r}), 149.45 (s, 1C, C$^{6'}$), 149.00 (s, 1C, C^{7}), 147.12 (s, 1C, C^{b}), 144.29 (s, 1C, C$^{7'}$), 144.00 (s, 1C, C$^{8'}$), 143.61 (s, 1C, C^{8}), 142.05 (s, 1C, C^{h}), 138.87 (s, 1C, C^{4}), 138.79 (s, 1C, C$^{4'}$), 134.74 (s, 1C, C^{m}), 131.96 (s, 1C, C^{d}), 130.90 (s, 1C, C$^{12'}$), 130.52 (s, 1C, C^{12}), 130.30 (s, 1C, C^{11}), 130.12 (s, 1C, C$^{11'}$), 130.05 (s, 1C, C^{g}), 129.45 (s, 1C, C^{e}), 129.33 (s, 1C, C^{f}), 128.11 (s, 1C, C^{p}), 127.96 (s, 1C, C^{o}), 127.25 (s, 1C, C^{c}), 125.27 (s, 1C, C$^{9'}$), 125.20 (s, 1C, C^{9}), 124.28 (s, 1C, C^{n}), 124.14 (s, 1C, C^{5}), 123.82 (s, 1C, C$^{5'}$), 122.86 (s, 1C, C$^{10'}$), 122.46 (s, 2C, C^{10}, C^{i}), 121.48 (s, 1C, C^{q}), 120.06 (s, 1C, C^{3}), 119.95 (s, 1C, C$^{3'}$) ppm. **Anal. Calcd for $C_{38}H_{26}N_4SClIr(CH_2Cl_2)_{0.8}$**: C 53.79, H 3.21, N 6.47, S 3.70; **Found**: C 54.23, H 3.36, N 6.43, S 3.96. ATR-IR (solid powder, cm^{-1}) selected bands: 1604, 1581-1514-1476-1455 ($\nu_{C=C}$+$\nu_{C=N}$), 1417, 1320 (ν_{C-N}) 1268, 1249, 1161 (ν_{C-C}), 1090, 1056-1029 (m, δ_{C-Hip}), 950, 822, 758-729 (δ_{C-Hoop}+ν_{C-S}). **Mass Spectrometry (ESI-MS)**: $\frac{m}{z}$ = 761 (100) [M−Cl]$^+$. **Molar Conductivity** (CH_3CN): 117.5 Scm^{2}mol^{-1}. **Solubility**: soluble in DMSO, CH_3CN, CH_2Cl_2, EtOH, partially soluble in MeOH, H_2O, insoluble in Et_2O and hexane.

7.4.10 [Ir-4]Cl ([Ir(piqi)$_2$(pybtz)]Cl)

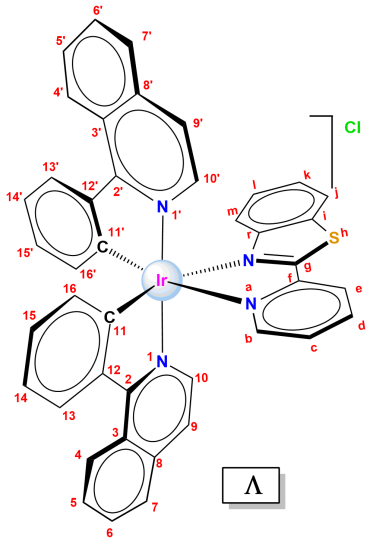

2-(2'-pirydyl)benzothiazole (0.0208 g, 0.0982 mmol) was added to a solution of [Ir(piqi)$_2$Cl]$_2$ (0.0500 g, 0.0393 mmol) in CH_2Cl_2:MeOH (4:5, 9 mL), and the mixture was stirred at 60 °C for 23 h and under a nitrogen atmosphere. The solution was completely evaporated and the product was precipitated with hexane. The solvent was filtered and the solid was washed with diethyl ether (2×5 mL). The resulting red powder was dried under vacuum. Yield: 52.9 mg (0.0624 mmol, 79 %).

^{1}H-NMR (400 MHz, **DMSO−d$_6$**, 25.0 °C) δ 9.03 (d, J = 6.4 Hz, 1H, H^4), 8.95 (d, J = 5.0 Hz, 1H, H$^{4'}$), 8.87 (d, J = 7.7 Hz, 1H, H^e), 8.39 (d, J = 8.2 Hz, 3H, H^{13}, H$^{13'}$, H^j), 8.33 (t, J = 7.6 Hz, 1H, H^d), 8.13–8.04 (m, 2H, H^7, H$^{7'}$), 7.94–7.89 (m, 2H, H^6,H^5), 7.86 (m, 2H, H$^{6'}$, H$^{5'}$), 7.74 (t, J = 5.1 Hz, 1H, H^c), 7.71 (d, J = 6.6 Hz, 1H, H$^{10'}$), 7.69 (d, J = 5.3 Hz, 1H, H^b), 7.60 (d, J = 3.8 Hz, 2H, H$^{9'}$, H^9), 7.53 (m, 2H, H^{10}, H^k), 7.22 (t, J = 7.7 Hz, 1H, H$^{14'}$), 7.17 (t, J = 7.9 Hz, 2H, H^{14}, H^l), 6.97 (t, J = 5.6 Hz, 1H, H$^{15'}$), 6.93 (t, J = 5.6 Hz, 1H, H^{15}), 6.51 (d, J = 8.7 Hz, 1H, H^m), 6.27 (d, J = 7.7 Hz, 1H, H$^{16'}$), 6.12 (d, J = 7.6 Hz, 1H, H^{16}) ppm. **^{13}C-NMR** (101 MHz, **DMSO−d$_6$**, 25.0 °C) δ 170.61 (s, 1C, C^g), 167.74 (s, 1C, C^2), 167.23 (s, 1C, C$^{2'}$), 151.11 (s, 1C, C$^{11'}$), 151.00 (s, 1C, C^f), 150.87 (s, 1C, C^{11}), 149.91 (s, 1C, C^b), 149.81 (s, 1C, C^n), 145.73 (s, 1C, C$^{12'}$), 145.12 (s, 1C, C^{12}), 141.70 (s, 1C, C$^{10'}$), 140.77 (s, 1C, C^{10}), 140.32 (s, 1C, C^d), 136.57 (s, 1C, C$^{8'}$), 136.49 (s, 1C, C^8), 134.40 (s, 1C, C^i), 132.13 (s, 3C, C$^{16'}$, C^6, C$^{6'}$), 130.93 (s, 1C, C^{16}), 130.67 (s, 1C, C^{13}), 130.63 (s, 1C, C^{15}), 130.60 (s, 1C, C$^{13'}$), 130.15 (s, 1C, C$^{15'}$), 129.91 (s, 1C, C^c), 129.51 (s, 1C, C^5), 129.42 (s, 1C,C$^{5'}$), 128.10 (s, 1C, C^l), 127.86 (s, 1C, C^k), 127.78 (s, 1C, C^7), 127.69 (s, 1C, C$^{7'}$), 127.25 (s, 1C, C^e), 126.32 (s, 2C, C^4, C$^{4'}$), 125.57 (s, 1C, C$^{3'}$), 125.32 (s, 1C, C^3), 124.36 (s, 1C, C^j), 122.67 (s, 1C, C^{14}), 122.60 (s, 1C, C$^{9'}$), 122.38 (s, 1C, C$^{14'}$), 122.26 (s, 1C, C^9), 121.07 (s, 1C, C^m) ppm. **Anal. Calcd for $C_{42}H_{28}N_4SClIr(CH_2Cl_2)_{1.2}$**: C 54.60, H 3.22, N 5.90, S 3.37; **Found**: C 54.40, H 3.25, N 5.83, S 3.37.

ATR-IR (solid powder, cm^{-1}) selected bands: 3028 (w, $\nu_{C=CH}$), 2970, 2355, 1574-1539-1447 ($\nu_{C=C}$+$\nu_{C=N}$), 1433, 1374, 1351, 1323 (ν_{C_N}), 1296, 1268, 1228, 1217, 1155 (ν_{C-C}), 1040-1028 (m, δ_{C-Hip}), 876, 814-757-742 (δ_{C-Hoop}+ν_{C-S}). **Mass Spectrometry (ESI-MS)**: $\frac{m}{z}$ = 813 (100) $[M-Cl]^+$. **Molar Conductivity** (CH_3CN): 117.4 Scm^2mol^{-1}. **Solubility**: soluble in DMSO, CH_3CN, CH_2Cl_2, EtOH, insoluble in Et_2O and hexane.

7.4.11 [Ir-5]Cl ([Ir(piqi)$_2$(qibtz)]Cl)

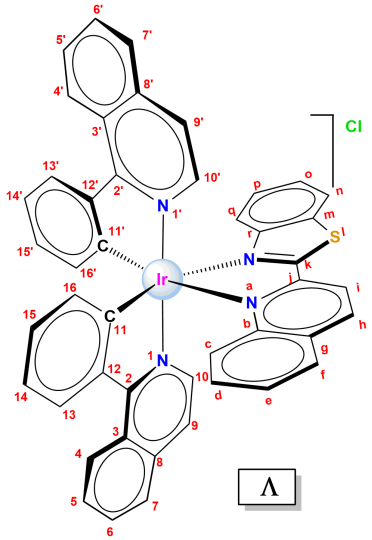

2-(2'-quinolinyl)benzothiazole (0.0248 g, 0.0947 mmol) was added to a solution of $[Ir(piqi)_2Cl]_2$ (0.0509 g, 0.040 mmol) in CH_2Cl_2:CH_3OH (4:5, 18 mL), and the mixture was stirred at 60 °C for 48 h under a nitrogen atmosphere. Then, the volume was reduced and the complex was precipitated by diethyl ether. The solvent was filtered and the solid was washed with diethylether (2×5 mL). The resulting red powder was dried under vacuum. Yield: 39.4 mg (0.0439 mmol, 55 %).

^{1}H-NMR (400 MHz, **DMSO−d_6**, 25.0 °C) δ 9.03 (d, J = 7.0 Hz, 1H, H^4), 8.96 (d, J = 8.8 Hz, 1H, H^h), 8.87 (d, J = 9.8 Hz, 1H, $H^{4'}$), 8.84 (d, J = 8.9 Hz, 1H, H^i), 8.45 (d, J = 9.0 Hz, 1H, $H^{13'}$), 8.43 (d, J = 8.0 Hz, 1H, H^n), 8.34 (d, J = 8.5 Hz, 1H, H^{13}), 8.15 (d, J = 7.2 Hz, 1H, H^l), 8.06 (d, J = 4.4 Hz, 1H, H^7), 8.00 (d, J = 7.8 Hz, 1H, $H^{7'}$), 7.93–7.86 (m, 3H, $H^{10'}$, H^6, H^5), 7.85–7.76 (m, 3H, $H^{6'}$, $H^{5'}$, H^c), 7.67–7.59 (m, 2H, H^{10}, H^e), 7.53 (m, 3H, $H^{9'}$, H^o, H^9), 7.31–7.19 (m, 2H, $H^{14'}$, H^d), 7.19–7.08 (m, 2H, H^14, H^p), 7.03–6.92 (m, 2H, H^{15}, $H^{15'}$), 6.29 (d, J = 8.4 Hz, 1H, H^q), 6.24 (d, J = 6.4 Hz, 1H, H^{16}), 6.22 (d, J = 6.4 Hz, 1H, $H^{16'}$) ppm. **^{13}C-NMR** (101 MHz, **DMSO−d_6**, 25.0 °C) δ 172.49 (s, 1C, C^k), 167.43 (s, 1C, C^2), 167.04 (s, 1C, $C^{2'}$), 153.10 (s, 1C, C^j), 152.07 (s, 1C, C^{11}), 150.39 (s, 1C, C^r), 147.86 (s, 1C, $C^{11'}$), 146.88 (s, 1C, C^b), 145.40 (s, 1C, $C^{12'}$), 144.99 (s, 1C, C^{12}), 142.49 (s, 1C, $C^{10'}$), 142.10 (s, 1C, C^h), 140.90 (s, 1C, C^{10}), 136.55 (s, 1C, $C^{8'}$), 136.38 (s, 1C, C^8), 134.73 (s, 1C, C^m), 132.18 (s, 1C, C^6), 132.10 (s, 1C, $C^{6'}$), 131.93 (s, 1C, C^d), 131.46 (s, 1C, C^{16}), 130.75 (s,

2C, C^{16}, $C^{13'}$), 130.68 (s, 1C, C^{13}), 130.48 (s, 1C, C^{15}), 130.35 (s, 1C, $C^{15'}$), 130.04 (s, 1C, C^{g}), 129.63 (s, 1C, C^{5}), 129.42 (s, 2C, $C^{5'}$, C^{e}), 129.33 (s, 1C, C^{f}), 128.11 (s, 1C, C^{p}), 127.96 (s, 1C, C^{o}), 127.82 (s, 1C, C^{7}), 127.66 (s, 1C, $C^{7'}$), 127.13 (s, 1C, C^{c}), 126.19 (s, 2C, C^{4}, $C^{4'}$), 125.56 (s, 1C, $C^{3'}$), 125.30 (s, 1C, C^{3}), 124.27 (s, 1C, C^{n}), 122.87 (s, 1C, $C^{14'}$), 122.51 (s, 1C, C^{14}), 122.47 (s, 1C, C^{i}), 122.43 (s, 1C, $C^{9'}$), 122.10 (s, 1C, C^{9}), 121.40 (s, 1C, C^{q}) ppm. **Anal. Calcd for $C_{46}H_{30}N_4SClIr(CH_2Cl_2)_{0.5}$**: C 59.36, H 3.32, N 5.96, S 3.41; **Found**: C 59.26, H 3.30, N 5.80, S 3.43. **Mass Spectrometry (ESI-MS)**: $\frac{m}{z}$ = 863 (100) $[M-Cl]^+$. **Molar Conductivity** (CH_3CN): 116.3 Scm^2mol^{-1}. **Solubility**: soluble in DMSO, CH_3CN, CH_2Cl_2, EtOH, insoluble in Et_2O and hexane.

7.4.12 [Rh-2]Cl ([Rh(ppy)$_2$(pybtz)]Cl)

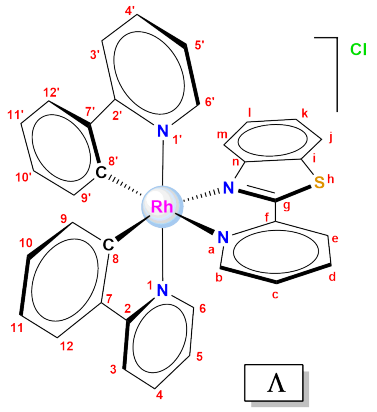

2-(2'-pirydyl)benzothiazole (0.0424 g, 0.200 mmol) was added to a solution of $[Rh(ppy)_2Cl]_2$ (0.0840 g, 0.0940 mmol) in CH_2Cl_2:MeOH (1:1, 18 mL), and the mixture was stirred at 50 °C for 20 h and under a nitrogen atmosphere. The volume was reduced and hexane was used to precipitate the product. Solvent was filtered and ethanol was added in order to dissolve the product while the impurities, as the dimeric reagent, are not soluble. The solution was filtered and evaporated. A yellow powder was formed. Yield: 55.7 mg (0.0845 mmol, 45 %). **^{1}H-NMR** (400 MHz, **$CDCl_3$–d,** 25.0 °C) δ 9.08 (d, J = 7.9 Hz, 1H, H^{e}), 8.52 (t, J = 7.5 Hz, 1H, H^{d}), 8.14 (d, J = 8.3 Hz, 1H, H^{j}), 7.95 (d, J = 8.3 Hz, 1H, H^{3}), 7.90–7.84 (m, 3H, H^{4}, H^{3}, H^{b}), 7.82 (t, J = 8.3 Hz, 1H, $H^{4'}$), 7.73 (d, J = 7.8 Hz, 2H, H^{9}, $H^{9'}$), 7.63–7.59 (t, 1H, H^{c}), 7.57 (d, J = 5.6 Hz, 1H, H^{6}), 7.48-7.43 (m, 2H, $H^{6'}$, H^{k}) 7.21-7.14 (m, 2H, H^{l}, $H^{10'}$), 7.13-7.07 (m, 2H, H^{10}, $H^{5'}$), 7.06-6.99 (m, 2H, H^{5}, $H^{11'}$), 6.97 (t, 1H, H^{11}), 6.82 (d, J = 8.5 Hz, 1H, H^{m}), 6.39 (d, J = 7.2 Hz, 1H, $H^{12'}$), 6.25 (d, J = 7.3 Hz, 1H, HH^{12}) ppm. **^{13}C-NMR** (101 MHz, **$CDCl_3$–d,** 25.0 °C) δ 168.41 (s, 1C, C^{g}), 166.84 (d,1C, C^{7}), 165.19 (s, 1C, $C^{2'}$), 165.18 (d, 1C, $H^{7'}$), 164.65 (s, 1C, C^{2}), 150.70 (s, 1C, C^{n}), 150.43 (s, 1C, C^{f}), 149.91 (s, 1C, C^{b}), 149.42 (s, 1C, C^{6}), 148.76 (s, 1C, $C^{6'}$), 144.18 (s, 1C, $C^{8'}$), 143.37 (s, 1C, C^{8}), 141.78 (s, 1C, C^{d}), 138.56 (s, 1C, C^{4}), 138.50 (s, 1C, $C^{4'}$), 135.13 (s, 1C, C^{i}), 133.50 (s, 1C, $C^{12'}$), 132.49 (s, 1C, C^{12}), 130.92 (s, 1C, C^{11}), 130.42 (s, 1C, $C^{11'}$), 129.01 (s, 1C, C^{c}), 128.45

(s, 1C, C^{l}), 127.90 (s, 1C, C^{k}), 127.77 (s, 1C, C^{e}), 124.85 (s, 1C, $C^{9'}$), 124.74 (s, 1C, C^{9}), 124.04 (s, 2C, C^{10}, $C^{10'}$), 123.91 (s, 1C, C^{j}), 123.74 (s, 1C, $C^{5'}$), 123.69 (s, 1C, C^{5}), 122.46 (s, 1C, C^{m}), 120.05 (s, 1C, C^{3}), 119.89 (s, 1C, $C^{3'}$) ppm. **Anal. Calcd for $C_{34}H_{24}N_4SClRh(CH_2Cl_2)$**: C 56.51, H 3.52, N 7.53; **Found**: C 56.58, H 3.48, N 7.77. **ATR-IR** (solid powder, cm^{-1}) selected bands: 3366 (water), 3039 (w, $\nu_{C=CH}$), 1604-1577-1479 (m, $\nu_{C=C+C=N}$), 1456, 1436, 1417, 1319 (ν_{C-N}), 1269, 1254, 1160 (m, ν_{C-C}), 1059-1024-1004 (m, δ_{C-Hip}), 792-756-741 (δ_{C-Hoop} + ν_{C-S}). **Mass Spectrometry (ESI-MS)**: $\frac{m}{z}$ = 623 (100) $[M-Cl]^+$, 411 (58) $[M-Cl-pybtz]^+$. **Molar Conductivity** (CH_3CN): 127.1 Scm^2mol^{-1}. **Solubility**: soluble in EtOH, $CHCl_3$, CH_2Cl_2, partially soluble in H_2O, insoluble in Et_2O and hexane, instable in DMSO.

7.4.13 [Rh-4]Cl ([Rh(piqi)$_2$(pybtz)]Cl)

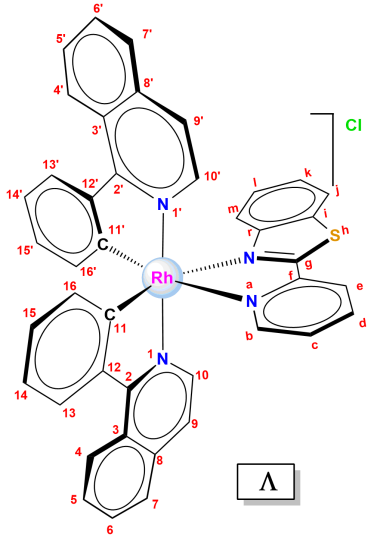

2-(2'-pirydyl)benzothiazole (0.0251 g, 0.1182 mmol) was added to a solution of $[Rh(piqi)_2Cl]_2$ (0.0500 g, 0.047 25 mmol) in CH_2Cl_2:CH_3OH (4:5 9 mL), and the mixture was stirred at 60 °C for 23 h under a nitrogen atmosphere. The complex was precipitated with hexane, dried under vacuum and the solid was washed with diethyl ether (2×5 mL). A green powder was obtained. Yield: 46.5 mg (0.0613 mmol, 65 %).
^{1}H-NMR (400 MHz, $CDCl_3$–d, 25.0 °C) δ 9.23 (d, J = 8.0 Hz, 1H, H^{e}), 8.95 (d, J = 7.9 Hz, 1H, H^{4}), 8.89 (d, J = 8.5 Hz, 1H, $H^{4'}$), 8.55 (t, J = 7.2 Hz, 1H, H^{d}), 8.33 (d, J = 7.5 Hz, 1H, H^{13}), 8.30 (d, J = 7.5 Hz, 1H, $H^{13'}$), 8.13 (d, J = 8.4 Hz, 1H, H^{j}), 7.94–7.89 (m, 2H, H^{7}, $H^{7'}$), 7.85–7.72 (m, 4H, $H^{6'}$, H^{6}, $H^{5'}$, H^{5}), 7.64 (d, J = 5.2 Hz, 1H, H^{b}), 7.55 (t, J = 7.6 Hz, 1H, H^{c}), 7.52 (d, J = 6.5 Hz, 1H, H^{10}), 7.46 (d, J = 6.5 Hz, 1H, $H^{9'}$), 7.45–7.39 (m, 2H, H^{9}, H^{k}), 7.37 (d, J = 6.3 Hz, 1H, $H^{10'}$), 7.26 (t, J = 7.6 Hz, 1H, $H^{14'}$), 7.20 (t, J = 7.6 Hz, 1H, H^{14}), 7.12 (t, J = 7.9 Hz, 1H, H^{l}), 7.02-6.96 (m, 2H, $H^{15'}$, H^{15}), 6.48 (d, J = 8.6 Hz, 1H, H^{m}), 6.33 (d, J = 7.8 Hz, 1H, $H^{16'}$), 6.19 (d, J = 7.8 Hz, 1H, H^{16}) ppm. **^{13}C-NMR** (101 MHz, $CDCl_3$–d, 25.0 °C) δ 169.06 (d, 1C, C^{11}),

168.61 (d, 1C, $C^{11'}$), 168.57 (s, 1C, C^{g}), 166.08 (s, 1C, $C^{2'}$), 165.51 (s, 1C, C^{2}), 150.64 (s, 1C, C^{n}), 150.44 (s, 1C, C^{f}), 149.76 (s, 1C, C^{b}), 146.38 (s, 1C, $C^{12'}$), 145.52 (s, 1C, C^{12}), 141.83 (s, 1C, C^{d}), 140.78 (s, 1C, C^{10}), 140.11 (s, 1C, $C^{10'}$), 137.31 (s, 1C, C^{8}), 137.28 (s, 1C, $C^{8'}$), 135.22 (s, 1C, C^{i}), 133.86 (s, 1C, $C^{16'}$), 132.77 (s, 1C, C^{16}), 131.88 (s, 1C, C^{6}), 131.79 (s, 1C, $C^{6'}$), 130.81 (s, 1C, C^{15}), 130.42 (s, 1C, C^{13}), 130.39 (s, 1C, $C^{13'}$), 130.12 (s, 1C, $C^{15'}$), 129.25 (s, 1C, C^{5}), 129.07 (s, 1C, $C^{5'}$), 128.90 (s, 1C, C^{c}), 128.27 (s, 1C, C^{l}), 128.11 (s, 1C, C^{7}), 128.06 (s, 2C, $C^{7'}$, C^{e}), 127.79 (s, 1C, C^{k}), 126.71 (s, 1C, C^{4}), 126.62 (s, 1C, $C^{4'}$), 126.56 (s, 1C, C^{3}), 126.47 (s, 1C, $C^{3'}$), 123.79 (s, 1C, C^{14}), 123.70 (s, 1C, $C^{14'}$), 123.58 (s, 1C, C^{j}), 122.40 (s, 1C, C^{m}), 122.20 (s, 1C, C^{9}), 122.13 (s, 1C, $C^{9'}$) ppm. **Anal. Calcd for $C_{42}H_{28}N_4SClRh(CH_2Cl_2)$**: C 61.19, H 3.58, N 6.64; **Found**: C 61.32, H 3.47, N 6.98. **ATR-IR** (solid powder, cm^{-1}) selected bands: 3029 (w, $\nu_{C=CH}$, 2361, 1570-1540-1488 (m, $\nu_{C=C}+\nu_{C=N}$), 1450, 1433, 1375, 1352, 1323 (ν_{C-C}), 1296, 1271, 1217, 1158 (ν_{C-N}), 1005 (δ_{C-Hip}), 874, 815, 772-755-739 (δ_{C-Hoop} + ν_{C-S}). **Mass Spectrometry (ESI-MS)**: $\frac{m}{z}$ = 723 (100) $[M-Cl]^+$. **Molar Conductivity** (CH_3CN): 122.5 Scm^2mol^{-1}. **Solubility**: soluble in EtOH, $CHCl_3$, CH_2Cl_2, insoluble in Et_2O and hexane, instable in DMSO.

7.4.14 [Rh-5]Cl ([Rh(piqi)$_2$(qibtz)]Cl)

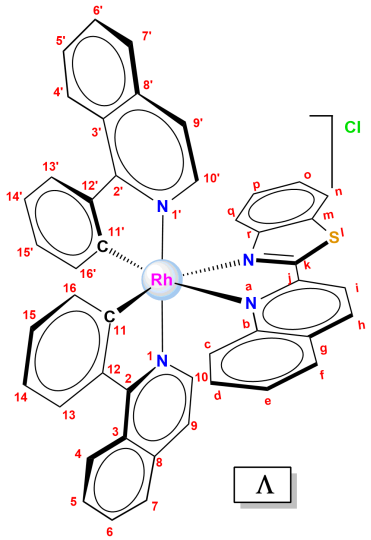

2-(2'-quinolinyl)benzothiazole (0.0318 g, 0.121 mmol) was added to a solution of $[Rh(ppy)_2Cl]_2$ (0.0500 g, 0.047 25 mmol) in a mixture of CH_2Cl_2/MeOH (4:5 18 mL), and the mixture was stirred at 60 °C for 23 h and under a nitrogen atmosphere. The solution was precipitated with hexane. The solvent was filtered and the solid was washed with diethylether (2×3 mL). The resulting greenish powder was dried under vacuum. Yield: 60.8 mg (0.0754 mmol, 80 %).
^{1}H-NMR (400 MHz, **$CDCl_3$−d,** 25.0 °C) δ 9.14 (d, J = 8.7 Hz, 1H, H^{i}), 9.03 (d, J = 8.2 Hz, 1H, H^{h}), 8.94 (d, J = 8.0 Hz, 1H, H^{4}), 8.84 (d, J = 9.3 Hz, 1H, $H^{4'}$), 8.36 (d, J = 7.8 Hz, 1H, H^{13}), 8.29 (d, J = 8.2 Hz, 1H, $H^{13'}$), 8.23

(d, J = 7.5 Hz, 1H, H^n), 8.02 (d, J = 8.2 Hz, 1H, H^f), 7.91 (d, J = 7.2 Hz, 1H, $H^{7'}$), 7.86 (d, J = 7.6 Hz, 1H, H^7), 7.83–7.71 (m, 4H, H^6, H^5, $H^{6'}$, $H^{5'}$), 7.69 (d, J = 6.6 Hz, 1H, $H^{10'}$), 7.64 (d, J = 9.1 Hz, 1H, H^c), 7.49 (m, 2H, H^e, H^{10}), 7.45–7.34 (m, 3H, H^o, $H^{9'}$, H^9), 7.30-7.16 (m, 3H, H^{14}, $H^{14'}$, H^d), 7.08 (t, 1H, H^p), 6.99 (dt, J = 6.5 Hz, 2H, $H^{15'}$, H^{15}), 6.32 (d, J = 7.7 Hz, 2H, H^{16}, $H^{16'}$), 6.28 (d, J = 8.5 Hz, 1H, H^q) ppm. **^{13}C-NMR (**101 MHz**, $CDCl_3$−d,** 25.0 °C**)** δ 170.06 (s, 1C, C^k), 169.5 (d, 1C, $C^{11'}$), 167.35 (d, 1C, C^{11}), 165.75 (d, 1C, J = 2.0 Hz, C^2), 165.24 (d, 1C, J = 2.4 Hz, $C^{2'}$), 151.56 (s, 1C, C^j), 151.37 (s, 1C, C^r), 147.74 (s, 1C, C^b), 146.00 (s, 1C, $C^{12)}$, 145.93 (s, 1C, $C^{12'}$), 142.87 (s, 1C, C^h), 141.25 (s, 1C, $C^{10'}$), 140.19 (s, 1C, C^{10}), 137.33 (s, 1C, $C^{8'}$), 137.25 (s, 1C, C^8), 135.43 (s, 1C, C^m) , 133.32 (s, 1C, $C^{16'}$), 133.08 (s, 1C, C^{16}), 132.12 (s, 1C, C^d), 131.84 (s, 1C, $C^{6'}$), 131.79 (s, 1C, C^6), 130.65 (s, 1C, $C^{13'}$), 130.52 (s, 2C, $C^{15'}$, C^g), 130.49 (s, 2C, C^{15}, C^{13}), 129.46 (s, 1C, C^f), 129.23 (s, 1C, C^5), 129.13 (s, 1C, C^e), 129.07 (s, 1C, $C^{5'}$), 128.20 (s, 1C, C^p), 128.19 (s, 1C, $C^{7'}$), 128.06 (s, 1C, C^7), 127.90 (s, 1C, C^c), 127.80 (s, 1C, C^o), 126.70 (d, 1C, J = 1.6 Hz, $C^{3'}$), 126.54 (s, 1C, $C^{4'}$), 126.52 (d, 1C, J = 1.7 Hz, C^3), 126.42 (s, 1C, C^4), 123.83 (s, 2C, C^{14}, C^n), 123.64 (s, 1C, $C^{14'}$), 123.48 (s, 1C, C^i), 122.65 (s, 1C, C^q), 122.16 (s, 1C, $C^{9'}$), 121.94 (s, 1C, C^9) ppm. **Anal. Calcd for $C_{46}H_{30}N_4SClRh(CH_2Cl_2)$**: C 63.14, H 3.61, N 6.27; **Found**: C 62.78, H 3.44, N 6.47. **ATR-IR** (solid powder, cm-1) selected bands: 3047 (w, $\nu_{C=CH}$), 2352, 1617-1591-1572-1541-1515 (m, $\nu_{C=C}$+$\nu_{C=N}$), 1454, 1434, 1379, 1348, 1271, 1216, 1148 (ν_{C-C}), 1088-1052-1034 (δ_{C-Hip}), 821, 759-732 (δ_{C-Hoop} + ν_{C-S}). **Mass Spectrometry (ESI-MS)**: $\frac{m}{z}$ = 773 (100) $[M-Cl]^+$. **Molar Conductivity** (CH_3CN): 93.7 Scm^2mol^{-1}. **Solubility**: soluble in EtOH, $CHCl_3$, CH_2Cl_2, insoluble in Et_2O and hexane, instable in DMSO.

Bibliography

[1] G. R. Fulmer, A. J. M. Miller, N. H. Sherden, H. E. Gottlieb, A. Nudelman, B. M. Stoltz, J. E. Bercaw and K. I. Goldberg (2010). *NMR Chemical Shifts of Trace Impurities: Common Laboratory Solvents, Organics, and Gases in Deuterated Solvents Relevant to the Organometallic Chemist*, Organometallics, 29 (9), 2176–2179.

[2] D. L. Ma, D. S. H. Chan and C. H. Leung (2014). *Group 9 Organometallic Compounds for Therapeutic and Bioanalytical Applications*, Accounts of Chemical Research, 47 (12), 3614-3631.

[3] C. D. Ertl, C. Momblona, A. Pertegás, J. M. Junquera-Hernández, M. G. La-Placa, A. Prescimone, E. Ortí, C. E. Housecroft, E. C. Constable and H. J. Bolink (2017). *Highly Stable Red-Light-Emitting Electrochemical Cells*, Journal of the American Chemical Society, 139 (8), 3237-3248.

[4] M. Nonoyama (1975) *Chelating C-Metallation of N-Phenylpyrazole with Rhodium(III) and Iridium(III)*, Journal of Organometallic Chemistry, 86 (2), 263-267.

[5] S. Sprouse, K. A. King, P. J. Spellane and R. J. Watts (1984). *Photophysical Effects of Metal-Carbon σ Bonds in Ortho-Metalated Complexes of Iridium(III) and Rhodium(III)*, Journal of the American Chemical Society, 106 (22), 6647-6653.

[6] R. Hu, X. Li, Y. Tong, D. Miao, Q. Pan, Z. Jiang, H. Gan and S. Han (2016). *Catalyst-Free Synthesis of 2-Arylbenzothiazoles in an Air/DMSO Oxidant System*, Synlett, 27 (09), 1387-1390.

[7] E. Baranoff, B. F. Curchod, J. Frey, R. Scopelliti, F. Kessler, I Tavernelli, U. Rothlisberger, M Gratzel and M. D. Nazeeruddin, (2011). *Acid-Induced Degradation of Phosphorescent Dopants for OLEDs and its Application to the Synthesis of Tris-Heteroleptic Iridium(III) Bis-Cyclometalated Complexes*, Inorganic Chemistry, 51 (1), 215-224.

[8] E. Baranoff and B. F. Curchod (2015). *FIrpic: Archetypal Blue Phosphorescent Emitter for Electroluminescence*, Dalton Transactions, 44 (18), 8318-8329.

[9] W. Lin, Q. Zhao, H. Sun, K. Y. Zhang, H. Yang, Q. Yu, X. Zhou, S. Guo, S. Liu and W. Huang (2015). *An Electrochromic Phosphorescent Iridium(III) Complex for Information Recording, Encryption, and Decryption*, Advanced Optical Materials, 3 (3), 368-375.

[10] H. Cao, H. Sun, Y. Yin, X. Wen, G. Shan, Z. Su, R. Zhong, W. Xie, P. Li and D. Zhu (2014). *Iridium (III) Complexes Adopting 1,2-diphenyl-1 H-benzoimidazole Ligands for Highly Efficient Organic Light-Emitting Diodes with Low Efficiency Roll-off and Non-Doped Feature*, Journal of Materials Chemistry C, 2 (12), 2150-2159.

[11] G. E. Schneider, A. Pertegás, E. C. Constable, C. E. Housecroft, N. Hostettler, C. D. Morris, J. A. Zampese, H. J. Bolink, J. M. Junquera-Hernández, E. Ortí, M. Sessolo (2014). *Bright and Stable Light-Emitting Electrochemical Cells Based on an Intramolecularly π-Stacked, 2-naphthyl-substituted Iridium Complex*, Journal of Materials Chemistry C, 2 (34), 7047-7055.

[12] K. P. Zanoni, B. K. Kariyazaki, A. Ito, M. K. Brennaman, T. J. Meyer and N. Y. Murakami Iha (2014). *Blue-Green Iridium (III) Emitter and Comprehensive Photophysical Elucidation of Heteroleptic Cyclometalated Iridium(III) Complexes*, Inorganic Chemistry, 53 (8), 4089-4099.

[13] M. G. Colombo, A. Hauser and H. U. Güdel (1994). *Competition between Ligand Centered and Charge Transfer Lowest Excited States in Bis Cyclometalated Rh^{3+} and Ir^{3+} complexes* in Electronic and Vibronic Spectra of Transition Metal Complexes I, pp. 143-171, Springer Berlin Heidelberg.

[14] M. Martínez-Alonso, J. Cerdá, C. Momblona, A. Pertegás, J. M. Junquera-Hernández, A. Heras, A. M. Rodríguez, G. Espino, H. Bolink and Ortí, E. (2017). *Highly Stable and Efficient Light-Emitting Electrochemical Cells Based on Cationic Iridium Complexes Bearing Arylazole Ancillary Ligands*, Inorganic Chemistry, 56 (17), 10298-10310.

[15] M. Maestri, D. Sandrini, V. Balzani, U. Maeder and A. Von Zelewsky (1987). *Absorption Spectra, Electrochemical Behavior, Luminescence Spectra, and Excited-State Lifetimes of Mixed-Ligand Ortho-Metalated Rhodium(III) Complexes*, Inorganic Chemistry, 26 (8), 1323-1327.

[16] D. Sandrini, M. Maestri, V. Balzani, U. Maeder and A. Von Zelewsky (1988). *Spectroscopic and Electrochemical Properties of New Mixed-Ligand Orthometalated Rhodium(III) Complexes*, Inorganic Chemistry, 27 (15), 2640-2643.

[17] G. Calogero, G. Giuffrida, S. Serroni, V. Ricevuto and S. Campagna (1995). *Absorption Spectra, Luminescence Properties, and Electrochemical Behavior of Cyclometalated Iridium(III) and Rhodium(III) Complexes with a Bis(pyridyl)triazole Ligand*, Inorganic Chemistry, 34 (3), 541-545.

[18] R. D. Costa, E. Ortí, H. J. Bolink, F. Monti, G. Accorsi and N. Armaroli (2012). *Luminescent Ionic Transition-Metal Complexes for Light-Emitting Electrochemical Cells*, Angewandte Chemie International Edition, 51 (33), 8178-8211.

[19] M. T. Indelli, C. Chiorboli and F. Scandola (2007) *Photochemistry and Photophysics of Coordination Compounds: Rhodium* in Photochemistry and Photophysics of Coordination Compounds I, pp. 215-255, Springer-Verlag Berlin Heidelberg.

[20] K. Y. Zhang, H. W. Liu, M. C. Tang, A. W. T. Choi, N. Zhu, X. G. Wei, K. C. Lau and K. K. W. Lo (2015). *Dual-Emissive Cyclometalated Iridium (III) Polypyridine Complexes as Ratiometric Biological Probes and Organelle-Selective Bioimaging Reagents*, Inorganic chemistry, 54 (13), 6582-6593.

[21] S. Ladouceur, L. Donato, M. Romain, B. P. Mudraboyina, M. B. Johansen, J. A. Wisner and E. Zysman-Colman (2013). *A Rare Case of Dual Emission in a Neutral Heteroleptic Iridium(III) Complex*, Dalton Transactions, 42 (24), 8838-8847.

[22] K. A. King and R. J. Watts (1987). *Dual Emission from an Ortho-Metalated Iridium(III) Complex*, Journal of the American Chemical Society, 109 (5), 1589-1590.

[23] Y. Ohsawa, S. Sprouse, K. A. King, M. K. DeArmond, K. W. Hanck and R. J. Watts (1987). *Electrochemistry and Spectroscopy of Ortho-Metalated Complexes of Iridium(III) and Rhodium(III)*, Journal of Physical Chemistry, 91 (5), 1047-1054.

[24] M. G. Colombo, A. Hauser and H. U. Guedel (1993). *Evidence for Strong Mixing between the LC and MLCT Excited States in Bis(2-phenylpyridinato-C^2,N')(2,2'-bipyridine)Iridium(III)*, Inorganic Chemistry, 32 (14), 3088-3092.

[25] M. G. Colombo and H. U. Guedel (1993). *Synthesis and High-Resolution Optical Spectroscopy of Bis[2-(2-thienyl)pyridinato-C^3,N'](2,2'-bipyridine)Iridium(III)*, Inorganic Chemistry, 32 (14), 3081-3087.

[26] S. Pal, S. Joy, H. Paul, S. Banerjee, A. Maji, E. Zangrando and P. Chattopadhyay (2017). *Understanding the Difference in Photophysical Properties of Cyclometalated Iridium(III) and Rhodium(III) Complexes by Detailed TDDFT and FMO Supports*, The Journal of Physical Chemistry C, 121 (21), 11632-11642.

[27] Y. S. Yeh, Y. M. Cheng, P. T. Chou, G. H. Lee, C. H. Yang, Y. Chi, C. F. Shu and C. H. Wang (2006). *A New Family of Homoleptic Ir(III) Complexes: Tris-Pyridyl Azolate Derivatives with Dual Phosphorescence*, ChemPhysChem, 7 (11), 2294-2297.

[28] S. Kumar, Y. Hisamatsu, Y. Tamaki, O. Ishitani and S. Aoki (2016). *Design and Synthesis of Heteroleptic Cyclometalated Iridium(III) Complexes Containing Quinoline-Type Ligands that Exhibit Dual Phosphorescence*, Inorganic chemistry, 55 (8), 3829-3843.

[29] L. Flamigni, A. Barbieri, C. Sabatini, B. Ventura and F. Barigelletti (2007). *Photochemistry and Photophysics of Coordination Compounds: Iridium* in Photochemistry and Photophysics of Coordination Compounds II, pp. 143-203, Springer-Verlag Berlin Heidelberg.

[30] R. Schmidt, C. Tanielian, R. Dunsbach and C. Wolff (1994). *Phenalenone, a Universal Reference Compound for the Determination of Quantum Yields of Singlet Oxygen O_2 ($^1\Delta_g$) sensitization*, Journal of Photochemistry and Photobiology A: Chemistry, 79 (1), 11-17.

[31] J. D. Knoll and C. Turro (2015). *Control and Utilization of Ruthenium and Rhodium Metal Complex Excited States for Photoactivated Cancer Therapy*, Coordination Chemistry Reviews, 282, 110-126.

[32] K. J. Castor, K. L. Metera, U. M. Tefashe, C. J. Serpell, J. Mauzeroll and H. F. Sleiman (2015). *Cyclometalated Iridium(III) Imidazole Phenanthroline Complexes as Luminescent and Electrochemiluminescent G-Quadruplex DNA Binders*, Inorganic Chemistry, 54 (14), 6958-6967.

[33] C. Rajput, R.Rutkaite, L. Swanson, I. Haq and J. A. Thomas (2006). *Dinuclear Monointercalating Ru^{II} Complexes that Display High Affinity Binding to Duplex and Quadruplex DNA*, Chemistry - A European Journal, 12 (17), 4611-4619.

[34] T. Wilson, M. P. Williamson and J. A. Thomas (2010). *Differentiating Quadruplexes: Binding Preferences of a Luminescent Dinuclear Ruthenium(II) Complex with Four-Stranded DNA Structures*, Organic and Biomolecular Chemistry, 8 (11), 2617-2621.

[35] A. T. Phan, Y. S. Modi and D. J. Patel (2004). *Propeller-Type Parallel-Stranded G-Quadruplexes in the Human c-myc Promoter*, Journal of the American Chemical Society, 126 (28), 8710-8716.

[36] A. Ambrus, D. Chen, J. Dai, R. A. Jones and D. Yang (2005). *Solution Structure of the Biologically Relevant G-Quadruplex Element in the Human c-MYC Promoter. Implications for G-Quadruplex Stabilization*, Biochemistry, 44 (6), 2048-2058.

[37] J. Dai, C. Punchihewa, A. Ambrus, D. Chen, R. A. Jones and D. Yang (2007). *Structure of the Intramolecular Human Telomeric G-Quadruplex in Potassium Solution: a Novel Adenine Triple Formation*, Nucleic Acids Research, 35 (7), 2440-2450.

[38] E. J. C. Olson, D. Hu, A. Hörmann, A. M. Jonkman, M. R. Arkin, E. D. A. Stemp, J. K. Barton and P. F. Barbara (1997). *First Observation of the Key Intermediate in the "Light-Switch" Mechanism of $[Ru(phen)_2dppz]^{2+}$*, Journal of the American Chemical Society, 119 (47), 11458-11467.

[39] V. Gabelica, E. Shammel Baker, M. P. Teulade-Fichou, E. De Pauw and M. T. Bowers (2007). *Stabilization and Structure of Telomeric and c-myc Region Intramolecular G-Quadruplexes: the Role of Central Cations and Small Planar Ligands*, Journal of the American Chemical Society, 129 (4), 895-904.

[40] H. Han and L. H. Hurley (2000). *G-Quadruplex DNA: a Potential Target for Anti-Cancer Drug Design*, Trends in Pharmacological Sciences, 21 (4), 136-142.

[41] P. Murat, Y. Singh and E. Defrancq (2011). *Methods for Investigating G-Quadruplex DNA/Ligand Interactions*, Chemical Society Reviews, 40 (11), 5293-5307.

[42] J. Andersson, L. H. Fornander, M. Abrahamsson, E. Tuite, P. Nordell and P. Lincoln (2012). *Lifetime Heterogeneity of DNA-Bound dppz Complexes Originates from Distinct Intercalation Geometries Determined by Complex–Complex Interactions*, Inorganic Chemistry, 52 (2), 1151-1159.

[43] A. K. Mårtensson and P. Lincoln (2015). *Binding of Ru(terpyridine)(pyridine)dipyridophenazine to DNA Studied with Polarized Spectroscopy and Calorimetry*, Dalton Transactions, 44 (8), 3604-3613.

[44] A. De Rache and J. L. Mergny (2015). *Assessment of Selectivity of G-Quadruplex Ligands via an Optimised FRET Melting Assay*, Biochimie, 115, 194-202.

Supporting Information

Table 7.S1: Crystal data and structure refinement for **[Ir-5]**$PF_6 \cdot CH_2Cl_2$ and **[Rh-2]**$PF_6 \cdot CH_3OH$.

	[Ir-5]$PF_6 \cdot CH_2Cl_2$	**[Rh-2]**$PF_6 \cdot CH_3OH$
Empirical Formula	$C_{47}H_{32}Cl_2F_6IrN_4PS$	$C_{35}H_{28}F_6N_4OPRhS$
Molecular Weight	1092.89	800.55
Temperature, K	173(2)	173(2)
Wavelength, Å	0.710 73	0.710 73
Crystal System	Monoclinic	Monoclinic
Space Group	$P2_1/n$	$P2_1/n$
a, Å	14.0138(15)	14.697(6)
b, Å	15.7590(17)	14.035(6)
c, Å	19.008(2)	16.550(7)
α, °	90	90
β, °	102.516(2)	106.962(7)
γ, °	90	90
Volume, $Å^3$	4098.1(8)	3265(2)
Z	4	4
Density (Calc.), $g\,cm^{-3}$	1.771	1.628
Abs Coeff., mm^{-1}	0.3548	0.707
F(000)	2152	1616
Crystal Size, mm^3	$0.5 \times 0.2 \times 0.2$	$0.390 \times 0.320 \times 0.110$
Theta Range for data Coll., °	1.647 to 28.220	1.633 to 28.153
Index Ranges	$-18 < h < 18$ $-20 < k < 20$ $-25 < l < 24$	$-18 < h < 19$ $-18 < k < 18$ $-20 < l < 21$
Reflections Collected	46 597	36 242
Independent Reflections	9423 [R(int)=0.0950]	7473 [R(int)=0.0787]
Completeness Theta =25.242°	99.8 %	99.8 %
Abs. Correction	Semi-empirical from equivalents	Semi-empirical from equivalents
Max. and Min. Transmission	0.746 and 0.444	0.746 and 0.527
Refinement Method	Full-matrix least-squares on F2	Full-matrix least-squares on F2
Data/Restraints /Parameters	9423/15/598	7473/0/444
Goodness-of-fit on F2	0.833	1.334
Final R Indices [I>2sigma(I)]	R1=0.0401, wR2=0.1082	R1=0.0551, wR2=0.1089
R Indices (all data)	R1=0.0514, wR2=0.1135	R1=0.0901, wR2=0.1165
Extinction Coefficient	n/a	n/a
Largest Diff. Peak and Hole, $e\,Å^3$	2.315 and −1.760	1.504 and −0.854

Table 7.S2: $\pi - \pi$ stacking interaction in the crystal structure of **[Ir-5]**$PF_6 \cdot CH_2Cl_2$ by MERCURY 3.0 program.

$\pi - \pi$ **Interaction (Rings)**	d_{centr}, Å	α, °	$d_{centr-pl}$, Å	β, °	d_{offset}, Å
C(1)-C(6)—C(34)-C(39)	3.621	9.78	3.466	16.83	1.05
			3.522	13.43	0.84

Table 7.S3: Hydrogen bonds for **[Ir-5]**$PF_6 \cdot CH_2Cl_2$ by MERCURY 3.0 program.

Interaction (Rings)	$dD---A$, Å	d_H---A, Å	DHA, °
C(5)-H(5)—F(4)	3.154	2.421	133.73
C(37)-H(37)—F(4)	3.216	2.563	126.16
C(51)-H(51A)—F(3)	3.180	2.561	120.52

Table 7.S4: CH-π interaction in the crystal structure of **[Ir-5]**$PF_6 \cdot CH_2Cl_2$ by MERCURY 3.0 program.

$\pi - \pi$ **Interaction (Rings)**	d_{centr}, Å	d_{H-ring}, Å	$d_{H-centr}$, Å	$\alpha_{CH-centr}$, °
C(30)-H(30)—C(34)-C(39)	3.593	2.850	2.657	168.7

Table 7.S5: Anion-π interaction in the crystal structure of **[Ir-5]**$PF_6 \cdot CH_2Cl_2$ by MERCURY 3.0 program.

$\pi - \pi$ **Interaction (Rings)**	d_{centr}, Å	d_{pl}, Å	α, °
PF_6—N(2)C(8)-C(12)	3.100	3.035	78.24

The PF_6^- counterions show positional disorder for the four F atoms of an equatorial plane, meaning that each of these atoms are localized in two different positions within the unit cells along the crystal network due to rotational dynamics.
The ancillary ligand also exhibits positional disorder in such a way that 60 % of the cation complexes show disposition A and 40 % disposition B along the crystal network.

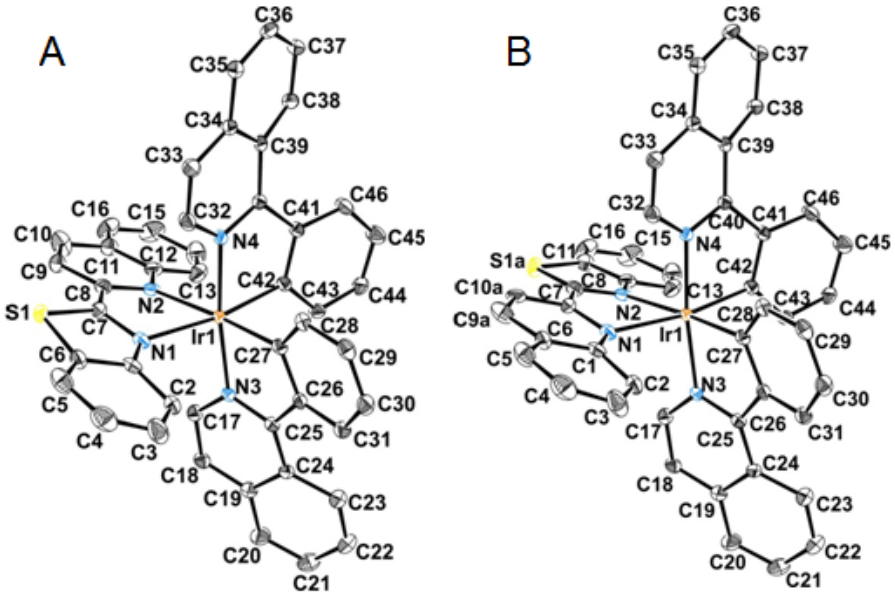

Figure 7.S1: Disposition A and B in the crystal structure.

Table 7.S6: Hydrogen bonds for **[Rh-2]**$PF_6 \cdot CH_2Cl_2$ by MERCURY 3.0 program.

Interaction (Rings)	$dD---A$, Å	d_H---A, Å	DHA, °
C(15)-H(15)—F(2)	3.210	2.644	118.74
C(16)-H(16)—F(2)	3.135	2.471	126.84
C(2)-H(2)—F(6)	3.227	2.593	124.50
C(13)-H(13)—O(1)	2.836	2.536	127.93

Table 7.S7: Anion-π interaction in the crystal structure of **[Rh-2]**$PF_6 \cdot CH_2Cl_2$ by MERCURY 3.0 program.

$\pi - \pi$ **Interaction (Rings)**	d_{centr}, Å	d_{pl}, Å	α, °
PF_6—N(3)C(13)-C(16)	3.086	3.018	77.43

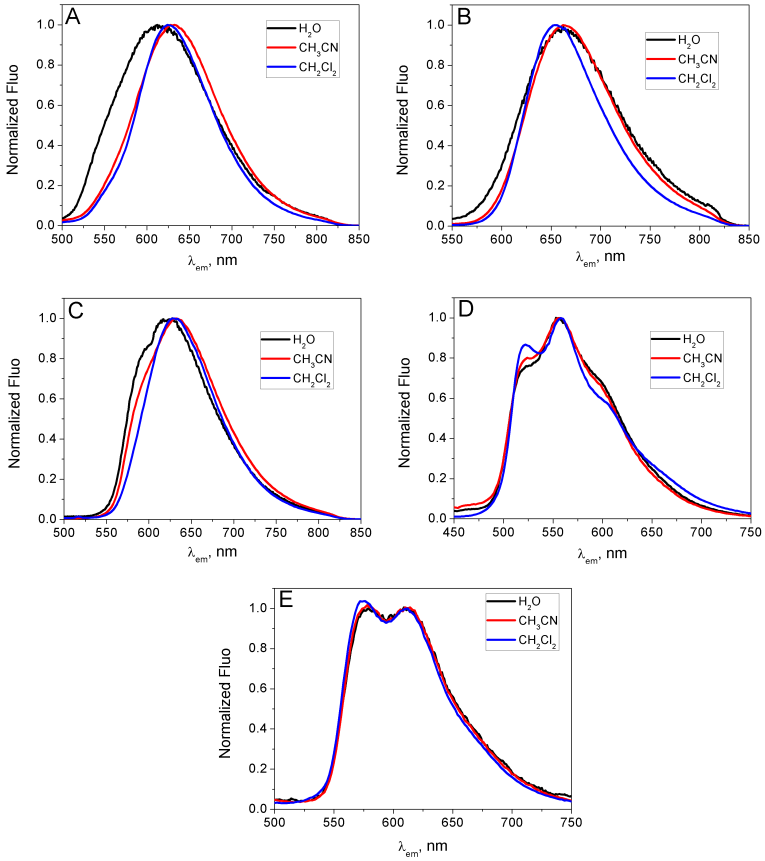

Figure 7.S2: Emission spectra of the metal complexes in water, acetonitrile and dichloromethane. (A) **[Ir-2]**Cl. (B) **[Ir-3]**Cl. (C) **[Ir-4]**Cl. (D) **[Rh-2]**Cl. (A) **[Rh-4]**Cl. T=25.0 °C.

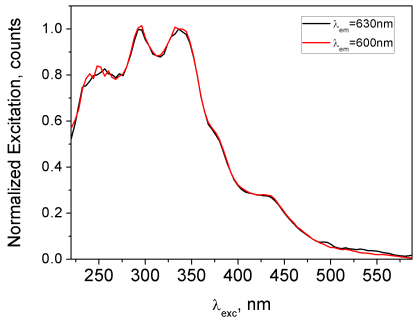

Figure 7.S3: Excitation profile of **[Ir-4]**Cl at two different emission wavelength, λ_{em}=600 nm and λ_{em}=630 nm in water. T=25.0 °C.

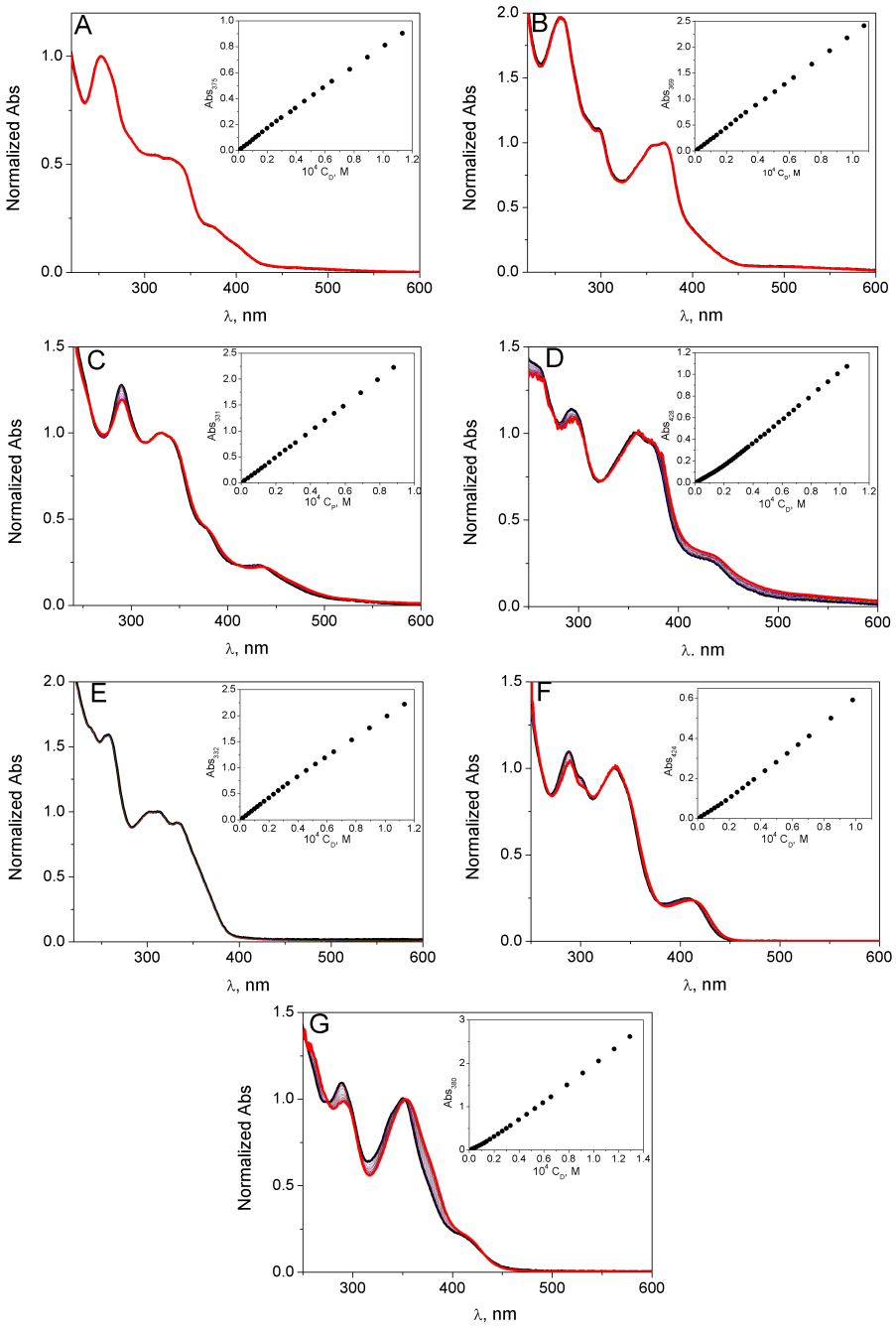

Figure 7.S4: Normalized spectra for dimerization; inset: absrobance track at increasing C_D. (A) **[Ir-2]**Cl. (B) **[Ir-3]**Cl. (C) **[Ir-4]**Cl. (D) **[Ir-5]**Cl. (E) **[Rh-2]**Cl. (F) **[Rh-4]**Cl. (G) **[Rh-5]**Cl. I=6.5 × 10^{-3} M, pH=7.0 and T=25.0 °C.

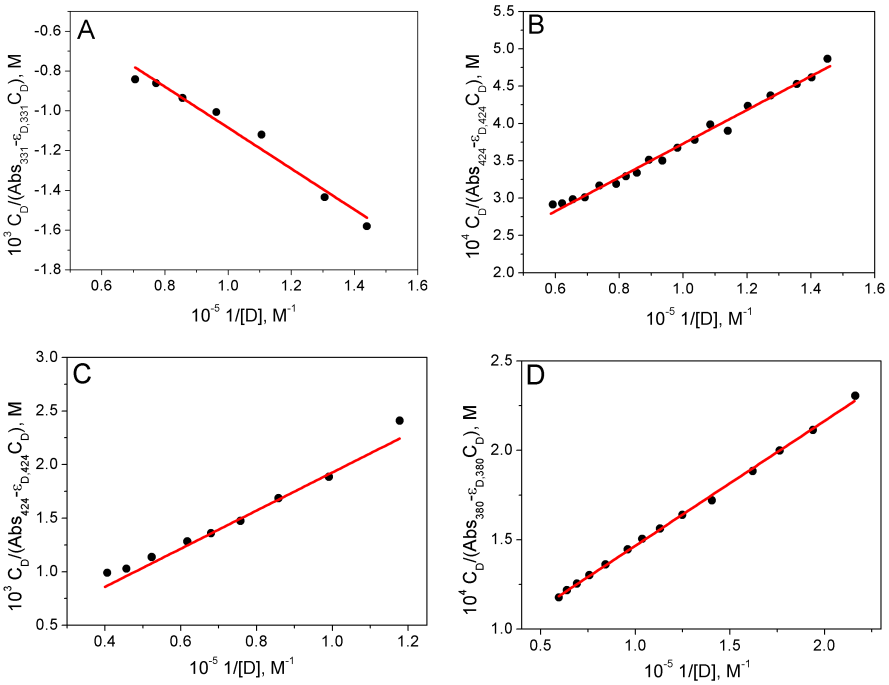

Figure 7.S5: Data treatment by means of Equation (2.67). (A) **[Ir-4]**Cl. (B) **[Ir-5]**Cl. (C) **[Rh-4]**Cl. (D) **[Rh-5]**Cl. I=6.5 × 10^{-3} M, pH=7.0 and T=25.0 °C.

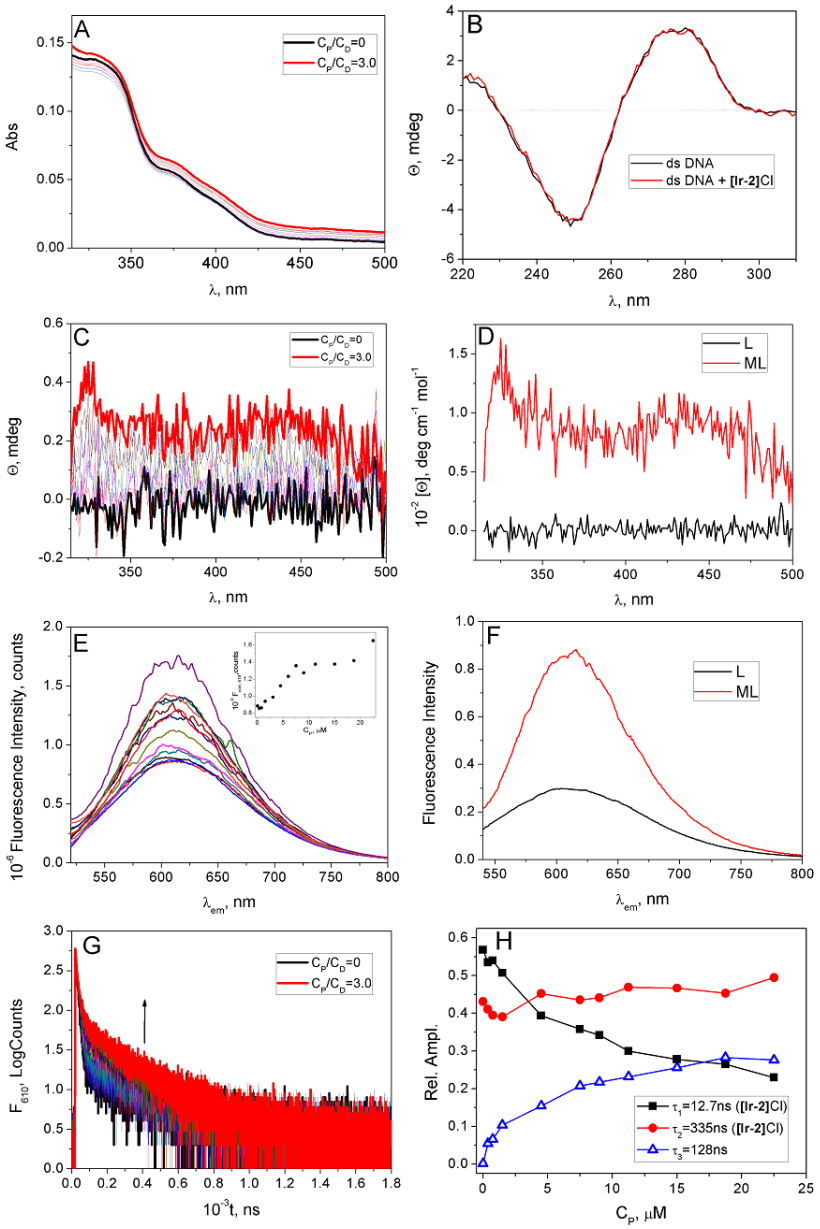

Figure 7.S6: **[Ir-2]**Cl/52B titration. (A) Uv-vis absorption spectra. (B) UV circular dichroism, C_P=7.5 × 10^{-7} M, C_D=7.5 × 10^{-6} M. (C) Induced Circular dichroism in the UV-vis range. (D) Calculated circular dichroism of L and ML in the UV-vis range. (E) Fluorescence titration, λ_{ex}=340 nm; inset: track at λ_{exc} = 610 nm. (F) Calculated emission spectra of L and ML. (G) Fluorescence decays, λ_{ex}=331 nm, λ_{em}=630 nm, peak preset 600 counts, time calibration 0.439 ns/channel, time range 1.6 µs. (H) Relative amplitudes of the lifetimes (for free **[Ir-2]Cl** τ=12.7, 335 ns). C_D=7.5 × 10^{-6} M, C_P=0-2.2 × 10^{-5} M, I=0.1 M (KCl), pH=7.0 (phosphate buffer) and T=25 °C.

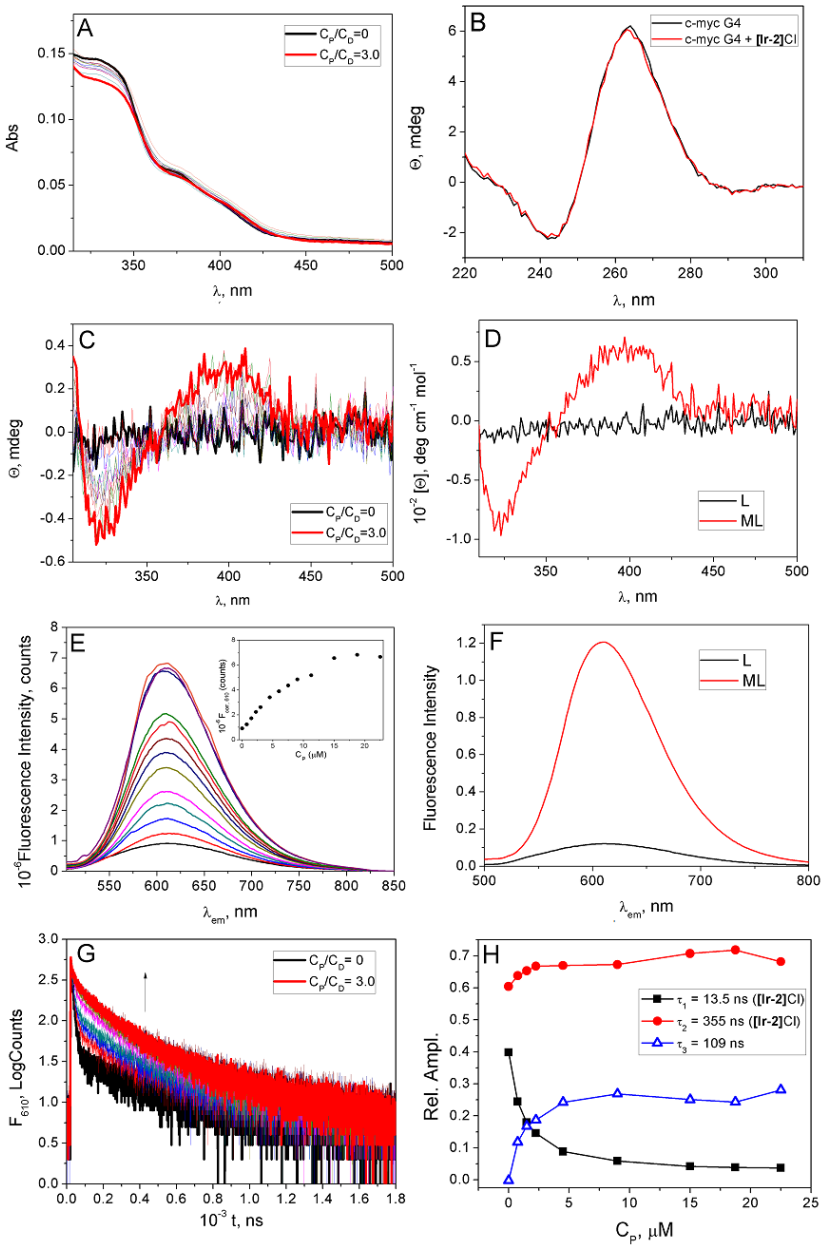

Figure 7.S7: **[Ir-2]**Cl/Pu22 titration. (A) Uv-vis absorption spectra. (B) UV circular dichroism, C_P=7.5 × 10^{-7} M, C_D=7.5 × 10^{-6} M. (C) Induced Circular dichroism in the UV-vis range. (D) Calculated circular dichroism of L and ML in the UV-vis range. (E) Fluorescence titration, λ_{ex}=375 nm; inset: track at λ_{em}=610 nm. (F) Calculated emission spectra of L and ML. (G) Fluorescence decays, λ_{ex}=373 nm, λ_{em}=610 nm, peak preset 600 counts, time calibration 0.439 ns/channel, time range 1.6 μs. (H) Relative amplitudes of the lifetimes (for free **[Ir-2]Cl** τ=13.5 (fixed), 355 ns (fixed)). C_D=7.5 × 10^{-6} M, C_P=0-2.2 × 10^{-5} M, I=0.1 M (KCl), pH=7.0 (phosphate buffer) and T=25 °C.

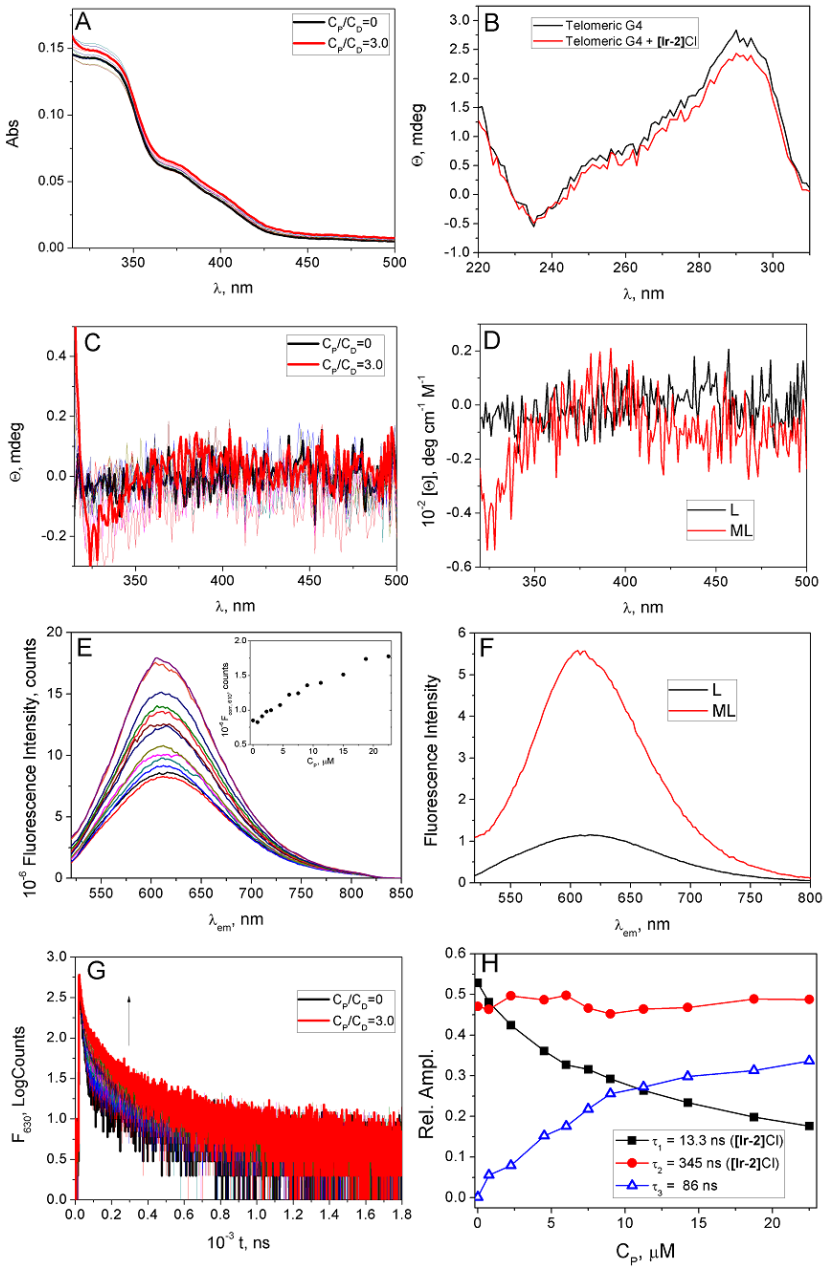

Figure 7.S8: **[Ir-2]**Cl/Tel22 titration. (A) Uv-vis absorption spectra. (B) UV circular dichroism, C_P=7.5 × 10^{-7} M, C_D=7.5 × 10^{-6} M. (C) Induced Circular dichroism in the UV-vis range. (D) Calculated circular dichroism of L and ML in the UV-vis range. (E) Fluorescence titration, λ_{ex}=375 nm; inset: track at λ_{em}=610 nm. (F) Calculated emission spectra of L and ML. (G) Fluorescence decays, λ_{ex}=373 nm, λ_{em}=610 nm, peak preset 600 counts, time calibration 0.439 ns/channel, time range 1.6 µs. (H) Relative amplitudes of the lifetimes (for free **[Ir-2]Cl** τ=13.3 (fixed), 345 ns (fixed)). C_D=7.5 × 10^{-6} M, C_P=0-2.2 × 10^{-5} M, I=0.1 M (KCl), pH=7.0 (phosphate buffer) and T=25 °C.

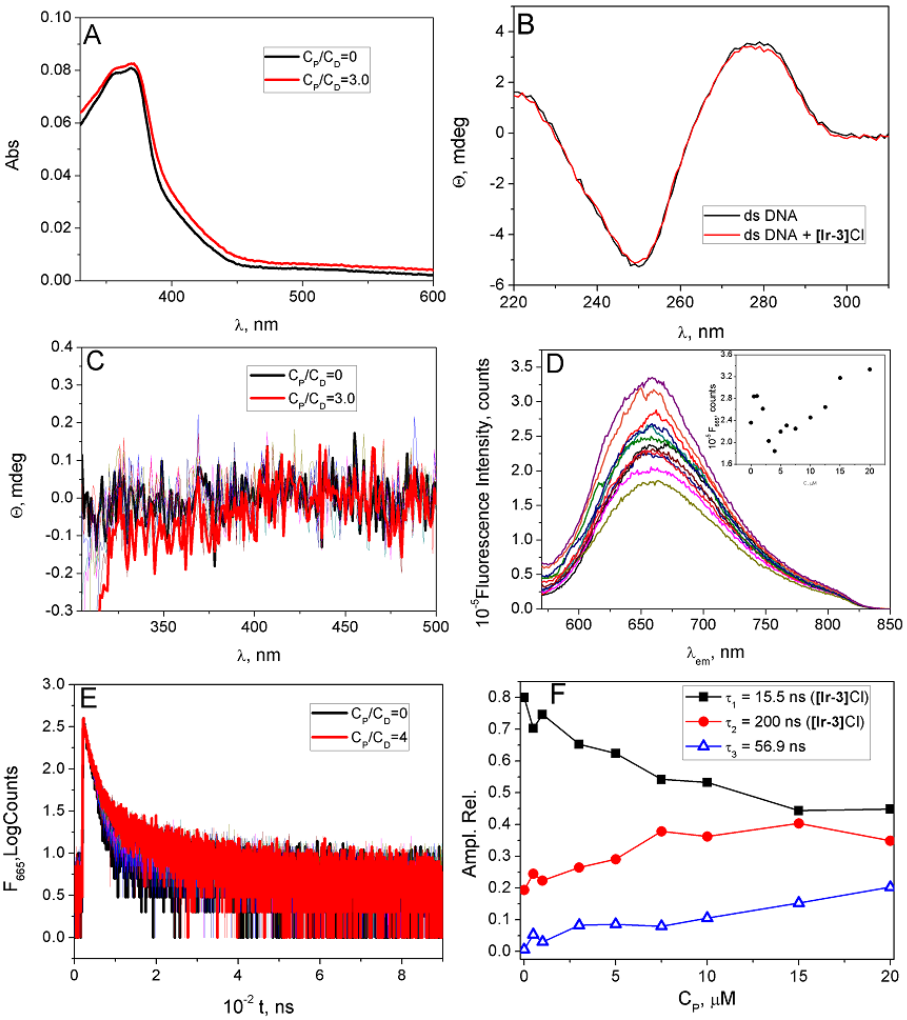

Figure 7.S9: **[Ir-3]**Cl/52B titration. (A) Uv-vis absorption spectra. (B) UV circular dichroism, C_P=5.0 × 10^{-7} M, C_D=5.0 × 10^{-6} M. (C) Induced Circular dichroism in the UV-vis range. (D) Fluorescence titration, λ_{ex}=369 nm; inset: track at λ_{em}=660 nm. (E) Fluorescence decays, λ_{ex}=373 nm, λ_{em}=610 nm„ peak preset 600 counts, time calibration 0.219 ns/channel, time range 0.8 µs. (F) Relative amplitudes of the lifetimes (for free **[Ir-3]Cl** τ=16.0, 208 ns (fixed)). C_D=5.0 × 10^{-6} M, C_P=0-2.0 × 10^{-5} M, I=0.1 M (KCl), pH=7.0 (phosphate buffer) and T=25 °C.

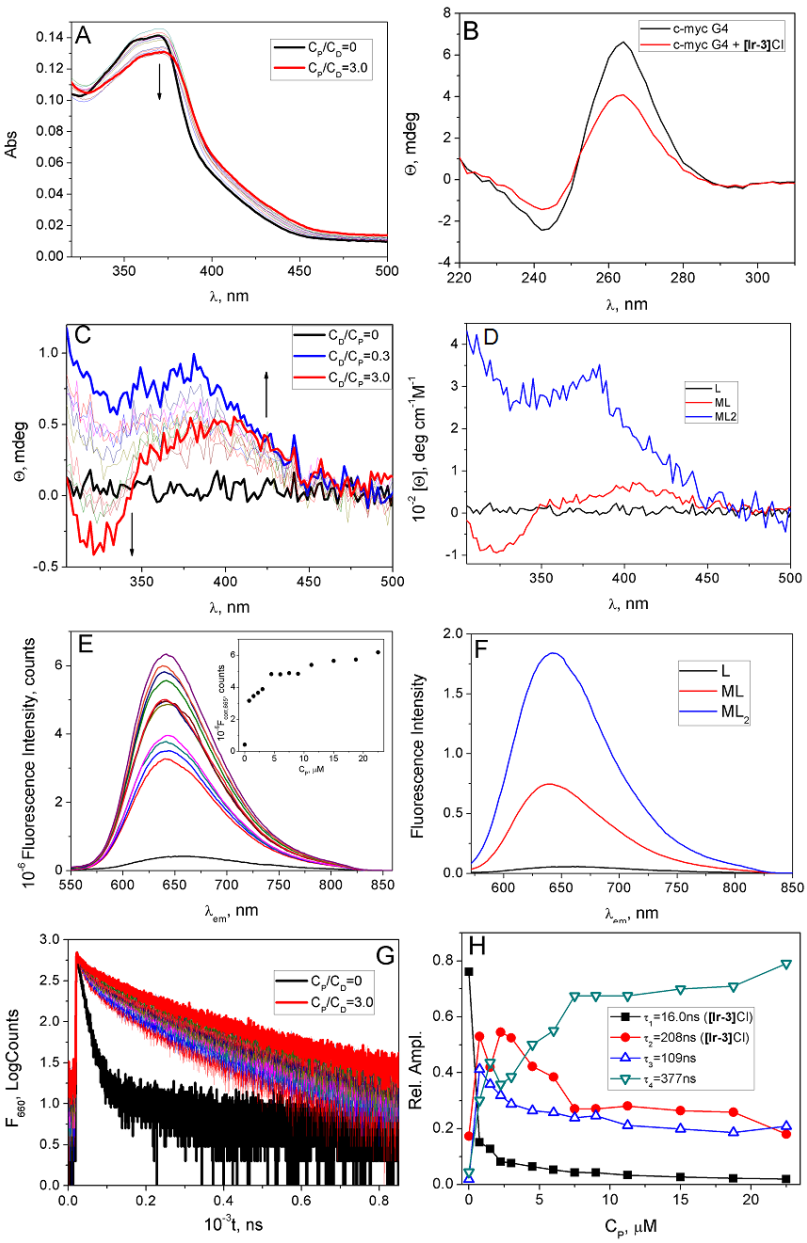

Figure 7.S10: **[Ir-3]**Cl/Pu22 titration. (A) Uv-vis absorption spectra. (B) UV circular dichroism, C_P=7.5 × 10^{-7} M, C_D=7.5 × 10^{-6} M. (C) Induced Circular dichroism in the UV-vis range. (D) Calculated circular dichroism of L, ML and ML_2 in the UV-vis range. (E) Fluorescence titration, λ_{ex}=400 nm; inset: track at λ_{em}=660 nm. (F) Calculated emission spectra of L, ML and ML_2. (G) Fluorescence decays, λ_{ex}=373 nm, λ_{em}=660 nm, peak preset 700 counts, time calibration 0.219 ns/channel, time range 0.8 µs. (F) Relative amplitudes of the lifetimes (for free **[Ir-3]Cl** τ=15.5 (fixed), 200 ns (fixed)). C_D=7.5 × 10^{-6} M, C_P=0-2.2 × 10^{-5} M, I=0.1 M (KCl), pH=7.0 (phosphate buffer) and T=25 °C.

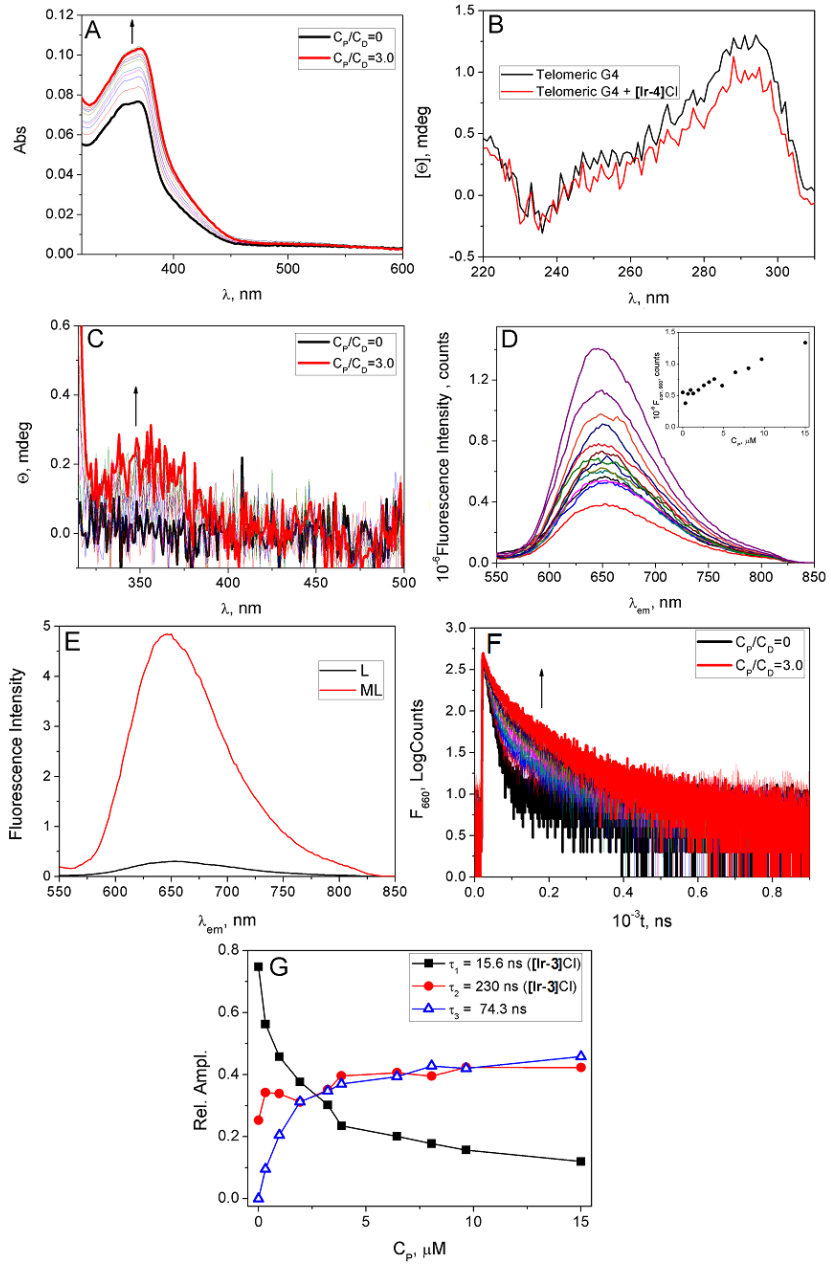

Figure 7.S11: **[Ir-3]**Cl/Tel22 titration. (A) Uv-vis absorption spectra. (B) UV circular dichroism, C_P=5.0 × 10^{-7} M, C_D=5.0 × 10^{-6} M. (C) Induced Circular dichroism in the UV-vis range. (D) Fluorescence titration, λ_{ex}=400 nm; inset: track at λ_{em}=660 nm. (E) Calculated emission spectra of L and ML. (F) Fluorescence decays, λ_{ex}=373 nm, λ_{em}=660 nm, peak preset 600 counts, time calibration 0.219 ns/channel, time range 0.8 µs. (G) Relative amplitudes of the lifetimes (for free **[Ir-3]Cl** τ=15.6, 230 ns). C_D=5.0 × 10^{-6} M, C_P=0-1.5 × 10^{-5} M, I=0.1 M (KCl), pH=7.0 (phosphate buffer) and T=25 °C.

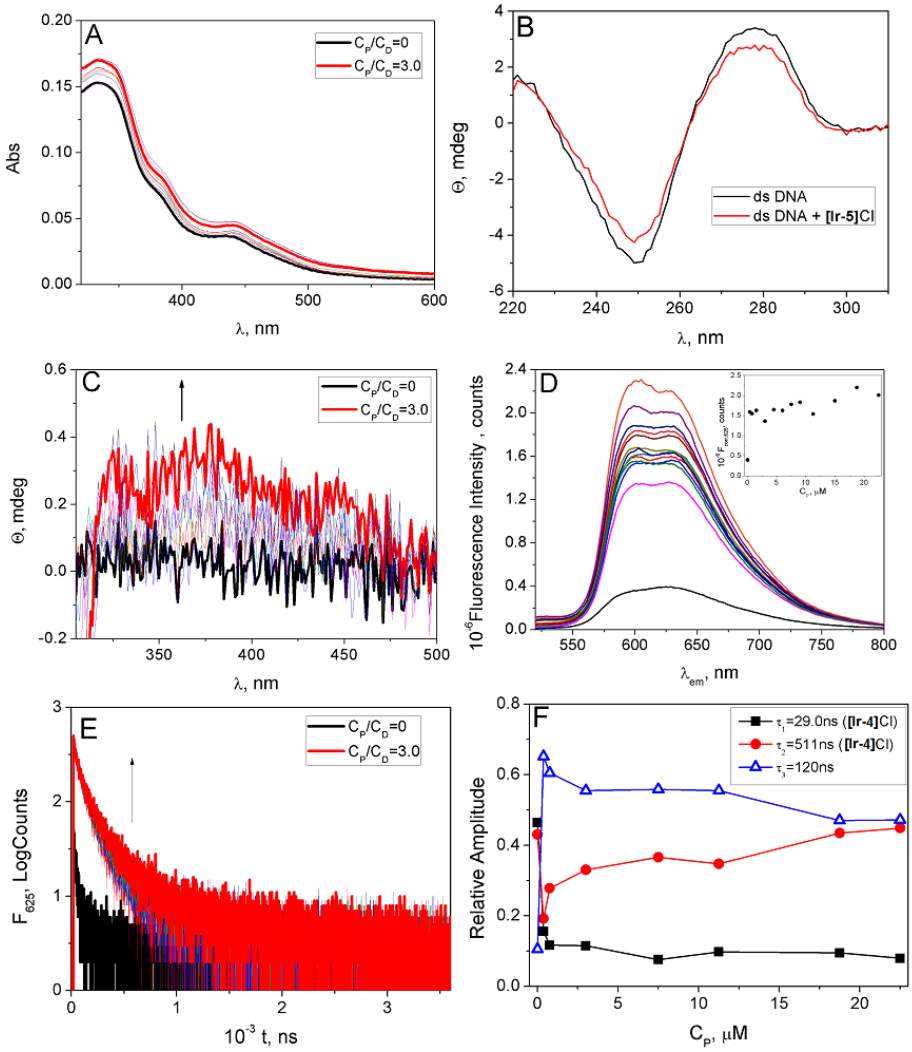

Figure 7.S12: **[Ir-4]**Cl/52B titration. (A) Uv-vis absorption spectra. (B) UV circular dichroism, C_P=7.5 × 10^{-7} M, C_D=7.5 × 10^{-6} M. (C) Induced Circular dichroism in the UV-vis range. (D) Fluorescence titration, λ_{ex}=335 nm; inset: track at λ_{em}=630 nm. (E) Fluorescence decays, λ_{ex}=331 nm, λ_{em}=630 nm, peak preset 500 counts, time calibration 0.439 ns/channel, time range 1.6 µs. (F) Relative amplitudes of the lifetimes (for free **[Ir-4]Cl** τ=29.0 (fixed), 511 ns (fixed)). C_D=7.5 × 10^{-6} M, C_P=0-2.2 × 10^{-5} M, I=0.1 M (KCl), pH=7.0 (phosphate buffer) and T=25 °C.

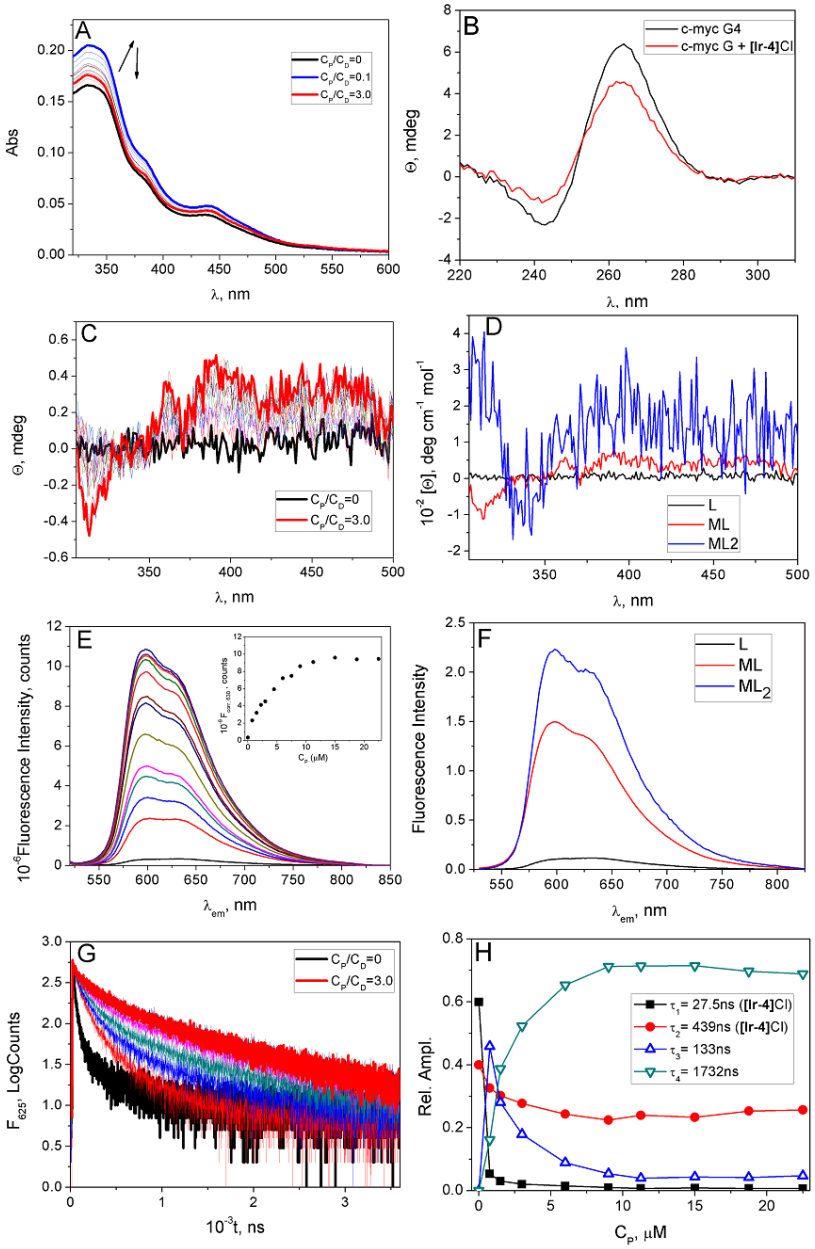

Figure 7.S13: **[Ir-4]**Cl/Pu22 titration. (A) Uv-vis absorption spectra. (B) UV circular dichroism, C_P=7.5 × 10^{-7} M, C_D=7.5 × 10^{-6} M. (C) Induced Circular dichroism in the UV-vis range. (D) Calculated circular dichroism of L, ML and ML_2 in the UV-vis range. (E) Fluorescence titration, λ_{ex}=438 nm; inset: track at λ_{em}=630 nm. (F) Calculated emission spectra of L, ML and ML_2. (G) Fluorescence decays, λ_{ex}=373 nm, λ_{em}=625 nm, peak preset 600 counts, time calibration 0.879 ns/channel, time range 3.2 μs. (H) Relative amplitudes of the lifetimes (for free **[Ir-4]Cl** τ=27.5, 439 ns). C_D=7.5 × 10^{-6} M, C_P=0-2.2 × 10^{-5} M, I=0.1 M (KCl), pH=7.0 (phosphate buffer) and T=25 °C.

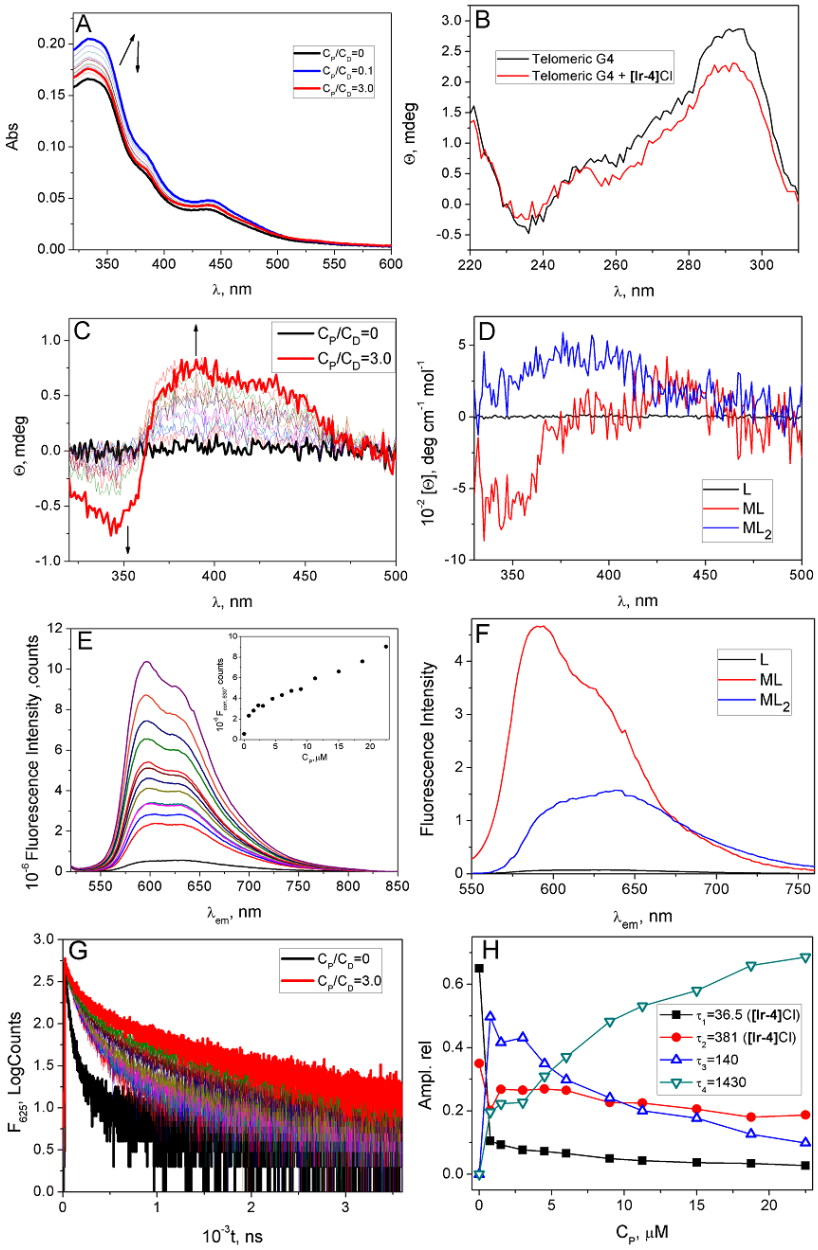

Figure 7.S14: **[Ir-4]**Cl/Tel22 titration. (A) Uv-vis absorption spectra. (B) UV circular dichroism, C_P=7.5 × 10^{-7} M, C_D=7.5 × 10^{-6} M. (C) Induced Circular dichroism in the UV-vis range. (D) Calculated circular dichroism of L and ML in the UV-vis range. (E) Fluorescence titration, λ_{ex}=438 nm; inset: track at λ_{exc}=610 nm. (F) Calculated emission spectra of L, ML and ML_2. (G) Fluorescence decays, λ_{ex}=373 nm, λ_{em}=625 nm, peak preset 600 counts, time calibration 0.879 ns/channel, time range 3.2 µs. (H) Relative amplitudes of the lifetimes (for free **[Ir-4]Cl** τ=36.5 (fixed), 381 ns (fixed)). C_D=7.5 × 10^{-6} M, C_P=0-2.2 × 10^{-5} M, I=0.1 M (KCl), pH=7.0 (phosphate buffer) and T=25 °C.

Overall Conclusions

In the present Thesis we treated the thermodynamic and kinetic interactions of inorganic and organometallic species with nucleic acids, the most investigated targets inside the cell.
In Part I, it is showed the stabilization study of aluminium ion in aqueous media by means of the dimethylarsinate anion, with the formation of a dimeric species, enabling aluminium to remain in solution (Chapter 3). This finding allowed the study of aluminium with RNA and it has been observed how a trivalent cation can modify the secondary structure of a polynucleotide (Chapter 4). In particular, it has been demonstrated that aluminium can induce aggregation even to RNA strands.
In Part II, we focused on the way of binding of organometallic complexes with DNA. The importance of the metal center and the ligands bound to it is evident by our studies. Ancillary ligands rules the reversible way of binding to DNA. For example, for the ruthenium arene complex the ancillary ligand promotes the minor groove binding (Chapter 5), whereas the benzoxazole ligand of the biscyclometalated complexes favours a partial intercalation of the systems (Chapter 6). Moreover, we verified how the ligand can determine selectivity towards different secondary structures of DNA (Chapter 7); in particular, for the new synthesized family of biscyclometalated complexes, the increase of the aromatic size of the cyclometalating and of the ancillary ligands enhances the selectivity towards non-canonical G-Quadruplex structure, together with high thermal stabilization of these forms. On the other side, the collected data suggest that the metal center plays only a modest role in the reversible interaction with DNA. However, the metal center is the main cause of the photophysical properties of the molecule. Actually, it determines the lowest excited state, which is essential for the luminescence processes. Ligands provide certain contribution on the emissive properties (lifetime, quantum yield and so on), but it is minority respect to the metal ion. But photophysical properties means also photoreactivity of the molecule, and we observed how the metal center has a relevant role on it. Rhodium complexes display promising singlet oxygen quantum yields in water, whereas Iridium does not, and a relation between singlet oxygen production and lifetime in water was found. Surely, the ligands can promote the photoreactivity of the metal complex, as well, by increasing the absorption at longer wavelengths, the lifetime and, overall, the interaction with the molecule. Actually, we have observed how the increase of the affinity towards the target modifies the photophysical properties of the molecules, namely its fluorescence and lifetime and, consequently, it could have some influence on the photoreactivity. Hence, all the studied properties, fluorescence, absorbance, affinity constants are closely linked together, and all of them contribute to the overall reactivity. To conclude, between the Rh and

Ir center, the Ir center seems to have the most promising properties. Actually, even though Rh complexes exhibit the highest effect of photoreactivity in the ultraviolet region, they lack the property which PDT is looking for, namely the photoactivation at low-energetic wavelengths. On the other hand, Ir center provides the molecule an interesting fluorescence, which can be switched-on by interaction, and the presence of suitable ligands can improve the photoreactivity of such species, even in the visible region ($\lambda_{ex} = 500\,\mathrm{nm}$).

Articles and Congresses

The work in the laboratory resulted, at the present, into two scientific articles in peer-reviewed journals and various contributions national and international congresses:

- **Articles**
  - *Binding of Aluminum/Cacodylate Complexes with DNA and RNA. Experimental and "in Silico" Study.* H. Lozano, N. Busto, M. Lari, J. M. Leal and B. García, SUBMITTED to New Journal of Chemistry, 4 th December 2017.
  - *Binding of Al(III) to Synthethic RNA. Metal-Mediated Strand Aggregation.* M. Lari, T. Biver, N. Busto, H. Lozano, J. M. Leal, F. Secco and B. García (2017), Dalton Transactions, 46, 16671-16681.
  - *Stabilization of Al(III) Solutions by Complexation with Cacodylic Acid: Speciation and Binding Features.* M. Lari, H. Lozano, N. Busto, T. Biver, J.M. Leal, S. Ibeas, J. A. Platts, F. Secco and B. García (2015), Physical Chemistry Chemical Physics, 17 (44), 29803-29813.
- **Congresses**
  - Oral Communication *New Bis-Cyclometalated Metal Complexes Coordinated to Heteroaromatic Ancillary Ligands: Photoreactivity and Selective Binding to G-Quadruplexes*, M. Lari, N. Busto, M. Martinez-Alonso, H. Lozano, G. Espino, J. M. Leal, B. García (2017), ISMEC 2017, 12 - 15 June, Dijon, France.
  - Poster Presentation *Photoreactivity of Newly Synthesized Cyclometalated Complexes: Effect of the Metal Centre*, M. Lari, M. Martinez-Alonso, N. Busto, G. Espino, J. M. Leal, B. García (2016), XIII EuroBIC, 28 August - 1 September, Budapest, Hungary.
  - Poster Presentation *Photocleavage and Chemical Properties of Arene-Organometallic Complexes depend of the Metal Center*, B. García, N. Busto, M. Lari, A. R. Rubio, C. Pérez, H. J. Lozano, J. M. Leal, M. Martinez-Alonso, G. Espino, (2016), ISMEC 2016, 7 - 10 June, Barcelona, Spain.
  - Poster Presentation *Plasmidic DNA Cleavage of a New Arene Ru(II) Hydrophenyl-benzothiazole derivative*, M. Lari, M. Martinez-Alonso, N. Busto, G. Espino, J. M. Leal, B. García (2015), ISMEC 2015, 24 - 28 June, Wroclaw, Poland.

- Oral Communication *Complejos Organometalicos de Ru(II) y su interacción con ADN*, N. Busto, J. Valladolid, H. J. Lozano, M. Lari, M. Martinez-Alonso, G. Espino, B. García (2015), IX Reunion Cientifica de Bioinorganica, 14 - 17 June, Cadiz, Spain.
- Poster Presentation *Anticancer Activity and Mechanistic Insights of New Ru(II) Half-Sandwich Complexes with Hydroxyphenylbenzazole Ligands*, M. Martinez-Alonso, M. Lari, G. Espino, B. García, A. M. Rodriguez, F. A. Jalón (2015), ISABC 13, 12 - 15 June, Galway, Ireland.
- Poster Presentation *Stabilisation and Nucleic Acids Binding of a +3 Ion: the Aluminium/Cacodylate/RNA System*, T. Biver, N. Busto, B. García, M. Lari, J. M. Leal, H. J. Lozano, F. Secco, M. Venturini (2014), XII EuroBIC, 24 - 28 August, Zurich, Switzerland.